PET Radiochemistry for the Investigation of the biology of pain and inflammation

A thesis submitted to the University of Manchester for the degree of PhD in the Faculty of Medical and Human Sciences

2015

Michael Fairclough

School of Medicine

Institute of Population Health, Imaging Sciences

Contents

Total Word Count **63,192**

Abbreviations

[^{11}C]BPN	[^{11}C]buprenorphine
[^{11}C]CH_3I	[^{11}C]methyl iodide
[^{11}C]CH_3OH	[^{11}C]methanol
[^{11}C]CH_3OTf	[^{11}C]methyl triflate
[^{11}C]CH_4	[^{11}C]methane
[^{11}C]CO_2	[^{11}C]carbon dioxide
[^{11}C]DPN	[^{11}C]diprenorphine
[^{18}F]DPN	6-*O*-(2-[^{18}F]fluoroethyl)-6-*O*-desmethyldiprenorphine
[^{18}F]F^-	[^{18}F]fluoride
[^{18}F]F_2	[^{18}F]fluorine
[^{18}F]FBA	[^{18}F]fluorobenzaldehyde
[^{18}F]FBEM	N-[2-(4-^{18}F-fluorobenzamido)ethyl]maleimide
[^{18}F]FDG	[^{18}F]fluorodeoxyglucose
[^{18}F]FEtTos	[^{18}F]fluoroethyltosylate
[^{18}F]SFB	N, succinimidyl-[^{18}F]fluorobenzoate
[^{64}Cu]PTSM	[^{64}Cu]-pyruvaldehyde-bis(N4-methylthiosemi-carbazone)
^{111}In	indium-111
^{11}C	carbon-11
^{15}O	oxygen-15
^{18}F	fluorine-18
^{64}Cu	copper-64
^{89}Zr	zirconium-89
^{99m}Tc	technetium-99
ACC	anterior cingulate cortex
ACD	acid citrate dextrose
ACR	American college of Rheumatology
AGC	automatic gamma counter
AgOTf	silver triflate
AMPA	α-amino-3-hydroxyl-5-methyl-4-isoxazole-propionate
APN	aminopeptidase N
Asn	asparagine
Asp	aspartic acid

ATP	adenosine triphosphate
BBB	blood brain barrier
BGO	bismuth germanate
BNTX	benzylidenenaltrexone
BPN	buprenorphine
cAMP	3’-5’-cyclic adenosine monophosphate
CBs	cannabinoids
CFP	cell-free plasma
CHCA	α-cyano-4-hydroxycinnamic acid
CN	chitosan nanoparticles
CNS	central nervous system
CT	computed tomography
CTOP	D-Phe-Cys-Tyr-D-Trp-Orn-Thr-Pen-Thr-NH2
DADLE	[D-Ala^2, D-Leu^5] enkephalin
DAMGO	[D-Ala^2, N-MePhe^4, Gly-ol]-enkephalin
DD	degree of deacetylation
DFO	desferrioxamine
DFO-Bz-NCS	*p*-isothiocyanatobenzyl-DFO
DFT	density function theory
DIPPA	2-(3,4-dichlorophenyl)-*N*-methyl-*N*-[1S-1-(-3-isothiocyanatophenyl)-2-(-1-pyrrolidinyl) ethyl] acetamide
DLS	dynamic light scattering
DMARDs	disease-modifying antirheumatic drugs
DMF	dimethylformamide
DMSO	dimethyl sulfoxide
DOCK^{40}	computer automated docking simulation
DOTA	1,4,7,10-tetraazacyclododecane-N,N',N",N'"-tetraacetic acid
DPDPE	[D-Pen2, D-Pen5]-enkephalin
DPN	diprenorphine
DSLET	Tyr-D-Ser-Gly-Phe-Leu-Thr
DTT	dithiothreitol
*E*ave(β^+)	β^+ average kinetic energy
EC_{50}	half maximal effective concentration
EDTA	ethylenediaminetetraacetic acid

EEG	electroencephalography
Emax(β^+)	β^+ maximum kinetic energy
FAAH	fatty acid amide hydrolase
fMRI	functional magnetic resonance imaging
GDP	guanosine-5'-diphosphate
GLLS	generalised linear least square
Glu	glutamic acid
gNTI	guanidinylnaltrindole
GPCRs	G-protein coupled receptors
GTP	guanosine-5'-triiphosphate
H_2O_2	hydrogen peroxide
HMPAO	hexamethylpropyleneamine oxime
HPLC	high performance liquid chromatography
HRRT	High Resolution Research Tomograph
ICBM	international consortium for brain mapping
IL-1	interleukin-1
IL-1R	interleukin-1 receptors
IL-1RA	interleukin-1 receptor antagonist
IL-1RAcP	interleukin-1 receptor accessory protein
IL-1RI	interleukin-1 receptor type I
IL-1RII	interleukin-1 receptor type II
IL-1α	interleukin-1 alpha
IL-1β	interleukin-1 beta
$K1_{DPN}$	[^{11}C]DPN rate of uptake from blood to tissue
K_{222}	Kryptofix-222
K_2CO_3	potassium carbonate
K_a	association constant
$LiAlH_4$	lithium aluminium hydride
LOR	line of response
LRPRP	leukocyte-rich platelet-rich plasma
mAb	monoclonal antibody
MALDI-MS	matrix-assisted laser desorption/ionisation mass spectroscopy
MeCN	acetonitrile
MPQ	McGill pain questionnaire

MPRAGE	magnetization prepared rapid gradient echo sequence
MRI	magnetic resonance imaging
MTT	3-(4,5-dimethylthiazol-2-yl)-2,5-diphenyltetrazolium bromide
N-[^{11}C]BPN	*N*-cyclopropyl[^{11}C]methyl-buprenorphine
N-[^{11}C]DPN	*N*-cyclopropyl[^{11}C]methyl-diprenorphine
NaH	sodium hydride
NEP	neprilysin
NMDA	N-methyl-D-aspartic acid
nor-BNI	nor-binaltorphimine
NOTA	1,4,7-triazacyclononane-N,N',N''-triacetic acid
NRS	numerical rating scale
NS	non-specific binding
NSAIDs	nonsteroidal anti-inflammatory drugs
N-suc-DFO-TFP-ester	*N*-succinyl-DFO-tetrafluorophenol ester
NTB	naltriben
NTI	naltrindole
NTII	NTI 5’ isothiocyanate
OA	osteoarthritis
OpRs	opioid receptors
ORL-1	opioid receptor like
Oxine	8-hydroxyquinoline
PBS	phosphate buffered saline
PEG	polyethylene glycol
PEI	polyethyleneimine
PET	positron emission tomography
PGP	P-glycoprotein pump
PRP	platelet-rich plasma
RA	rheumatoid arthritis
rCBF	regional cerebral blood flow
rhIL-1RA	recombinant human interleukin-1 receptor antagonist
ROI	regions-of-interest
S1	primary somatosensory corticies
S2	secondary somatosensory corticies
SAH	subarachnoid haemorrhage

sar	sarcophagine
SDS-PAGE	sodium dodecyl sulphate polyacrylamide gel electrophoresis
SE-HPLC	size exclusion HPLC
SEM	scanning electron microscope
sIL-1RAcP	soluble interleukin-1 receptor accessory protein
sIL-1RI	soluble interleukin-1 receptor type I
sIL-1RII	soluble interleukin-1 receptor type II
SIOM	7-Spiroindanyloxymorphone
S_N2	bi-molecular nucleophilic substitution
S_NAr	nucleophilic aromatic substitution
SNC80	4-[(*R*)-[(2*S*,5*R*)-4-allyl-2,5-dimethylpiperazin-1-yl](3-methoxyphenyl)methyl]-*N*,*N*-diethylbenzamide
SPE	solid phase extraction
Spe	specific binding
SPECT	single-photon cemission computed tomography
SPIONs	super-paramagnetic iron oxide nanoparticles
SPM8	Statistical Parametric Mapping
$t_{½}$	half-life
TCEP	*tris*(2-carboxyethyl)phosphine
THF	tetrahydrofuran
TIPP	[(H-Tyr-Tic-Phe-Phe-OH)]
TNF	tumor necrosis factor
Tot	total binding
TPP	pentasodium tripolyphosphate
Trityl	triphenylmethyl
TRPV1+	transient receptor+ potential ion channels
TSPO	translocator protein
UGT	uridine glucuronosyl transferase
VD	volume of distribution
VD_{DPN}	[^{11}C]DPN volume-of-distribution
WBC	white blood cells
β^+	positron
β-FNA	β-funaltrexamine

List of Figures

List of Tables

List of Equations

Abstract

University of Manchester for the degree of PhD medicine (PopHealth) in the Faculty of Medical and Human Sciences.

Michael Fairclough

PET Radiochemistry for the Investigation of the biology of pain and inflammation

28/03/2015

Positron emission tomography (PET) is an important and powerful nuclear imaging modality and is essential in a range of medical fields. A suitable radiotracer must be identified in order for PET imaging to provide high quality and quantifiable data about the pathology. This includes the design and implementation of optimal radiochemistry that will reliably deliver the radiotracer that can answer the pertinent biological questions being asked.

PET can be used to study the biological processes which are involved in pain perception and inflammatory responses that can occur in a number of chronic and acute conditions. This thesis aims to demonstrate how PET radiochemistry can enhance our knowledge of these biological processes and permits access to the underlying molecular mechanisms behind pain and inflammation.

This thesis has been written in an alternative format, comprising the different areas which have been investigated. The work encompasses the study of the endogenous opioid system using the opioid receptor antagonist [^{11}C]diprenorphine. This includes the design and automation of [^{11}C]diprenorphine radiochemistry followed by the development of a method to reliably analyse its metabolism. Finally the application of [^{11}C]diprenorphine in a clinical PET study, investigating opioid receptor occupancy by endogenous opioids as well as up-regulation of opioid receptors in the brain, is described.

In the study of inflammation a pro-inflammatory cytokine, recombinant human interleukin-1 receptor antagonist (rhIL-1RA), was radiolabelled with novel ^{18}F radiochemistry permitting pharmacokinetic study in pre-clinical models. This is followed by the design of a new technique to radiolabel white blood cells with ^{89}Zr for quantifiable cell trafficking with PET. For this technique, chitosan nanoparticles are used to deliver the radio-metal cargo into white blood cells with a proposed application in inflammatory models. The process of chitosan nanoparticle construction is described alongside development of a procedure that is optimised for use in the proposed application.

This thesis covers a variety of topics illustrating the contribution of PET radiochemistry in the area of pain and inflammation. The synergy between identification of new biological targets and development of radiotracers and radiolabelling strategies ensure PET radiochemistry will continue to contribute to our knowledge of pain and inflammation and aid understanding of its role in countless medical conditions.

Declaration

No portion of the work referred to in the thesis has been submitted in support of an application for another degree or qualification of this or any other university or other institute of learning.

Copyright Statement

Dedication

This thesis is dedicated to my parents; my mum, Jean, who has always been my biggest inspiration and has always believed in me and supported me throughout my life. My dad, Eddie, who I wish could have been alive today so that I could show him how his love and support has brought me to this point in my life.

This thesis is also dedicated to my friends Si and Gibbo who have always given me their support, wise words and necessary beer consumption as experiments have gone awry or results have seemed unexplainable.

Finally I would like to dedicate this thesis to my wonderful partner Olivia (my Livvy). She has put up with my moaning and panicking, but without her love and support I would never have made it to this point. I love you all very much.

X

Special thanks must also go to my supervisory team, Adam, Christian, Gavin, Herve and Anthony as well as the Radiochemistry and QC teams at WMIC especially Mike.

CHAPTER 1: Introduction (Part 1) – The endogenous opiate system

Pain in Rheumatoid Arthritis

Pain is part of the body's defence system, the sensation of pain encourages the body to remove itself from potentially damaging (noxious) stimuli, protects the damaged tissue area as it heals (through inflammatory pain) and warns or forces us to rest our bodies. Pain can be initiated by the stimulation of sensory neurons (nociceptive pain) or through damage or malfunction to the central (spinal cord and brain) or peripheral (nerves outside of the spinal cord and brain) nervous system where pain may be initiated by primary or afferent lesions (neuropathic pain). Nociceptors can respond to thermal, mechanical (pressure applied to tissue or laceration) or chemical stimuli[1]. Once a nociceptor is activated by noxious stimuli, a nerve impulse carries electrical action potentials along the axon of the neuron to the spinal cord. Nociceptors have two types of axon A-δ fibres and C fibres. A-δ fibres have a myelin sheath (which is found on the axon of a neuron and acts as an electrical insulator for the neuron increasing the speed at which electrical impulses propagate along the axon helping to prevent electrical current leaving the axon). The myelin sheath of A-δ fibres allows action potentials to travel about 20 m/s to the central nervous system whereas C fibres which are non-myelinated meaning action potentials are slower to propagate through the axon. This means that nociceptors are able to transmit pain signals at different speeds, A-δ fibres broadcast the pain signals rapidly (associated with immediate and sharp pain on activation of the nociceptor) while C fibres broadcast the pain signal more slowly which is associated with a dull pain felt some time after the injury or noxious stimuli occurs.

The C fibres and A-δ fibres carry the pain signal to the dorsal horn of the spinal cord. From here the pain signals are carried up the spinal cord and brain stem and finally interpreted in the cerebral cortex as pain[1]. Sensitisation of the spinal cord or central nervous system, due to lowering of pain threshold or lengthening in duration of nociceptor response to noxious stimuli, involves α-amino-3-hydroxyl-5-methyl-4-isoxazole-propionate (AMPA) receptors, N-methyl-D-aspartic acid (NMDA) receptors and calcium channels. Excitatory neurotransmitters including substance P and glutamate are released at the terminals of pain fibres and act upon NMDA and AMPA receptors leading to Ca^{2+} channels being opened. This increased

Ca^{2+} transport causes spontaneous action potentials conveying a pain message to the brain.

Rheumatoid arthritis is a systemic inflammatory disorder primarily manifesting in the joints and is a cause of chronic pain. Although the causes of rheumatoid arthritis are incompletely understood, autoimmunity (in which the body fails to recognise native, healthy tissue causing an immune response to be initiated against its own healthy cells and tissue) plays a primary role in its progression. Rheumatoid arthritis afflicts around 400,000 adults (0.81 % of the adult population) in the UK with women (1.16%) being around three times more likely to be affected than men (0.44%)[2]. Rheumatoid arthritis can affect many of the major organs and tissues in the body but primarily has an influence on a synovial joint. The synovium contains a membrane which lines the joint and when functioning correctly acts to protect it by controlling what can enter into the synovial cavity. The synovial membrane will also produce a lubricant (synovial fluid) which acts to reduce friction between the cartilage of the two bones which make up the joint. However in a joint which is affected by rheumatoid arthritis the synovium becomes inflamed. This inflammation is caused by the chemotaxis of fluids and immune cells including $CD4^+$ T cells, B cells and macrophages into the synovium cavity[3]. The chronic pain caused by rheumatoid arthritis can cause major distress and disability as well as a diminished quality of life. Without a direct cure for the disorder, pain alleviation seems to be the best course of action to improve the quality of life for rheumatoid arthritis patients. Current treatments include nonsteroidal anti-inflammatory drugs (NSAIDs) which supress inflammation and also improve pain and swelling, disease-modifying anti-rheumatic drugs (DMARDs) which are slower-acting compounds with the aim of improving the symptoms of rheumatoid arthritis and biological response modifiers which target the inflammatory mediators in tissue damage[4].

The Pain Matrix

With the development of neuroimaging techniques such as positron emission tomography (PET) and functional magnetic resonance imaging (fMRI) as well as electrophysiological techniques such as electroencephalography (EEG) it has become possible to gain a better understanding of how the brain works, how it processes signals and how different regions work together. Using non-invasive neuroimaging techniques to measure brain activity whilst applying noxious stimuli

can give researchers a better understanding of how various cortical regions process pain signals or are activated during pain and how these regions may be linked or communicate with one another. PET studies have been carried out with radiotracers that image regional cerebral blood flow (rCBF) such as [^{15}O]CO_2[5] and [^{15}O]H_2O[6, 7]. These radiotracers rely on haemodynamic responses in the brain and changes in rCBF can be linked to the level of neuronal activity[8]. Other radiotracers are used which will specifically bind to opioid receptors[9, 10] allowing the visualisation of receptor occupancy and distribution during painful and non-painful events. Regions within the brain which have been consistently identified (often through neuroimaging techniques) as responding to nociceptive stimuli are often given the collective term 'the pain matrix'[11]. The major cerebral regions which make up the pain matrix include the primary (S1) and secondary (S2) somatosensory cortices, the insula and the anterior cingulate cortex (ACC). These regions can be split further into 2 networks, the lateral pain system which involves S1 and S2 regions and the medial pain system which involves the ACC region. Sensory-discriminative aspects of pain such as the intensity, duration and location of pain propagate through the lateral pain network while the medial pain network is responsible for the affective aspects of pain perception [12]. However some reviews have concluded that the term 'pain matrix' should be used with some caution as brain responses measured by neuroimaging techniques which are invoked by a noxious stimuli can not only reflect nociceptive specific brain responses but also non-nociceptive salient sensory input[11].

The Endogenous Opioid System

Opioids are one of the most powerful analgesic drugs available and are used clinically to relieve both acute and chronic pain. Although the human body produces its own natural (endogenous) opioids such as endorphins, dynorphins and enkephalins, synthetic or semi-synthetic opioids can be used clinically to enhance their effect. Synthetic or semi-synthetic opioids have a well-established role in pain relief however they can also have negative side-effects associated with them such as tolerance, depression, constipation, breathing difficulties and addiction or dependence[13]. One possible route to treat chronic pain is to target and inhibit the zinc metallopeptidases which breakdown endogenous Met- and Leu-enkephalin increasing their availability to elicit their analgesic effect. Dual enkephalinase

inhibitors which target the two zinc metallopeptidases responsible for the breakdown of enkephalins are currently being trialled as a possible treatment of chronic pain in a number of pathologies[14].

Opioids, synthetic or endogenous, all mediate their effects through the endogenous opioid receptor system of which there are 3 principle sub-types δ (delta), μ (mu) and κ (kappa). In addition to these sub-types, there is also an ORL-1 (opioid receptor like) receptor type which has a large degree of homology to the 'classical' opioid receptors in terms of structure yet is distinct in pharmacology[15]. Each receptor sub-type has a different affinity for different opioids, and the physiological processes elicited by opioids can be mediated by a single receptor sub-type or by a combination of receptor sub-types. The receptors on which opiates induce their effect are membrane bound G-protein coupled receptors (GPCRs). These receptors possess 7 transmembrane domains which are linked by 3 extracellular and 3 intracellular loops; they possess an extracellular N-terminus and an intracellular C-terminus as represented in Figure 1.

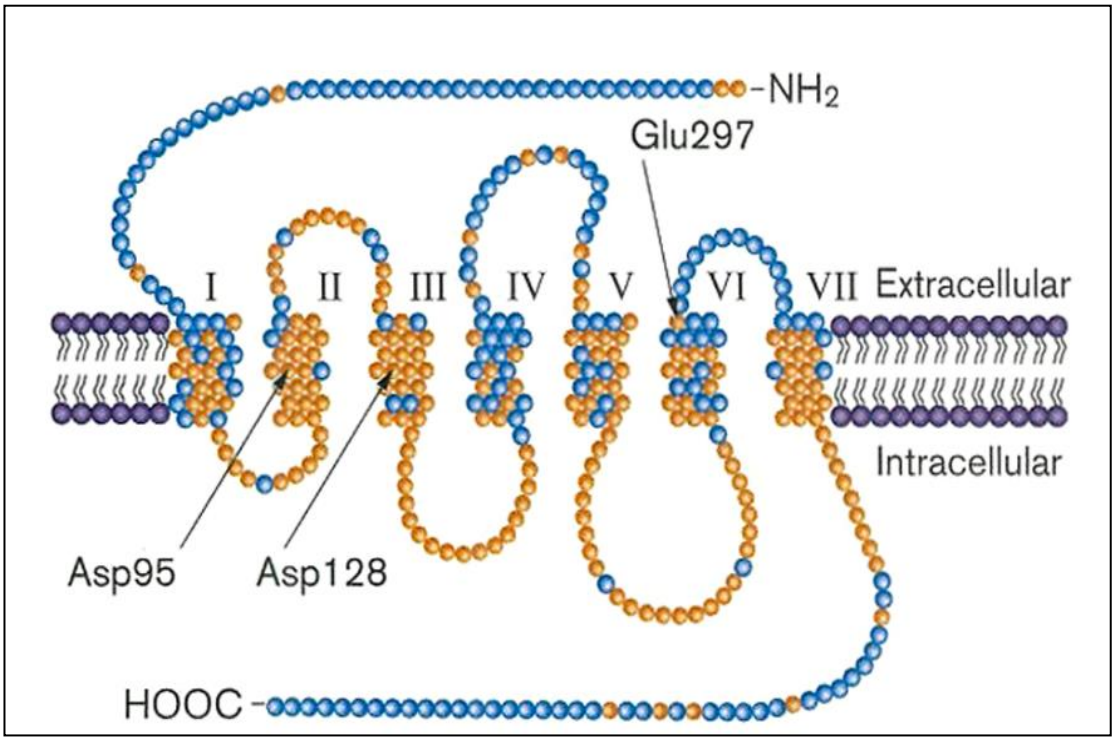

Figure 1: Schematic representation of 7-membrane GPCR. Orange circles represent amino acids which are identical between the three opioid receptor sub-types and blue circles show amino acids that differ between receptor sub-types[16].

GPCRs are able to sense signal molecules or ligands on the outside of the cell which induces signal transduction pathways and then ultimately generates cellular responses. G-proteins use guanosine-5’-diphosphate (GDP) as controls to their signalling pathway. When GDP is bound the G-protein is inactive, however exchanging the bound GDP for guanosine-5'-triphosphate (GTP) activates the G-protein. Signal transduction begins with the inactive G-protein which is coupled to the receptor as a tetramer composing of 3 sub-units G-alpha, G-beta and G-gamma. As an appropriate ligand binds, the receptor changes conformation, which causes a sub-unit to bind a molecule of GTP and then dissociate from the other sub-units therefore activating the G-protein. On activation of the G-protein, the opioid receptor is then negatively coupled to adenylyl cyclase (which catalyses the conversion of adenosine triphosphate (ATP) to 3’-5’-cyclic adenosine monophosphate (cAMP), Figure 2) which regulates ionic conductances by inhibiting Ca^{2+} ion channels and potentiating K^{+} channels.

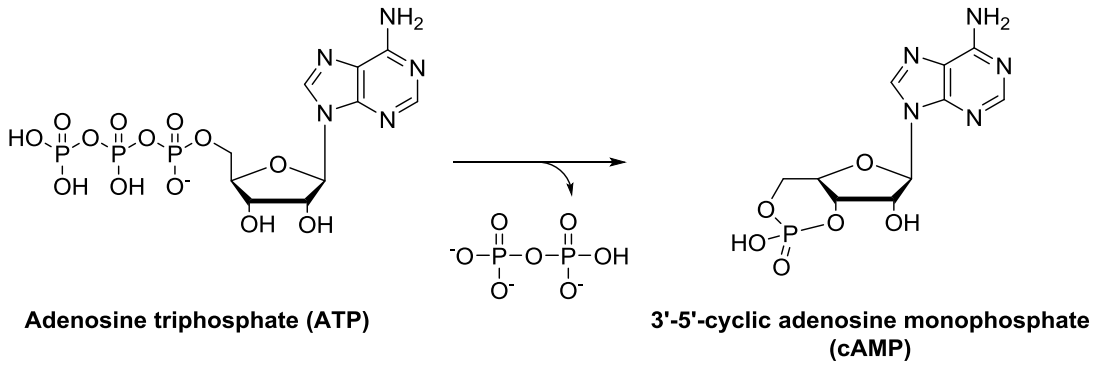

Figure 2: Conversion of ATP to cAMP

Evidence that opioid receptors can be categorised as GPCRs is convincing, as binding of agonist[1] but not antagonist[2] to the receptor is regulated by guanine nucleotides. In addition cellular responses attributed to agonist binding (such as inhibition of adenyl cyclase and ion channels opening and closing) requires GTP and can be blocked by pertussis toxin (a typical feature of G-proteins)[17]. The inhibition of adenyl cyclase and consequential reduction in cAMP which results when opioids bind to the receptor reduces transcription of several genes with cAMP responsive

[1] A ligand (molecule or peptide) that binds to a receptor and produces a biological response.
[2] A ligand (molecule or peptide) that binds to a receptor and does not activate (blocks) a biological response.

promoter elements. Included in the genes, which are regulated, are those which encode for opioid peptide precursors, meaning that opioids could exert feedback control of opioid synthesis [17].

As mentioned when an agonist binds to a GPCR, K^+ ion channels are opened allowing an efflux of K^+ ions from the cell causing hyperpolarization of the cell membrane. This inhibits the firing of neurons and prevents neurotransmitter release which would otherwise be stimulated by sensory nociceptors. The Ca^{2+} ion channels which are closed as a result of G-protein activation inhibit Ca^{2+} currents into cells. Opioids and other agonists are able to both open K^+ and close Ca^{2+} channels in the same cell, the coupling to these ion channels is preserved in specific patches of membrane, therefore no messenger is needed for this process[17].

Techniques such as site-directed mutagenesis and computer automated docking simulation (DOCK[40] programs) have been used to reveal areas of opioid receptors essential for ligand recognition and to identify pharmacophores of opioid receptor ligands[18, 19]. It has been shown that there is a high degree of homology between the three principal receptor sub-types (δ, μ and κ) with the 7 trans-membrane helices showing ~ 70% identity and the extra and intra-cellular loops showing approximately 60% identity[19]. The fragments of opioid receptors which show the most diversity are at the amine terminals, carboxyl terminals, the 2nd and 3rd extra cellular loops and transmembrane segment 4[18]. Mutagenesis studies have been used to aid in identifying the specific area of opioid receptors that are responsible for ligand binding and to support the design of new opioid drugs with enhanced properties for therapeutic use. Regions of amino acid sequence diversity between the different opioid receptor sub-types appear to be responsible for the functional differences of the receptors (i.e. different ligand binding and affinities). Although the extracellular loops of the receptors may differ (2nd and 3rd loops in particular) in amino acid sequence the intracellular loops are very similar, so it can be concluded that it is in the extracellular loops (although not exclusive to) that ligand recognition for each opioid receptor sub-type occurs. Given the similarities of amino acid sequence in the intracellular loops (only at the carboxyl terminus can a difference be seen) it is expected that all three receptor sub-types couple to similar cellular effectors systems and mediate these in similar ways[18]. However the coupling of κ and δ receptors to adenyl cyclase has been known to undergo

desensitisation[20] which can be exhibited as the receptor uncoupling from the G-protein with an enzyme receptor kinase being responsible for the phosphorylation of the receptor. However μ receptors are much more resilient to this desensitisation from adenyl cyclase. Since the intracellular loops of the 3 opiate receptor sub-types are very similar in amino acid sequence, it could be at the carboxyl terminus region where the differences in sensitivity to agonists are determined.

Biology of the opioidergic system.

Delta and μ opioid receptors reportedly regulate the transmission of pain messages cooperatively. However it has been found that the δ and μ opioid receptors are expressed by different subsets of primary afferents[16]. Mu opioid receptors are expressed by heat sensitive transient receptor+ potential ion channels (TRPV1+). These are ligand gated non-selective cation channels and are activated by a number of chemical and physical stimuli including heat at temperatures greater than 43 ºC. These receptors are found in both the central and peripheral nervous system. Mu opioid receptors are also expressed in peptidergic unmyelinated nociceptors in the skin[16]. In contrast to this, δ opioid receptors are predominantly expressed in mechanosensitive myelinated primary afferents and TRPV1 negative nociceptors[16]. It has been demonstrated that the δ opioid receptor is trafficked to the surface of cells under resting conditions, independently of the neuropeptide substance-P[16] which is released from terminals of pain responsive neurons following painful stimuli. Previously, it was understood that the δ opioid receptor was only trafficked to cells in a response to the release of substance-P. Since the δ and μ opioid receptors are distributed differently in pain fibres (TRPV1+ and peptidergic unmyelinated nociceptors for μ receptors and mechanosensitive myelinated TRPV1 negative for δ receptors) it has been shown that each receptor selectively regulates different pain stimuli[16]. The δ opioid receptor mediates mechanical analgesia and does not require heat sensitive TRPV1+ nociceptors, while in contrast to this the μ opioid receptor which is expressed by heat sensitive TRPV1+ nociceptors mediates heat pain.

Opioid drugs offer powerful analgesia for chronic pain, however, as mentioned earlier they are associated with a number of side effects such as addiction and tolerance as well as physical side effects including nausea, constipation and breathing difficulties. However there has been some research into a new generation of opioids that evoke their analgesic action on opioid receptors outside of the central

nervous system and in doing so avoid all centrally mediated unwanted side effects[21]. The endogenous ligands which bind to these peripheral receptors are produced within the skin and in immunocytes. Opioid receptors and neuropeptides are synthesised in dorsal root ganglia and are transported along intra-axonal microtubules into central and peripheral neurons. From here opioid receptors are then incorporated into the neuronal membrane where they can then be activated by endogenous (or exogenous) opioids. Opioid receptors are then coupled to G-proteins and when an opioid ligand-receptor coupling is established there is a direct (or indirect through suppression of cAMP) suppression of Na^+ or Ca^{2+} currents. This leads to a reduction of substance P release and ultimately causes the attenuation of pain; this process is depicted in Figure 3.

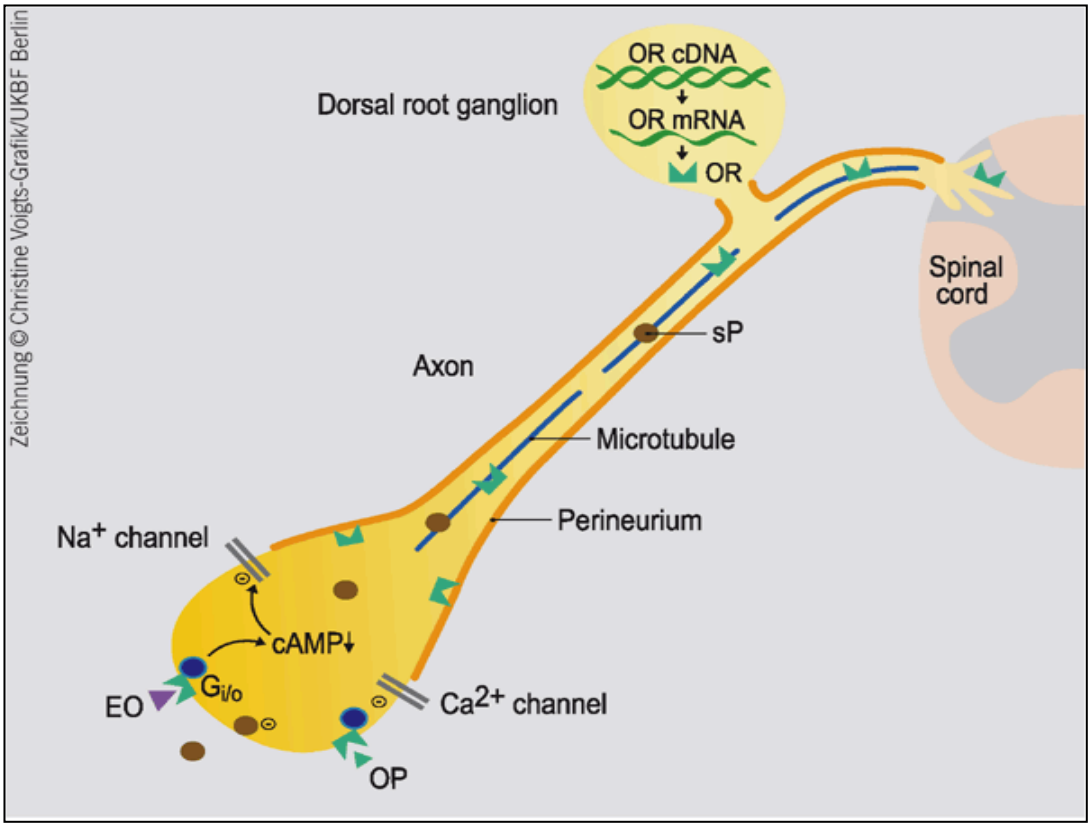

Figure 3: Opiod receptor transport and signalling in primary afferent neurons[21]. OR = opioid receptor, EO = endogenous opioid, OP = exogenous opioid and sP = substance P.

It has been suggested that opioids are actively transported from the brain to the blood stream via the P-glycoprotein pump (Pgp pump) within the blood brain barrier (BBB). In the dorsal root ganglia the production and expression of opioid receptors is increased by peripheral tissue inflammation. As a result axonal transport

of opioid receptors is enhanced, leading to their up-regulation and this increases opioid agonist efficacy at peripheral nerve terminals[21].

Pharmacology of the opioid receptor sub-types

As depicted in Figure 1, GPCRs have aspartic acid residues in regions 2 and 3 (residues 95 and 128). These aspartic acid residues have an important role to acts as a counter ion to basic regions of ligands to assist ligand receptor binding through electrostatic interactions[18]. It is possible to ascertain the effect on the binding of agonists and antagonists to the receptor by performing a mutagenesis of the negatively charged aspartic acid residue at position 95 (Asp^{95}) to a neutral asparagine residue (Asn^{95}). On performing this mutagenesis experiment it was found that agonist binding decreased while the affinity for antagonist was unaffected[18]. This showed that this residue (Asp^{95}) is important in agonist binding, however since transmembrane sequence 2 is similar in all 3 principal opioid receptor types, this residue is unlikely to be part of the receptor responsible for selective agonist binding. This experiment was also carried out at the Asp^{128} residue with similar results in that antagonist binding decreased as Asp^{128} was mutated to Asn^{128}.

Cloning of the κ opioid receptor showed that amino acid residues at the amino terminal played an important role in the binding of the non-selective opioid antagonist naloxone. Residue glutamic acid^{297} (Glu^{297}, as seen in Figure 1) was also shown to be of importance and on mutation of Glu^{297} to a lysine residue (essentially changing a carboxyl group to an amino group) a 100-fold reduction of norbinaltorphimine (nor-BNI, a specific κ ligand antagonist) was found[18]. The μ opioid receptor has a lysine residue corresponding to the Glu^{297} residue of the κ opioid receptor. However μ-receptors have a 100-fold lower affinity for norBNI compared with κ-receptors. This shows that residue Glu^{297} acts as a counter ion (COO^-) to attract the norBNI ligand. The corresponding amino acid residue of a δ opioid receptor is tryptophan, which is a sterically-hindered and bulky residue which can block receptor binding pockets, as anticipated norBNI has a low affinity for δ opioid receptors[19].

The endogenous opioid ligand dynorphin-A is a specific κ opioid receptor agonist. By cloning of the κ-opioid receptor it was found that the 2nd extracellular loop has many more residues carrying negative charges compared to the δ and μ

receptors[18]. Dynorphin-A carries an excess of basic charges which suggests that electrostatic interactions may be of importance in its opioid receptor binding character. Although agonist and antagonist bind to specific sites of the κ receptor there still remains competition for the binding sites, this suggests that binding of a ligand to the receptor could cause changes in the shape or conformation of the receptor and therefore hindering the binding of other ligands. In addition some of the important binding sites of the receptor may overlap in 3-dimensional space meaning that some sites become blocked as other sites become occupied[18].

Agonists of the δ and μ receptors also bind to specific regions of G-proteins. [D-Ala^2, N-MePhe^4, Gly-ol]-enkephalin (DAMGO) is a selective μ receptor agonist which has affinity for the 1st extracellular loop as well as transmembrane helices 2 and 3 of μ opioid receptors[22]. Morphine also has strong affinity for the μ opioid receptor but uses amino acid residues in the 3rd extracellular loop and transmembrane helices 5, 6 and 7[18]. Agonist of the δ opioid receptor such as [D-Pen2, D-Pen5]-enkephalin (DPDPE) and Tyr-D-Ser-Gly-Phe-Leu-Thr (DSLET) have affinity for the 3rd extracellular loop and transmembrane helices 5 and 7 of the δ opioid receptor. The chemical structures of some of the opiates discussed are depicted in Figure 4.

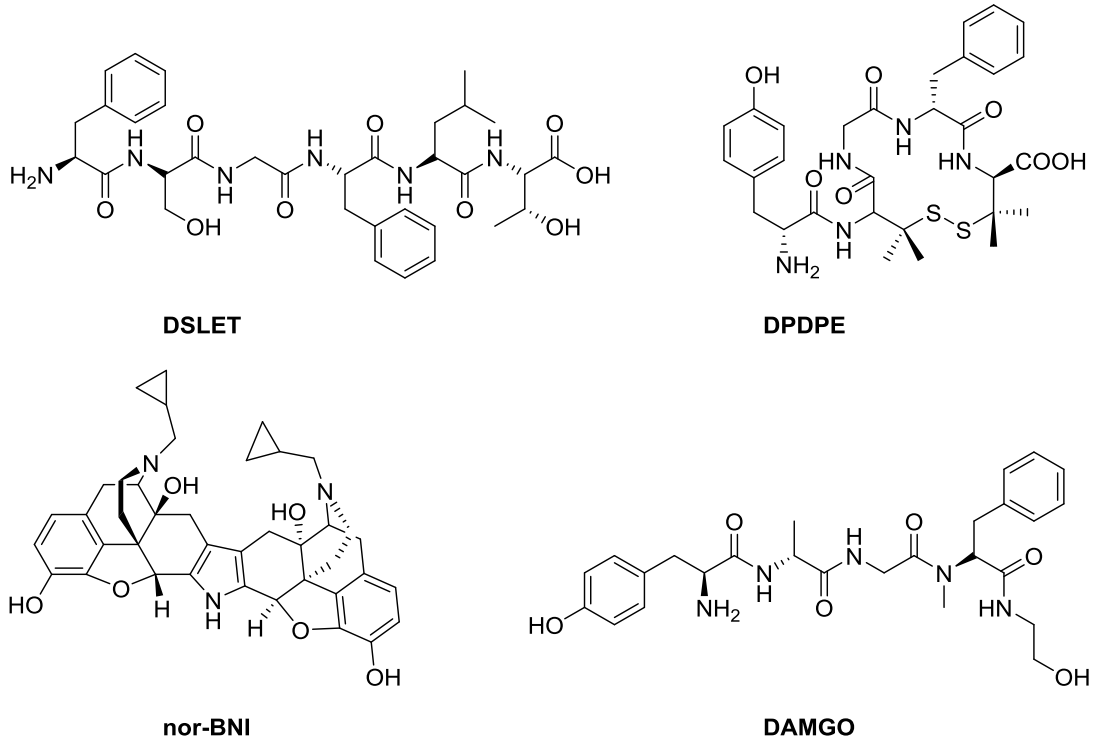

Figure 4: The chemical structure of a selection of opiates with affinity for δ, μ and κ opioid receptors.

Site-directed mutagenesis and receptor cloning has proven to be an important tool in revealing critical regions for ligand binding. These types of study may aid researchers in their search to design new opiate drugs that can provide powerful analgesia with limited side-effects.

It has been shown that site-directed mutagenesis studies can help to reveal specific binding pockets and receptor regions which are important for ligand binding. In addition to this, computer-aided docking simulation programs (DOCK) and the message-address concept can aid in the identification of pharmacophores of opiate ligands[19]. The message-address concept uses the theory that ligands contain certain recognition elements that are responsible for their varying binding affinity to the different opioid receptor sub-types. The message is the shared or universal part of the molecules structure while the address part is the variable portion giving the molecule its unique affinity for a particular receptor. For opiate molecules the message part of the molecule is a tyramine moiety, whilst the address part is a sub-unit attached to the 3rd carbon ring examples are depicted in Figure 5.

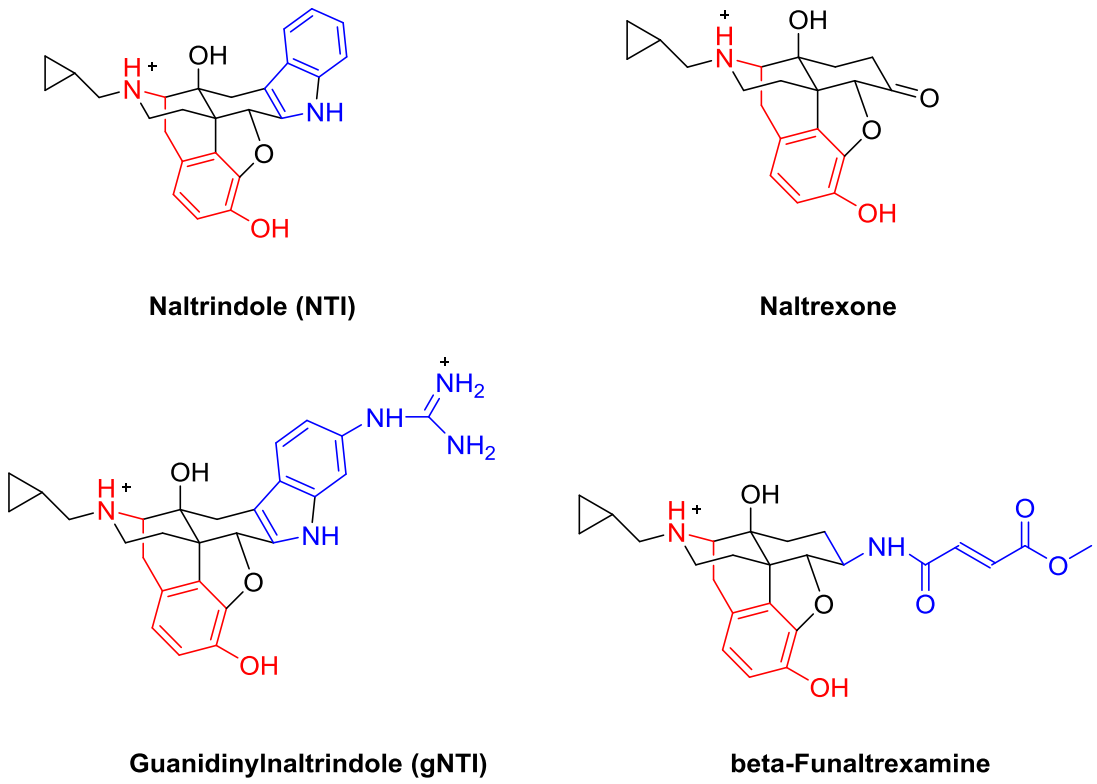

Figure 5: Message-address concept. The red part of the molecule indicates the message part of the molecule while the address part is blue.

In general an opiate which does not possess an address part will bind indiscriminately to the 3 opioid receptor sub-types; an example is naltrexone which is seen in Figure 5. It is possible to see how the message portion of opiate ligands are able to interact with certain amino acids of opiate receptors. The amine of the tyramine moiety is protonated at physiological pH. This means it is possible for an electrostatic interaction to be established between the protonated amine and, for example, a carboxyl functionality (COO^-). Since ligand binding occurs within a specific region of the receptor this electrostatic interaction is thought to occur at an aspartic acid residue located in transmembrane helices 3 (AspIII:08) of opiate receptors[19]. The phenolic ring of the tyramine message part of opiates interacts with a histidine residue on transmembrane helices 6 (HisVI:17) where hydrogen bonding is established between a lone pair of electrons belonging to the nitrogen atom of the histidine and the hydrogen atom of the phenol ring[19]. Opiates which are non-selective for opioid receptor sub-types are most often smaller molecules than selective opiates because they don't possess the address part of the molecule. However, it is likely that hydrophobic pockets in the vicinity of AspIII:08 and HisVI:17 accommodate the rest of the molecule and facilitates their binding to the receptor. Performing sequence analysis of opioid receptors revealed that there was a cluster of hydrophobic amino acid residues such as phenylalanine and tryptophan found partway down transmembrane helices 3 to 6. It is these residues that may account for the hydrophobic property which accommodates the remainder of the non-selective opiate after the message segment has bound[19].

Using computer models and site-directed mutagenesis, two locations were isolated as being important (and unique) in each of the opioid receptor sub-types[19, 23]. Residue 23 at transmembrane segment 6 (VI:23) and residue 3 at transmembrane segment 7 (VII:03) were identified as being the important residues which were orientated correctly for ligand interactions and consequential binding. Site directed mutagenesis at these sites showed that two mechanisms were important for giving opioid receptors selectivity for different ligands. The two identified mechanisms were mutual attraction (ligands are attracted to a matching amino acid residue or group of residues in the receptor) and steric exclusion[19] (in which an amino acid residue or a group of residues prevent a favourable or mutual attraction to occur by steric hindrance).

In κ opioid receptors the amino acids at locations (VI:23) and (VII:03) were glutamic acid and tyrosine respectively. Ligands which are selective for the κ opioid receptor such as gNTI (Figure 5) commonly have a very basic address moiety which is able to interact with the glutamic acid residue at position (VI:23) of the κ opioid receptor, forming a salt bridge. The tyrosine residue at position (VII:03) of the κ opioid receptor was shown to have little effect on the binding of κ selective opiates, however large hydrophobic residues such as tryptophan and phenylalanine in close vicinity are believed to stabilise the hydrophobic character of the address moiety[19].

The δ opioid receptor has amino residues of tryptophan and leucine at positions (VI:23) and (VII:03). For δ selective opiates such as NTI (see Figure 5) an indole moiety is commonly incorporated into the address and is stabilised by the tryptophan and leucine residues which form a hydrophobic pocket for the indole to occupy[19].

β-Funaltrexamine (β-FNA, see Figure 5) is an irreversible μ antagonist. Recognition by the μ opioid receptor is thought to occur in 2 steps[24]. The first step involves the β-FNA ligand binding reversibly to a distinct binding pocket of the μ receptor. This reversible binding acts to orientate the ligand in the correct position for the next step which is an irreversible binding reaction of β-FNA with a nucleophilic site within the receptor. Mutagenesis studies have shown the amino acid residue which is responsible for the nucleophilic reaction with β-FNA to be a lysine residue at transmembrane helix 5 of the μ receptor[25, 26]. The amine functionality (NH_2) of the lysine amino acid acts as the nucleophile in a Michael addition and attacks the α,β-unsaturated carboxyl group of the β-FNA ligand as depicted in Figure 6.

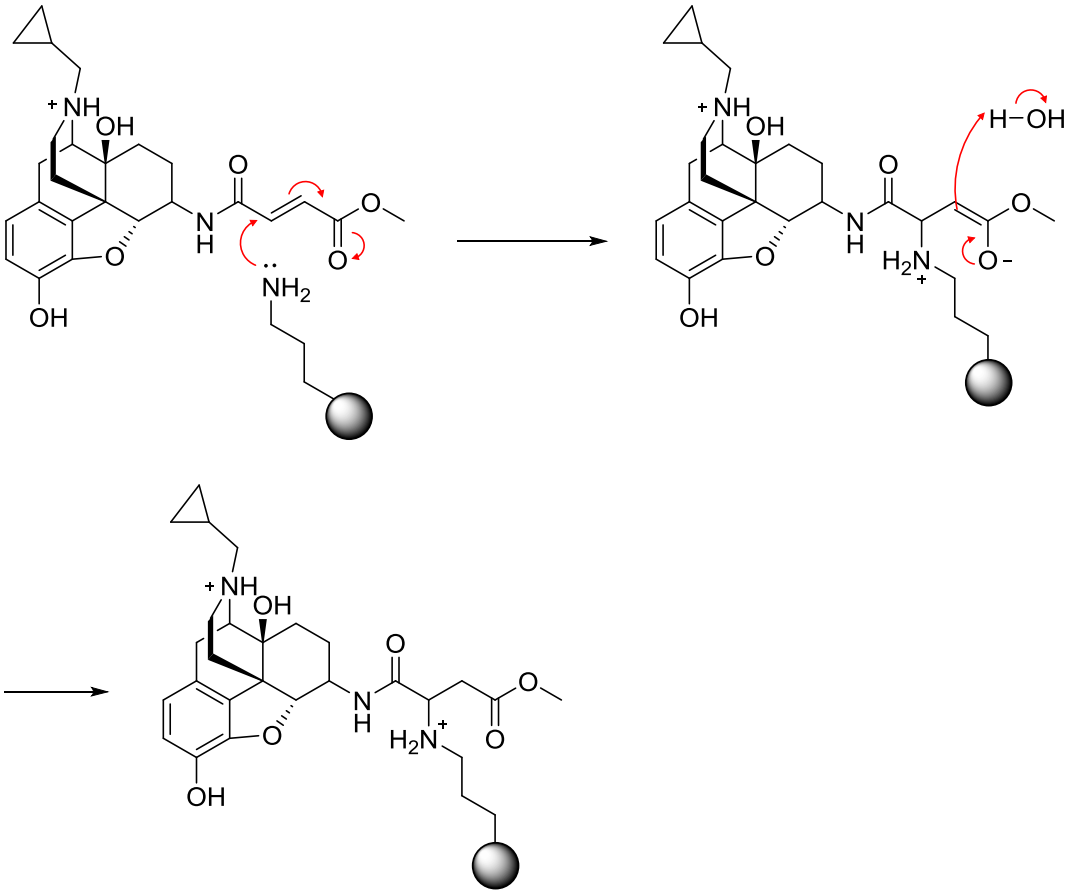

Figure 6: Lysine amino acid residue on transmembrane helix 5 of the μ opioid receptor is involved in the nucleophilic attack of the β-FNA ligand to form an irreversible covalent bond.

This then forms an irreversible bond of the ligand to the μ opioid receptor. What is interesting however is κ opioid receptors have a homologous lysine residue but β-FNA does not bind to kappa receptors, this could be due to the fact that residues close to lysine V:05 do not provide a good enough binding pocket in the kappa opioid receptor to orientate the β-FNA ligand correctly to be attacked by the nucleophilic lysine. Site directed mutagenesis and computational programs such as DOCK[40] help to give researchers a much clearer understanding of how opioid receptor-ligand affinities are established and maintained. The results from these studies give new insights which can lead to the design of new opiates with molecular structures that are optimised for receptor binding affinities.

Some of the opiates which have been discussed, endogenous, synthetic or semi-synthetic along with their binding selectivity and action (agonist, antagonist or mixed) can be found in Table 1.

	μ-opioid receptor	δ-opioid receptor	κ-opioid receptor	ORL1
Endogenous peptide	• Endomorphin-1/2 • β-endorphin	• [Lue^5]-enkephalin • [Met^5]-enkephalin • Deltrophin I/II	• Dynorphin A • Dynorphin B • β-neoendorphin	• Nociceptin / Orphanin FQ
Peptide Agonist	• [D-Ala^2,MePhe^4,Gly-ol^5] enkephalin (DAMGO) • PL 017 • [D-Ala^2, D-Leu^5] enkephalin (DADLE)	• [D-Ala^2, D-Leu^5] enkephalin (DADLE) • ([D-Pen2, D-Pen5]-enkephalin (DPDPE) • [Tyr-D-Ser-Gly-Phe-Leu-Thr] enkephalin (DSLET)	• E2078	• [Arg^{14}, Lys^{15}]nociceptin • UFP-102 •
Peptide Antagonist	• D-Phe-Cys-Tyr-D-Trp-Orn-Thr-Pen-Thr-NH2 (CTOP)	• ICI 174,864 • [(H-Tyr-Tic-Phe-Phe-OH)] TIPP		• UFP-101 • peptide III-BTD
Synthetic Agonist	• Fentanyl • Morphine • Sufentanil • Buprenorphine (partial)	• 4-[(*R*)-[(2*S*,5*R*)-4-allyl-2,5-dimethylpiperazin-1-yl](3-methoxyphenyl)methyl]-*N*,*N*-diethylbenzamide (SNC80) • 7-Spiroindanyloxymorphone (SIOM)	• U-69,593 • U-50,488 • ICI 204,448 • Nalfurafine • 6’-Guanidinonaltrindole (6’gNTI)	• Ro64-6198

	μ-opioid receptor	δ-opioid receptor	κ-opioid receptor	ORL1
Antagonist	• β-FNA • Naloxonazine • Naloxone • Diprenorphine	• Benzylidenenaltrexone (BNTX) • Naltriben (NTB) • Naltrindole (NTI) • NTI 5' isothiocyanate (NTII) • Diprenorphine • Naloxone	• 2-(3,4-dichlorophenyl)-*N*-methyl-*N*-[1S-1-(-3-isothiocyanatophenyl)-2-(-1-pyrrolidinyl) ethyl] acetamide (DIPPA) • 5'gNTI • Nor-binaltorphimine • Diprenorphine • Buprenorphine • Naloxone	• SB 612111 • J-113397 • JTC-801
Area of Receptor Agonist binds (Kane *et al*)[19].	• Agonist DAMGO 1st extracellular loop and transmembrane helices VI and VII	• Agonist DPDPE and agonist DSLET 3rd extracellular loop and transmembrane helices V-VII	• Agonist Dynorphin A 2nd extracellular loop	
Amino acids at locations VI:23 and VII:03 unique to each receptor (Kane *et al*)[19].	• VI:23 glutamic acid (297) • VII:03 tyrosine (312)	• VI:23 tryptophan (284) • VII:03 leucine (300)	• VI:23 lysine (303) • VII:03 tryptophan (318)	

Table 1: A selection of endogenous and synthetic opiates along with their opioid receptor affinities. Data taken from IUPHAR/BPS Guide to Pharmacology http://www.guidetopharmacology.org[27].

Introduction (Part 2) – An Introduction to Positron Emission Tomography (PET) and the use of PET for studying the opioidergic system.

Positron Emission Tomography

Positron emission tomography (PET) is an extremely powerful nuclear imaging technique which allows for the visualisation of *in vivo* physiological processes at a molecular level. The technique relies on the use of radioactive isotopes which decay by positron emission (or β^+ decay), a process in which a proton of the unstable radionuclide is converted to a neutron resulting in the release of a positron (antimatter to an electron) and a neutrino (ν). This nuclear process is depicted in equation 1 where X = positron emitting isotope A = atomic mass Z = atomic number (number of protons) and Y = Daughter isotope.

$$ {}^{A}_{Z}X \rightarrow {}^{A}_{Z-1}Y + \nu + \beta^+ $$

Equation 1: Positron emission

The positron released from this process, will travel a small distance in tissue (a few mm, depending on its kinetic energy) before colliding with an electron causing an annihilation event which releases 2 photons of equal energy (511 keV) as represented in equation 2.

$$ e^- + \beta^+ \rightarrow \gamma\ (511\ \text{KeV}) + \gamma\ (511\ \text{KeV}) $$

Equation 2: Positron/electron annihilation.

The release of the 2 photons occurs at almost exactly 180 º from the annihilation event and it is these photons which are detected during a PET scan. The detectors of a PET scanner are built into a ring which surrounds the subject being scanned. Each detector in the ring is linked in coincidence with its opposite detector. Many of the photons produced in an annihilation event between a positron and an electron will not be detected by the ring of detectors, however some of the 511 KeV photons which are emitted will be in the plane of the detector ring and opposite detectors of the ring will be hit by the photons. If two scintillation detector elements

are hit within a small time window (7-15 ns for a typical clinical scanner)[28] then this is logged as two photons occurring from an annihilation event and a line of response (LOR) is recorded with the annihilation event occurring at some point along the LOR. Raw PET data is collected over a period of time and upon completion of data collection, image reconstruction algorithms can be run. The reconstruction algorithms can be run in conjunction with computed tomography (CT) algorithms to produce a cross sectional image of the distribution of radioactivity in the anatomical area being studied. During image reconstruction, corrections must be made for attenuation (in which photons are scattered from the LOR), random events – which is related to photons not belonging to the same annihilation event hitting detectors and detector dead time – which becomes important as the rate of photons hitting a detector increases[29]. Figure 7 shows a schematic illustration of a PET scan.

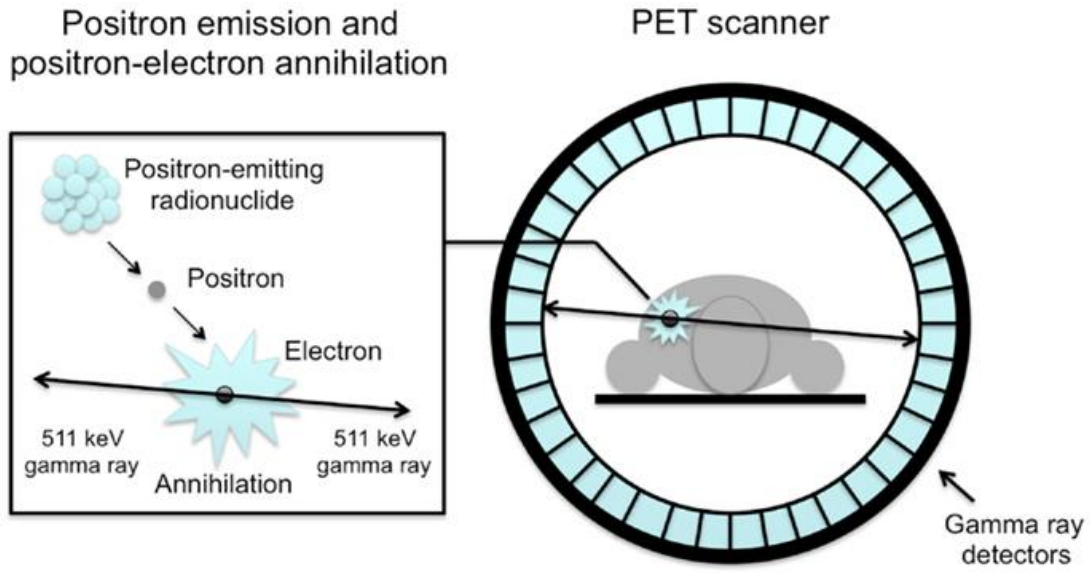

Figure 7: Schematic illustration of positron-electron annihilation and the coincidence detection used in PET imaging[30].

In terms of sensitivity PET (10^{-9} – 10^{-12} M) is superior to other imaging modalities such as CT (10^{-3} M) and magnetic resonance imaging (10^{-5} M)[31]. It is this high sensitivity offered by PET which allows users to view physiological processes at a molecular level, whether that is cell trafficking, ligand-receptor binding or drug pharmacokinetics. What should also be taken into consideration however is the spatial resolution of the imaging modality. For PET, spatial resolution depends on many factors one of which is the range that the emitted positron can

travel in tissue. Positron range differs for various isotopes and depending on the kinetic energy of the released positron. The spatial resolution of PET is 1-2 mm[32] which when compared with the high resolution of CT (50 µm) and MRI (100 µm) appears to be a limiting factor of PET imaging. However it is the superior sensitivity and versatility of PET with many radiotracers available to target various biological targets or drug molecules which can be radiolabelled with PET isotopes that make this imaging modality so attractive.

Some of the important positron emitting isotopes which are used for PET can be seen in Table 2. Of particular note is that carbon, nitrogen, oxygen and fluorine have positron emitting isotopes. These atoms are found in abundance in natural organic compounds as well as pharmacologically active compounds, which means that, as long as chemical pathways are available, the stable isotope can be substituted with its positron emitting counterpart without affecting the molecules behaviour (such as binding to receptor, lipophilicity or metabolism for example). Particular attention should also be paid to the radioactive half-life ($t_{½}$) of the PET isotopes. First of all the radiochemistry route to incorporate the isotope into the molecule to be radiolabelled must be matched to the half-life. A radiolabelling procedure (including radiochemistry, purification and formulation for injection) which takes longer than 3 half-lives of the PET isotope being used is likely to be less useful due to the amount of radioactivity which is lost during this time. The second consideration about half-life is that the biological process being probed is matched to the half-life of the isotope being used. For example if the radiolabelled molecule or ligand has a fast uptake to its target or has fast bio-distribution kinetics then an isotope such as carbon-11 (^{11}C, $t_{½}$ = 20 minutes) would be a suitable isotope to use. Isotopes with a longer half-life such as copper-64 (^{64}Cu, $t_{½}$ = 12.7 hours) and zirconium-89 (^{89}Zr, $t_{½}$ = 78.4 hours) allows PET imaging for much longer time points and is suitable to match the longer *in vivo* pharmacokinetics of large bioactive molecules including antibodies (immuno-PET), nanoparticles and peptides[33]. ^{64}Cu may also have some application in targeted radiotherapy due to its emission of an auger electron[34]. Oxygen-15 (^{15}O, $t_{½}$ = 2.1 minutes) has a very short half-life meaning that to incorporate this isotope into a bioactive molecule is not plausible. ^{15}O is still a very important and useful PET isotope however, being used as $[^{15}O]H_2O$ or $[^{15}O]CO_2$ to measure cerebral blood flow (hemodynamic response), blood volume and oxygen

metabolism[35]. ^{89}Zr and ^{64}Cu have a much lower β^+ branching (23% and 17% respectively) compared to the other isotopes in table 2 and this is also something which should be carefully considered and corrected for in the PET experiment. The other decay modes of these isotopes need to be carefully considered in terms of effects of absorbed radiation dose to the patient being scanned. Also associated gamma emissions may reduce the coincidence count rate performance. For example, ^{89}Zr has a gamma photon emitted at 909 keV, the energy difference from the 395.5 keV β^+ (average kinetic energy) and the 511 keV gamma photon of the annihilation event is big enough for there to be no interference with the PET scan but organ dose considerations need to be made. Some selected gamma energies are given in Table 2.

Also of particular importance, and especially in receptor occupancy studies, is the specific radioactivity of the radiotracer. For these receptor studies the notion of tracer amount is important, the small amount of radiolabelled molecule injected means there is no observable biological effect to the subject. Specific radioactivity is the ratio of radioactive isotope to stable isotope (often referred to as carrier) and will usually carry the unit GBq/µmol (or Ci/µmol). Each radioisotope has a theoretical maximum specific radioactivity which is the specific radioactivity if every atom of a sample is radioactive. The theoretical maximum specific radioactivity is related to the radioactive decay constant λ (s^{-1}) which is the probability that a nucleus will decay per second and is related to $t_{1/2}$ by the following equation.

$$\lambda = \frac{ln2}{t_{1/2}}$$

Equation 3: Relationship between radioactive decay constant (λ) and radioactive half-life ($t_{1/2}$).

The rate of radioactive decay is related λ as in equation 4 where N = the number of un-decayed nuclei. The theoretical maximum specific radioactivity for a radioisotope can be calculated if the decay constant is known and by inserting the Avogadro number of molecules.

$$\frac{dN}{dt} = -\lambda N$$

Equation 4: Rate of radioactive decay.

The theoretical maximum specific radioactivity for ^{11}C and ^{18}F is 3.4 x 10^5 and 6.3 x 10^4 GBq/µmol respectively[36]. However the specific radioactivity which is reached at the end of a radiochemistry production is much lower due to isotopic dilution. Addition of stable isotope from target material, atmosphere, chemical reagents, solvents and synthesis equipment decrease this specific radioactivity. For receptor occupancy studies the specific activity must be high (the dose contains a low amount of carrier) as molecules or ligands which are labelled with the stable form of the isotope will compete for receptor occupancy and may bind irreversibly to a receptor site. This will limit the number of sites that are available for the radiolabelled counterpart to bind.

Isotope	Half-life ($t_{½}$)	Decay Mode (%)	Positron Energy (MeV)
^{13}N	10 min	β^+ (100)	$E_{max}(\beta^+)$ = 1.19 $E_{ave}(\beta^+)$ = 0.491
^{15}O	2.1 min	β^+ (100)	$E_{max}(\beta^+)$ = 1.73 $E_{ave}(\beta^+)$ = 0.735
^{11}C	20.4 min	β^+ (99.8) EC (0.2)	$E_{max}(\beta^+)$ = 0.98 $E_{ave}(\beta^+)$ = 0.385
^{18}F	109.7 min	β^+ (97) EC (3) γ = 1.655 MeV	$E_{max}(\beta^+)$ = 0.64 $E_{ave}(\beta^+)$ = 0.25
^{64}Cu	12.7 h	β^+ (17) EC (44) β^- (39) γ = 1.346 MeV	$E_{max}(\beta^+)$ = 0.65 $E_{ave}(\beta^+)$ = 0.278
^{89}Zr	78.4 h	β^+ (23) EC (77) γ = 0.909 MeV	$E_{max}(\beta^+)$ = 0.89 $E_{ave}(\beta^+)$ = 0.397
^{68}Ga (produced by a generator)	68 min	β^+ (89) EC (11)	$E_{max}(\beta^+)$ = 1.89 $E_{ave}(\beta^+)$ = 0.844
^{124}I	4.18 d	β^+ (23) γ (77) 0.602 MeV, 1.7 MeV	$E_{max}(\beta^+)$ = 1.53 , 2.15 $E_{ave}(\beta^+)$ = 0.686, 0.974

Table 2: Commonly used PET isotopes, data taken from International Atomic Energy Agency[37].

Carbon-11 - [^{11}C]

The relatively short half-life of ^{11}C ($t_{½}$ = 20.4 minutes) means that radiochemistry routes to incorporate this isotope into molecules must be fast. If the radiochemistry, purification, formulation and dispensing of the ^{11}C labelled tracer takes too long then there may not be enough radioactive dose to perform the PET scan. The general rule of thumb is that the production process should be complete within 3 half-lives of the isotope being used. However there are many examples of ^{11}C PET studies in the literature and rapid radiochemistry routes have been facilitated by efficient and reliable automated radiochemistry systems and advances in HPLC (high performance liquid chromatography) and SPE (solid phase extraction) purification technologies.

^{11}C is commonly produced in a cyclotron via the ^{14}N(p,α)^{11}C nuclear reaction, in which a nitrogen gas target is bombarded with protons. By the addition of hydrogen or oxygen (typically 1-1.5%) to the target gas ^{11}C can be produced as either [^{11}C]methane ([^{11}C]CH_4) or [^{11}C]carbon dioxide ([^{11}C]CO_2) in the target. Other nuclear reactions to produce ^{11}C are available such as ^{10}B(d,n)^{11}C which uses a solid boron target[38]. Cyclotron produced [^{11}C]CO_2 can be used to make [^{11}C]methyl iodide ([^{11}C]CH_3I), one of the most important ^{11}C labelling agents to perform methylations with nucleophilic precursors. The synthesis of [^{11}C]CH_3I can be carried out via one of two synthetic routes. The first method is referred to as the 'wet' method[39] and is described in the formula below. This method uses lithium aluminium hydride to reduce [^{11}C]CO_2 to [^{11}C]methanol ([^{11}C]CH_3OH), which is then converted to [^{11}C]CH_3I by the addition of hydroiodic acid, as seen in Figure 8.

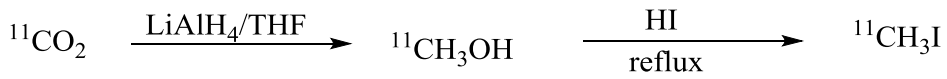

Figure 8: The 'wet method' route to [^{11}C]CH_3I.

The 'wet' method gives a high yield of [^{11}C]CH_3I but the main drawback of this method is that stable carbon (^{12}C) is introduced during the production process[40]. Crouzel *et al* reported [^{11}C]CH_3I radiochemical yields of 80% decay corrected from [^{11}C]CO_2 and specific radioactivities from 74-175 GBq/μmol[39]. Stable carbon could be introduced as CO_2 absorbed from the atmosphere being absorbed into the $LiAlH_4$ solution, as methanol formed from THF remaining in the $LiAlH_4$ solution following the evaporation step, or from impurities in the cyclotron target body and gas (not

specific to the 'wet' method of [^{11}C]CH_3I generation)[41]. This drawback of the 'wet' method means that the low specific activity of the generated [^{11}C]CH_3I will be carried into the final molecule which is to be methylated with ^{11}C. A second route to [^{11}C]CH_3I known as the 'gas phase' method yields higher specific activity and is described in Figure 9 below[42].

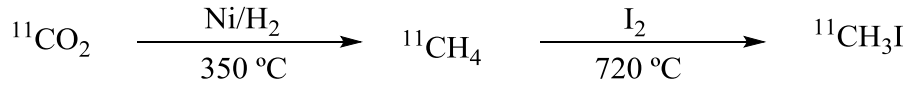

Figure 9: The 'gas phase' route to [^{11}C]CH_3I.

For the 'gas phase' method cyclotron generated [^{11}C]CO_2 is initially reduced to [^{11}C]CH_4 with hydrogen gas passed over a nickel catalyst. The [^{11}C]CH_4 produced is then reacted at elevated temperatures with iodine vapour in a free radical iodination step. To achieve the maximum conversion of [^{11}C]CH_4 to [^{11}C]CH_3I the [^{11}C]CH_4 is recirculated a number of times through the oven which contains the iodine. A Porapak trap is used to remove the [^{11}C]CH_3I from the circulation at each pass and when maximum conversion has been achieved the Porapak trap is heated to remove [^{11}C]CH_3I after which it can be sent to a radiochemistry system[40, 42]. As well as the advantage of giving a higher specific activity of [^{11}C]CH_3I the 'gas phase' route can be used either with a [^{11}C]CO_2 target as described here or with [^{11}C]CH_4 target which circumvents the need for the initial reduction step and should also help to produce higher specific activity [^{11}C]CH_3I. Larsen *et al* reported specific radioactivities of 550 GBq/µmol for [^{11}C]CH_3I, although the radiochemical yields were reduced (46% non-decay corrected)[42].

[^{11}C]CH_3I is used to perform ^{11}C-methylation at oxygen, nitrogen and sulfur nucleophilic sites of molecules, however [^{11}C]methyl triflate ([^{11}C]CH_3OTf) can also be used for this type of ^{11}C reaction. [^{11}C]CH_3OTf can be produced directly from [^{11}C]CH_3I by a metathesis reaction with silver triflate (AgOTf)[43] as seen in the reaction scheme in Figure 10 below.

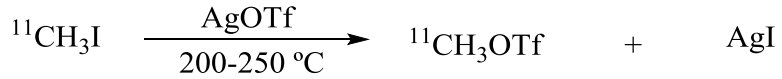

Figure 10: Conversion of [^{11}C]CH_3I to [^{11}C]CH_3OTf.

[^{11}C]CH_3I is passed in a gentle stream of nitrogen or helium, through a column containing AgOTf on graphitised carbon pre-heated to 250 – 300 ºC[40, 43],

Jewett *et al*, described radiochemical yields of [^{11}C]CH_3OTf as high as 95% from [^{11}C]CH_3I[43]. [^{11}C]CH_3OTf has been used to produce [^{11}C]FLB-457, a radiotracer with high affinity for dopamine receptors[44]. In this study [^{11}C]CH_3OTf was produced from [^{11}C]CH_3I which was generated via both the 'wet method' as well as the 'gas phase method'. A comparison of the specific radioactivity of [^{11}C]FLB-457 from [^{11}C]CH_3OTf produced via the 'wet method' (78 GBq/μmol) was shown to be lower than that produced from the 'gas phase method' (126 GBq/μmol)[44].

The triflate group of [^{11}C]CH_3OTf is a better leaving group for nucleophilic S_N2 reactions than the iodide atom of [^{11}C]CH_3I. The triflate group has the ability to pull electron density away from then ^{11}C-methyl moiety using the electronegativity of the fluorine atoms (Pauling value $\chi = 3.98$) and electron density is also conjugated towards the oxygen atoms of the sulfonyl group in cross conjugation via the d-orbitals of sulfur. It is the combination of these properties which make triflate an excellent leaving group and as a consequence the ^{11}C-methyl group is labile to attack by a nucleophilic group. The benefits of using the highly reactive [^{11}C]CH_3OTf for ^{11}C-methylation reactions include the need for much less forceful reaction conditions (lower temperatures, pressures and reaction times) which is a benefit considering the short half-life of ^{11}C. Also [^{11}C]CH_3OTf is much less volatile when compared to [^{11}C]CH_3I and so can be trapped more easily in small volumes of solvents and at room temperatures. Also the increased reactivity means that in many cases less precursor is needed, which can aid the final purification step as well as bring the overall costs of production down[40]. The highly reactive nature of [^{11}C]CH_3OTf may also have some inherent drawbacks associated with it related to chemo and regioselectivity. If a precursor molecule has more than one nucleophilic site which can react then [^{11}C]CH_3OTf may not be the reagent of choice as both sites may be ^{11}C-methylated. That is unless one nucleophilic site is first chemically protected, but this will require a second step following radiolabelling to remove the protecting group which may impinge on the yield and is not always ideal given the short half-life of ^{11}C. Some examples of O-, N- and S- alkylations with [^{11}C]CH_3I as well as [^{11}C]CH_3OTf are given in Figure 11 below.

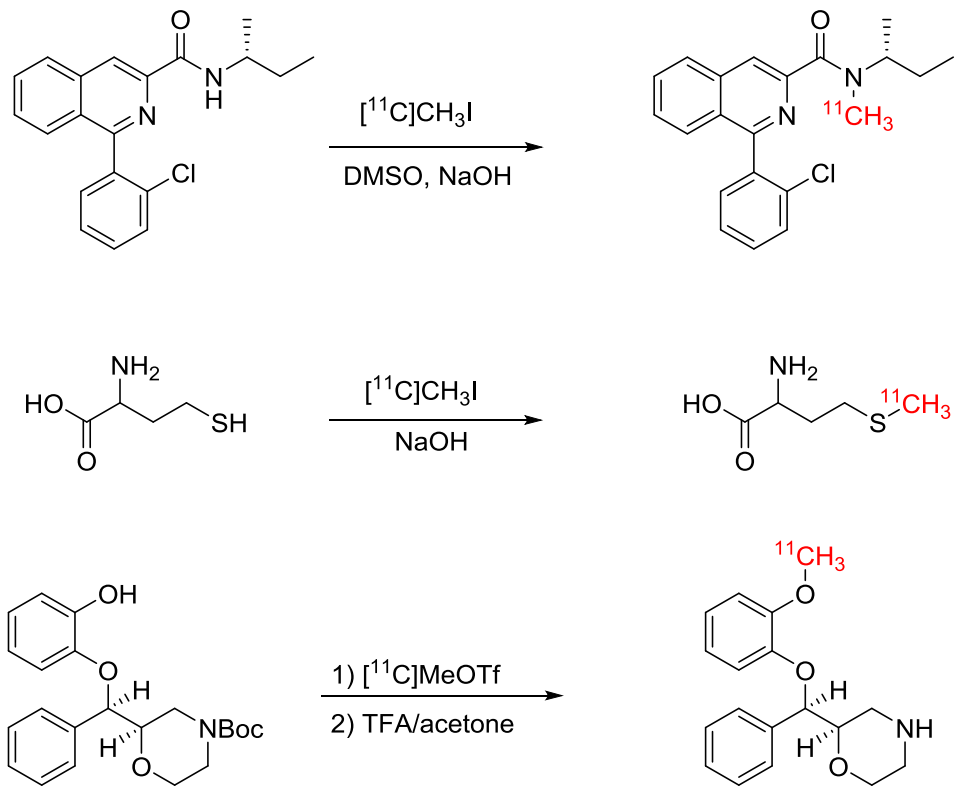

Figure 11: Examples of ^{11}C-methylation reactions at nitrogen (PK11195, top), sulfur (methionine, middle) and oxygen ([^{11}C]MeNER, bottom) containing molecules.

[^{11}C]CH_3I and [^{11}C]CH_3OTf heteroatom methylations occur in the presence of an excess of the N-, O- or S- containing precursor. This stoichiometry allows for a fast incorporation of the ^{11}C radiolabel with a satisfactory radiochemical yield[40]. The radiochemistry can be performed in a solvent system, on a solid support (captive solvent method) or on a microfluidic system depending on how complex the radiochemistry route is and the number of steps involved. The most widely used of these routes is the solvent system; in this system the radiolabelling precursor ([^{11}C]CH_3I or [^{11}C]CH_3OTf) is first of all trapped in an appropriate polar aprotic solvent such as dimethylformamide (DMF), dimethyl sulfoxide (DMSO) or acetonitrile (MeCN) which will facilitate a nucleophilic S_N2 reaction. The solvent may already contain the precursor and an appropriate base or these can be added following the trapping. The role of the base is either to deprotonate the reactive functional group of the precursor (OH, NH or SH) and make it more nucleophilic, or trap hydrogen iodide which is produced during the ^{11}C-methylation and displace the reaction equilibrium. For trapping [^{11}C]CH_3I a low temperature is required (although this is not possible with the high melting point of DMSO, (18 ºC) due to its volatility and also because [^{11}C]CH_3I is carried, in a high dilution, by a high nitrogen gas flow.

The reaction vessel is sealed and can be heated to begin the radiolabelling. Once this is complete the crude reaction mixture containing the radiolabelled product as well as some starting material and possible side products is transferred to a HPLC column to isolate the radiolabelled product which can be followed by SPE formulation.

Solid support or captive solvent system methods represent simple and easily automated approaches to ^{11}C-methylation[40, 45]. The captive solvent method involves the trapping [^{11}C]CH_3I on a small stainless steel loop which is pre-coated with the precursor to be radiolabelled. Once trapped in the loop with the precursor the [^{11}C]CH_3I is allowed some time to react with the precursor after which the contents of the loop are washed onto a HPLC column for purification[45]. Another type of solid support ^{11}C-methylation occurs on a C18 or C8 SPE cartridge[46]. The concept is the same as with the loop method in which the desmethyl precursor molecule is loaded onto the SPE cartridge shortly before [^{11}C]CH_3I is trapped and allowed to react with the precursor. Following this the crude reaction mixture is eluted from the cartridge with an appropriate solvent and sent for HPLC purification.

Radiochemistry being performed on microfluidic systems is a more recent approach to the field microfluidic systems to allow the user to perform reactions on a micro- or nano-litre scale in continuous flow micro-reactors[40]. These systems can allow the user to perform multiple reactions to optimise reaction conditions and subsequently the radiochemical yields of the tracer being developed. Parameters such as reagent concentration, temperatures and reaction time (which is controlled by the infusion rate of reagents into the micro-reactor and hence the amount of time reagents spend in the reactor) can be easily controlled as these systems allow for the manipulation of microlitre volumes of liquids. Another advantage of the system is that an increase to the specific surface area in which the reagents react allows an improvement of mass and heat transfer in the system which subsequently enhances reaction kinetics[47]. Being able to manipulate microlitre volumes of reagents means that there is a cost benefit in regards to reagents and consumables and with the introduction of the lab on a chip technology the amount of space required is reduced as well as the ease of shielding the system. Both ^{11}C and ^{18}F radiochemistry has been developed on such systems[47-49].

Fluorine-18 - [^{18}F]

^{18}F is an ideal isotope to be used for PET; with a moderately long half-life ($t_{½}$ = 109.7 minutes) a high abundance of positron emission (97 % β^+, 3 % electron capture) and a low positron energy (β^+_{max} = 0.64 MeV). These properties are advantageous to PET experiments, for example; the high ratio of β^+ emissions is beneficial to detector count rate and therefore the sensitivity of detection. Also ^{18}F has a β^+_{max} which is relatively low when compared to ^{11}C (0.98 MeV), ^{124}I (1.53 MeV and 2.15 MeV) and ^{86}Ga (1.89 MeV). This lower β^+_{max} energy of ^{18}F means the emitted positron has a shorter range in tissue (2 mm[28]) before an electron annihilation event and leads to better resolution PET images. Another consequence of the low β^+_{max} energy is a smaller radiation dose to patients being scanned.

However it is important to also consider the physiochemical properties of fluorine. Other than hydrogen (1.20 Å), fluorine has the smallest van der Waals radius (1.47 Å)[50]. The small radius of fluorine means that a mono-fluorinated derivative of an endogenous molecule may be equivalent to the endogenous molecule in terms of steric demand and as such should have the same biodistribution and metabolic pathway. The second property to consider is electronegativity, fluorine has the largest electronegativity (Pauling value χ = 3.98) amongst all of the elements. This strong electronegative character means that if fluorine is substituted into a molecule an effect on neighbouring functional groups may occur and the reactivity of the molecule may be modulated, in addition the *p*Ka of the molecule may well change. Another important property to consider is the strength of the C-F bond (with a bond dissociation energy of 105.4 kcal/mol)[50]. The strength of the C-F bonds means they are more stable to metabolic transformations *in vivo* making ^{18}F substituted molecules an attractive radiolabelling strategy.

There are two forms of ^{18}F which are commonly produced in cyclotron targets; [^{18}F]fluoride ([^{18}F]F^-) and [^{18}F]fluorine ([^{18}F]F_2). The fluoride version is made by the nuclear reaction ^{18}O(p,n)^{18}F in which an oxygen-18 enriched H_2O target is bombarded with protons. [^{18}F]F_2 is made by the nuclear reaction ^{20}Ne(d,α)^{18}F in which a neon gas target is bombarded with deuterons. Stable fluorine must be added in the production [^{18}F]F_2 to act as a carrier in order to remove it from the wall of the cyclotron target, this means that [^{18}F]F_2 is often produced with a low specific radioactivity. However there is an alternative route to [^{18}F]F_2 which involves a two

shoot target approach, providing the isotope in a higher yield[51]. The two shoot method involves the $^{18}O(p,n)^{18}F$ nuclear reaction in the first shot, in which an oxygen-18 gas target is proton bombarded. This produces $[^{18}F]F^-$ which is adsorbed on to the walls of the target. Following the first shot, the costly oxygen-18 gas is recovered by cryotrapping before ^{18}F is released from the target walls as $[^{18}F]F_2$. This is achieved by a second cyclotron irradiation (second shot) of a noble gas and stable fluorine gas mix which will cause the exchange of fluorine atoms form the cyclotron target wall and the release of $[^{18}F]F_2$.

Being able to obtain ^{18}F in these two forms offers great versatility to the chemistry that can be performed with them. The radiochemist has the option of using either nucleophilic non-carrier added $[^{18}F]F^-$ or carrier added electrophilic $[^{18}F]F_2$[52]. With $[^{18}F]F_2$, electrophilic substitution by reaction with a nucleophile and addition across a double bond are common ways of incorporating the radioisotope. Nucleophilic $[^{18}F]F^-$ will arrive from the cyclotron in oxygen-18 enriched water and the $[^{18}F]F^-$ is trapped on an anion exchange cartridge while the oxygen-18 enriched water is collected in a separate vial. The retained $[^{18}F]F^-$ is then eluted from the cartridge with a solution of potassium carbonate (K_2CO_3) containing the cryptand Kryptofix-222 (K_{222}). This cryptand selectively complexes potassium cations (K^+) and so $[^{18}F]F^-$ is eluted from the cartridge as a complex of $[^{18}F]KF/K_{222}$ which is soluble in solvents such as MeCN. Furthermore the decrease in charge density on the chelated potassium, dissociates the ion pair $[^{18}F]KF$ and increases the nucleophilicity of the $[^{18}F]F^-$. Next, the $[^{18}F]KF/K_{222}$ complex needs to be dried via azeotropic distillation with MeCN. If the azeotropic distillation step is not completed then the $[^{18}F]F^-$ would simply react with the water to form $[^{18}F]HF$. Using $[^{18}F]F^-$ directly to label molecules is not usually a good option as often the molecules being radiolabelled contain electron rich aromatic rings which are nucleophilic like $[^{18}F]F^-$, also forcing reaction conditions are often required which may cause side reactions in the target molecule[52]. $[^{18}F]F^-$ can be reacted directly onto a small molecule if it contains a good chemical leaving group such as a tosylate or triflate. However due to the multi-functionalities of macromolecules $[^{18}F]F^-$ cannot always be directly used to radiolabel them. Instead an ^{18}F labelled small organic prosthetic group capable of being covalently linked to the macromolecule under mild reaction conditions is required. The prosthetic group will possess a reactive chemical function such as

tosylate or a carbonyl. Some common ^{18}F prosthetic groups include [^{18}F]fluoroethyltosylate ([^{18}F]FEtTos), [^{18}F]fluroethylbromide, [^{18}F]fluorobenzaldehyde ([^{18}F]FBA), N, succinimidyl-[^{18}F]fluorobenzoate ([^{18}F]SFB) and [^{18}F]fluoroacetaldehyde as depicted in Figure 12 below.

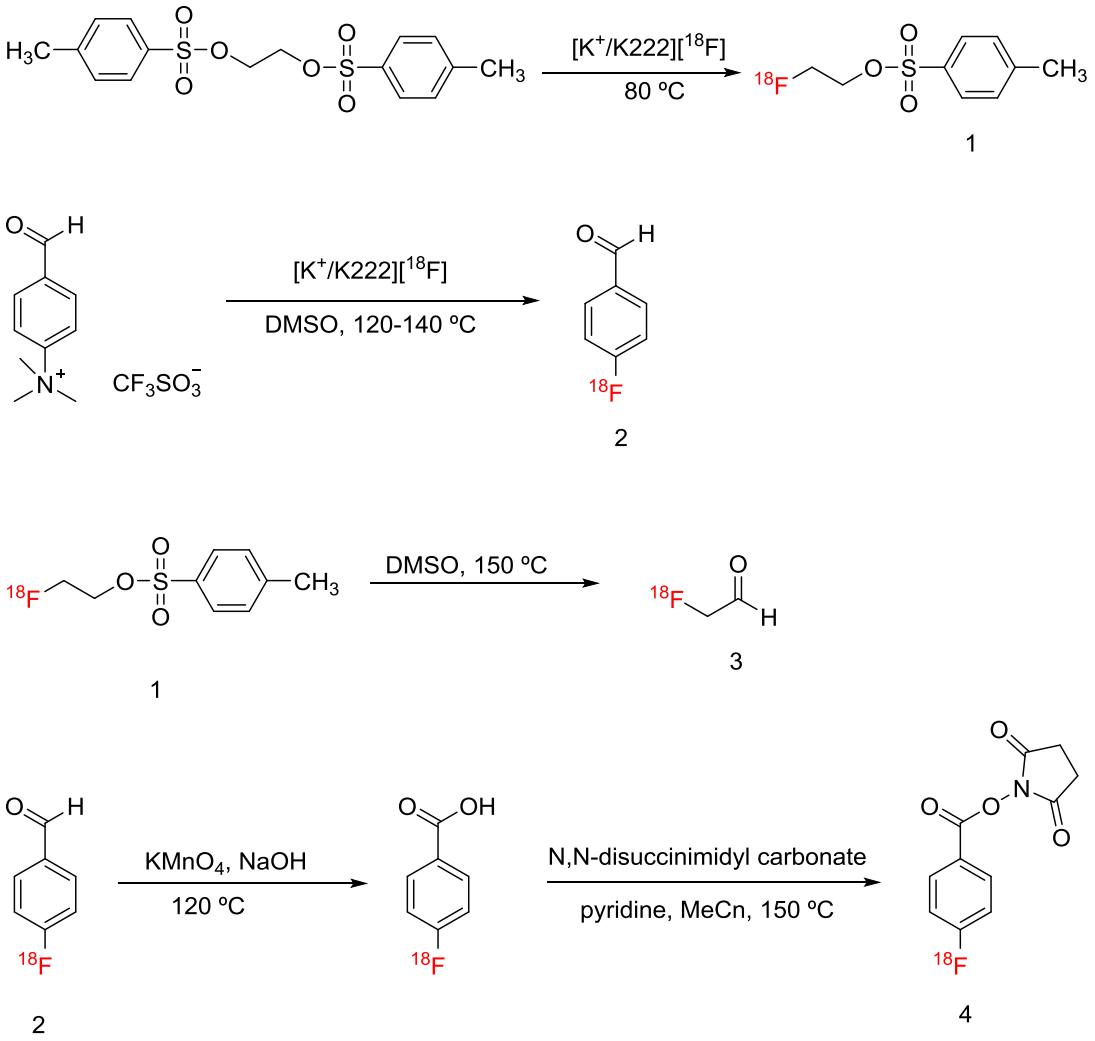

Figure 12: Common ^{18}F prostetic groups and some of the typical approaches to preparing them. 1) [^{18}F]fluoroethyltosylate, 2) [^{18}F]FBA, 3) [^{18}F]fluoroacetaldehyde and 4) [^{18}F]FSB.

^{18}F prosthetic groups can then be utilised to label small molecules as well as peptides, proteins and antibodies[53-56]. Careful consideration should be given to the ^{18}F radiolabelling precursor to be used. For the ^{18}F radiolabelling of small molecules which act upon a receptor for example minimal changes to the molecular structure should be made during the radiolabelling procedure. If the molecular structure is altered too much this may affect the binding properties of the ligand to its receptor as well as the pharmacokinetics of the molecule and may also effect the lipophilicity of the molecule which may be important if the target receptor is located in the brain and

the molecule needs to cross the BBB. Considerations also need to be made to the metabolic stability of the prosthetic group. An aliphatic ^{18}F prosthetic group will generally have less metabolic stability when compared to an aromatic ^{18}F prosthetic group. Nucleophilic aromatic (S_NAr) ^{18}F-fluorination is of great importance in the field of ^{18}F radiochemistry. For S_NAr ^{18}F-fluorination reactions the aromatic ring must be activated by an electron withdrawing moiety (such as a halogen, cyano or a nitro group) in the *ortho* or *para* position to the leaving group[57].

[^{18}F]FBA can be synthesised by a simple nucleophilic aromatic substitution reaction (S_NAr) and [^{18}F]fluoroacetaldehyde is prepared from [^{18}F]FEtTos and a Kornblum oxidation with DMSO followed by distillation see Figure 13 below. The volatility of fluroacetaldehyde means that the ^{18}F product can be distilled from the reaction mixture avoiding the need for an intermediate purification step. The product is also easily trapped in water and is shown to be highly hydrophilic in its hydrate form[54]. The carbonyl group is easily accessible with no steric effects to deter a nucleophilic attack and other reaction types such as aldol and Mannich reactions could be used with this ^{18}F prosthetic group. All of these attributes make [^{18}F]fluoroacetaldehyde a promising peptide labelling agent.

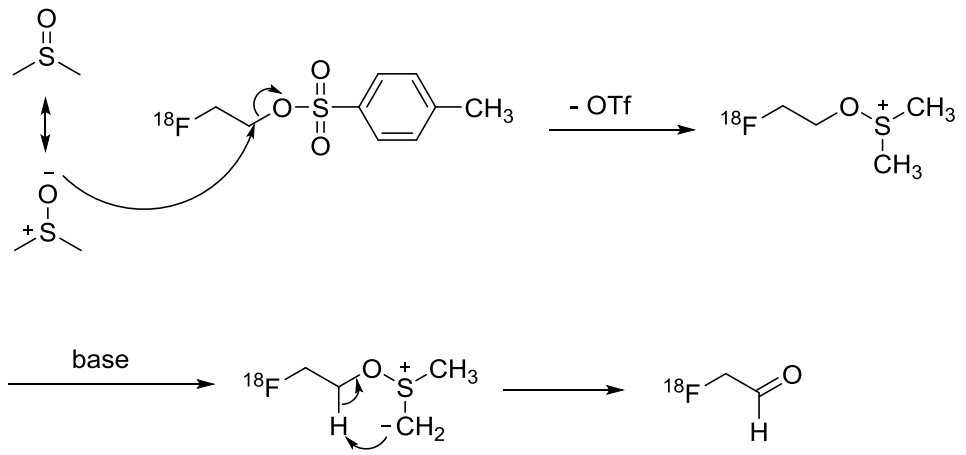

Figure 13: Kornblum oxidation of [^{18}F]FEtTos with DMSO to produce [^{18}F]fluoroacetaldehyde.

[^{18}F]fluoroacetaldehyde and [^{18}F]FBA can then be used to radiolabel peptides and proteins via a reductive amination reaction on a lysine residue of the target peptide which is depicted in Figure 14.

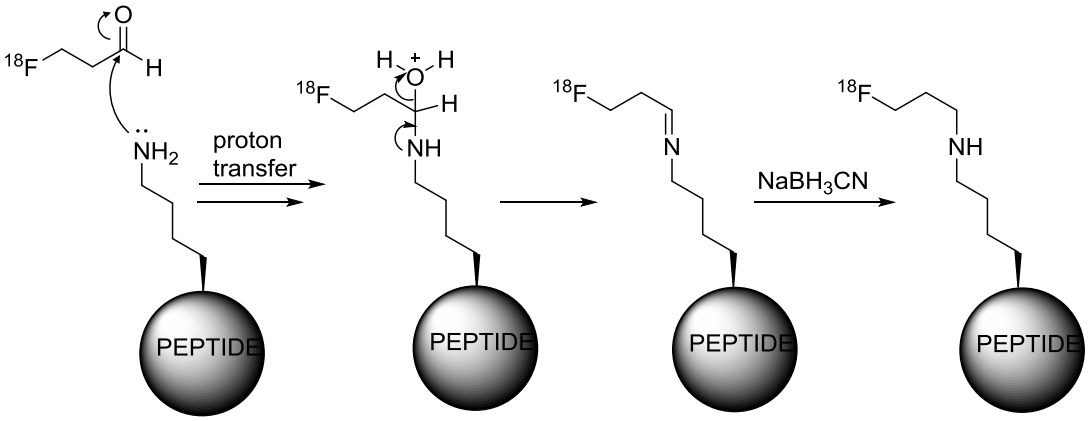

Figure 14: Reductive amination reaction between lysine residue on a peptide/antibody and [^{18}F]fluoroacetaldehyde.

Using this strategy for radiolabelling peptides with ^{18}F requires careful thought as the method will radiolabel random lysine residues of the peptide with ^{18}F. This strategy may not be appropriate if the radiolabelling occurs at a lysine residue which is essential to the proteins biological activity or is involved in the proteins binding to receptors. In order to gain site-specific radiolabelling, chemically modified peptides may be used, one such example uses aminooxy functionalised peptides[58]. A reaction between the aminooxy functionalised peptide and an ^{18}F labelled carbonyl (such as with [^{18}F]FBA or [^{18}F]fluoroacetaldehyde) to form an oxime. The benefits of the chemoselective ligation approach[59] are the high chemoselectivity and regioselectivity offered, the use of an unprotected aminooxy peptide precursor giving the benefit of a 1-step radiolabelling scheme and the reaction can proceed in aqueous media at pH 4-7[58].

The extensive use of ^{18}F PET means that more ^{18}F-prosthetic groups and reaction routes to incorporate the isotope into peptides, proteins and antibody fragments are being developed by radiochemists. For example, it has been demonstrated how the lysine moiety of peptides can be targeted for site specific radiolabelling, but cysteine moieties can also be used. The cysteine residues of peptides and antibody fragments can be coupled through a michael addition with a ^{18}F-prosthetic group containing a maleimide functionality or a maleimide derivative can be coupled to the peptide in an initial step before being radiolabelled with an ^{18}F-prosthetic. This approach has been demonstrated with [^{18}F]SFB[60] as well as with [^{18}F]FBA[61, 62] as seen in Figure 15.

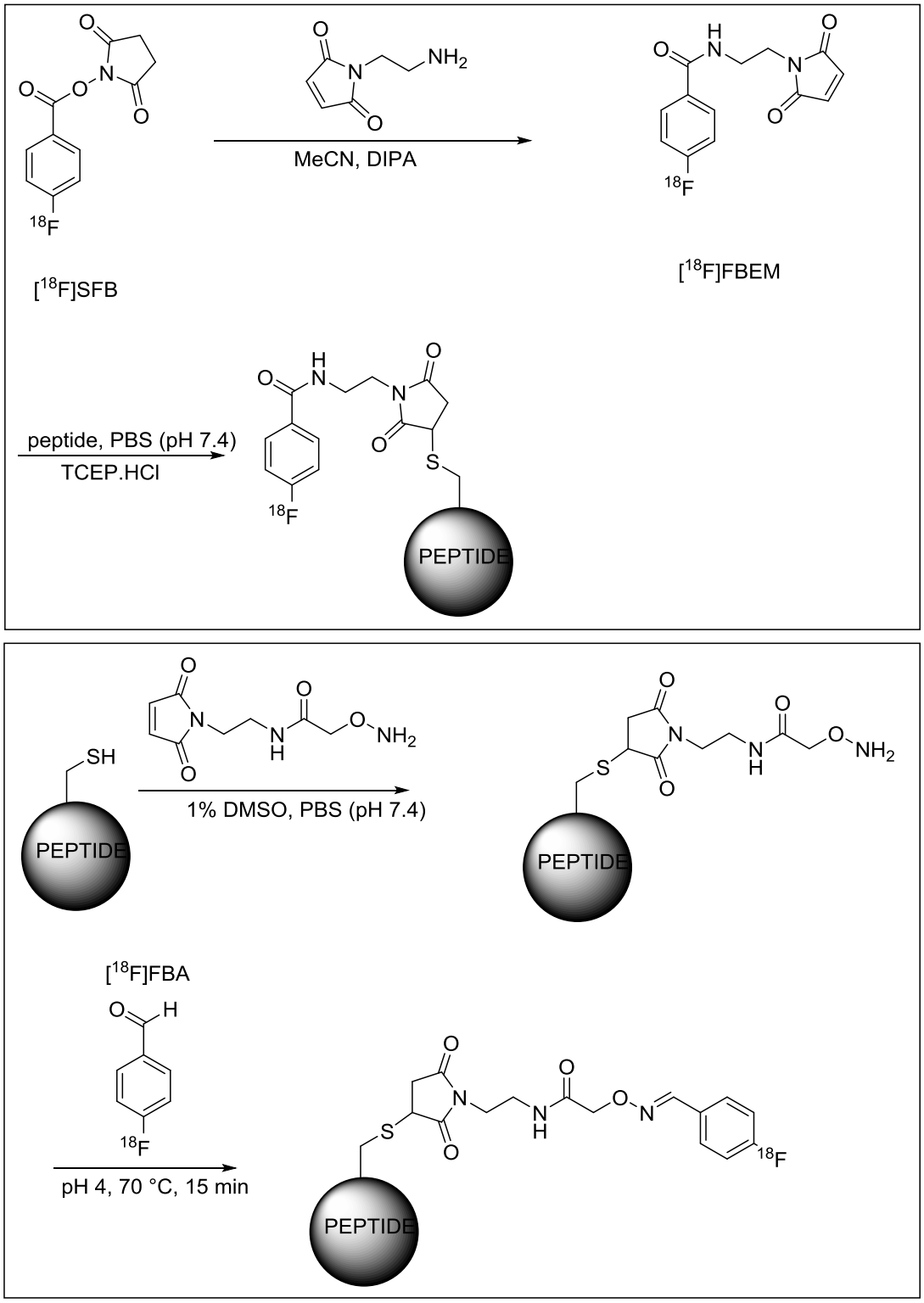

Figure 15: Cysteine targeted radiolabelling of peptides. The top scheme shows a route using the prosthetic group [^{18}F]SFB and the bottom scheme shows a route which uses the prosthetic group [^{18}F]FBA.

For targeting the thiol groups of cysteine residues in peptides and proteins the di-sulfide bridge must be reduced. Cai *et al* used *tris*(2-carboxyethyl)phosphine

(TCEP) to liberate thiol groups which could be reacted by Michael addition with N-[2-(4-^{18}F-fluorobenzamido)ethyl]maleimide ([^{18}F]FBEM, produced from [^{18}F]SFB) to provide chemoselective radiolabelling of RGD-peptide in an 80% incorporation yield (non-decay corrected)[60]. The approach by Cheng *et al* and Namavari *et al* was to take their target biomolecules and anchor on an aminooxy reactive group via a bi-functional linker which contained a maleimide group at one end and an aminooxy group at the opposite end. In both cases dithiothreitol (DTT) was used to reduce the disulfide linkages of the target molecules. A Michael addition then occurs between the thiol group of the affibody or protein and the maleimide group of the bifunctional linker to give the aminooxy functionalised bio-molecule[61, 62]. The aminooxy functionality can then be reacted with the aldehyde [^{18}F]FBA to give the radiolabelled protein through an oxime linkage. In comparison to the [^{18}F]FBEM route, the overall radiochemical yield is lower (26-30% decay corrected[61]) using this approach.

^{18}F radiochemistry is a large and extensive research field and often the need to produce a ^{18}F-prosthetic group as a first step of the radiochemistry poses a big challenge to fully automate the production of an ^{18}F-radiolabelled tracer. The entire process is multi-step and involves the trapping and elution of [^{18}F]F$^-$ form the cyclotron, azeotropic drying of [^{18}F]F$^-$, reaction of [^{18}F]F$^-$ to produce a prosthetic group followed by purification, reaction of the ^{18}F-prosthetic group with the target molecule/peptide (in some cases followed by a deprotection reaction), purification of the final product and formulation for injection. Automating all of these steps will often require modification of radiochemistry systems in some respect or working over multiple radiochemistry platforms.

Copper-64 - [^{64}Cu]

The long half-life of ^{64}Cu ($t_{½}$ = 12.7 hours) makes it an extremely useful PET isotope to study biological processes which have long *in vivo* kinetic. The positron branching of ^{64}Cu is reasonably low at 18% of decays occurring by β^+ emission, however an Auger electron emission also occurs which has some therapeutic potential making this isotope useful for targeted radiotherapy as well as for PET scans[34]. ^{64}Cu can be produced in a cyclotron via the nuclear reaction ^{64}Ni(d,2n)^{64}Cu in which a highly enriched nickel-64 (^{64}Ni) target is bombarded with deuterons to produce ^{64}Cu amongst some other impurities[63]. Following cyclotron irradiation the

target disk is dissolved in strong HCl and is transferred onto an anion exchange resin column where ^{64}Cu is purified and finally eluted as $[^{64}Cu]CuCl_2$[64].

Copper chemistry is dominated by chelation chemistry and different types of ligands which complex to the metal can determine the oxidation state that copper sits in. For example highly covalent and polarisable or 'soft' ligands (thioether, nitrile and cyanide for example) will stabilise the Cu^+ oxidation state. Less polarisable ligands which show less covalency (such as perchlorate ions (ClO_4^-) or sulfate ions (SO_4^{2-})) will favour the disproportionation of Cu^+ to Cu metal and the Cu^{2+} oxidation state[34]. For Cu^+ the 3d electron shell is filled and the coordination numbers and geometries of the complexes formed with Cu^+ are governed by steric considerations of the ligands. Complexes of Cu^+ may occur with coordination numbers 2, 3 and 4 with linear, trigonal planar and tetrahedral geometries. Cu^{2+} has a $3d^9$ electron configuration meaning that ligand field stabilisation energy becomes important. Coordination numbers of 4, 5 and 6 are adopted by Cu^{2+} and the octahedral and tetrahedral geometries of these complexes undergo Jahn Teller distortions due to the $3d^9$ electron configuration[34]. Cu^+ complexes are less suited to being used for radiolabelling because the ligands are relatively labile and therefore have low *in vivo* stability. However complexes of Cu^{2+} are much less labile toward the exchange of ligands which is in some part due to the activation energy from the ligand field stabilisation[34].

For ^{64}Cu to be utilised as a radiopharmaceutical the metal needs to be chelated to a strong and non-labile ligand to remain stable *in vivo*. It should be noted that thermodynamic stability of a ^{64}Cu complex does not always infer kinetic stability *in vivo* as in a biological system and at tracer concentrations, the complex will be challenged by metal binding proteins and enzymes as well as by natural metabolism. The body has many native copper transport proteins and enzymes which utilise copper so the administered ^{64}Cu must be complexed to a ligand which is not easily exchangeable for these proteins and amino acids. And finally the copper complex must not be susceptible to redox chemistry in the body, In general high levels of ^{64}Cu found in the liver during a PET scan indicates the instability of the ^{64}Cu complex[65].

There is much research interest in bi-functional ^{64}Cu chelators that are able to form very stable complexes with copper and have a reactive functionality linked to them which allows the complex to be coupled to biologically active molecules like proteins, antibodies or nanoparticles[65]. Macrocyclic chelators of copper are well studied, examples include 1,4,7-triazacyclononane-N,N',N''-triacetic acid (NOTA), 1,4,7,10-tetraazacyclododecane-N,N',N'',N'''-tetraacetic acid (DOTA) and bicyclic sarcophagine ligands (Sar) derivatives as can be seen in Figure 16.

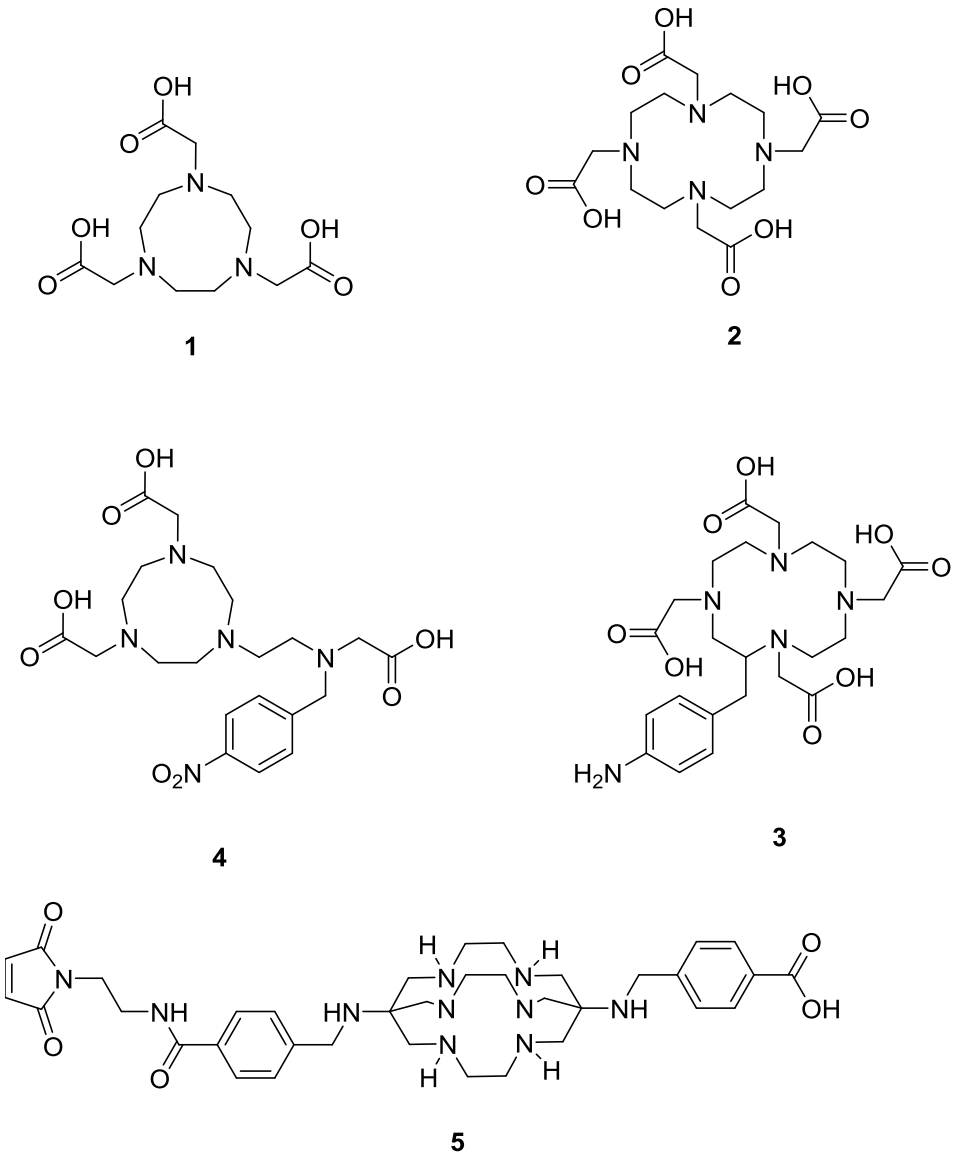

Figure 16: some common macrocylcic chelators and bi-functional chelators of ^{64}Cu. 1) NOTA, 2) DOTA 3) *N*-NE3TA 4) *p*-NH_2-Bn-DOTA and 5) BaMalSar.

NOTA is able to trap ^{64}Cu in a cage like structure via the 3 amine molecules of the macrocycle and the metal is held further in place by the 3 carboxyl pendants to

form a 6 coordinate complex to from a distorted trigonal prismatic geometry[66]. The 4-membered macrocylcic ligand DOTA complexes ^{64}Cu using the 4 amine functionalities of the cyclen ring as well as 2 of the carboxylic arms. This forms a 6 coordinate complex in a pseudo octahedral geometry[66] with 2 of the carboxylic arms not being used to chelate the metal, leaving them free to be used as a linker. Some examples of adding reactive groups to both NOTA and DOTA macrocycles to produce bi-functional chelators which can be coupled to bioactive molecules[67] can be seen in Figure 16. Incorporation of ^{64}Cu into a selection of NOTA and DOTA bi-functional complexes will occur under mild conditions (room temperature or 37 ºC) up to a maximum of 90 minutes[65]. The Sar bifunctional ligand BaMalSar (Figure 16) can be conjugated to bioactive molecules through the maleimide group. One group demonstrated that BaMalSar could be conjugated to cyclic peptides before being radiolabelled with ^{64}Cu and was used for tumour targeting with PET[68]. Cai *et al*, compared the *in vivo* stability of a [^{64}Cu]DOTA and a [^{64}Cu]Sar complex coupled to an RGD peptide, and found greater *in vivo* stability with the [^{64}Cu]Sar complex this was confirmed with preclinical PET images in which the [^{64}Cu]DOTA derivative was shown to release ^{64}Cu which was taken up in the liver[69].

One elegant way for radiolabelling antibodies with ^{64}Cu is based on a pre-targeting strategy which uses Diels-Alder click chemistry[70]. With this strategy the initial step is to modify the antibody of choice with a transcyclooctene, the modified antibody is injected and allowed to accumulate at the target site. Once the free antibody has been cleared from the body (1 or 2 days perhaps) [^{64}Cu]-NOTA modified tetrazine is injected which will target the modified antibody which is already at the biotarget. A [4+2] click cycloaddition reaction will occur between the cyclooctene of the modified antibody and the tetrazine modified [^{64}Cu]-NOTA coupling the two to produce the ^{64}Cu radiolabelled antibody at the target site[70]. A schematic of this chemistry can be seen in Figure 17.

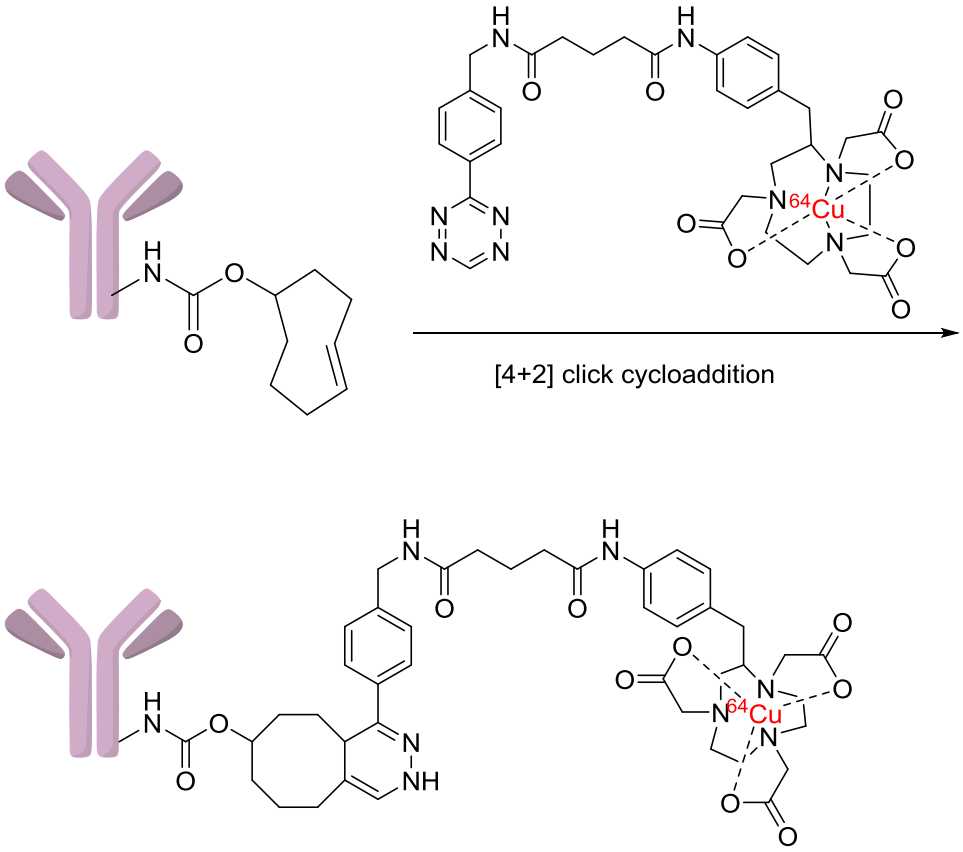

Figure 17: A [4+2] click cycloaddition of a modified antibody with [^{64}Cu]-NOTA modified with tetrazine.

[^{64}Cu] finds a use beyond bi-functional chelation to image proteins and antibodies. Since copper is a trace metal found in the body, there are many proteins and enzymes which are utilised in the transport, uptake, distribution and excretion of copper in the body. Copper *in vivo*, will be complexed by albumin, ceruloplasmin, transcuperin or histidine for transport purposes or to form a copper pool for transport to the liver and kidney[71]. Also the redox properties of copper are exploited in enzymatic systems since the metal can accept and donate electrons, changing oxidation states from Cu^{+}, Cu^{2+} and Cu^{3+}. There are a variety of enzymes which utilise copper as a cofactor for respiratory oxidation and neurotransmitter synthesis for example[71]. The imbalance of copper in the body is associated with a number of pathological conditions such as Wilson's disease, which causes an accumulation of copper in the liver, kidney and brain, or Menkes disease, which is associated with a deficiency of copper containing enzymes. Copper radionuclides have a use for the diagnosis and for the monitoring of conditions such as these. Also changes to copper metabolism may be observed in a number of inflammatory disease and changes to copper metabolism pathways can be imaged non-invasively and quantitatively using

[^{64}Cu]$CuCl_2$ PET for example[34, 71]. [^{64}Cu]-histidine complexes have also been used as a diagnostic technique of Wilson's disease in rats[72]. It was postulated that the delivery of ^{64}Cu as [^{64}Cu]-histidine would lead to biliary excretion of radio-copper in an ATP7B dependent manner[72].

There are many other important applications of ^{64}Cu PET. Of particular interest is the use of ^{64}Cu to radiolabel cells for trafficking and tumour imaging [73-75]. Different carriers have been investigated to transport ^{64}Cu into various types of cells via mechanisms of phagocytic engulfment[74] or other receptor mediated uptake pathways such as pinocytosis. Pala *et al* used chitosan coated magnetic nanoparticles as the carrier of ^{64}Cu to offer a dual imaging (PET and MR) application[74]. Another group used [^{64}Cu]-pyruvaldehyde-bis(N4-methylthiosemi-carbazone), ([^{64}Cu]-PTSM), to radiolabel cells[73]. It was found that [^{64}Cu]-PTSM acts as a redox active transporter of Cu^{2+} into cells. The lipophilic complex enters the cell by passive diffusion, the internalised $^{64}Cu^{2+}$ is reduced to $^{64}Cu^{+}$ causing the metal to dissociate from the PTSM complex. This renders the ^{64}Cu trapped inside the cell as Cu^{+} while the PTSM structure can diffuse out of the cell. Radiolabelling of white blood cells for scintigraphy with single-photon emission computed tomography (SPECT) with radio isotopes such as indium-111 (^{111}In) and technetium-99m (^{99m}Tc) is used regularly in clinical assessment of inflammation. However (PET) offers superior quantification and sensitivity and is attractive for monitoring the regional signal from migrated radiolabelled cells to pathological tissue in infectious and inflammatory diseases.

In conclusion copper is a very important PET isotope owing to its long half-life allowing for the study of biological processes with longer *in vivo* kinetics. As demonstrated here, radio-copper can be chelated to appropriate macrocyclic molecules making it stable *in vivo* and the subsequent chelated copper can be coupled to peptides and antibodies of interest. Additionally radio-copper can be used to diagnose and monitor pathological conditions associated with the imbalance of copper in the body as well as studying changes in copper metabolism, a consequence of a number of inflammatory conditions.

Zirconium-89 - [^{89}Zr]

The positron emitting isotope ^{89}Zr has emerged as a promising candidate for radiolabelling antibodies and antibody fragments for immuno-PET[33, 76-78]. [^{89}Zr] has a radioactive half-life of 78.4 hours and decays by β^+ with 23 % efficiency. The relatively low energy of the emitted positron (0.4 MeV) of ^{89}Zr in comparison to ^{64}Cu (0.65 MeV) results in improved spatial resolution of PET images using ^{89}Zr. Also the quality of the PET image is not affected by the decay characteristics of ^{89}Zr, a relatively high energy gamma photon (909 keV) does not interfere with the 511 keV gamma photons which are detected during a PET scan. The long half-life ($t_{½}$ = 78.4 hours) allows for circulation times to permit optimal biodistribution and target uptake of antibodies labelled with ^{89}Zr.

[^{89}Zr] is commonly produced via the nuclear reaction ^{88}Y(p,n)^{89}Zr, in which a disc of natural yttrium is bombarded by a proton beam in the cyclotron. Purification of ^{89}Zr from yttrium and other radio-impurities can be achieved using a hydroxamate column. Zirconium-89 is removed from the hydroxamate resin with an oxalic acid solution (1.0M) to give a product in high radiochemical purity[79].

In a similar fashion to [^{64}Cu], the radiometal ^{89}Zr also requires a chelator to transport the isotope *in vivo* as well as to offer *in vivo* stability. Zirconium, in the +4 oxidation state, is a hard Lewis acid and will therefore form stable complexes with hard Lewis bases such as hydroxamate ligands. Desferrioxamine (DFO) is a hexadentate ligand which has hydroxymate groups available for the binding of Zr^{+4} see Figure 18. DFO is also a natural product and is a siderophore (an iron chelating compound made by microorganisms) produced by *Streptomyces pilosus*, a family of Actinobacteria.

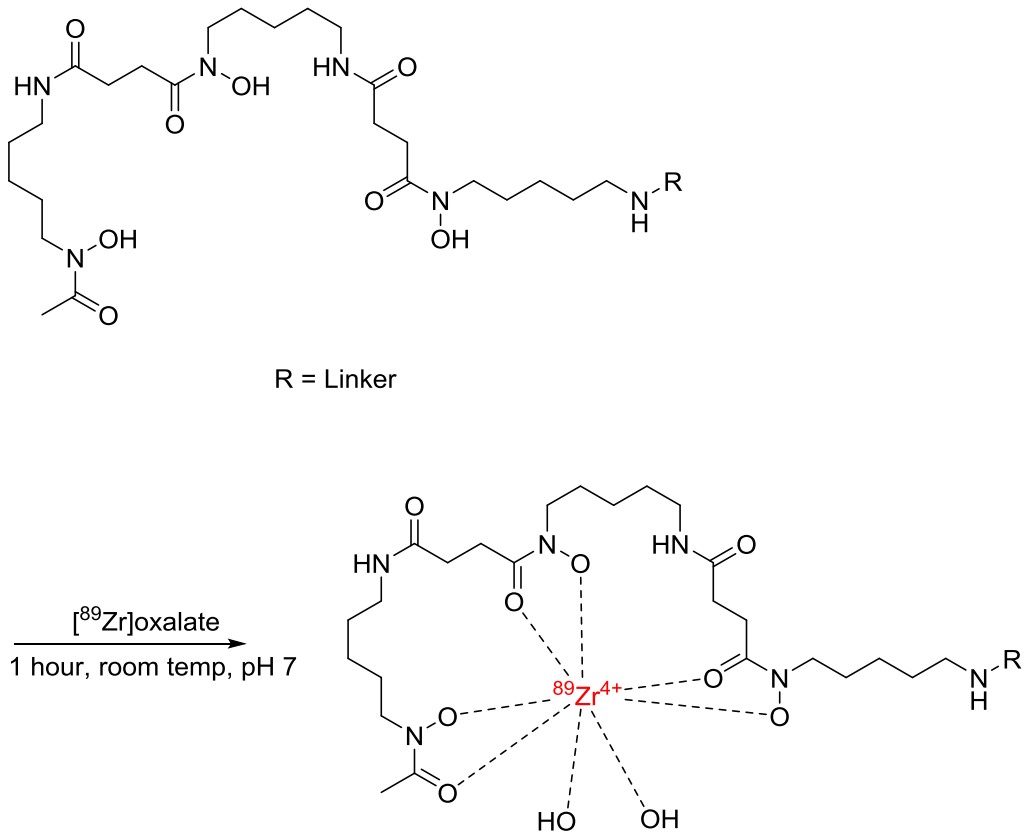

Figure 18: DFO chelation to ^{89}Zr

DFO is already used in the clinical setting to chelate and therefore remove iron and aluminium from a patient who has an overload of either metal. Because of this, the biodistribution and toxicity of DFO were well studied making it's translation as a chelating agent for ^{89}Zr in immuno-PET more straightforward. DFO complexes to Zr^{4+} using three of the hydroxamate groups, the coordination sphere is made complete by the addition of two water molecules to make an 8 coordinate complex which is thermodynamically favourable, as determined by density function theory (DFT)[77]. DFO can be linked to a biomolecule using a number of different functional groups such as isothiocyanates or via an activated ester, in this way DFO can be reacted with lysine groups of proteins and antibodies. There are two modified chelators which are employed in coupling DFO to peptides and antibodies through random lysine groups, *N*-succinyl-DFO-tetrafluorophenol ester (*N*-suc-DFO-TFP-ester) and *p*-isothiocyanatobenzyl-DFO (DFO-Bz-NCS)[80]. The method for conjugating these modified chelators to biomolecules differs slightly for each. Preparation of N-suc-DFO-TFP-ester occurs in a multi-step process, in the first step DFO is reacted with succinic anhydride to produce N-succinyl-DFO. Next iron is chelated to the complex, this protects the hydroxamate groups of DFO from reacting

with tetrafluorophenol ester. In a final step the tetrafluorophenol group is added to form N-suc-DFO-TFP-ester. To conjugate N-suc-DFO-TFP-ester to random lysine groups of antibodies or proteins a basic pH is required and the conjugate can form a stable amide bond with lysine residues[80]. To proceed with the ^{89}Zr radiolabelling the iron must first be removed from the chelate, this is achieved by an exchange with ethylenediaminetetraacetic acid (EDTA) in a molar excess. One advantage of this method is that it is possible to get a UV signal for HPLC analysis of Fe-N-suc-DFO-TFP-ester (430 nm wavelength) meaning that it is possible via size exclusion chromatography to assess the chelator to antibody ratio.

Some of the disadvantages with using N-suc-DFO-TFP-ester as the chelator of ^{89}Zr is that the multi-step procedure is time consuming and the antibody that is being conjugated may not be stable to conditions used to exchange the iron form the chelate prior to radiolabelling. As a result DFO-Bz-NCS was investigated as a chelator[81]. DFO-Bz-NCS is commercially available and can be conjugated to lysine moieties of peptides and antibodies via a thiourea linkage. The conjugation conditions gave a chelate : monoclonal antibody (mAb) ratio of approximately 1.5:1. [^{89}Zr]-Bz-NCS-mAb was produced in > 85% radiochemical yield and was shown to be stable in serum for up to 7 days with < 5% of ^{89}Zr released[81]. However, some consideration needs to be given to the buffer used to store the radiolabelled DFO-Bz-NCS-mAb, any buffers which contain chloride ions should be avoided as radiolysis of these ions to form hypochlorite (OCl^-) will react with the thiourea unit of the linker and release ^{89}Zr from the antibody[76]. Figure 19 shows both N-suc-DFO-TFP-ester and DFO-Bz-NCS linkage to random lysine groups of monoclonal antibodies (mAb).

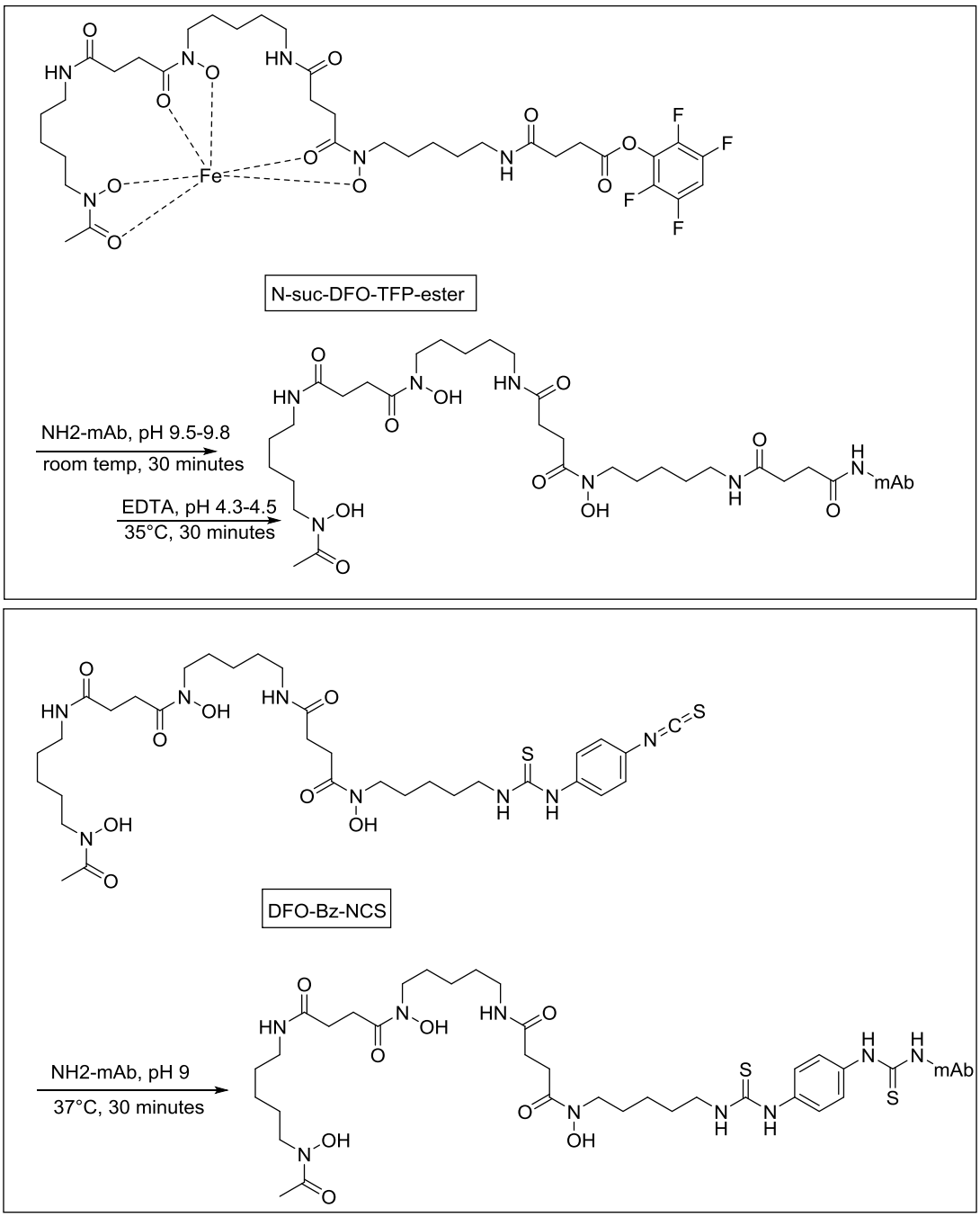

Figure 19: Conjugation of N-suc-DFO-TFP-ester and DFO-Bz-NCS to lysine groups of monoclonal antibodies.

It should be noted that other strategies have been used to conjugate antibodies to the DFO ligand prior to radiolabelling with ^{89}Zr. For example cysteine groups can be engineered onto antibodies at specific sites to not interrupt the biological activity of the antibody and these then may be targeted by DFO with thiol reactive linkers[82]. This strategy offers regioselective conjugation of DFO to antibody. Also, in a similar manner to that which was described for [^{64}Cu], Diels-Alder click chemistry can be used to introduce DFO into biomolecules. Tetrazine-modified DFO can be reacted

with norbornene modified antibodies in a bioorthogonal cycloaddition reaction to couple the chelate with the antibody[83].

There are still some issues to be resolved with the use ^{89}Zr PET however. If ^{89}Zr is released from the chelate *in vivo* the radiometal may accumulate in mineral bone, giving a radiation dose to the bone marrow. Different studies have shown an accumulation of ^{89}Zr in bone ranging from 3% to 15%[33] at 72 - 168 hours post injection. A number of factors are thought to contribute to the loss of stability of [^{89}Zr]-DFO complexes, including the structure of the ligand, with linear ligands such as DFO being less stable than macrocyclic ligands such as the ^{64}Cu chelators NOTA and DOTA. Also the cavity size which is created by the chelator and the radius of the metal ion has an effect. If the sizes of the cavity and the ionic radius are similar a more stable complex is formed, however if the metal is not completely engulfed by the ligand then the complex is less stable. Zr-DFO complexes only take 6 of the possible 8 coordination sites and so there is some possibilities for metal loss form the complex[33].

In order to prevent and minimise the loss of ^{89}Zr from DFO, alternative chelators need to be developed which will not allow for the release of ^{89}Zr *in vivo*. It seems logical that to get a more stable complex of ^{89}Zr in the preferred octadentate geometry then a ligand which possesses four hydroxamate groups would be ideal. The three hydroxomate groups of DFO requires two water molecules to complete the coordination sphere of the complex, whereas four hydroxomate groups would saturate the coordination sphere and presumably create a more stable complex with ^{89}Zr. Currently DFO is the only known chelator for ^{89}Zr, however some preliminary work has been completed to examine new potential chelates for ^{89}Zr. Some studies have investigated four bi-dentate hydroxamte groups to chelate Zr in a 4:1 Ligand:Zr complex[84]. Groups have also studied the use of octadentate ligands such as 3,4,3-(LI-1,2-HOPO) (Figure 20) which has a carbon backbone with four hydroxypyridinone groups which are used for ^{89}Zr chelation[85].

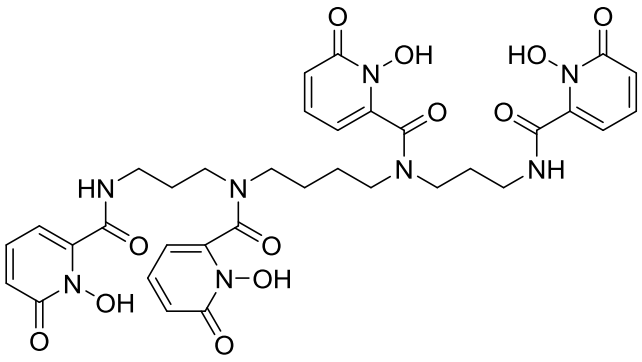

Figure 20: The octadentate ^{89}Zr chelator 3,4,3-(LI-1,2-HOPO).

[^{89}Zr] has ideal physical decay characteristics to be used for immune-PET studies over long periods due to its long half-life of 78.4 hours. The long half-life also means that good tumour to background ratios for antibodies can be attained and biological processes at late time points can be imaged. The low energy of the emitted positron also offers the potential of high spatial resolution of the PET images. The 909 keV gamma photon, which is produced during the decay of ^{89}Zr, can be easily gated off from the 511 keV gamma photons which are detected during a PET scan. However the 909 keV may also pose a problem in terms of radiation dose to the subject and to non-target organs. However as more advanced and more sensitive PET/CT scanners are developed the opportunity to obtain high quality PET images with a smaller injected radioactivity dose may be achievable.

However, in comparison to ^{64}Cu the 78.4 hour half-life of ^{89}Zr is more beneficial when studying long biological half-life processes. Additionally β^+ branching is slightly higher (23%) for ^{89}Zr when compared to ^{64}Cu (17%) which gives a slightly improved count rate and sensitivity in PET scans. Also, the 909 keV gamma photon emitted by ^{89}Zr is also much lower when compared to the 1.34 MeV gamma photon of ^{64}Cu and the 1.7 MeV gamma photon produced by [^{124}I] which must be considered in relation to patient radiation doses. Finally, in contrast to copper, zirconium does not have any naturally occurring plasma protein carriers and therefore there is less competition to displace ^{89}Zr from its chelate.

Synthetic Opiates used with PET

Opioid receptors were first seen in the CNS by radioligand binding techniques in rodents in the 1970s[86]. When the technique of PET was introduced it

proved an invaluable tool in many fields, including providing an extensive understanding of the opioidergic system. The synthetic opiate diprenorphine (DPN) is a non-selective opiate antagonist. DPN and buprenorphine (BPN) both belong to a family of compounds called the Bentley compounds Figure 21.

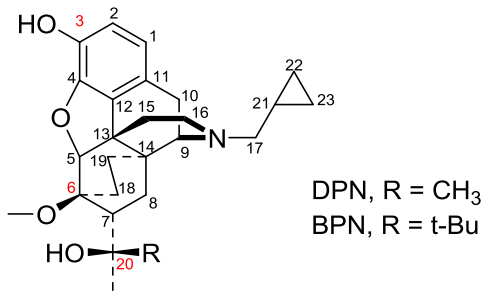

Figure 21: Chemical structures of DPN and BPN.

The first of these compounds to be labelled with a PET isotope was N-[^{11}C]methyletorphine in 1981. The radiochemistry used [^{11}C]formaldehyde as the labelling agent[87]. In the case of DPN and BPN, *N*-cyclopropyl[^{11}C]methyl-diprenorphine (*N*-[^{11}C]DPN) was originally described in 1985[88] which was soon followed with the radiolabelling of BPN with ^{11}C by the same radiolabelling route in 1987[89] as seen in Figure 22.

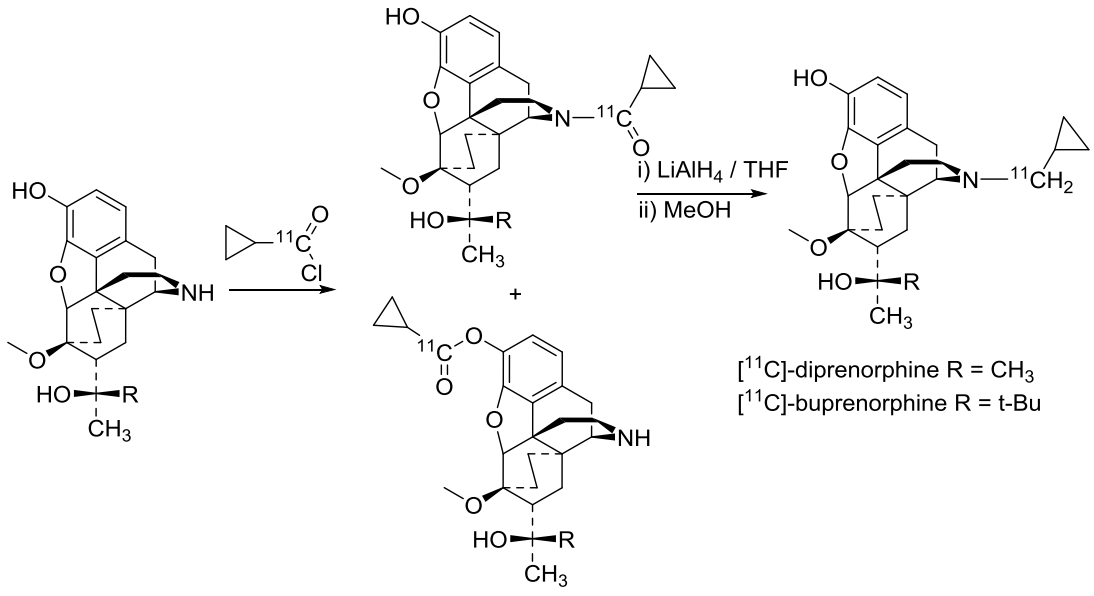

Figure 22: ^{11}C-labelled DPN and BPN via [^{11}C]cyclopropanecarbonyl chloride.

The precursor molecules are acylated with [^{11}C]cyclopropanecarbonyl chloride to form a ^{11}C-amide as well as a ^{11}C-ester at the phenol functionality as a minor-product[88]. The ^{11}C-amide product which is formed is then reduced with

$LiAlH_4$ in tetrahydrofuran (THF), *N*-[^{11}C]DPN was produced in 35% radiochemical yield and *N*-[^{11}C]BPN was produced in 20% radiochemical yield via this method[88, 89]. *N*-[^{11}C]BPN and *N*-[^{11}C]DPN were both used for *in vivo* imaging of baboon as well as mouse brain with PET[90]. Comparing the two radiotracers suggested that *N*-[^{11}C]DPN was the more promising ligand for the imaging of opioid receptors using PET, as it produced a significantly higher striatum/cerebellum ratio compared to *N*-[^{11}C]BPN. However both radioligands were rapidly metabolised via *N*-dealkylation, resulting in the loss of the labelled moiety. Therefore it was suggested that labelling at the C-6 position (see Figure 21) would result in a more metabolically stable tracer. Previous groups[91, 92] reported a procedure for labelling DPN at the 6-methoxy position, again in two steps but using [^{11}C]CH_3I as the labelling agent. When Lever *et al.,* reported this procedure they used a precursor which was protected at the C-3 position with *t*-butyldimethylsilyl (to prevent methylation at the C-3 phenoxy group), however this gave the product labelled at the C-3 as well as the C-6 position (with a ratio of 6:4 with diprenorphine and a ratio of 8:2 with buprenorphine, in both cases the desired products produced in the minor fraction)[93]. This showed that the t-butyldimethylsilyl protecting group was unstable in the presence of the strong base sodium hydride (NaH). A strong base is essential for deprotonation of the hydroxyl group at the 6 methoxy position to yield the more reactive alkoxide group (RO^-) which is then able to react with [^{11}C]CH_3I in an S_N2 nucleophilic substitution. Therefore a protecting group which would remain stable in highly basic conditions was required. The protecting group needed to be stable in the presence of NaH to allow preferential generation of the anion and subsequent methylation at the C-6 position but also needed to be easily removed once the methylation reaction was complete, Luthra *et al*[93] investigated three alternative protecting groups. The protecting groups investigated were triisopropylsilyl, triisobutylsilyl and triphenylmethyl (trityl). It was found that the trityl protecting group was both stable in basic conditions and was acid labile, making it easy to remove post methylation at the 6-methoxy position. The trityl protected precursor for both BPN and DPN can be prepared in 2-steps. The first step requires demethylation of the molecule with $LiAlH_4$ (using CCl_4/THF), to give the tri-hydroxy compound. In the second step the trihydroxy compound is reacted with triphenylmethylchloride in the presence of triethylamine. It is essential that the trityl-protected precursors are well-separated from the starting materials, diprenorphine or buprenorphine as this will ensure that

the corresponding ^{11}C labelled compounds are produced in high specific activity. The trityl protected precursor can then be radiolabelled at the 6-methoxy position with ^{11}C in two steps, firstly methylation with $[^{11}C]CH_3I$ or $[^{11}C]CH_3OTf$ under basic conditions followed by the removal of the trityl group with hydrochloric acid, Figure 23 below depicts the radiolabelling of DPN via the trityl protected precursor.

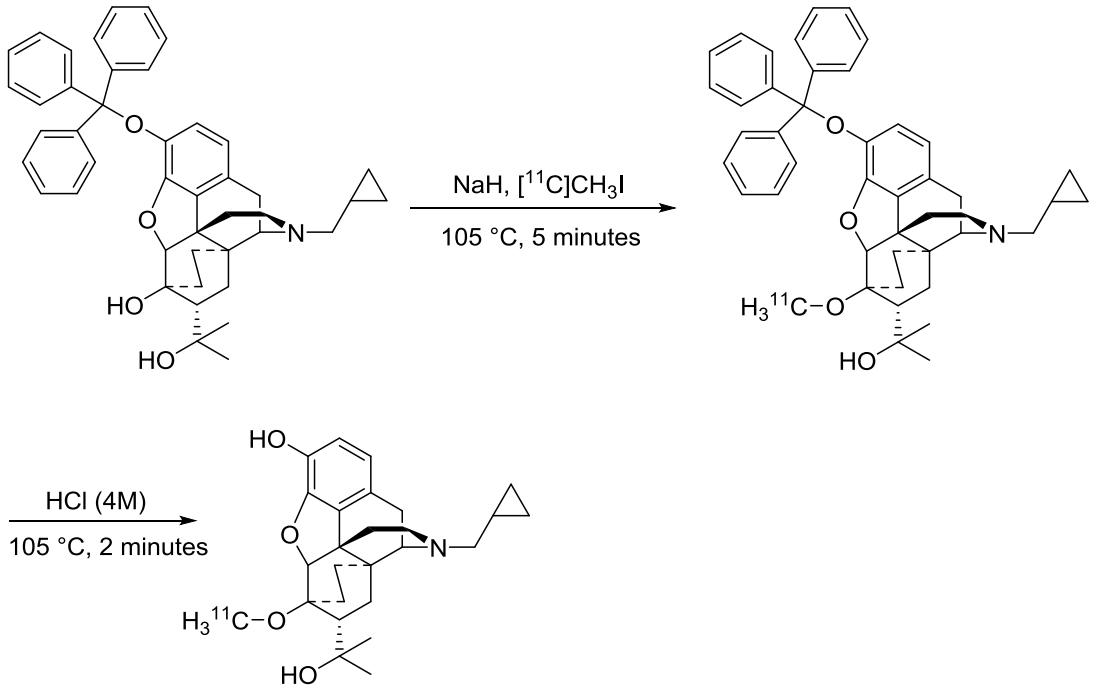

Figure 23: Synthesis of [^{11}C]DPN via the trityl protected precursor [3-*O*-trityl, 6-*O*-desmethyl]-diprenorphine (TDPN).

[^{11}C]DPN has favourable pharmacological properties and is one of the most widely used PET ligands to study the endogenous opioid system[9, 94-97]. However, the short half-life of ^{11}C may hamper some PET studies in which longer biological kinetics or longer term effects are being investigated. For these types of studies DPN labelled with ^{18}F may be a better alternative. Two ^{18}F labelled DPN derivatives have been produced by ^{18}F-fluoroethylation using [^{18}F]FEtTos at the hydroxyl C-6 position or at the N-17 position substituting the methylcyclopropyl group. These reactions produce respectively the 6-*O*-[2-[^{18}F]fluoroethyl)-6-*O*-desmethyldiprenorphine ([^{18}F]DPN) and the *N*-[^{18}F]fluoroethyl-DPN derivatives[98] (Figure 24).

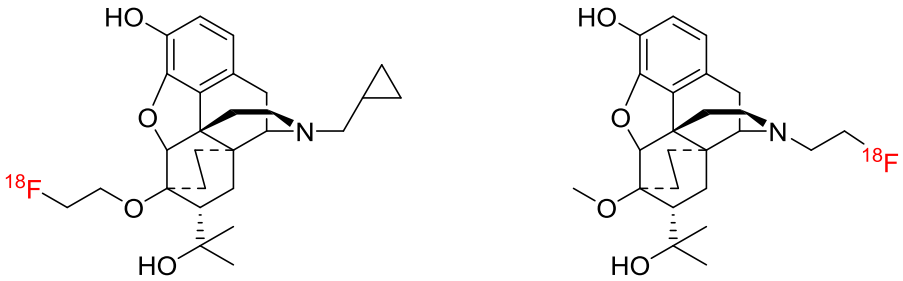

Figure 24: 6-*O*-[2-[^{18}F]fluoroethyl)-6-*O*-desmethyldiprenorphine and *N*-[^{18}F]fluoroethyl-DPN.

The *N*-[^{18}F]fluoroethyl-DPN derivative proved unsuccessful showing low binding affinity to the opioid receptors. This revealed the significance of the methylcyclopropyl moiety in the affinity and selectivity of the molecule to opioid receptors. [^{18}F]DPN proved to be the most promising ^{18}F labelled DPN for PET studies. Nevertheless one major hurdle for the automated radiosynthesis of [^{18}F]DPN molecules remains. That is the requirement to purify the intermediate [^{18}F]FEtTos prior to its reaction with the DPN precursor. [^{18}F]FEtTos must be separated from the di-tosylate precursor in order to avoid cross linking reactions of two DPN molecules.

The binding pattern of [^{18}F]DPN was compared with opioid sub-type selective ligands ^{3}H-DAMGO (μ-selective), ^{3}H-DPDPE (δ-selective) and ^{3}H-U69,593 (κ-selective) and saturation experiments carried out using concentrations of [^{18}F]DPN at twice their dissociation constant. [^{11}C]DPN had been shown previously to have fast brain uptake kinetics and in comparison, [^{18}F]DPN showed a lower brain uptake but with a slower brain clearance compared to [^{11}C]DPN[98]. The lower brain uptake of [^{18}F]DPN may be due to the molecule possessing a lower BBB permeability as a result of the additional [^{18}F]fluoroethoxy group on the molecule. Another major difference found between [^{11}C]DPN and [^{18}F]DPN was the rate of metabolism in mice, with [^{18}F]DPN showing a faster metabolism[98]. Despite this the similarities in the pharmacokinetics and receptor binding of [^{18}F]DPN compared to [^{11}C]DPN and the longer half-life of ^{18}F allows for longer scanning periods and more complex scanning protocols with displacement studies as an example[98].

[^{11}C]DPN is an opioid receptor antagonist with high affinity for all opioid receptor sub-types (non-selective). Activation of the endogenous opioid system by experimental painful stimuli or by a clinical pain stimulus causes an increase of endogenous opioid peptide release leading to enhanced opioid receptor occupancy [97]. This has been seen in patients with inflammatory pain, where a decrease in

[^{11}C]DPN opioid receptor binding was observed. Two possible reasons for this have been cited, one is that when a painful stimulus is applied to the body, endogenous opioids are released and compete with [^{11}C]DPN for opioid receptor occupancy. Endogenous opiates may have a higher affinity for receptors and so displace [^{11}C]DPN. Another possible explanation is that [^{11}C]DPN opioid receptor binding decrease is representative of a loss of opioid receptor bearing neurons, which is most likely to occur following lesions in the central nervous system. If the reason for the loss of opioid receptor binding was due to endogenous opioid release blocking receptors, this should be observed in all types of neuropathic pain whether central or peripheral. If however the loss of opioid receptor binding is due to the loss of opioid receptor bearing neurons then this would be seen in central neuropathic pain only. Using [^{11}C]DPN and PET, Maarrawi *et al*., investigated changes in central opioid receptor binding in a sample of patients having neuropathic pain with a balanced number of central and peripheral cases. By comparing the two sets it would be possible to decipher if the loss of opioid receptor binding was due to secretion of endogenous opioids or due to the loss or inactivation of receptor bearing neurons in neuropathic pain. Relative to control subjects both peripheral and central pain subjects showed significant decrease in opioid receptor binding in a number of regions. In the central pain group the decrease of opioid receptor binding was asymmetrical and predominated in the brain hemisphere contralateral to the neuropathic pain. However the group with peripheral neuropathic pain showed bilateral and symmetrical decrease in opioid receptor binding most likely as a result of the release of endogenous opioids[97]. A lateralised decrease in [^{11}C]DPN opioid receptor binding was seen exclusively to central pain patients. The most likely explanation for this is the loss or inactivation in opioid receptor bearing neurons, however this was not co-localised with lesions in the brain. However, focal lesions are able to cause neuronal damage at distant but interconnected sites and so metabolic inactivation of opiodergic synapses at regions connected with damaged areas was given as a possible explanation for this[97]. Differences in opioid receptor binding between central and peripheral pain groups may help to understand their differing susceptibility to opioid therapy. The study by Maarrawi *et al* is one of many examples of how PET is increasing our understanding of the biology and pathology of pain and inflammation whether from the central nervous system or from a peripheral source.

[^{11}C]DPN has also been used to quantify cerebral kinetics in PET studies[94]. In this study three different protocols were used to fit the kinetics to a tissue model (Figure 25).

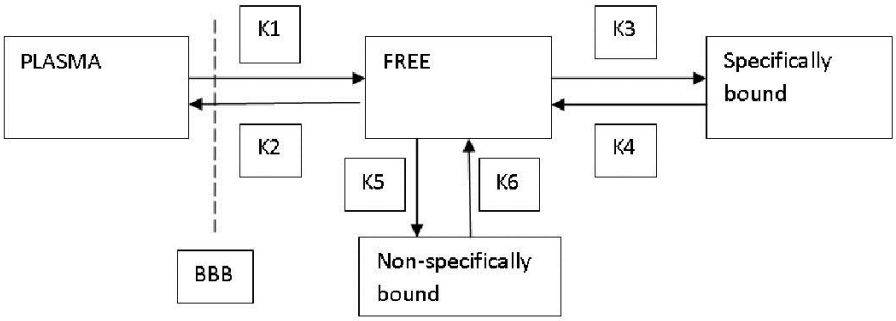

Figure 25: Compartmental model showing uptake and binding of [^{11}C]DPN, showing rate constants (K) for each compartment.

Three separate protocols were used, i) tracer only, in which an intravenous injection of [^{11}C]DPN containing a sub-pharmacological quantity (0.2-0.5 µg/kg body weight) of cold DPN is administered. ii) pulse chase, in which [^{11}C]DPN is injected and 30 minutes after injection a displacement dose of the opioid antagonist naloxone is injected. iii) pre-saturation, in which a dose of naloxone (chosen to saturate all [^{11}C]DPN sites) is administered 5 minutes prior to the injection of [^{11}C]DPN. The tracer only protocol establishes the total binding of [^{11}C]DPN to receptors and allows for the calculation of K_d (the concentration of [^{11}C]DPN needed to occupy 50% of the receptor sites, a measure of the affinity of a ligand for a receptor). By pre-saturating receptors with naloxone (a non-selective competitive antagonist) and then administrating [^{11}C]DPN, non-specific binding can be calculated, since all specific sites are occupied by naloxone, any binding sites taken up by [^{11}C]DPN are non-specific. And finally the pulse chase protocol experiment was used to establish the specific binding of [^{11}C]DPN at opioid receptors. Jones *et al*., found that these protocols fit the 3 compartmental model (Figure 25), however none of the scanning protocols could show changes to K_d as this would require sequential scanning with [^{11}C]DPN at differing specific activities.

BPN is structurally, very similar to DPN, only differing in a tertiary butyl group replacing a methyl group at C-20 which gives BPN a chiral centre at this position and makes BPN more lipophilic compared to DPN. This lipophilic group in

the BPN molecule has been shown to cause some rearrangements to the molecular structure. One group proposed an acid catalysed rearrangement, forming a furan ring, in an intramolecular reaction between the 6-methoxy position and substituents at the C-20 position[99] (Figure 26).

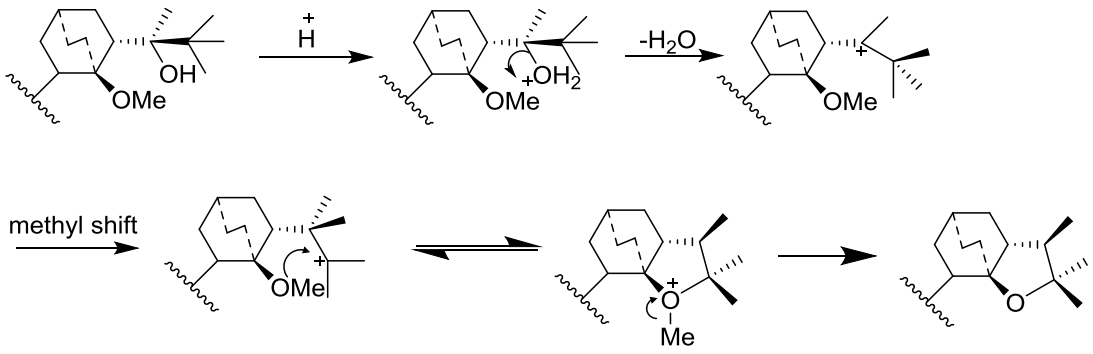

Figure 26: Proposed acid catalysed re-arrangement of BPN.

In other conformational studies of the Bentley compounds, it was found that for BPN, hydrogen bonding occurred between the alcohol group at the C-20 position and the oxygen atom belonging to the methoxy group at the C-6 position[100]. However this H-bonding is only a possibility in the S diastereoisomer where the t-butyl group is in the lowest energy conformer[100].

BPN has been used clinically for the treatment of mild to severe pain since the 1970s and is also used to treat opiate addiction[101]. A complex pharmacodynamics means that BPN can be thought of as a non-selective, mixed agonist-antagonist semi-synthetic opiate. BPN has a partial agonist[3] effect at μ opioid receptors and acts as an antagonist at κ opioid receptors. BPN has a slow onset and a long duration of action at μ opioid receptors where it acts as a partial agonist. Being a partial agonist gives BPN an advantage in the treatment of opioid addiction as it is much more difficult to cause an overdose and side effects such as respiratory depression can be avoided[101].

It was discovered that BPN also had agonist effect at the orphan receptor ORL1[102], a receptor which has a large degree of homology to the μ, δ and κ opioid receptors in terms of structure but is distinct in pharmacology. Nociceptin is the endogenous ligand to the ORL1 receptor; it is a heptadecapeptide and shows both

[3] Ligands which can activate receptors but have only partial efficacy.

hyperalgesic and antinociceptive properties *in vivo*[102]. Bloms-Funke *et al*., compared the action of BPN and nociceptin in a series of experiments. Knowing that opioid receptors are coupled to G-proteins and activation of the G-protein occurs when GTP is bound, the group made a cell membrane using agonist-stimulated [^{35}S]GTPγS incorporated into cells with OLR1. Dose response curves were then established using nociceptin and BPN and both compounds stimulated [^{35}S]GTPγS. From this BPN was characterised as a partial agonist at ORL1 with differing potency and efficacy compared to nociceptin, the results show an EC_{50} value of 0.0013 μmol/l for nociceptin and an EC_{50} value of 0.079 μmol/l for BPN[102].

Another group synthesised a number of BPN analogs in an attempt to improve the analgesic effects of BPN and to reduce potential abuse and unwanted side effects[103]. This group created an analog of BPN in which the t-butyl group on C-20 was replaced with a cyclobutyl moiety, this compound was identified as a selective κ opioid receptor partial agonist, which offers antinociceptive effects with a low potential for illicit abuse[103].

By radiolabelling synthetic opiates it is possible to study their cerebral pharmacodynamics, which offers the potential to design new opiates with better nociceptive effects but with limited side effects. A PET study with radiolabelled opiates also offers ways of understanding the biology of pain, as well as how the endogenous opioid system functions. A number of PET ligands which are non-selective, such as DPN, or are selective for a particular opioid receptor sub-type (e.g. [^{11}C]carfentanil for the μ receptor) are available and can be used to probe the endogenous opioid system under numerous experimental states.

Introduction (Part 3) – Inflammation and Rheumatoid Arthritis

Inflammation as a therapeutic target

Inflammation is a biological response to a harmful stimulus such as tissue trauma, infiltration of pathogens into the body or an accumulation of necrotic cells and can be classified as acute or chronic. Acute inflammation will have a rapid onset and the inflammation may quickly become severe whereas chronic inflammation will have a much slower onset and may lead to long term inflammation that may last for months or even years. In response to acute inflammation we may expect locally increased blood supply, increased vascular permeability and increased influx of leukocytes and other inflammatory mediators to the affected area[104]. Acute inflammation is often associated with the infiltration of neutrophils to the site of inflammation or noxious stimuli, whereas in chronic inflammation the infiltrating cells are predominantly mononuclear cells including lymphocytes, monocytes and macrophages[104].

During painful inflammation endogenous opioids including β-endorphin, met-enkephalin and dynorphinA are found in circulating leukocyte cells as well as in lymph nodes[21]. These cells are recruited to migrate to injured and inflamed peripheral tissue, the transport of the cells is directed by adhesion molecules. The first step of migration is the 'rolling' of leukocyte cells along the walls of blood vessels and this is mediated by selectin[21] (a family of adhesion molecules). Once the leukocytes are 'rolling' they become exposed to tissue derived chemokines, which are small cytokines that induce chemotaxis, a phenomenon by which cells direct their movement according to certain chemicals in the environment. Leukocytes are then pulled out of the circulatory system, by integrins toward the site of damage or inflammation and fix the cells to endothelia[21] (a thin layer of cells which form on the interior of blood vessels). Integrins are a type of receptor that mediate attachment between cells and the tissue surrounding it, typically the receptors inform a cell of the molecules in its environment that evoke a response in the cell. In this case the integrin receptors inform the cell of the inflamed tissue, which fixes the cell to the endothelia. Finally the cell migrates through the vessel wall, directed by another set of adhesion molecules and immunoglobulin ligands.

Autoimmune diseases such as rheumatoid arthritis are characterised by painful inflammation and hence the migration of leukocytes to inflamed tissue. By radiolabelling leukocytes (as well as other types of white blood cell) and imaging their migration through the body, it may be possible to provide a quantitative *in vivo* measurement of inflammation and a diagnostic tool for various inflammatory diseases. Since white blood cells (and in particular neutrophils) are central to any inflammatory response, monitoring their distribution and kinetics is important in understanding their role in inflammation as well as devising rational therapeutic strategies and potentially more effective treatments of rheumatoid arthritis and the pain associated with the disorder. SPECT and PET are non-invasive, sensitive and quantitative medical imaging modalities which are well suited to following, *in vivo*, the selective migration of specific immune cells to a source of inflammation.

Inflammation Imaging

There are a number of strategies which can be used to image inflammation and infection with molecular imaging techniques such as SPECT and PET. These imaging modalities can be used to characterise, diagnose and monitor inflammatory conditions such as inflammatory bowel disease, rheumatoid arthritis and degenerative joint disease. Some of the most well-established clinical approaches include indium-111 (^{111}In) or technetium-99m (^{99m}Tc) labelled leukocyte for SPECT imaging and [^{18}F]FDG PET imaging. However, the field of inflammation imaging is expanding and with more strategies being studied to probe inflammation more radiopharmaceuticals are being explored.

One particular strategy may be to target leukocytes which are migrating to and localising in the site of infection/inflammation. By radiolabelling the migrating leukocyte cells the radioactivity will be delivered to the site of inflammation and can be detected. Of course for this strategy and all other inflammation imaging methods, careful consideration needs to be given to the physical half-life of the radioisotope employed. Radiolabelling of leukocyte cells may occur *ex vivo* or *in vivo*, for the *ex vivo* strategy whole blood must be extracted from the patient and the mixed leukocytes need to be isolated. Next, the leukocytes can be radiolabelled and following this the radiolabelled leukocytes are re-injected. Radiolabelling leukocytes *in vivo* often involves the use of antibody antigen interactions such as radiolabelled

antigranulocyte or receptors on the leukocytes can be targeted for example with radiolabelled chemotactic peptides or cytokines such as interleukin-8[104, 105].

Another route to inflammation imaging would be to target with a radiopharmaceutical, mediators of the inflammatory process which migrate to, or may already be present at, the site of inflammation. Alternatively a radiolabelled form of the mediator can be used directly. An example of this type of strategy is E-selectin which is an adhesion molecule expressed on activated endothelial cells. Anti-E-selectin monoclonal antibodies have been radiolabelled with ^{111}In and used to image rheumatoid arthritis with SPECT[106].

[^{18}F]FDG may also be used to image inflammation, however the drawback of using this strategy is the non-specificity of [^{18}F]FDG. Infiltrating granulocytes have an increased demand for glucose as a source of energy and this can be imaged with [^{18}F]FDG. However [^{18}F]FDG is taken up in any cells which have increased glucose metabolism such as tumour cells as well as in scar tissue/wound repair[107] which makes the tracer non-specific to inflammation and infection imaging.

Examples of inflammation imaging strategies have been described above, and many different radiopharmaceuticals can be used. However it is important to consider their characteristics. The radio tracer should have good accumulation and be well retained in the site of infection or inflammation. Additionally there should be a good target to background ratio, so the time at which images are taken (to allow for background clearance) should be taken into careful consideration. Accumulation of the radiopharmaceutical into non-target organs should be minimal to minimise the radioactive dose to patients and there should be no toxicity associated with the radiopharmaceutical. Ideally, a radiotracer that can detect the early onset of inflammation is desirable. A radiopharmaceutical for inflammation imaging, which meets all of these characteristics, seems ambitious and so compromises may be made depending on the type of inflammation being studied and what is required of the radiopharmaceutical.

The Interleukin receptor family and interleukin-1 receptor antagonist (IL-1RA)

Immune and inflammatory responses can occur in the brain as a reaction to diverse insults such as seizures and Alzheimer's disease[108]. Inflammation in the brain causes an increase in circulating immune cells such as microglial cells. These

immune cells can express, release and respond to pro-inflammatory mediators such as cytokines. Interleukin-1 (IL-1) is a well-studied pro-inflammatory cytokine, and there is evidence that IL-1 plays a key part in neurodegenerative conditions, both acute (such as a stroke) and chronic (such as Alzheimer's disease)[108]. The IL family is thought to comprise at least 10 molecules and IL-1 was originally described over 50 years ago[108]. IL-1 consists of 2 proteins, IL-1α and IL-1β, which are synthesised as precursor proteins (Pro-IL-1α and Pro-IL-1β) by many cell types of both the peripheral and central immune system. The biologically active Pro-IL-1α is cleaved by a protein enzyme called calpain. Pro IL-1β, in contrast, is not biologically active; this precursor can however be cleaved by the caspase-1 enzyme to produces a biologically active 17 kDa protein. How the active form of the protein is secreted from cells is not yet fully understood, though it is suggested that a number of possible pathways could be involved that are dependent on the nature and intensity of the inflammatory stimulus[109].

Once bound to IL-1 receptors (IL-1R), both IL-1α and IL-1β will exert a comparable effect biologically. There are three types of IL-1R, these include, IL-1RI, IL-1RAcP and IL-1RII. As IL-1 binds to IL-1RI, the complex then associates with IL-1RAcP (also known as receptor accessory protein) to form a larger complex which allows intracellular signalling. The type II receptor, (IL-1RII), does not have an intracellular signalling domain, meaning that when IL-1 binds, no signalling occurs and IL-1RII acts as a decoy receptor. All of the three receptor types can also exist in soluble form as sIL-1RI, sIL-1RAcP and sIL-1RII. Both sIL-1RII and sIL-1RAcP, are able to inhibit IL-1 mediated signal transduction. sIL-1RII does this by binding the precursor proIL-1β making it unavailable to be cleaved to the active form. And sIL-1RAcP is inhibitory to IL-1 by binding to IL-1RI and therefore making the receptor unavailable.

The IL-1 group of cytokines is rather unique as the cells which express IL-1 also express the competitive IL-1 antagonist (IL-1RA). Secretion of the genes which encode for IL-1β and IL-1α can be induced by pro-inflammatory stimuli such as other cytokines, cellular injury and cellular hypoxia[108]. IL-1β and IL-1α are up-regulated rapidly at the mRNA level and within hours at the protein level in response to toxic stimuli, whereas expression of IL-1RA is delayed[108]. The administration of exogenous IL-1 into healthy neuronal cells in the brains of animals has been shown

not to cause injury, however if IL-1 is administered with other cytokines a synergic effect has been seen leading to neurotoxicity[108]. This shows that IL-1 may be unable to act independently, but may require other cytokines to exhibit its pro-inflammatory nature.

Preclinical experiments have been carried out with IL-1RA which have shown that protection against neuronal injury stimulated by the administration of toxic doses of excitotoxins (excitatory amino-acid receptor agonists such as glutamate) is evident by the administration of exogenous IL-1RA as well as by stimulating an over-expression of endogenous IL-1RA[108]. IL-1RA is neuroprotective as it disrupts the formation of the IL-1→IL-1RI→IL-1RAcP complex by binding to and blocking IL-1RI receptors. In addition to directly using IL-1RA to block IL-1RI receptors other strategies may be used, for example administrating antibodies which neutralise IL-1β or inhibit the cleavage and release of IL-1β by deleting the gene which encodes for caspase-1. Also, deletion of genes which encodes for both IL-1α and IL-1β has been shown to reduce brain damage in mice[108]. However, deletion of either gene alone has proven ineffective as a neuroprotective action suggesting a compensation effect may occur between IL-1α and IL-1β. In contrast, deletion of the gene encoding for IL-1RA increases brain damage in mice adding further evidence to the neuroprotective action of IL-1RA[108]. However, is interleukin receptor blockade the correct target for neuroprotective effects? IL-1 only needs to occupy a small number of receptors before a biological response in target cells is observed, so most cells have an abundance of unoccupied receptors[108]. In order to successfully block and saturate all IL-1RI receptors, there is a requirement to have a large concentration of the antagonist IL-1RA. Another strategy may be to target production and release of biologically active IL-1 receptor ligands directly or perhaps target downstream signalling events.

IL-1RA has been demonstrated to be neuroprotective in preclinical studies of experimentally induced ischaemic brain damage and has a potential as a therapeutic strategy in stroke[110]. IL-1RA may also shows promise for therapeutic treatment of inflammatory pain, however the pharmacokinetics are still not completely understood. By radiolabelling IL-1RA with [^{18}F] and using PET, the pharmacokinetics of [^{18}F]IL-1RA could be better understood. IL-1RA was radiolabelled randomly at a free amine sites (such as lysine residues) or at the amino

terminal site, and the binding of [^{18}F]IL-1RA to IL-1 receptors was studied using PET[55, 111]. The radiolabelling of IL-1RA with [^{18}F] is discussed in the proceeding chapters of this thesis.

Cannabinoids (CBs) are another type of molecule which show neuroprotective and anti-inflammatory actions on glial cells and neurons by inhibiting the release of pro-inflammatory molecules including cytokines and IL-1 amongst others[112]. CBs act at G-protein coupled receptors of which two types are identified, the CB_1 receptor which is mainly found in the brain and the CB_2 receptor which is mostly expressed in the immune system. The neuroprotective properties are thought to be mediated through a variety of mechanisms including the inhibition of calcium influx into cells and the inhibition of glutamate release to reduce neuronal cell death. CBs are known to inhibit the release of pro-inflammatory molecules including IL-1 and cytokines, Molina-Holgado *et al.*, also suggest that CBs induce the release of IL-1RA and negatively regulate the action of IL-1β in the brain via IL-1RA blocking IL-1 receptors. These results demonstrate the complex and in some parts still unknown downstream signalling mechanisms provoked by the IL-1 cytokines.

However, a peptide which is smaller than IL-1RA (17 kDa) may also be able to accumulate in joints and might also be a good tracer for inflammation in rheumatoid arthritis, could be investigated. One potential target is anti-TNF (tumor necrosis factor) antibodies. Like interleukin, TNF is another family of pro-inflammatory cytokines inhibited by anti-TNF. There is potential to use anti-TNF therapies in treatment of rheumatoid arthritis, however further investigation into its pharmacokinetics needs to be considered such as blood brain barrier permeability since the size of anti-TNF antibodies range from 150–165 kDa. Radiolabelling anti-TNF would be required to carry out these pharmacokinetics experiments.

Radiolabelling white blood cells for cell trafficking and diagnosis

Radiolabelling with SPECT isotopes ^{111}In and ^{99m}Tc

White blood cells are actively recruited to sites of inflammation and their migration to the inflammatory/infectious foci may be tracked using radioactive probes. Radiolabeled leukocyte scintigraphy with SPECT using ^{99m}Tc ($t_{½}$ = 6 hours) and ^{111}In ($t_{½}$ = 67 hours) chelates is the most widely used clinical procedures for the

assessment of inflammatory diseases[113]. The physical properties of the radio-isotope used for SPECT imaging is of high importance, the energy of the gamma rays should be compatible with the gamma camera. And as usual the radioactive half-life must be compatible with the physiological process under investigation. The longer radioactive half-life offered by ^{111}In allows for longer scanning sessions and a greater delay between injection of radiolabelled white blood cells and image acquisition. ^{111}In does however have some disadvantages including low resolution images and high tissue radiation doses received to the patient. The shorter half-life of ^{99m}Tc means that image acquisition occurs typically a couple of hours post administration and a further advantage of using ^{99m}Tc is that the photon energy is well suited for gamma-camera allowing for high resolution images[113].

Any radiometal, in its ionic form, will not be able to permeate the cell membrane of white blood cells; a chelator is required to transport the radio-metal into the cell. It is important that the radio-metal has high stability in the complex and there is a minimum loss of free radiometal. The first chelate described for this purpose was 8-hydroxyquinoline (oxine)[114, 115]. Bidentate oxine binds to ^{111}In via nitrogen and oxygen atoms to form a 3:1 ligand to metal complex. This lipophilic and pH neutral ^{111}In complex is able to enter the cell via passive diffusion, once inside the cell the complex is reported to break down and ^{111}In binds to intracellular components, forming a stable radiolabel[114]. However, a significant drawback to using [^{111}In]oxine, the radiolabelling efficiency is low in the presence of plasma as ^{111}In will exchange from oxine to transferrin. This prompted further research into a new chelator for ^{111}In white blood cell labelling and tropolone was introduced as an alternative to oxine. Like oxine, tropolone forms a 3:1 ligand to metal complex which is water soluble. Importantly, blood cells can be radiolabelled with [^{111}In]tropolone in the presence of plasma, meaning that damage to cells is reduced as the step to remove or wash plasma from the cells is omitted and the time taken to perform radiolabelling is reduced[116]. The water solubility of the [^{111}In]tropolone complex also means that no ethanol (a possible source of cytotoxicity) is required to solubilise the complex as is the requirement with [^{111}In]oxine. On further investigation [^{111}In]tropolone was suspected to have a detrimental effect on chemotaxis of radiolabelled neutrophils in contrast to [^{111}In]oxine which showed

little change to chemotaxis of neutrophil cells radiolabelled with this complex[117]. Figure 27 depicts some of the ^{111}In complexes discussed here.

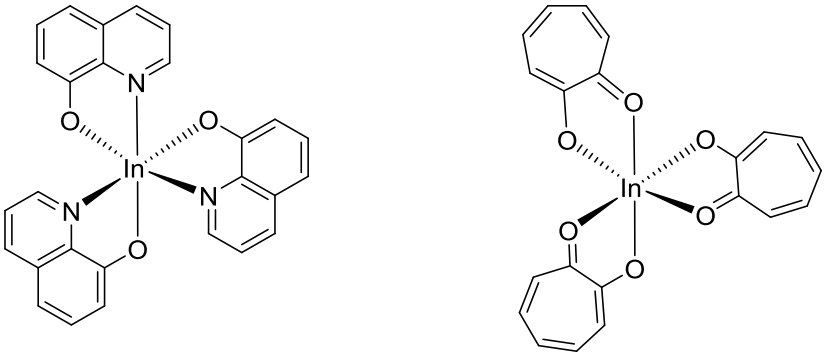

Figure 27: [^{111}In]oxine (left) and [^{111}In]tropolone (right).

Radiolabelling of leukocytes with ^{99m}Tc has the benefit that the gamma-ray energy of 140 keV is equivalent to the wavelength emitted by conventional X-ray diagnostic equipment making the gamma-ray easily detectable for SPECT imaging. ^{99m}Tc requires a chelator to deliver the radiometal into the cell in the same way as ^{111}In does and the chelator of choice for ^{99m}Tc is hexamethylpropyleneamine oxime (HMPAO). In this complex, the [^{99m}Tc]TcO^{3+} core, with technetium in the +5 oxidation state, is co-ordinated by 4 nitrogen atoms of the HMPAO ligand giving the complex an overall neutral charge (Figure 28). The lipophilic [^{99m}Tc]HMPAO complex passes into white blood cells, through the cell membrane by passive diffusion. Once inside the cell, [^{99m}Tc]HMPAO is trapped and a number of possible mechanisms for this have been postulated. One mechanism suggests that once inside the cell, [^{99m}Tc]HMPAO is broken down into a more hydrophilic complex, becoming trapped as it is not possible for this complex to pass through the cell membrane[118]. Another possible mechanism is that [^{99m}Tc]HMPAO binds to non-diffusible proteins inside the cell again trapping the radiometal inside the cell[118].

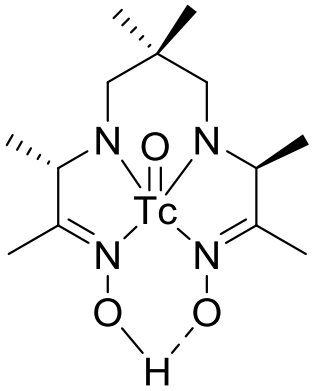

Figure 28: [^{99m}Tc]HMPAO complex.

However, ^{99m}Tc radiolabelled leukocytes are less stable than ^{111}In radiolabelled leukocytes, and every hour 5-7% of the radiolabel elutes from the white blood cells into the kidneys and bladder[119]. This means that imaging must be performed within 3 hours of administration.

For white blood cell radiolabelling to be successfully used as a tool for inflammation and infection imaging and diagnosis, the radiolabelled white blood cells must maintain their viability and function. There are a number of ways to assess that cell function has not been altered following radiolabelling. The Trypan blue assay can selectively dye non-viable cells blue while cells with an intact cell membrane will remain uncoloured. A similar test can be carried out with 3-(4,5-dimethylthiazol-2-yl)-2,5-diphenyltetrazolium bromide (MTT), this is a colourimetric assay in which yellow MTT is reduced to purple formazan in living cells. In addition flow cytometry can be used to assess cell phenotypes and changes to the integrity of cell membranes. Flow cytometry operates by passing cells through a laser beam and measuring the scattered light and/or fluorescence that is emitted from the cell. Certain cell phenotypes can be made to fluoresce if they are exposed to fluorescently labelled antibodies specific for that cell phenotype, flow cytometry can then be used to sort the different cell phenotypes. In a similar way live and dead cells can be stained with fluorescent dyes and sorted by flow cytometry.

Cell viability may also be tested *in vivo* by investigating the bio-distribution of radiolabelled autologous cells. Following administration, viable cells should pass rapidly through the lungs followed by uptake in the liver and spleen; on the other hand damaged cells may be retained in the lungs. Although some caution must be

used when accessing cells in this way as some pathologies may involve the recruitment of white blood cells to the lungs and liver. Another method of investigating that the function of the cells has not been altered by radiolabelling is to carry out chemotaxis studies. In radiolabelled granulocytes it was shown that there is a significant decrease in chemotaxis in [^{111}In]oxine labelled cells which was much smaller with [^{99m}Tc]HMPAO radiolabelled cells[120].

Radiolabelling cells with PET isotopes

White blood cell trafficking with PET isotopes such as ^{18}F, ^{64}Cu, ^{89}Zr and ^{68}Ge to monitor and diagnose inflammatory disorders is receiving great interest recently. PET is an ideal imaging modality to follow the migration of white blood cells to sources of inflammation *in vivo*. PET has advantages over SPECT for this purpose, as the sensitivity offered by PET (10^{-11}-10^{-12} M) is at least 1 – 2 orders of magnitude higher than SPECT (10^{-10} M)[73]. The signal from white blood cells radiolabelled with PET isotopes can be quantified (after scatter, partial volume and motion correction techniques[121]), something which is not as easily achieved with SPECT. The *in-vivo* tracking of radiolabelled white blood cells using PET means that it is possible to track the selective recruitment of white blood cells during pathogenesis, detect possible and probable infectious/inflammatory foci and devise and follow rational therapeutic strategies for patients with inflammatory disorders by carrying out longitudinal studies.

Various approaches have been investigated to track radiolabelled white blood cells *in vivo* with PET and using ^{64}Cu. Pyruvaldehyde-bis(N^4-methylthiosemi-carbazone) (PTSM) was used to chelate ^{64}Cu and this complex (Figure 29) was used to radiolabel rat glioma (C6) cells for cell trafficking[73].

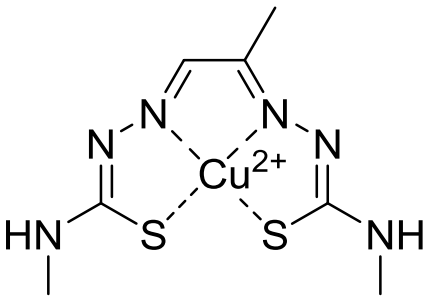

Figure 29: [^{64}Cu]PTSM complex

Cu^{2+} forms a stable complex with PTSM ($K_a = 10^{18}$)[73] and the lipophilic [^{64}Cu]PTSM complex passes through the cell membrane. Inside the cell the redox-active [^{64}Cu]PTSM complex is broken down as the $^{64}Cu^{2+}$ is reduced to $^{64}Cu^{+}$ by intracellular components and is released from the complex. $^{64}Cu^{+}$ becomes trapped inside of the cell due to its ionic charge and the PTSM molecule can diffuse back out of the cell[73]. Adonai *et al.,* demonstrated that [^{64}Cu]PTSM cell uptake occurred rapidly up to 3 hours of incubation with C6 cells. The cell uptake of [^{64}Cu]PTSM becomes constant between 3 and 5 hours of incubation, however efflux studies showed that C6 cells which had been radiolabelled for 5 hours retained more ^{64}Cu than those which had been incubated for 3 hours[73]. The reason for this was that the reduction of [^{64}Cu]PTSM to liberate $^{64}Cu^{+}$ continued between 3 and 5 hours of incubation trapping more of the radiometal. However [^{64}Cu]PTSM does show a high rate of efflux of ^{64}Cu from the cell (approximately 50% of the radiolabel lost after 5 hours)[73]. Possible explanations for the loss could be active cellular elimination or saturation of uptake.

Another group looked at the possibility of using a polymer (polyethyleneimine, (PEI)) and labelling it with ^{64}Cu to form [^{64}Cu]polyethylenimine ([^{64}Cu]PEI) as well as [^{64}Cu]PEI-polyethylene glycol ([^{64}Cu]PEI-PEG) to monitor the migration of cells[75]. It was postulated that the amine moieties of PEI could chelate the ^{64}Cu metal ion. It was found that PEI could chelate ^{64}Cu well with radiolabelling yields in excess of 90%[75]. The uptake of these ^{64}Cu radiotracers was assessed in a U87-MG cell line and the efflux of ^{64}Cu from the cells was investigated too. The cell uptake of [^{64}Cu]PEI in U87-MG cells reached a maximum of 20% which was lower to the cell uptake attained for [^{64}Cu]PTSM which reached a maximum of 70-80% in the same cell line[75]. In addition [^{64}Cu]PEI showed a greater efflux of activity form cells (61% at 27 hours) in comparison to [^{64}Cu]PTSM (36% at 27 hours)[75]. However, [^{64}Cu]PEI-PEG showed an improved cell uptake (maximum of 50%) compared to [^{64}Cu]PEI as well as a reduction of the leakage of the radiolabel from the U87-MG cells[75]. A mechanism of cellular uptake was proposes for [^{64}Cu]PEI which involved an initial protonation of a proportion of the amines of PEI at physiological pH to form a cationic species. The protonated [^{64}Cu]PEI complex would be electrostatically attracted to negative cell surface components (possibly heparin sulfate proteoglycans). As some of the amines of

[^{64}Cu]PEI remain un-protonated a buffering effect is created in the endosome of the cell and a proton sponge effect due to charge repulsion and osmotic pressure in the endosome allows [^{64}Cu]PEI to enter the cell[122]. Once inside of the cell a similar copper bio-reductive mechanism that traps ^{64}Cu from the PTSM complex is used. Despite the differences in cell uptake and efflux between [^{64}Cu]PEI and [^{64}Cu]PTSM it was concluded that [^{64}Cu]PEI and [^{64}Cu]PTSM radiolabelled cells showed comparable cell trafficking capability in preclinical PET in mice with the radiolabelled cells behaving in a similar way[75]. [^{64}Cu]PEI-PEG was investigated to overcome the problems of cytotoxicity of [^{64}Cu]PEI. PEGylation reduced the cytotoxicity of the radiolabel and an improved cellular uptake of [^{64}Cu]PEI-PEG was observed[75].

Another approach to blood cell radiolabelling with a PET probe was undertaken with chitosan-coated magnetic nanoparticles[74]. Super-paramagnetic iron oxide nanoparticles (SPIONs) can be detected by magnetic resonance imaging and have a reactive surface which can be coated with biomolecules. SPIONs can be coated with chitosan (Figure 30), a biocompatible and non-antigenic co-polymer of glucosamine and *N*-acetylglucosamine with metal ion chelating properties[123] that is able to complex to PET radio-metals such as ^{64}Cu or ^{89}Zr.

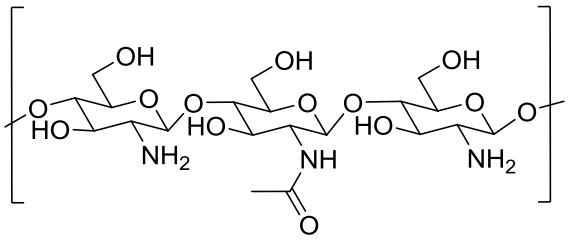

Figure 30: chitosan, a co-polymer of glucosamine and *N*-acetylglucosamine.

This means that chitosan coated magnetic nanoparticles can be labelled with ^{64}Cu yielding a dual PET/MRI imaging probe[74]. Pala *et al*. reported that 75 MBq/mg ^{64}Cu labelled chitosan coated magnetic nanoparticle was achieved. When these radiolabelled nanoparticles were incubated with granulocyte cells 75% of the ^{64}Cu was taken up into the cells by phagocytosis. After 4 hours, 20% of the ^{64}Cu was lost from the granulocyte cells indicating a good retention of the engulfed probe[74].

^{89}Zr has ideal physical properties to be used for cell trafficking over long periods of time owing to its long half-life (78.41 hours). In comparison to ^{64}Cu, ^{89}Zr has a higher positron emission branching ratio of 22.3% compared to 17.5% for ^{64}Cu. Furthermore the relatively low energy of the emitted positron (E_{ave} β^+ = 396 keV) results in high resolution ^{89}Zr images comparable to those observed with ^{64}Cu. Dextran nanoparticles have been labelled with ^{89}Zr and used for *in-vivo* macrophage imaging[124]. Short dextran chains were cross-linked with epichlorohydrin to form nanoparticles (13 nm) and these were modified with DFO in order to chelate ^{89}Zr. With this approach it was demonstrated that ^{89}Zr labelled dextran nanoparticles showed a good uptake in macrophages[124]. However the main drawback to this approach is the complexity of the nanoparticle, coupling to DFO and end-capping of amine groups which requires the use of toxic organic reagents.

A more simplified approach to *in vivo* cell trafficking with ^{89}Zr has been undertaken using the well-established ^{111}In chelating agent oxine[125]. [^{111}In]oxine has been used for many years to monitor the migration of circulating white blood cells with SPECT and the agents toxicity is well established. $^{89}Zr^{+4}$ forms a 1:4 complex with oxine ligands to form [^{89}Zr]oxinate$_4$ complex and the radiolabelling yield of [^{89}Zr]oxinate$_4$ from [^{89}Zr]oxalate was reported to be 60%[125]. However the radiolabelling process involves using chloroform which is not ideal if the technique is to be used in a clinical setting. The uptake of [^{89}Zr]oxinate$_4$ in human white blood cells occurs rapidly and is complete after 30 minutes of incubating the [^{89}Zr]oxine complex with 9 x 10^7 leukocyte cells. The leukocyte cell labelling efficiency was shown to be 54% compared to 47% with [^{111}In]oxine[125]. 85% of the ^{89}Zr was retained by leukocyte cells 24 hours post radiolabelling which was higher than that reported for [^{111}In]oxine[125]. Nevertheless the effect that radiolabelling leukocytes with [^{89}Zr]oxinate$_4$ had on their function and viability was not investigated.

The intermediate and long radioactive half-life of ^{64}Cu and ^{89}Zr respectively are ideally suited to cell trafficking studies. Efforts to radiolabel cells with the shorter half-life PET isotopes [^{18}F] ($t_{½}$ = 109 minutes) and [^{11}C] ($t_{½}$ = 20 minutes) have also been made. [^{18}F]fluorodeoxyglucose ([^{18}F]FDG) is a marker for glucose uptake in tissues and cells. [^{18}F]FDG has been used to radiolabel leukocyte cells however there are a number of limitations associated with this approach. First [^{18}F]FDG is not specific and will be taken up in a number of different cells and

tissues other than white blood which are metabolically active. This means that the radiolabelling efficiency of [^{18}F]FDG leukocytes is variable and reports have claimed a high efflux of ^{18}F from cells[126]. When compared to ^{64}Cu and ^{111}In radiolabelled white blood cells, [^{18}F]FDG was shown to have lower labelling efficiency as well as a higher efflux of radioactivity from the cells[127].

The 20 minute radioactive half-life of ^{11}C does not seem an encouraging property for cell trafficking, however ^{11}C is used to radiolabel macrophages and to image synovitis in rheumatoid arthritis[128]. [^{11}C]PK11195 binds to translocator proteins (TSPO) which can be found on activated macrophages and monocytes, intravenous administration of [^{11}C]PK11195 allows a non-invasive method of imaging clinical synovitis in rheumatoid arthritis. The short half-life of ^{11}C means that there is lower patient dose however it does restrict the production to clinics and hospitals which have an on-site cyclotron available. [^{18}F]DPA-714 is another radiotracer which binds to TSPO, and which has been tested in a preclinical model of rheumatoid arthritis[129]. The longer half-life of ^{18}F compared to ^{11}C is an obvious benefit of using this radiotracer which with more investigation could find its place as a useful PET tracer to image rheumatoid synovitis in the clinic.

The benefits of PET over SPECT such as improved sensitivity, improved resolution and quantification of signal warrants further investigation of PET probes to monitor the migration of white blood cells *in vivo*. Being able to image the infiltration of white blood cells into inflammatory and infected joints with PET could be an invaluable tool for both early diagnoses of arthritic disorders as well as to monitor treatments for these disorders. The characteristics which must be met for a good *in vivo* white blood cell trafficking technique with PET include i) a simple and efficient cell radiolabelling technique, with a radiometal of suitable physical properties for cell tracking (half-life and positron branching) ii) the radiolabelled cells must behave in the same way as the native unlabelled cells and iii) the radiolabelling process should not damage the cells iv) the radiolabel should remain in the cell and not be leaked to prevent localisation in other organs and prevent high patient doses. A technique which matches these criteria could prove to be of high importance and increase the understanding of the biology of inflammatory responses and arthritis.

References

[1] A. P. C. Rocha, D. C. Kraychete, L. Lemonica, L. R. d. Carvalho, G. A. M. d. Barros, J. B. d. S. Garcia, R. K. Sakata, *Revista Brasileira de Anestesiologia* **2007**, *57*, 94.

[2] D. Symmons, G. Turner, R. Webb, P. Asten, E. Barrett, M. Lunt, D. Scott, A. Silman, *Rheumatology* **2002**, *41*, 793.

[3] G. S. Firestein, *Nature* **2003**, *423*, 356.

[4] A. Gaffo, K. G. Saag, J. R. Curtis, *American Journal of Health-System Pharmacy* **2006**, *63*, 2451.

[5] A. K. P. Jones, W. D. Brown, K. J. Friston, L. Y. Qi, R. S. J. Frackowiak, *Proceedings of the Royal Society of London. Series B: Biological Sciences* **1991**, *244*, 39.

[6] M. Boly, M. E. Faymonville, C. Schnakers, P. Peigneux, B. Lambermont, C. Phillips, P. Lancellotti, A. Luxen, M. Lamy, G. Moonen, P. Maquet, S. Laureys, *Lancet Neurol* **2008**, *7*, 1013.

[7] R. C. Coghill, C. N. Sang, J. M. Maisog, M. J. Iadarola, *Pain Intensity Processing Within the Human Brain: A Bilateral, Distributed Mechanism, Vol. 82*, **1999**.

[8] M. Ingvar, *Philosophical Transactions of the Royal Society of London. Series B: Biological Sciences* **1999**, *354*, 1347.

[9] A. K. P. Jones, H. Watabe, V. J. Cunningham, T. Jones, *European Journal of Pain* **2004**, *8*, 479.

[10] H.-Y. Wey, C. Catana, J. M. Hooker, D. D. Dougherty, G. M. Knudsen, D. J. J. Wang, D. B. Chonde, B. R. Rosen, R. L. Gollub, J. Kong, *NeuroImage* **2014**, *102, Part 2*, 275.

[11] G. D. Iannetti, A. Mouraux, *Experimental Brain Research* **2010**, *205*, 1.

[12] D. E. Bentley, A. Watson, R. D. Treede, G. Barrett, P. D. Youell, B. Kulkarni, A. K. Jones, *Clin Neurophysiology* **2004**, *115*, 1846.

[13] C. E. Inturrisi, *The Clinical Journal of Pain* **2002**, *18*, S3.

[14] B. P. Roques, M. C. Fournie-Zaluski, M. Wurm, *Nature Reviews Drug Discovery* **2012**, *11*, 292.

[15] J.-C. Meunier, *European Journal of Pharmacology* **1997**, *340*, 1.

[16] G. Scherrer, N. Imamachi, Y.-Q. Cao, C. Contet, F. Mennicken, D. O'Donnell, B. L. Kieffer, A. I. Basbaum, *Cell* **2009**, *137*, 1148.

[17] G. D. Chiara, A. R. North, *Trends in Pharmacological Sciences* **1992**, *13*, 185.

[18] A. D. Blake, G. Bot, T. Reisine, *Chemistry & Biology* **1996**, *3*, 967.

[19] B. Kane, B. Svensson, D. Ferguson, *The AAPS Journal* **2006**, *8*, E126.

[20] K. Raynor, H. Kong, J. Hines, G. Kong, J. Benovic, K. Yasuda, G. I. Bell, T. Reisine, *Journal of Pharmacology and Experimental Therapeutics* **1994**, *270*, 1381.

[21] C. Stein, M. Schafer, H. Machelska, *Nature Medicine* **2003**, *9*, 1003.

[22] W. W. Wang, M. Shahrestanifar, J. Jin, R. D. Howells, *Proceedings of the National Academy of Sciences* **1995**, *92*, 12436.

[23] K. Befort, L. Tabbara, D. Kling, B. Maigret, B. L. Kieffer, *Journal of Biological Chemistry* **1996**, *271*, 10161.

[24] L. Y. Liu-Chen, S. X. Li, R. J. Tallarida, *Molecular Pharmacology* **1990**, *37*, 243.

[25] C. Chen, J. Yin, J. K. de Riel, R. L. DesJarlais, L. F. Raveglia, J. Zhu, L.-Y. Liu-Chen, *Journal of Biological Chemistry* **1996**, *271*, 21422.

[26] A. Manglik, A. C. Kruse, T. S. Kobilka, F. S. Thian, J. M. Mathiesen, R. K. Sunahara, L. Pardo, W. I. Weis, B. K. Kobilka, S. Granier, *Nature* **2012**, *485*, 321.
[27] A. Borsodi, G. Caló, C. Chavkin, M. Christie, O. Civelli, B. Cox, L. Devi, C. Evans, G. Henderson, V. Höllt, B. Kieffer, I. Kitchen, M.-J. Kreek, L.-Y. Liu-Chen, J.-C. Meunier, P. Portoghese, T. Shippenberg, E. Simon, L. Toll, J. Traynor, H. Ueda, Y. Wong, IUPHAR/BPS Guide to Pharmacology.
[28] R. C. Walker, G. L. Purnell, L. B. Jones-Jackson, K. L. Thomas, J. A. Brito, E. J. Ferris, *Neurotoxicology* **2004**, *25*, 533.
[29] T. G. Turkington, *Journal of Nuclear Medicine Technology* **2001**, *29*, 4.
[30] A. A. van der Veldt, E. F. Smit, A. A. Lammertsma, *Frontiers in Oncology* **2013**, *3*, 208.
[31] P. A. Schubiger, in *Molecular Imaging with PET — Open Questions?, Vol. 64* (Eds.: P. A. Schubiger, L. Lehmann, M. Friebe), Springer Berlin Heidelberg, **2007**, pp. 1.
[32] M. Rudin, R. Weissleder, *Nature Review Drug Discovery* **2003**, *2*, 123.
[33] G. Fischer, U. Seibold, R. Schirrmacher, B. Wängler, C. Wängler, *Molecules* **2013**, *18*, 6469.
[34] P. J. Blower, J. S. Lewis, J. Zweit, *Nuclear Medicine and Biology* **1996**, *23*, 957.
[35] M. M. Ter-Pogossian, P. Herscovitch, *Seminars in Nuclear Medicine* **1985**, *15*, 377.
[36] E. L. Cole, M. N. Stewart, R. Littich, R. Hoareau, P. J. H. Scott, *Current topics in Medicinal Chemistry* **2014**, *14*, 875.
[37] I. A. E. Agency, *Cyclotron Produced Radionuclides: Physical Characteristics and ProductionMethods*, **2009**.
[38] M. L. Firouzbakht, D. J. Schlyer, A. P. Wolf, *Nuclear Medicine and Biology* **1998**, *25*, 161.
[39] C. Crouzel, B. Långström, V. W. Pike, H. H. Coenen, *International Journal of Radiation Applications and Instrumentation. Part A. Applied Radiation and Isotopes* **1987**, *38*, 601.
[40] F. Wuest, M. Berndt, T. Kniess, in *PET Chemistry, Vol. 64* (Eds.: P. A. Schubiger, L. Lehmann, M. Friebe), Springer Berlin Heidelberg, **2007**, pp. 183.
[41] V. Gómez-Vallejo, J. Llop, *Applied Radiation and Isotopes* **2009**, *67*, 111.
[42] P. Larsen, J. Ulin, K. Dahlstrøm, M. Jensen, *Applied Radiation and Isotopes* **1997**, *48*, 153.
[43] D. M. Jewett, *International Journal of Radiation Applications and Instrumentation. Part A. Applied Radiation and Isotopes* **1992**, *43*, 1383.
[44] J. Sandell, O. Langer, P. Larsen, F. Dolle, F. Vaufrey, S. Demphel, C. Crouzel, C. Halldin, *Journal of Labelled Compounds and Radiopharmaceuticals* **2000**, *43*, 331.
[45] A. A. Wilson, A. Garcia, L. Jin, S. Houle, *Nuclear Medicine and Biology* **2000**, *27*, 529.
[46] C. Pascali, A. Bogni, R. Iwata, D. Decise, F. Crippa, E. Bombardieri, *Journal of Labelled Compounds and Radiopharmaceuticals* **1999**, *42*, 715.
[47] H. Audrain, *Angewandte Chemie International Edition* **2007**, *46*, 1772.
[48] S. Y. Lu, P. Watts, F. T. Chin, J. Hong, J. L. Musachio, E. Briard, V. W. Pike, *Lab Chip* **2004**, *4*, 523.

[49] J. M. Gillies, C. Prenant, G. N. Chimon, G. J. Smethurst, B. A. Dekker, J. Zweit, *Applied Radiation and Isotopes* **2006**, *64*, 333.
[50] D. O'Hagan, *Chemical Society Reviews* **2008**, *37*, 308.
[51] R. J. Nickles, M. E. Daube, T. J. Ruth, *The International Journal of Applied Radiation and Isotopes* **1984**, *35*, 117.
[52] F. Wuest, in *PET Chemistry: The Driving Force in Molecular Imaging*, **2007**, pp. 51.
[53] G. Vaidyanathan, M. R. Zalutsky, *Nature Protocols* **2006**, *1*, 1655.
[54] C. Prenant, J. Gillies, J. Bailey, G. Chimon, N. Smith, G. C. Jayson, J. Zweit, *Journal of Labelled Compounds and Radiopharmaceuticals* **2008**, *51*, 262.
[55] C. Prenant, C. Cawthorne, M. Fairclough, N. Rothwell, H. Boutin, *Applied Radiation and Isotopes* **2010**, *68*, 1721.
[56] B. Schoultz, B. Reed, J. Marton, F. Willoch, G. Henriksen, *Molecules* **2013**, *18*, 7271.
[57] H. H. Coenen, in *PET Chemistry: The Driving Force in Molecular Imaging, Vol. 64* (Eds.: P. A. Schubiger, L. Lehmann, M. Friebe), Springer Berlin Heidelberg, **2007**, pp. 15.
[58] T. Poethko, M. Schottelius, G. Thumshirn, U. Hersel, M. Herz, G. Henriksen, H. Kessler, M. Schwaiger, H.-J. Wester, *Journal of Nuclear Medicine* **2004**, *45*, 892.
[59] G. A. Lemieux, C. R. Bertozzi, *Trends in Biotechnology* **1998**, *16*, 506.
[60] W. Cai, X. Zhang, Y. Wu, X. Chen, *Journal of Nuclear Medicine* **2006**, *47*, 1172.
[61] M. Namavari, O. Padilla De Jesus, Z. Cheng, A. De, E. Kovacs, J. Levi, R. Zhang, J. Hoerner, H. Grade, F. Syud, S. Gambhir, *Molecular Imaging and Biology* **2008**, *10*, 177.
[62] Z. Cheng, O. P. De Jesus, M. Namavari, A. De, J. Levi, J. M. Webster, R. Zhang, B. Lee, F. A. Syud, S. S. Gambhir, *Journal of Nuclear Medicine* **2008**, *49*, 804.
[63] J. Zweit, A. M. Smith, S. Downey, H. L. Sharma, *International Journal of Radiation Applications and Instrumentation. Part A. Applied Radiation and Isotopes* **1991**, *42*, 193.
[64] T. Toyota, T. Hanafusa, T. Oda, I. Koumura, T. Sasaki, E. Matsuura, H. Kumon, T. Yano, T. Ono, *Journal of Radioanalytical and Nuclear Chemistry* **2013**, *298*, 295.
[65] M. S. Cooper, M. T. Ma, K. Sunassee, K. P. Shaw, J. D. Williams, R. L. Paul, P. S. Donnelly, P. J. Blower, *Bioconjugate Chemistry* **2012**, *23*, 1029.
[66] T. J. Wadas, E. H. Wong, G. R. Weisman, C. J. Anderson, *Chemical Reviews* **2010**, *110*, 2858.
[67] R. A. De Silva, S. Jain, K. A. Lears, H.-S. Chong, C. S. Kang, X. Sun, B. E. Rogers, *Nuclear Medicine and Biology* **2012**.
[68] S. Liu, D. Li, C. W. Huang, L. P. Yap, R. Park, H. Shan, Z. Li, P. S. Conti, *Theranostics* **2012**, *2*, 589.
[69] H. Cai, Z. Li, C.-W. Huang, A. H. Shahinian, H. Wang, R. Park, P. S. Conti, *Bioconjugate Chemistry* **2010**, *21*, 1417.
[70] B. M. Zeglis, K. K. Sevak, T. Reiner, P. Mohindra, S. D. Carlin, P. Zanzonico, R. Weissleder, J. S. Lewis, *Journal of Nuclear Medicine* **2013**, *54*, 1389.
[71] R. Hueting, *Journal of Labelled Compounds and Radiopharmaceuticals* **2014**, *57*, 231.

[72] R. Bahde, S. Kapoor, K. K. Bhargava, M. L. Schilsky, C. J. Palestro, S. Gupta, *Journal of Nuclear Medicine* **2012**, *53*, 961.
[73] N. Adonai, K. N. Nguyen, J. Walsh, M. Iyer, T. Toyokuni, M. E. Phelps, T. McCarthy, D. W. McCarthy, S. S. Gambhir, *Proceedings of the National Academy of Sciences of the United States of America* **2002**, *99*, 3030.
[74] A. Pala, M. Liberatore, P. D'Elia, F. Nepi, V. Megna, M. Mastantuono, A. Al-Nahhas, D. Rubello, M. Barteri, *Molecular Imaging and Biology* **2011**, 1.
[75] Z.-B. Li, K. Chen, Z. Wu, H. Wang, G. Niu, X. Chen, *Molecular Imaging and Biology* **2009**, *11*, 415.
[76] M. J. W. D. Vosjan, L. R. Perk, G. W. M. Visser, M. Budde, P. Jurek, G. E. Kiefer, G. A. M. S. van Dongen, *Nature Protocols* **2010**, *5*, 739.
[77] J. P. Holland, V. Divilov, N. H. Bander, P. M. Smith-Jones, S. M. Larson, J. S. Lewis, *Journal of Nuclear Medicine* **2010**, *51*, 1293.
[78] Y. Zhang, H. Hong, W. Cai, *Current Radiopharmaceuticals* **2011**, *4*, 131.
[79] J. P. Holland, Y. Sheh, J. S. Lewis, *Nuclear Medicine and Biology* **2009**, *36*, 729.
[80] F. C. J. van de Watering, M. Rijpkema, L. Perk, U. Brinkmann, W. J. G. Oyen, O. C. Boerman, *BioMed Research International* **2014**, *2014*, 13.
[81] L. Perk, M. Vosjan, G. Visser, M. Budde, P. Jurek, G. Kiefer, G. van Dongen, *European Journal of Nuclear Medicine and Molecular Imaging* **2010**, *37*, 250.
[82] J. N. Tinianow, H. S. Gill, A. Ogasawara, J. E. Flores, A. N. Vanderbilt, E. Luis, R. Vandlen, M. Darwish, J. R. Junutula, S.-P. Williams, J. Marik, *Nuclear Medicine and Biology* **2010**, *37*, 289.
[83] B. M. Zeglis, P. Mohindra, G. I. Weissmann, V. Divilov, S. A. Hilderbrand, R. Weissleder, J. S. Lewis, *Bioconjugate Chemistry* **2011**, *22*, 2048.
[84] F. Guerard, Y. S. Lee, R. Tripier, L. P. Szajek, J. R. Deschamps, M. W. Brechbiel, *Chemical Communications (Cambridge)* **2013**, *49*, 1002.
[85] M. A. Deri, S. Ponnala, B. M. Zeglis, G. Pohl, J. J. Dannenberg, J. S. Lewis, L. C. Francesconi, *Journal of Medicinal Chemistry* **2014**, *57*, 4849.
[86] T. Sprenger, A. Berthele, S. Platzer, H. Boecker, T. R. Tölle, *European Journal of Pain* **2005**, *9*, 117.
[87] M. Maziere, J. Godot, G. Berger, C. Prenant, D. Comar, *Journal of Radioanalytical and Nuclear Chemistry* **1981**, *62*, 279.
[88] S. K. Luthra, V. W. Pike, F. Brady, *Journal of the Chemical Society - Series Chemical Communications* **1985**, *NO. 20*, 1423.
[89] S. K. Luthra, V. W. Pike, F. Brady, *Applied Radiation and Isotopes* **1987**, *38*, 65.
[90] C.-Y. Shiue, L.-Q. Bai, R.-R. Teng, C. D. Arnett, S. L. Dewey, A. P. Wolf, D. W. McPherson, J. S. Fowler, J. Logan, M. J. Holland, E. J. Simon, *International Journal of Radiation Applications and Instrumentation. Part B. Nuclear Medicine and Biology* **1991**, *18*, 281.
[91] J. R. Lever, R. F. Dannals, A. A. Wilson, H. T. Ravert, H. N. Wagner Jr, *Tetrahedron Letters* **1987**, *28*, 4015.
[92] J. R. Lever, S. M. Mazza, R. F. Dannals, H. T. Ravert, A. A. Wilson, H. N. Wagner, *International Journal of Radiation Applications and Instrumentation. Part A. Applied Radiation and Isotopes* **1990**, *41*, 745.
[93] S. K. Luthra, F. Brady, D. R. Turton, D. J. Brown, K. Dowsett, S. L. Waters, A. K. P. Jones, R. W. Matthews, J. C. Crowder, *Applied Radiation and Isotopes* **1994**, *45*, 857.

[94] A. K. P. Jones, V. J. Cunningham, S.-K. Ha-Kawa, T. Fujiwara, Q. Liyii, S. K. Luthra, J. Ashburner, S. Osman, T. Jones, *Journal of Neuroscience Methods* **1994**, *51*, 123.
[95] A. K. P. Jones, S. K. Luthra, B. Maziere, V. W. Pike, C. Loc'h, C. Crouzel, A. Syrota, T. Jones, *Journal of Neuroscience Methods* **1988**, *23*, 121.
[96] D. D. Dougherty, J. Kong, M. Webb, A. A. Bonab, A. J. Fischman, R. L. Gollub, *Behavioural Brain Research* **2008**, *193*, 63.
[97] J. Maarrawi, R. Peyron, P. Mertens, N. Costes, M. Magnin, M. Sindou, B. Laurent, L. Garcia-Larrea, *Pain* **2007**, *127*, 183.
[98] H.-J. Wester, F. Willoch, T. R. Tolle, F. Munz, M. Herz, I. Oye, J. Schadrack, M. Schwaiger, P. Bartenstein, *Journal of Nuclear Medicine* **2000**, *41*, 1279.
[99] K. Grivas, S. W. Breeden, C. Ganter, S. M. Husbands, J. W. Lewis, *Tetrahedron Letters* **1999**, *40*, 1795.
[100] G. H. Loew, D. S. Berkowitz, *Journal of Medicinal Chemistry* **2002**, *22*, 603.
[101] M. J. Kreek, K. S. LaForge, E. Butelman, *Nature Reviews Drug Discovery* **2002**, *1*, 710.
[102] P. Bloms-Funke, C. Gillen, A. J. Schuettler, S. Wnendt, *Peptides* **2000**, *21*, 1141.
[103] H. S. Park, H. Y. Lee, Y. H. Kim, J. K. Park, E. E. Zvartau, H. Lee, *Bioorganic & Medicinal Chemistry Letters* **2006**, *16*, 3609.
[104] H. J. Rennen, O. C. Boerman, W. J. Oyen, F. H. Corstens, *European Journal of Nuclear Medicine and Molecular Imaging* **2001**, *28*, 241.
[105] S. Gratz, H. J. J. M. Rennen, O. C. Boerman, W. J. G. Oyen, F. H. M. Corstens, *Journal of Nuclear Medicine* **2001**, *42*, 917.
[106] P. T. Chapman, F. Jamar, E. T. Keelan, A. M. Peters, D. O. Haskard, *Arthritis & Rheumatism* **1996**, *39*, 1371.
[107] M. Gorenberg, R. BAR-SHALOM, O. ISRAEL, *The British Journal of Radiology* **2008**, *81*, 821.
[108] S. M. Allan, P. J. Tyrrell, N. J. Rothwell, *Nature Reviews Immunology* **2005**, *5*, 629.
[109] G. Lopez-Castejon, D. Brough, *Cytokine & Growth Factor Reviews* **2011**, *22*, 189.
[110] E. Pinteaux, N. J. Rothwell, H. Boutin, *Glia* **2006**, *53*, 551.
[111] C. Cawthorne, C. Prenant, A. Smigova, P. Julyan, R. Maroy, K. Herholz, N. Rothwell, H. Boutin, *British Journal of Pharmacology* **2010**, no.
[112] F. Molina-Holgado, E. Pinteaux, J. D. Moore, E. Molina-Holgado, C. Guaza, R. M. Gibson, N. J. Rothwell, *The Journal of Neuroscience* **2003**, *23*, 6470.
[113] C. J. Palestro, C. Love, K. Bhargava, K., *Quarterly Journal of Nuclear Medicine and Molecular Imaging* **2009**, *53*, 105
[114] M. L. Thakur, A. W. Segal, L. Louis, M. J. Welch, J. Hopkins, T. J. Peters, *Journal of Nuclear Medicine* **1977**, *18*, 1022.
[115] M. L. Thakur, J. P. Lavender, R. N. Arnot, D. J. Silvester, A. W. Segal, *Journal of Nuclear Medicine* **1977**, *18*, 1014.
[116] H. J. Danpure, S. Osman, F. Brady, *British Journal of Radiology* **1982**, *55*, 247.
[117] K. P. Gunter, J. N. Lukens, J. A. Clanton, P. J. Morris, R. L. Janco, D. English, *Radiology* **1983**, *149*, 563.
[118] E. F. J. de Vries, M. Roca, F. Jamar, O. Israel, A. Signore, *European Journal of Nuclear Medicine and Molecular Imaging* **2010**, *37*, 842.

[119] F. H. M. Corstens, J. W. M. van der Meer, *The Lancet* **1999**, *354*, 765.
[120] J. Bertrand-Caix, G. Freyburger, L. Bordenave, S. Labrouche, R. Bareille, F. Lefebvre, C. Baquey, D. Ducassou, *Journal of Nuclear Medicine* **1996**, *37*, 863.
[121] A. Rahmim, H. Zaidi, *Nuclear Medicine Communications* **2008**, *29*, 193.
[122] J.-P. Behr, *CHIMIA International Journal for Chemistry* **1997**, *51*, 34.
[123] A. J. Varma, S. V. Deshpande, J. F. Kennedy, *Carbohydrate Polymers* **2004**, *55*, 77.
[124] E. J. Keliher, J. Yoo, M. Nahrendorf, J. S. Lewis, B. Marinelli, A. Newton, M. J. Pittet, R. Weissleder, *Bioconjugate Chemistry* **2011**, *22*, 2383.
[125] P. Charoenphun, L. K. Meszaros, K. Chuamsaamarkkee, E. Sharif-Paghaleh, J. R. Ballinger, T. J. Ferris, M. J. Went, G. E. Mullen, P. J. Blower, *European Journal of Nuclear Medicine and Molecular Imaging* **2014**.
[126] D. Pellegrino, A. A. Bonab, S. C. Dragotakes, J. T. Pitman, G. Mariani, E. A. Carter, *Journal of Nuclear Medicine* **2005**, *46*, 1522.
[127] K. K. Bhargava, R. K. Gupta, K. J. Nichols, C. J. Palestro, *Nuclear Medicine and Biology* **2009**, *36*, 545.
[128] C. J. van der Laken, E. H. Elzinga, M. A. Kropholler, C. F. M. Molthoff, J. W. van der Heijden, K. Maruyama, R. Boellaard, B. A. C. Dijkmans, A. A. Lammertsma, A. E. Voskuyl, *Arthritis & Rheumatism* **2008**, *58*, 3350.
[129] G. Pottier, N. Bernards, F. Dollé, R. Boisgard, *Arthritis Research & Therapy* **2014**, *16*, R69.

Publication 1 (page 95)

CHAPTER 2: The automated radiosynthesis and purification of the opioid receptor antagonist, [6-*O*-methyl-^{11}C]Diprenorphine on the GE TRACERlab FX_{FE} radiochemistry module.

Published in:

Journal of Labelled Compounds and Radiopharmaceuticals, Volume 57, Issue 5, Pages: 388-396, 2014.

The automated radiosynthesis and purification of the opioid receptor antagonist, [6-*O*-methyl-^{11}C]Diprenorphine on the GE TRACERlab FX_{FE} radiochemistry module.

Michael Fairclough,[a*] Christian Prenant,[a] Gavin Brown,[a] Adam McMahon,[a] Jonathan Lowe,[a] and Anthony Jones[b]

[a]*Wolfson Molecular Imaging Centre, The University of Manchester, 27 Palatine Road, Manchester M20 3LJ, UK.*

[b]*Human Pain Research Group, The University of Manchester, Clinical Sciences Building, Salford Royal NHS Foundation Trust, Salford M6 8HD, UK.*

Abstract

[6-*O*-methyl-^{11}C]Diprenorphine ([^{11}C]Diprenorphine) is a positron emission tomography (PET) ligand used to probe the endogenous opioid system *in vivo*. Diprenorphine acts as an antagonist at all of the opioid receptor sub-types i.e. μ (mu), κ (kappa) and δ (delta). The radiosynthesis of [^{11}C]diprenorphine using [^{11}C]methyl iodide produced via the 'wet' method on a home-built automated radiosynthesis set-up has been described previously. Here we describe a modified synthetic method to [^{11}C]diprenorphine performed using [^{11}C]methyl iodide produced via the gas phase method on a GE TRACERlab FX_{FE} radiochemistry module. Also described is the use of [^{11}C]methyl triflate as the carbon-11 methylating agent for the [^{11}C]diprenorphine syntheses. [^{11}C]Diprenorphine was produced to good manufacturing practice (GMP) standards for use in a clinical setting. The method reported gives a higher specific activity product than previously reported by *Luthra* et al., which is advantageous for receptor occupancy studies. The radiochemical purity of [^{11}C]diprenorphine is similar to that reported by *Luthra et al.*, although the radiochemical yield produced in the method described herein is reduced, an issue that is inherent in the gas phase radiosynthesis of [^{11}C]methyl iodide. The yields of [^{11}C]diprenorphine are nonetheless sufficient for clinical research applications. Other advantages of the method described herein are an improvement to both reproducibility and reliability of the production as well as simplification of the purification and formulation steps. We suggest that our

automated radiochemistry route to [^{11}C]diprenorphine should be the method of choice for routine [^{11}C]diprenorphine productions for PET studies, and the production process could easily be transferred to other radiochemistry modules such as the TRACERlab FX C pro.

Keywords: [^{11}C]Diprenorphine; Opioid receptors; Methyl triflate; Positron emission tomography; Automated radiosynthesis.

Introduction

[^{11}C]diprenorphine (figure 1) is a key radioligand used to study opioid receptor density with Positron Emission Tomography (PET)[1-9]. The radioligand has high affinities (Ki values of 0.2 nM) for all sub-types of opioid receptor[10] (μ, δ and κ) behaving as an antagonist at μ/δ receptor types and as a weak agonist at κ opioid receptor types[2]. Previously, [^{11}C]diprenorphine has been used with PET for various physiological studies, including central post-stroke pain[11], studies of epileptic seizure[12] and in the assessment of pain and exercise induced changes in endogenous opioid receptor binding[13] to name but a few.

An automated radiosynthesis of [^{11}C]diprenorphine was described as early as 1994[6] which utilised the 'wet' chemistry method for the production of [^{11}C]methyl iodide[14] with the radiochemistry being implemented on an in-house automated chemistry system. Diprenorphine has also been radiolabelled with carbon-11 at the C-17 position[15] (*N*-[^{11}C]diprenorphine), however it was suggested that diprenorphine is rapidly metabolised via *N*-dealkylation[16], resulting in the loss of the radiolabelled moiety. More recently the automated synthesis of a fluorine-18 labelled analogue, 6-*O*-[2-[^{18}F]fluoroethyl)-6-*O*-desmethyldiprenorphine ([^{18}F]diprenorphine), was reported [17]. This analogue shows great similarities in the pharmacokinetics and receptor binding properties with [6-*O*-methyl-^{11}C]diprenorphine. However [^{18}F]diprenorphine showed lower brain uptake with the radio-metabolites accounting for a 20% contribution to the brain signal[17]. Also [^{18}F]diprenorphine has less favourable dosimetry compared to its carbon-11 counterpart. Therefore the interest in using [^{11}C]diprenorphine for *in vivo* opioid receptor studies with PET prompted us to develop the automation of a modified synthetic procedure using an all-purpose configured TRACERlab FX_{FE} radiochemistry system, in order to produce [^{11}C]diprenorphine routinely in compliance with GMP. GMP is a set of guidelines and principles that are required in

the manufacture of pharmaceuticals, in Europe this is set out in EudraLex and is enforced in the UK by the Medicines and Healthcare products Regulatory Agency (MHRA) Producing [^{11}C]diprenorphine to comply with GMP requires a reliable and robust production method to produce a sterile medicinal product suitable for human administration. This means the production process is carried out within an aseptic cleanroom environment and in dedicated synthesis cells and dispensing isolators with special air handling systems and particle counting. The final product must be sterile and endotoxin free and must comply to various limits for chemical and radiochemical purity.

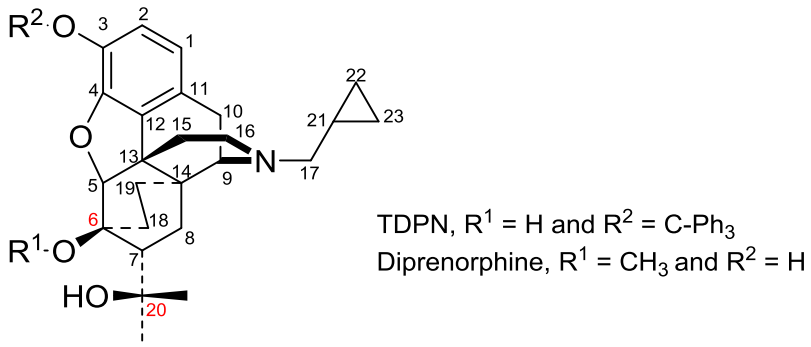

Figure 1: Atomically labelled diprenorphine and [3-*O*-trityl, 6-*O*-desmethyl]-diprenorphine (TDPN) molecules.

There are clear benefits to fully automating the radiosynthesis of a PET radioligand such as [^{11}C]diprenorphine. Firstly the reliability and reproducibility of the procedure can be optimised to give a robust production process. Automation of the process also allows the radiochemist to work safely with high levels of radioactivity whilst maintaining the ability to monitor reaction parameters and the purification of the radioligand via a computer interface.

The radiochemical route to [^{11}C]diprenorphine adapted from that reported previously[6], includes two steps: carbon-11 methylation of the protected precursor molecule [3-*O*-trityl, 6-*O*-desmethyl]-diprenorphine (TDPN) followed by acid hydrolysis of the triphenylmethyl protecting group (figure 2).

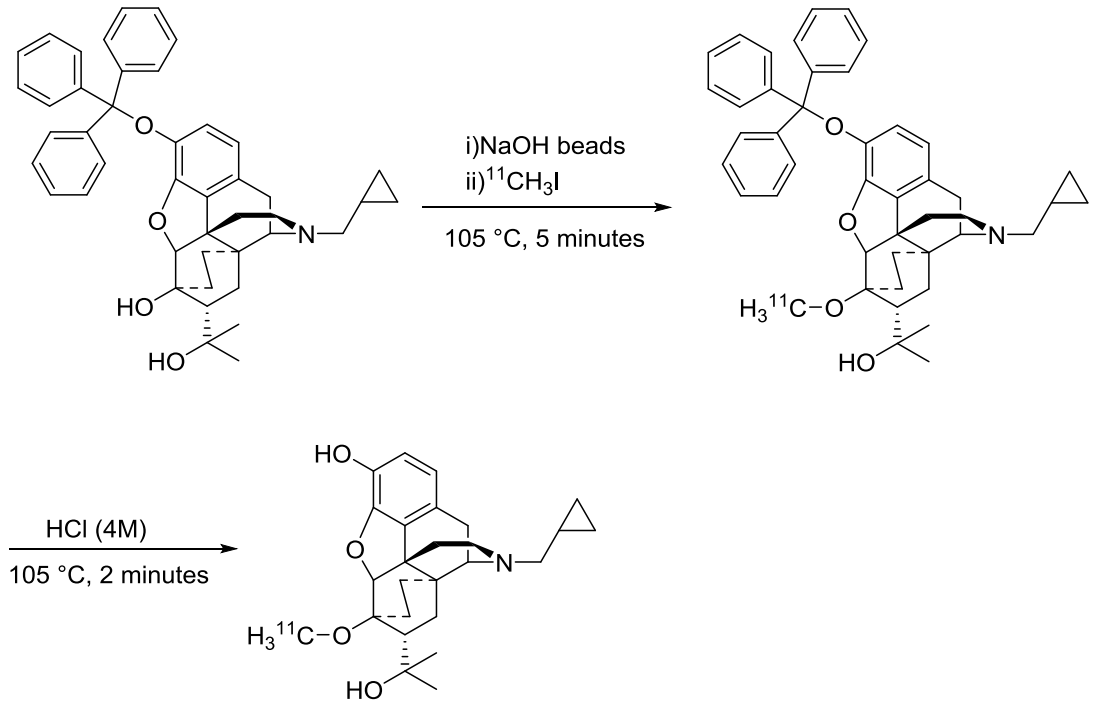

Figure 2: Two-step reaction scheme to [^{11}C]diprenorphine.

One of the key differences from that described in the literature was the use of sodium hydroxide (NaOH) as an alternative to sodium hydride (NaH) to carry out the carbon-11 methylation reaction. We suggest a mechanism which involves, in the first step, the deprotonation of a hydroxyl group at the C-6 position of the TDPN precursor molecule with NaOH a significantly weaker base than NaH. Also the 'gas phase' method for the radiosynthesis of [^{11}C]methyl iodide[18] was used which produces [^{11}C]methyl iodide with higher specific radioactivity compared to the 'wet' method[19]. The optimisation and automation steps described substantially improve the reliability and reproducibility of the [^{11}C]diprenorphine production to GMP standards for clinical PET scans.

[^{11}C]Methyl triflate was also considered as an alternative carbon-11 methylating agent to the more frequently used [^{11}C]methyl iodide. [^{11}C]Methyl triflate has increased reactivity when compared to [^{11}C]methyl iodide but has the drawback of reacting indiscriminately with the two hydroxyl groups in C6 and C20 , resulting in a lower radiochemical purity of the [^{11}C]diprenorphine produced compared to radiosyntheses from [^{11}C]methyl iodide.

Materials and Equipment

Diprenorphine.HCl (reference standard) and 3-*O*-trityl-diprenorphine (TDPN, precursor) were both purchased from ABX advanced biochemical compounds (Dresden, Germany). C18 Sep-Pak plus cartridges and the C18 µ-Bondapak, 10 µm, 125 Å, 7.8mm x 300mm HPLC column were purchased from Waters Ltd (Hertfordshire, UK). Kinetex C18, 2.6 µm, 100 Å, 4.6mm x 100mm HPLC columns were purchased from Phenomenex. 0.22 µm PVDF filters were purchased from Millipore (Hertfordshire, UK) and Minisart RC 15 0.45 µm pore filters were purchased from Sartorius Stedim Biotech (Surrey, UK). All other reagents were purchased from Sigma Aldrich Company Ltd (Dorset, UK), and were used without further purification.

The TRACERlab FX_{FE} chemistry system, supplied by GE Healthcare was the platform used to perform the [^{11}C]diprenorphine radiochemistry. The system was a modified form of a standard TRACERlab FX_{FE} system with a smaller reactor head (also supplied by GE Healthcare) and subsequently a smaller reaction vessel fitted (approximately 3 mL maximum volume).

Methods

Production of [^{11}C]carbon dioxide.

[^{11}C]Carbon dioxide was produced using a GE PETtrace 16 MeV cyclotron via the $^{14}N(p,\alpha)^{11}C$ nuclear reaction of a nitrogen gas target containing 1% oxygen. Typically, bombardment was carried out for 30 minutes with a proton beam current of 50 µA.

Production of [^{11}C]methyl iodide.

[^{11}C]Carbon dioxide was converted to [^{11}C]methyl iodide via the gas phase method[18] using the GE PETtrace MeI Microlab system. Cyclotron produced [^{11}C]carbon dioxide is reduced with hydrogen to [^{11}C]methane over a nickel catalyst. The [^{11}C]methane is mixed with vapour from iodine crystals in a quartz column at 720 ˚C to produce [^{11}C]methyl iodide which is trapped on a Porapak N trap whilst unreacted [^{11}C]methane is recirculated through the iodine column. Finally the Porapak N trap is heated to release the trapped [^{11}C]methyl iodide which is delivered to the TRACERlab FX_{FE} system directly where it is trapped in DMF (500 µL) at 0 °C.

Production of [^{11}C]methyl trifluoromethanesulfonate.

[^{11}C]Methyl triflate was prepared as previously described[20] by passing [^{11}C]methyl iodide in a gentle stream of helium carrier gas, through a small glass column (OD = 6 mm, ID = 4 mm and length = 250 mm) containing silver triflate heated to 250 ˚C. The [^{11}C]methyl triflate produced is trapped directly in the reaction vessel attached to the TRACERlab FX_{FE} radiochemistry system in DMF (500 µL) at room temperature.

Production of [6-*O*-methyl-^{11}C]diprenorphine using [^{11}C]methyl iodide.

A solution of [3-*O*-trityl, 6-*O*-desmethyl]-diprenorphine (TDPN, 1.0 mg, 1.53 µmol) in dimethylformamide (DMF, 500 µL) was added to a reaction vessel containing dry sodium hydroxide beads (20-40 mesh size, 10 mg, 250 µmol). The reaction vessel was attached to the TRACERlab FX_{FE} system and the mixture was left to stir at room temperature for approximately 5 minutes to generate the alkoxide group at the C-6 position of the TDPN molecule. Following this, [^{11}C]methyl iodide, 15.7 – 26.8 GBq (425 – 723 mCi), was trapped in the reaction vessel at 0 ˚C. The carbon-11 methylation reaction was carried out at 105 ˚C for 5 minutes with stirring. Next the reaction mixture was cooled to 25 ˚C and HCl (250 µL, 4M) was added. The reaction mixture was then heated to 105 ˚C for 2 minutes with stirring. The reaction vessel was cooled to 25 ˚C and a NaOH solution (2M, 500 µL) was added followed by the addition of phosphate buffer solution (1.0M, pH 7.4, 500 µL). The reaction mixture was then loaded on to a HPLC purification column (Waters C18 µ-Bondapak, 10 µm, 125 Å, 7.8mm x 300mm) with a mobile phase of 50:50 ammonium formate (0.1M) + sodium phosphate dibasic (10mM):acetonitrile at a flow rate of 4 mL/min and the HPLC eluent was continuously monitored for radioactivity signal and UV absorbance at a wavelength of 254 nm (Figures 3 and 4). [^{11}C]Diprenorphine, eluting from the HPLC column between 12 and 13 minutes was collected in a flask containing water (40 mL) before it was loaded on to a C18 solid phase extraction cartridge (Waters C18 plus). Following this, the C18 cartridge was washed with water (10 mL), before being eluted with ethanol (1 mL) into a two necked collection flask. 0.9% saline (12 mL) was added and the final product was dispensed into 3 sterile nitrogen filled vials inside a grade A dispensing isolator via a 0.22 µM membrane filter (Millipore, Millex-GV PVDF). The final volume of formulated product was 13 mL which was distributed as approximately 1.5 mL into each of two

quality control vials for sterility, endotoxin and final product identity testing and 10 mL into the patient administration vial.

Production of [6-*O*-methyl-^{11}C]diprenorphine using [^{11}C] methyl triflate

[^{11}C] Methyl triflate 10.62 – 22.20 GBq (287 – 600 mCi), was trapped at room temperature in a reaction vessel containing a solution of TDPN (1.0 mg, 1.53 µmol) in DMF (500 µL). Various bases were investigated to facilitate the carbon-11 methylation reaction including NaH, NaOH (in the form of solution as well as beads) and 1,8 diazabicyclo[5.4.0]undec-7-ene (DBU). The bases were added to the TDPN solution prior to trapping of [^{11}C]methyl triflate. The [^{11}C] methylation reaction was carried out at 30 ˚C for 2.5 minutes under stirred conditions. Next the carbon-11 labelled molecule was deprotected with HCl as described above for the radiosynthesis with [^{11}C]methyl iodide and processed similarly for the HPLC purification and formulation steps.

[6-*O*-methyl-^{11}C]Diprenorphine quality control.

Quality control HPLC analysis was performed on a Prominence HPLC system from Shimadzu (Milton Keynes, UK) using Laura 3 software from LabLogic, (South Yorkshire, UK). The HPLC system was run with a CBM-20A controller, a LC-20AB solvent delivery system and a SPD-20A absorbance detector. HPLC analysis to determine the chemical and radiochemical purity of the sample was carried out using a Kinetex C18, 2.6 µm, 100 Å, 4.6mm x 100mm HPLC column. The mobile phase used was 65:35 ammonium formate (0.1M, pH 5.25):methanol, the eluent was continuously monitored for radioactivity signal using a LabLogic Flow-count and UV response at a wavelength of 254 nm. [6-O-methyl-^{11}C]diprenorphine eluted from the HPLC column at 4 minutes. Further to the HPLC analysis of the [^{11}C]diprenorphine QC sample, testing of endotoxin levels was performed with an Endosafe portable test system (PTS) from Charles River (L'Arbresle, France).Gas phase analysis of residual solvents (ethanol, acetone, DMF and acetonitrile) was carried out using a Shimadzu GC-2010 gas chromatograph. An Rtx-624, 30 m, 0.32mm id, 1.8 µm column from Thames Restek (Buckinghamshire, UK) was used and a 2.5 µL injection was made with an injection port temperature of 220 ˚C and a column temperature of 40 ˚C. A column flow rate of 1.4 mL/min was used with an FID detector.

Results

[6-*O*-methyl-^{11}C]Diprenorphine from [^{11}C]methyl iodide

[^{11}C]Diprenorphine was produced to GMP standards in approximately 33 minutes from [^{11}C]methyl iodide trapping (48 minutes from end of bombardment EOB), on a TRACERlab FX_{FE} automated radiochemistry system. Radiosyntheses using [^{11}C]methyl iodide (produced from a 30 minute target irradiation with a 50 µA proton beam current) typically delivered a sterile solution of 1067 – 2967 MBq (an average of 1625 MBq) of [^{11}C]diprenorphine formulated in saline at end of synthesis (EOS). An average radiochemical yield of 32% (± 5.8%, based on 80 syntheses decay corrected to [^{11}C]methyl iodide trapping time) was attained. A typical specific radioactivity of 242.1 GBq/µmol was reached (ranging from 31.8 – 908.3 GBq/µmol) representing an average of 0.43 µg/mL of stable diprenorphine carrier, with 97.0 % radiochemical purity (± 1.4%, based on 80 [^{11}C]diprenorphine syntheses). A typical HPLC UV and gamma chromatogram of the crude [^{11}C]diprenorphine reaction mixture produced using [^{11}C]methyl iodide can be seen in Figures 3 and 4.

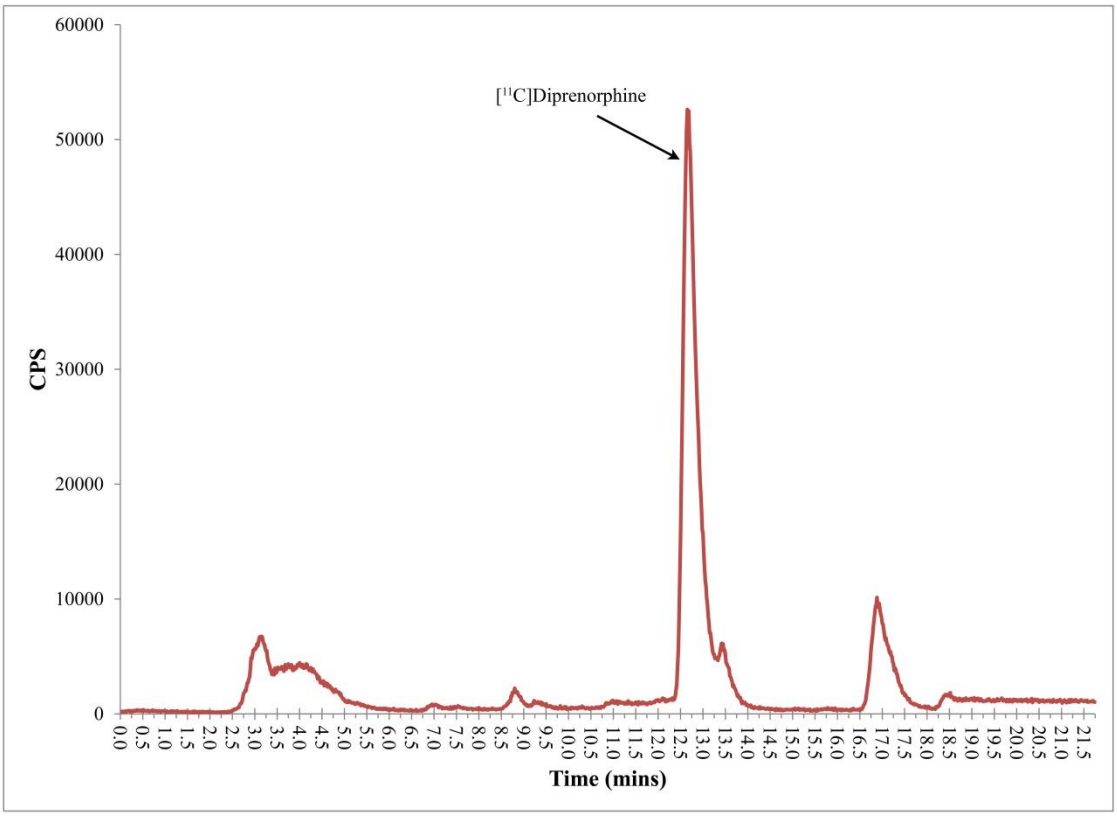

Figure 3: HPLC gamma trace of [^{11}C]diprenorphine produced with [^{11}C]methyl iodide.

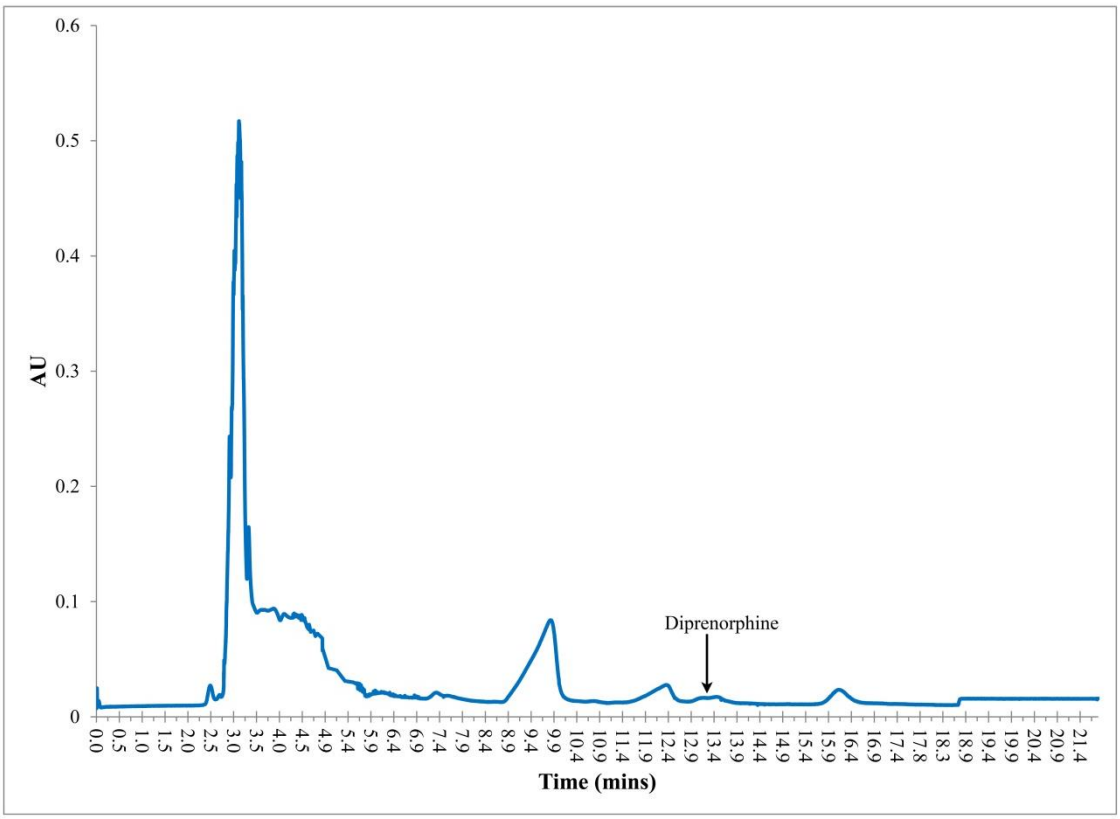

Figure 4: HPLC UV trace of [^{11}C]diprenorphine produced with [^{11}C]methyl iodide.

The base used to deprotonate the hydroxyl group and to produce the alkoxide derivative of the TDPN molecule proved to be key to the optimisation of the carbon-11 methylation reaction. A comparison of different bases used for the carbon-11 methylation reaction and the amount of formulated [^{11}C]diprenorphine produced at EOS is given in Table 1.

Base used to deprotonate 6-*O* position of TDPN	**Number of productions**	**Average amount of formulated [^{11}C]diprenorphine at EOS (10 mL)**	**Average Radiochemical Yield (decay corrected)**	**Average Radiochemical Purity**
NaH (2.5 mg)	20	962 MBq (± 451 MBq)	19.6 % (± 8.2 %)	95.1 % (± 1.7 %)
NaOH (10M, 5 µL) prepared from pellets	4	999 MBq (± 478 MBq)	18.0 % (± 7.5 %)	96.9 % (± 1.5 %)
NaOH (12M, 4 µL) from commercial supplier	19	1462 MBq (± 657)	33 % (± 11 %)	97.6 % (± 1.0 %)
NaOH beads (20-40 mesh, approximately 10 mg, 0.5 mmol)	19	1744 MBq (± 532.7)	36.6 % (± 11.6 %)	97.3 % (± 1.2 %)

Table 1: Comparison of various bases used for the production of [^{11}C]diprenorphine (using [^{11}C]methyl iodide) and the amount of formulated [^{11}C]diprenorphine produced at EOS.

[6-*O*-methyl-^{11}C]Diprenorphine from [^{11}C]methyl triflate

Syntheses of [^{11}C]diprenorphine using [^{11}C]methyl triflate typically delivered 200-2327 MBq (an average of 1303 MBq) of formulated product at EOS. An average radiochemical yield of 22.3% (± 10.9% based on 10 syntheses and decay corrected to [^{11}C]methyl triflate trapping time) was achieved. A typical specific radioactivity of 370 GBq/µmol (ranging from 8.2 – 990.7 GBq/µmol) was reached representing 0.24 µg/mol of stable diprenorphine carrier in the final formulated product, with an average of 93.5% radiochemical purity (± 5.1%based on 10 [^{11}C]diprenorphine syntheses). A typical HPLC UV and gamma chromatogram of the crude [^{11}C]diprenorphine reaction mixture for productions of the radiotracer using [^{11}C]methyl triflate can be seen in Figures 5 and 6.

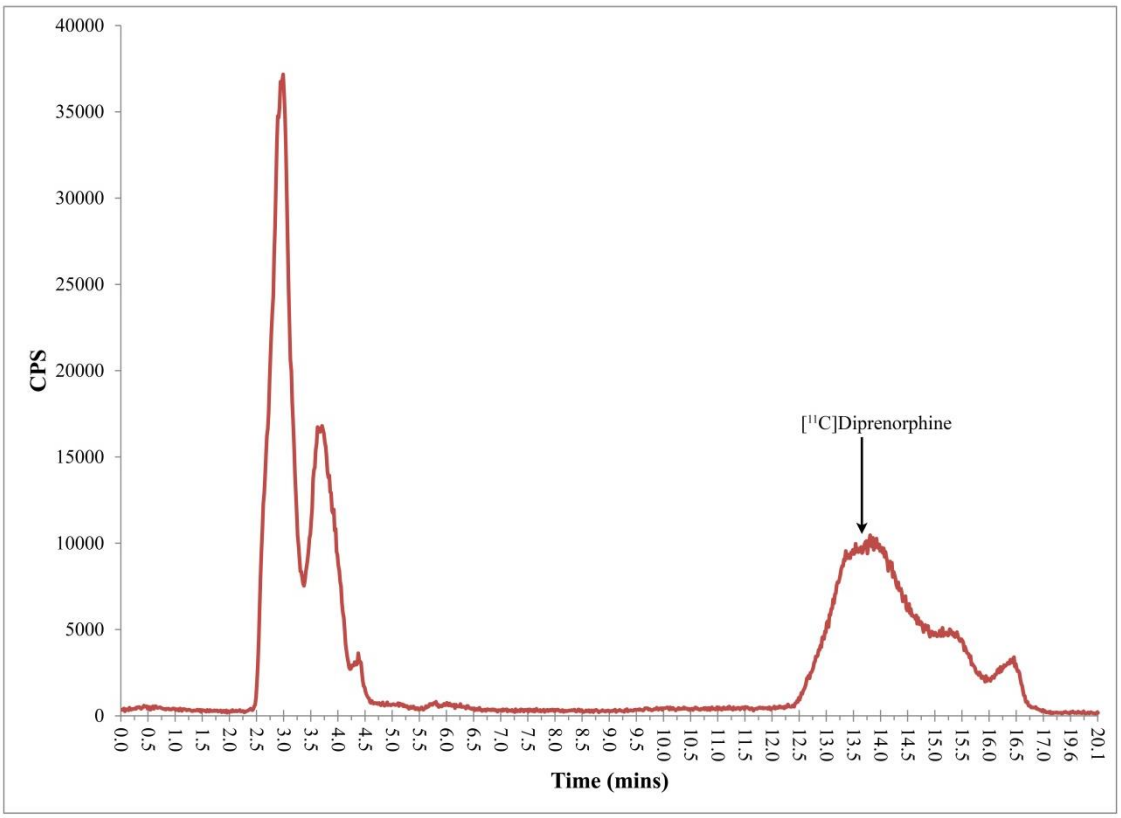

Figure 5: HPLC gamma trace of [^{11}C]diprenorphine produced with [^{11}C]methyl triflate.

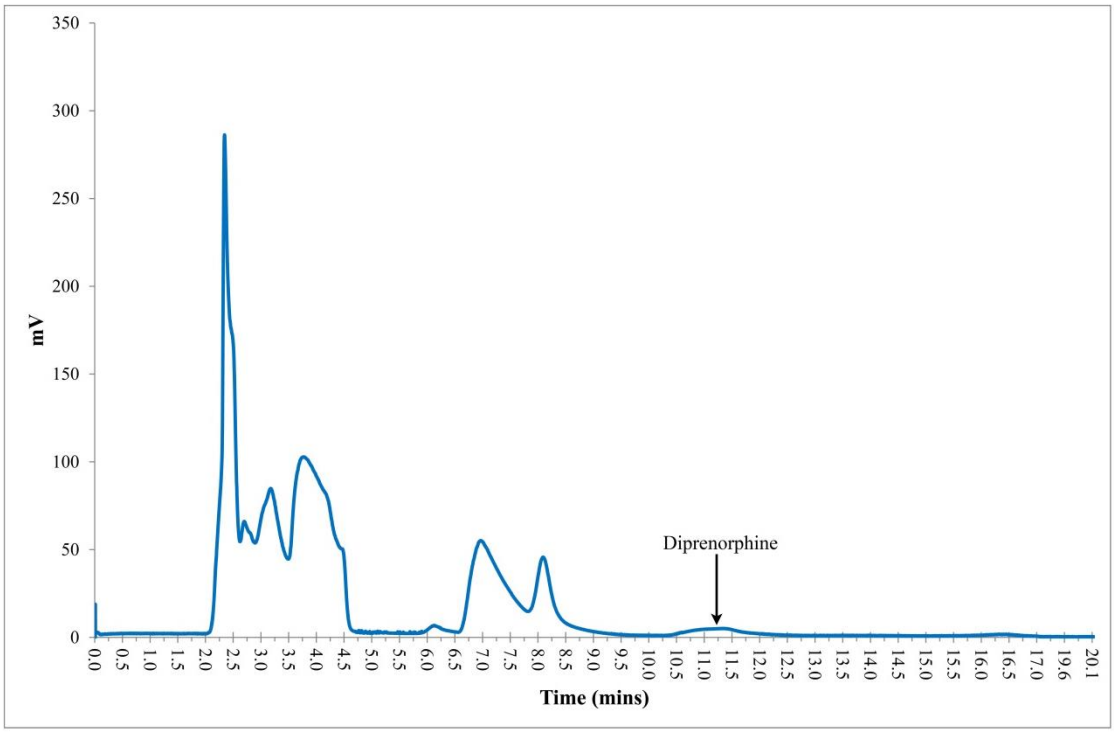

Figure 6: HPLC UV trace of [^{11}C]diprenorphine produced using [^{11}C]methyl triflate.

Experiments investigating the use of various bases for the carbon-11 methylation reaction were also carried out for productions of [^{11}C]diprenorphine with

[^{11}C]methyl triflate. A summary of the results from these experiments can be seen in Table 2.

Base used to deprotonate 6-*O* position of TDPN	**Number of productions**	**Average amount of formulated [^{11}C]diprenorphine at EOS (10 mL)**	**Average Radiochemical Yield (decay corrected)**	**Average Radiochemical Purity**
NaH (2.5 mg)	8	1423 MBq	24.7 % (± 9.4 %)	91.8 % (± 4.9 %)
NaOH (10M, 5 µL) prepared from pellets	1	1484 MBq	24 %	95.7 %
NaOH beads (20-40 mesh, approximately 10 mg, 0.5 mmol)	2	104 MBq	2.3 % (± 0.4 %)	97.6 % (± 3.5 %)
1,8-diazabicycloundec-7-ene (DBU) (15 µL)	1	No [^{11}C]diprenorphine produced	n/a	n/a

Table 2: Comparison of various bases used for the production of [^{11}C]diprenorphine (using [^{11}C]methyl triflate) and the amount of formulated [^{11}C]diprenorphine produced at EOS.

[6-*O*-methyl-^{11}C]Diprenorphine Quality Control

The final volume of formulated [^{11}C]diprenorphine dispensed was 13 mL which was distributed as approximately 1.5 mL into each of two quality control vials for sterility and final product identity testing and 10 mL into the patient administration vial. One of the QC vials was sent off site for sterility testing whilst the other QC vial was used for in-house QC testing. The internal QC testing performed included colour and clarity, pH, chemical and radiochemical purity, residual solvents, endotoxin testing (LAL) and filter integrity testing. The colour and clarity testing was passed in every production and a pH of 6 for the final formulated product was attained. The solvents which were quantified in the residual solvent analysis included ethanol (average value of 64300 ppm ± 4900 ppm against a limit of 100000 ppm), DMF (average value of 0 ppm against a limit of 880 ppm), acetone (average value of

2 ppm ± 4 ppm against a limit of 5000 ppm) and acetonitrile (average value of 6 ppm ± 8 ppm against a limit of 410 ppm). Endotoxin testing consistently returned results of < 2.5 endotoxin forming units/mL (EU/mL) against a limit of < 17.5 EU/mL. Filter integrity testing of the product filter was carried out by performing a bubble point pressure test in every incidence the filters passed the filter integrity testing. A typical HPLC chromatogram showing the radiochemical and chemical purity can be seen in Figures 7 and 8 respectively.

In addition to internal QC testing external sterility testing of the formulated [^{11}C]diprenorphine was completed, on each occasion the sample was determined to be sterile. Furthermore microbiological sampling was conducted in the dispensing isolator where [^{11}C]diprenorphine was dispensed. This consisted of contact and settle plate samples being taken at the beginning and at the end of the production session. The results from the incubated microbiological plates showed no growth on each occasion of a [11C]diprenorphine production.

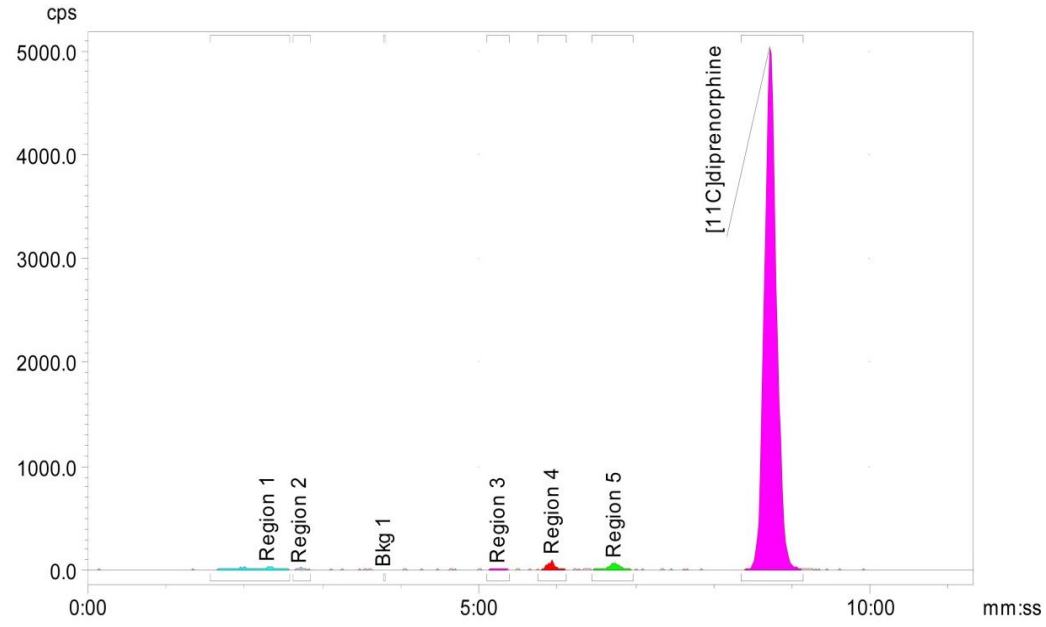

Name	Start (mm:ss)	End (mm:ss)	Retention (mm:ss)	Height (cps)	Area (Counts)	%ROI (%)	%Total (%)
Region 1	1:34	2:35	2:18	40.0	674.9	1.17	1.17
Region 2	2:37	2:51	2:43	29.6	134.3	0.23	0.23
Region 3	5:06	5:23	5:15	27.5	172.2	0.30	0.30
Region 4	5:45	6:07	5:56	110.1	647.8	1.12	1.12
Region 5	6:27	6:58	6:44	76.7	684.5	1.18	1.19
[^{11}C]diprenorphine	8:21	9:09	8:43	5031.3	55604.9	96.01	96.56
					57918.7	100.00	100.58

Figure 7: HPLC gamma trace from QC analysis of [^{11}C]diprenorphine.

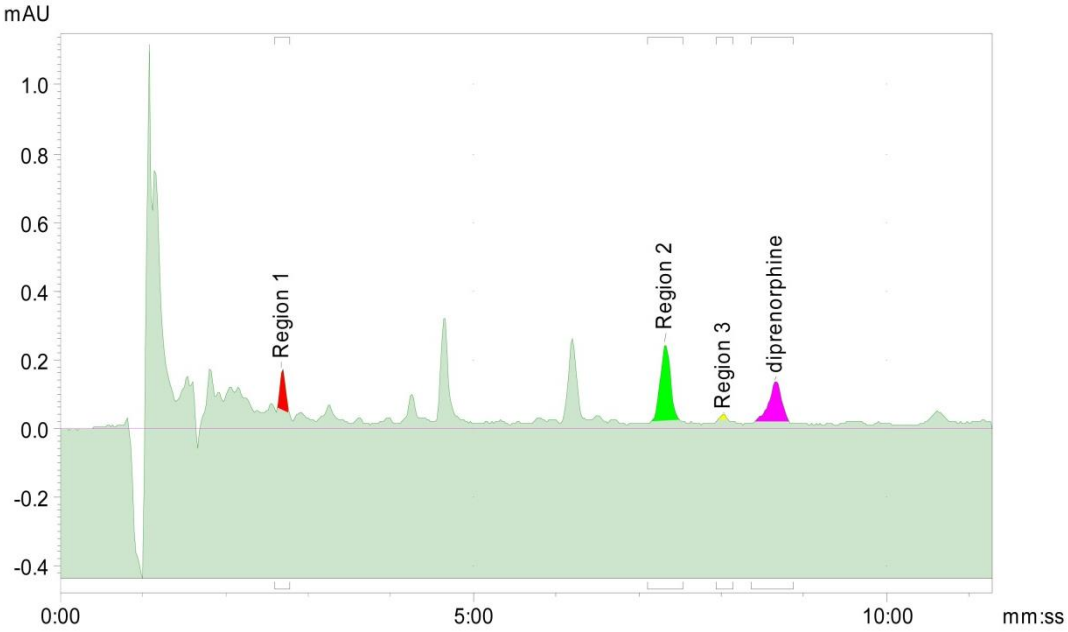

Name	Start (mm:ss)	End (mm:ss)	Retention (mm:ss)	Height (mAU)	Area (mAU)	%ROI (%)	%Total (%)
Region 1	2:35	2:46	2:41	0.2	0.5	12.46	1.64
Region 2	7:07	7:32	7:19	0.2	2.0	50.53	6.66
Region 3	7:56	8:09	8:02	0.0	0.1	2.57	0.34
diprenorphine	8:22	8:52	8:39	0.1	1.4	34.44	4.54
					4.0	100.00	13.19

Figure 8: HPLC UV trace from QC analysis of [^{11}C]diprenorphine.

Discussion

[6-*O*-methyl-^{11}C]Diprenorphine radiochemistry and automation

The automated radiosynthesis of [^{11}C]diprenorphine occurs as a two-step process as seen in the reaction scheme depicted in Figure 2. The first step is a base promoted bi-molecular nucleophilic substitution reaction (S_N2 mechanism) at the 6-hydroxy position of the precursor molecule (TDPN) with [^{11}C]methyl iodide. This is followed by a chemical deprotection at the C-3 position of [6-*O*-methyl-^{11}C]TDPN under acidic conditions to yield [6-O-methyl-^{11}C]diprenorphine.

In the first stage of the reaction the TDPN molecule is treated with a base to produce the more nucleophilic alkoxide derivative increasing the regioselectivity of the labelling at the C-6 position of the molecule. Previously, NaH was the base used to carry out this deprotonation[6], however we encountered some drawbacks associated with using this base. Radioactive side products with short retention times are always

observed in the HPLC chromatography of the crude reaction mixture, yet when NaH was used these radioactive side products were larger and consequently the amount of [^{11}C]diprenorphine observed at EOS was reduced (a sample HPLC chromatogram can be found in the supplementary data). A possible explanation for this could be that the reaction solvent (DMF) may be more unstable and be hydrolysed in NaH[21] (especially at elevated temperatures) which could give rise to the increase of early eluting radiolabelled side products and possibly carbon-11 methylated DMF. Another drawback related to using NaH was that it was necessary to use a filter to remove insoluble material from the reaction mixture prior to HPLC purification. However with a regenerated cellulose membrane filter a significant amount of crude reaction mixture (743 MBq) was retained on the filter bed. Another implication of using a filter for NaH in this position was that a fluid sensor which detects the presence of liquid in the tubing leading to the HPLC injection loop and allows the HPLC injection to be automated was rendered unusable. Finally there is some difficulty associated with the handling and storage of NaH due to the compound being highly moisture sensitive and reactive. With these drawbacks taken into consideration an alternative base was sought after to carry out the deprotonation at the C-6 hydroxyl position of TDPN prior to carbon-11 methylation.

NaOH was investigated as an alternative base and was used as a commercial 12M solution, a 10M solution prepared from pellets and also in a bead form (20-40 mesh). NaOH is less basic and less reactive when compared to NaH, evoking fewer side reactions whilst still producing the alkoxide at the C-6 position of TDPN. This reduced the early eluting radioactive side products observed by HPLC and increased amount of [^{11}C]diprenorphine at EOS. As shown in Table 1, using NaOH beads directly led to the highest amount of formulated [^{11}C]diprenorphine at EOS from [^{11}C]methyl iodide (1848 MBq of formulated [^{11}C]diprenorphine at EOS (n = 19)). The average amount of formulated [^{11}C]diprenorphine produced when NaH was used as the base was the lowest (946 MBq of [^{11}C]diprenorphine at EOS (n = 14)). Of the different forms of NaOH investigated NaOH beads gave the best yield at EOS. Using NaOH beads directly rather than in an aqueous solution eliminates water from the reaction mixture which presumably minimises radiochemical side products. Also the presence of water would decrease the amount of alkoxide produced by the base. Using sodium hydroxide beads for the carbon-11 methylation stage of the

radiosynthesis not only produced more [^{11}C]diprenorphine at EOS but also allows safer storage and handling compared to NaH and simplifies the automation of the production process.

Cleavage of the triphenylmethyl protecting group was optimally carried out using HCl at 105˚ C. Following the hydrolysis the reaction mixture was neutralised and buffer was added to the reaction mixture prior to HPLC purification. It was found that controlling the pH of the crude reaction mixture was essential to ensure a consistent retention time of [^{11}C]diprenorphine on the C18 HPLC column. If the reaction mixture has a low pH then the amine group of [^{11}C]diprenorphine is protonated making the molecule less lipophilic causing it to elute from the HPLC column earlier and increasing the possibility of co-elution with chemical and radiochemical impurities. To ensure the HPLC resolution was consistently good, sodium phosphate dibasic (10mM) was added to the mobile phase to give consistent retention times as well as improving the chemical purity of the final product.

A sample enrichment step prior to HPLC purification reported in Luthra *et al*.[6] was excluded from our radiochemistry procedure and the formulation step was also simplified by omitting the use of a rotary evaporator. HPLC purification of [^{11}C]diprenorphine was instead followed by isolation of the product on a C18 solid phase extraction (SPE) cartridge, and final formulation in 0.9% saline. The optimisation of these steps allowed us to reduce the time of the production process, an important factor when working with the short half-life of carbon-11 (t ½ = 20.38 minutes). Following SPE purification and formulation, [^{11}C]diprenorphine was dispensed into a class A dispensing isolator via a 0.22 µm membrane filter to give a final product suitable for injection.

We report an average [^{11}C]diprenorphine radiochemical purity of 97% when produced from [^{11}C]methyl iodide. The 3% radiochemical impurities could consist of diprenorphine labelled at the C20 position. If this was the case we could expect a radio peak eluting close to the [^{11}C]diprenorphine peak in the QC radiotrace as we would expect the molecules to have similar lipophilicity properties. However we see multiple small peaks in the QC gamma trace which make up the 3% impurities. Some are closely eluting to the [^{11}C]diprenorphine peak and could be attributed to radiolabelling at the C20 position of TDPN.

[^{11}C]Methyl trifluoromethanesulphonate ([^{11}C]methyl triflate) as carbon-11 methylating synthon to [6-*O*-methyl-^{11}C]diprenorphine.

[^{11}C]Methyl triflate was considered as an alternative carbon-11 methylating agent to the more commonly used [^{11}C]methyl iodide for the production of [^{11}C]diprenorphine. Previously [^{11}C]methyl triflate has been used as the carbon-11 methylating agent for the preparation of PET ligands and radiotracers [22-24]. A potential advantages of the more reactive [^{11}C]methyl triflate[25] is that the required methylation reaction conditions are more gentle. This means lower reaction temperatures, shorter reaction times and smaller amounts of desmethyl precursor can be used for the carbon-11 methylating steps[25]. Short reaction times are a clear benefit considering the constraints of the short half-life of carbon-11 and low reaction temperatures suggests a reduced possibility of undesired side reactions or possible precursor molecule degradation occurring. Using less precursor material also has cost benefits as well as making final product purification potentially easier. Finally the lower volatility of [^{11}C]methyl triflate compared to [^{11}C]methyl iodide makes trapping [^{11}C]methyl triflate in reaction solutions more facile.

[^{11}C]Diprenorphine was produced with [^{11}C]methyl triflate under mild reaction conditions, however increased radioactive side products and lower radiochemical purity of the final product were observed. It was postulated that the low radiochemical purity of the final product was due to the lack of selectivity between the two hydroxyl groups in the C6 and C20 positions of TDPN offered by the highly reactive [^{11}C]methyl triflate and the solvent DMF. TDPN (Figure 1) has three possible sites for carbon-11 methylation, the two hydroxyl functions at positions C-6 and C-20 and the tertiary amine group bridging the C-9 and C-16 positions. Carbon-11 methylation of the amine group would lead to quarternisation at this position to yield a more hydrophilic compound which would be less retained on a C18 HPLC column. The use of a base to generate the alkoxide derivative of the hydroxyl groups results in an increase of the regioselectivity of the carbon-11 methylation at the alkoxyl at the C-6 bridgehead position, favoured over the sterically hindered and less nucleophilic hydroxyl group at the C-20 position. There is likely to be competition between the nucleophilic sites at the C-6 and C-20 positions for the carbon-11 methylating agent, which is more of an issue when the more reactive [^{11}C]methyl triflate is used. Figures 5 and 6 depict a gamma and UV HPLC chromatogram of a

[^{11}C]diprenorphine reaction mixture produced from a synthesis with [^{11}C]methyl triflate. On the radio-trace (Figure 5) a complex synthesis mixture results in a [^{11}C]diprenorphine peak broadening with the peak being shifted to a later retention time. In addition [^{11}C]diprenorphine can be seen co-eluting with two other radioactive compounds which correspond to the low radiochemical purity at EOS. This could support the hypothesis of possible radiolabelling at the C-20 position of the molecule when using the less selective and more reactive [^{11}C]methyl triflate. Carbon-11 methylation at the C-20 position would produce a molecule with a similar retention time to [^{11}C]diprenorphine which would possibly co-elute giving rise to reduced radiochemical purity.

The synthesis of [^{11}C]diprenorphine using [^{11}C]methyl triflate produces less [^{11}C]diprenorphine at EOS with a lower radiochemical purity compared to a synthesis with [^{11}C]methyl iodide. Comparing the gamma HPLC chromatograms of syntheses from [^{11}C]methyl iodide (Figure 3) and [^{11}C]methyl triflate (Figure 5) we can see the radiochemical impurities which elute between 2 and 5 minutes when using [^{11}C]methyl triflate. The lesser retained radiochemical impurities suggests the compounds are relatively polar and could possibly be a result of [^{11}C]methyl triflate reacting with the reaction solvent DMF or with the small quantities of water which may be present in the reaction mixture. As [^{11}C]methyl triflate is being consumed in these side reactions, the implication is that there is less available to react with TDPN to produce [^{11}C]diprenorphine, resulting in lower yields.

The bases considered for the methylation reaction using [^{11}C]methyl triflate included NaH, NaOH and 1,8-diazabicycloundec-7-ene (DBU), all differing in the strength of basicity. A summary of the results can be seen in table 2. When DBU was used as the base no [^{11}C]diprenorphine was produced in the reaction mixture. DBU was used as it is a highly steric, non-nucleophilic base and the hypothesis was that these characteristics would allow the [^{11}C]methyl triflate to react with the precursor molecule preferentially at the C-6 position. Interestingly, no [^{11}C]diprenorphine was produced with [^{11}C]methyl triflate and DBU, which suggests that a stronger base is required to selectively label TDPN at the C-6 position with [^{11}C]methyl triflate.

Relative chemoselective reactivity of [^{11}C]methyl iodide and [^{11}C]methyl triflate towards O- and N-methylation has been reported with contradictory results, Schou *et*

al.[26] found it necessary when using [^{11}C]methyl triflate for the radiolabelling of *(s,s)* [^{11}C]-MeNER to use a protecting group on a morpholino nitrogen in order to gain selectivity for a hydroxyl group but oppositely [^{11}C]methyl iodide reacted exclusively on the phenolic precursor in the presence of excess sodium hydroxide and no significant *N*-methylation was observed. Oppositely for the production of [^{11}C]PIB, Mathis *et al.*[27] concluded that protection at the hydroxyl group is required for successful N-[^{11}C]methylation with [^{11}C]methyl iodide while Wilson *et al.*[28] reported the labelling of PIB using [^{11}C]methyl triflate with exclusively alkylation on the aniline nitrogen of the unprotected precursor. Thus the selectivity of [^{11}C]methyl triflate toward O- and N-methylation depends on the precursor and can be lower or higher than that of [^{11}C]methyl iodide. For [^{11}C]diprenorphine we have found that the selectivity of [^{11}C]methyl triflate towards the two free hydroxyl groups of the precursor in the C60 and C20 is lower than that of [^{11}C]methyl iodide. We therefore suggest that [^{11}C]methyl triflate is not an appropriate route for the radiosynthesis of [^{11}C]diprenorphine as it produces a lower yield in [^{11}C]diprenorphine with a lower radiochemical purity at EOS compared to [^{11}C]methyl iodide.

Perhaps trapping [^{11}C]methyl triflate at 0 ˚C may improve the labelling yield of [^{11}C]diprenorphine and supress the amount of radiolabelled side product resulting from a reaction with DMF.

Conclusion

A fully automated, reliable, and robust [^{11}C]diprenorphine production process was achieved using a TRACERlab FX_{FE} radiochemistry platform, to deliver high specific radioactivity [^{11}C]diprenorphine with high radiochemical purity to be used in clinical PET studies. The improvement to the specific radioactivity is on average 10 times higher than that reported in the literature[6], which is important for a ligand which is targeting neuroreceptors. [^{11}C]Diprenorphine was produced to GMP standards in approximately 33 minutes from [^{11}C]methyl iodide trapping time (48 minutes from EOB), to be used to probe the endogenous opioid system *in vivo* using PET. Starting from 15.7 – 26.8 GBq (425 – 723 mCi) of [^{11}C]methyl iodide, 1067 – 2967 MBq (an average of 1625 MBq) [^{11}C]diprenorphine formulated for human administration was produced with an average radiochemical yield of 32 % (based on 80 syntheses decay corrected to [^{11}C]methyl iodide trapping time). A typical specific radioactivity of 242.1 GBq/µmol was attained (ranging from 31.8 – 908.3

GBq/μmol) representing an average of 0.43 μg/mL of stable diprenorphine carrier, with 97 % radiochemical purity (based on 80 syntheses).

We have described a modified synthetic method automated on a GE TRACERlab FX_{FE} radiochemistry module to produce high radiochemical purity [^{11}C]diprenorphine. Automation of the radiosynthesis on the TRACERlab FX_{FE} platform improves both the reliability and reproducibility of the production process which is demonstrated in the simplified formulation and purification steps resulting from the in-built SPE separation process. Optimisation of the radiochemistry route included using NaOH beads for the carbon-11 methylation stage of the radiosynthesis. This produced more [^{11}C]diprenorphine at EOS with a cleaner reaction mixture but also allowed easier handling compared to NaH. [^{11}C]Methyl iodide proved superior to [^{11}C]methyl triflate for this radiosynthesis and more reliable for routine production. [^{11}C]Methyl triflate showed high reactivity but poor selectivity in the carbon-11 methylation of TDPN producing a more complex crude synthetic mixture which was poorly resolved by HPLC purification with some carbon-11 labelled side products co-eluting with [^{11}C]diprenorphine. With the optimisation and automation described in this work we suggest that this automated radiochemistry route to [^{11}C]diprenorphine should be the method of choice for routine [^{11}C]diprenorphine productions for PET studies. The synthesis method described here utilises a GE PETtrace MeI Microlab system combined with a GE TRACERlab FX_{FE} radiochemistry module. However we believe the production process could easily be transferred to other radiochemistry modules such as the TRACERlab FX C pro where the full production could be done on a single module.

References

[1] A. K. P. Jones, H. Watabe, V. J. Cunningham, T. Jones, *European Journal of Pain* **2004**, *8*, 479.

[2] J. R. Lever, *Current Pharmaceutical Design* **2007**, *13*, 33.

[3] D. D. Dougherty, J. Kong, M. Webb, A. A. Bonab, A. J. Fischman, R. L. Gollub, *Behavioural Brain Research* **2008**, *193*, 63.

[4] S. P. Hume, A. R. Lingford-Hughes, V. Nataf, E. Hirani, R. Ahmad, A. N. Davies, D. J. Nutt, *Journal of Pharmacology and Experimental Therapeutics* **2007**, *322*, 661.

[5] A. K. P. Jones, V. J. Cunningham, S.-K. Ha-Kawa, T. Fujiwara, Q. Liyii, S. K. Luthra, J. Ashburner, S. Osman, T. Jones, *Journal of Neuroscience Methods* **1994**, *51*, 123.

[6] S. K. Luthra, F. Brady, D. R. Turton, D. J. Brown, K. Dowsett, S. L. Waters, A. K. P. Jones, R. W. Matthews, J. C. Crowder, *Applied Radiation and Isotopes* **1994**, *45*, 857.
[7] J. Maarrawi, R. Peyron, P. Mertens, N. Costes, M. Magnin, M. Sindou, B. Laurent, L. Garcia-Larrea, *Pain* **2007**, *127*, 183.
[8] J. J. Frost, H. S. Mayberg, B. Sadzot, R. F. Dannals, J. R. Lever, H. T. Ravert, A. A. Wilson, H. N. Wagner, Jr., J. M. Links, *Journal of Cerebral Blood Flow and Metabolism* **1990**, *10*, 484.
[9] R. F. Dannals, *Journal of Labelled Compounds and Radiopharmaceuticals* **2013**, *56*, 187.
[10] G. Henriksen, F. Willoch, P. S. Talbot, H.-J. Wester, *Drug Development Research* **2006**, *67*, 890.
[11] F. Willoch, F. Schindler, H. J. Wester, M. Empl, A. Straube, M. Schwaiger, B. Conrad, T. R. Tölle, *Pain* **2004**, *108*, 213.
[12] A. Hammers, M.-C. Asselin, R. Hinz, I. Kitchen, D. J. Brooks, J. S. Duncan, M. J. Koepp, *Brain* **2007**, *130*, 1009.
[13] H. Boecker, G. Henriksen, T. Sprenger, I. Miederer, F. Willoch, M. Valet, A. Berthele, T. R. Tölle, *Methods* **2008**, *45*, 307.
[14] C. Crouzel, B. Långström, V. W. Pike, H. H. Coenen, *International Journal of Radiation Applications and Instrumentation. Part A. Applied Radiation and Isotopes* **1987**, *38*, 601.
[15] C.-Y. Shiue, L.-Q. Bai, R.-R. Teng, C. D. Arnett, S. L. Dewey, A. P. Wolf, D. W. McPherson, J. S. Fowler, J. Logan, M. J. Holland, E. J. Simon, *International Journal of Radiation Applications and Instrumentation. Part B. Nuclear Medicine and Biology* **1991**, *18*, 281.
[16] B. Sadzot, J. C. Price, H. S. Mayberg, K. H. Douglass, R. F. Dannals, J. R. Lever, H. T. Ravert, A. A. Wilson, H. N. Wagner, M. A. Feldman, J. J. Frost, *J Cereb Blood Flow Metab* **1991**, *11*, 204.
[17] H.-J. Wester, F. Willoch, T. R. Tolle, F. Munz, M. Herz, I. Oye, J. Schadrack, M. Schwaiger, P. Bartenstein, *J Nucl Med* **2000**, *41*, 1279.
[18] P. Larsen, J. Ulin, K. Dahlstrøm, M. Jensen, *Applied Radiation and Isotopes* **1997**, *48*, 153.
[19] V. Gómez-Vallejo, J. Llop, *Applied Radiation and Isotopes* **2009**, *67*, 111.
[20] D. M. Jewett, *International Journal of Radiation Applications and Instrumentation. Part A. Applied Radiation and Isotopes* **1992**, *43*, 1383.
[21] M. Jacques, *Tetrahedron* **2009**, *65*, 8313.
[22] K. Någren, C. Halldin, *Journal of Labelled Compounds and Radiopharmaceuticals* **1998**, *41*, 831.
[23] K. Någren, L. Müller, C. Halldin, C.-G. Swahn, P. Lehikoinen, *Nuclear Medicine and Biology* **1995**, *22*, 235.
[24] T. D. Wegman, B. Maas, P. H. Elsinga, W. Vaalburg, *Applied Radiation and Isotopes* **2002**, *57*, 505.
[25] F. Wuest, M. Berndt, T. Kniess, *Ernst Schering Research Foundation Workshop* **2007**, 183.
[26] M. Schou, C. Halldin, J. Sóvágó, V. W. Pike, B. Gulyás, P. D. Mozley, D. P. Johnson, H. Hall, R. B. Innis, L. Farde, *Nuclear Medicine and Biology* **2003**, *30*, 707.
[27] C. A. Mathis, Y. Wang, D. P. Holt, G.-F. Huang, M. L. Debnath, W. E. Klunk, *Journal of Medicinal Chemistry* **2003**, *46*, 2740.

[28] A. A. Wilson, A. Garcia, A. Chestakova, H. Kung, S. Houle, *Journal of Labelled Compounds and Radiopharmaceuticals* **2004**, *47*, 679.

**Correspondence to: M. Fairclough, Wolfson Molecular Imaging Centre, The University of Manchester, 27 Palatine Road, Manchester M20 3LJ, UK. Tel.: +44(0)1612750034*

E-mail: michael.fairclough@manchester.ac.uk

Supplementary Data

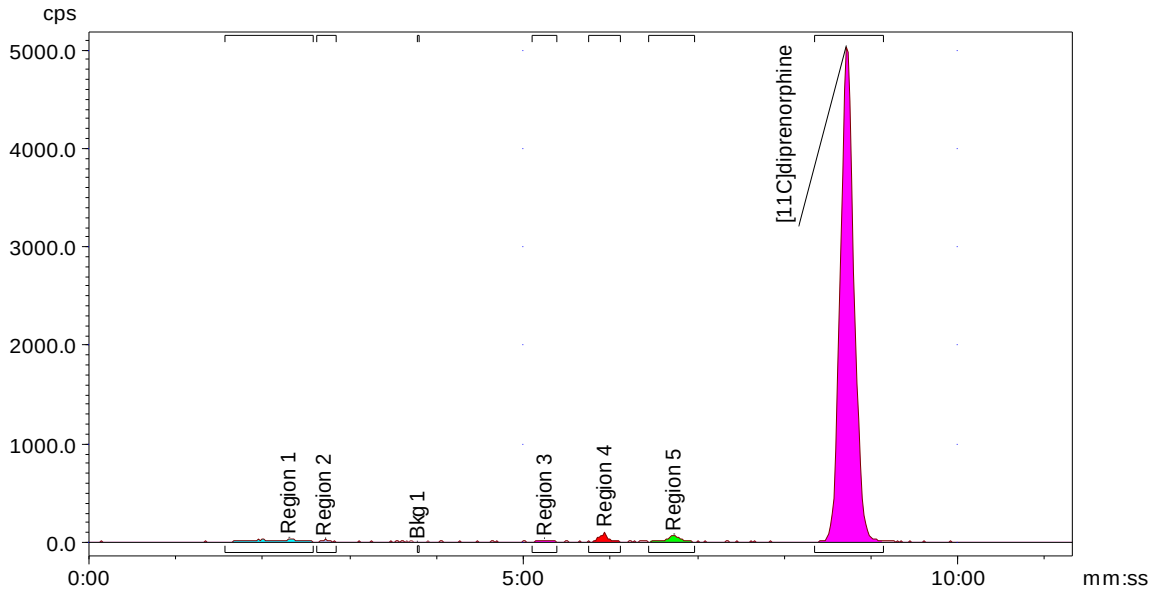

Name	Start (mm:ss)	End (mm:ss)	Retention (mm:ss)	Height (cps)	Area (Counts)	%ROI (%)	%Total (%)
Region 1	1:34	2:35	2:18	40.0	674.9	1.17	1.17
Region 2	2:37	2:51	2:43	29.6	134.3	0.23	0.23
Region 3	5:06	5:23	5:15	27.5	172.2	0.30	0.30
Region 4	5:45	6:07	5:56	110.1	647.8	1.12	1.12
Region 5	6:27	6:58	6:44	76.7	684.5	1.18	1.19
[11C]diprenorphine	8:21	9:09	8:43	5031.3	55604.9	96.01	96.56
					57918.7	100.00	100.58

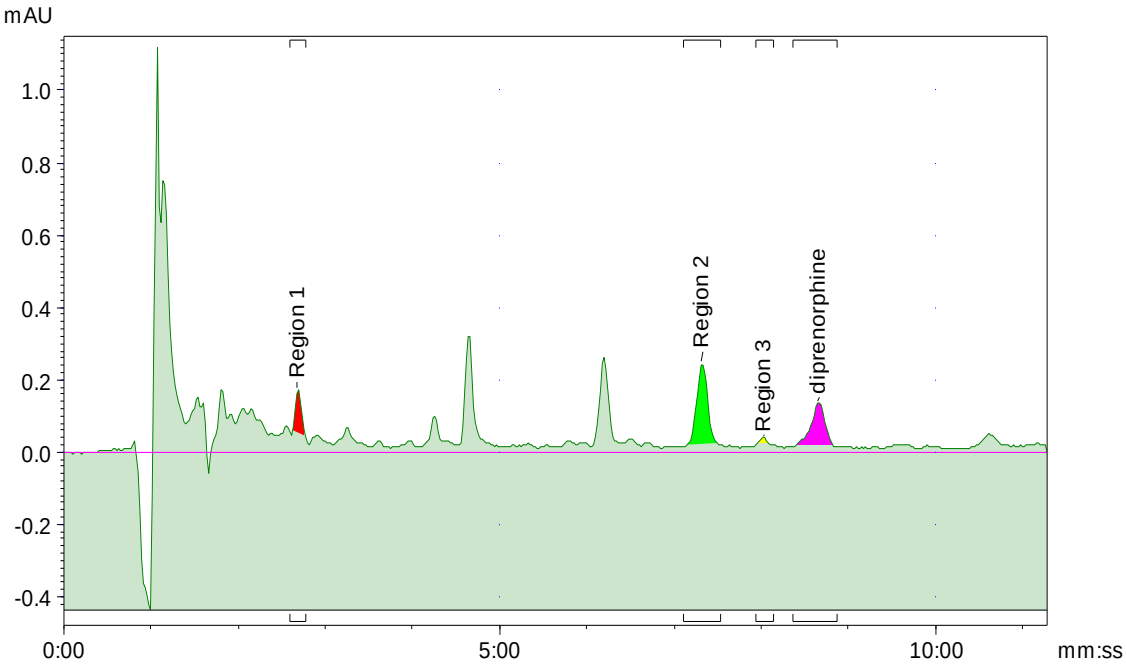

Name	Start (mm:ss)	End (mm:ss)	Retention (mm:ss)	Height (mAU)	Area (mAU)	%ROI (%)	%Total (%)
Region 1	2:35	2:46	2:41	0.2	0.5	12.46	1.64
Region 2	7:07	7:32	7:19	0.2	2.0	50.53	6.66
Region 3	7:56	8:09	8:02	0.0	0.1	2.57	0.34
diprenorphine	8:22	8:52	8:39	0.1	1.4	34.44	4.54
					4.0	100.00	13.19

Figure 9: Radioactivity (top) and UV (bottom) HPLC traces from QC analysis of [^{11}C]diprenorphine.

Publication 2 (page 119)

CHAPTER 3: A highly reproducible method for the Measurement of [6-*O*-methyl-^{11}C]diprenorphine and its radiometabolites based on Solid Phase Extraction (SPE) and radio-HPLC

Prepared for Publication

A highly reproducible method for the Measurement of [6-*O*-methyl-^{11}C]diprenorphine and its radio-metabolites based on Solid Phase Extraction (SPE) and radio-HPLC

Michael Fairclough,[a*] Adam McMahon,[a] Elizabeth Barnett,[a] Julian Matthews,[a] Christopher A Brown[b] and Anthony Jones[c]

[a]Wolfson Molecular Imaging Centre, The University of Manchester, 27 Palatine Road, Manchester M20 3LJ, UK. [b]CamPain group, Department of Anaesthesia, University of Cambridge, Cambridge, United Kingdom, CB2 0QQ. [c]Human Pain Research Group, The University of Manchester, Clinical Sciences Building, Salford Royal NHS Foundation Trust, Salford M6 8HD, UK.

Abstract

Described here is a method for the measurement of the radio-metabolites of the positron emission tomography (PET) radiotracer [6-*O*-methyl-^{11}C]diprenorphine ([^{11}C]diprenorphine) using an in-line solid phase extraction (SPE) combined with radio-HPLC analysis. With this method we observe a high degree of within-subject reproducibility of metabolite profile with consistent differences between subjects. This is indicative of the reliability and reproducibility that our method of metabolite analysis of [^{11}C]diprenorphine offers. We conclude that the metabolite data for multiple PET scans in the same subjects using this method of metabolite analysis is so well matched that it may be possible to apply a single set of metabolite data for a participant over multiple PET scans as the variability is so low. We believe that our method of analysis of [^{11}C]diprenorphine metabolites should be the method of choice for clinical and PET scanning. In addition, different SPE stationary phases are assessed for their efficiency for loading, retention and elution of the parent molecule and its metabolites. Having assessed C4, phenyl and C18 stationary phase we concluded that a C18 SPE packed stainless column assembly (300 mm x 48 mm) was optimal for our method. Finally, *in silico* predictions of diprenorphine metabolism were compared to the *in vivo* metabolism of [^{11}C]diprenorphine induced by hepatic microsomal digestion and analysed by MALDI mass spectrometry. It was found that there was a high degree of agreement between the two methods and in particular the formation of the diprenorphine-3-glucuronide metabolite.

Introduction

[6-*O*-methyl-^{11}C]diprenorphine ([^{11}C]diprenorphine) is an important positron emission tomography (PET) radioligand which binds to multiple subtypes of opioid receptor (μ, δ and κ sites) with high affinities (Ki values of approximately 0.2 nM)[1]. Diprenorphine acts as an antagonist at μ and δ opiate receptors and as a weak agonist at the κ receptors[2]. Opiate receptors are associated with a wide variety of physiological processes including analgesia, epilepsy[3], central post-stroke pain[4] dysphoria and euphoria[5]. [^{11}C]diprenorphine PET Is a powerful tool to study the role of the endogenous opioid system in these biological processes, allowing quantitative imaging of opioid receptor density and displacement[2, 5-10] by endogenous opioids. However, [^{11}C]diprenorphine will undergo metabolism in vivo and this is significant for PET imaging. If radiolabelled metabolites are produced on the timescale of a clinical PET scan then a method is required to determine the radiometabolite concentrations as a function of time.

Having the ability to identity ^{11}C labelled metabolites is also important in order to estimate their influence on the scan data, for example, knowing the ability of the radiometabolite to cross the blood-brain barrier and their affinity for opiate receptors is of high importance when modelling [^{11}C]diprenorphine binding in the brain accurately. At various time points during the PET scanning session the ratio of parent [^{11}C]diprenorphine to each radio-metabolite needs to be established. An accurate correction for arterial plasma radiometabolite concentrations is necessary, so that a correct plasma input function can be derived for [^{11}C]diprenorphine in order to accurately model quantitative binding of [^{11}C]diprenorphine to available opioid receptors in the brain.

A variety of methods are available for the extraction and measurement of radiotracer metabolites. The measurement of radio-metabolites in human plasma is very challenging. The radio-metabolite concentrations are low and diminish with time, requiring that relatively large volumes of plasma (5 mL) be analysed. Such volumes of plasma cannot be analysed directly using analytical HPLC (< 4.6 mm I.D. columns) without overloading the column, yielding very poor chromatographic resolution and dramatically shortening HPLC column life. Chromatographic detection normally employs flow-through detectors, giving an immediate, real time measurement of chromatographic peak height and area, however the short sample

residence time in the detector leads to poor detection limits. This can be improved by collecting fractions of eluent and measuring each fraction off-line in a radio-detector, thus extending measurement time significantly, limited only by the availability of radio-detectors for the number of samples generated. Large plasma samples can (and have) been injected onto preparative scale HPLC columns, however these have correspondingly higher mobile phase flow rates and generate larger volume fractions for off-line detection. Widely available multi-well detectors such as the Perkin Elmer 10-well automatic gamma counter are limited in sample capacity and the chromatography is best performed with an analytical scale column generating fractions in the volume range of 1 – 3 mL.

The alternative to direct analysis (HPLC column injections) is to remove the protein fraction from the sample and try to pre-concentrate the metabolites into smaller volume samples. This has been achieved in a number of ways 1) protein precipitation 2) liquid-liquid extraction 3) metabolite trapping by SPE. The efficacy of these methods will depend on the lipophilicity of the parent tracer and metabolites and the extent to which these species are co-precipitated with plasma proteins. However these methods have inherent problems associated with them. Performing protein precipitation/extraction can lead to the loss of metabolites which may be bound to the plasma proteins and using a vacuum manifold with SPE cartridge extraction may lead to the loss of any volatile metabolites which may be present in the sample. We believe that the use of in-line SPE cartridge to clean-up and concentrate the sample followed by HPLC analysis is the optimum method of metabolite analysis. With this method it is possible to start with a 5 mL blood sample which can be processed and worked up so that metabolite measurements can be performed on an analytical HPLC column. Figures 1 – 3 depict the configuration of the in-line SPE followed by HPLC set-up for [^{11}C]diprenorphine analysis.

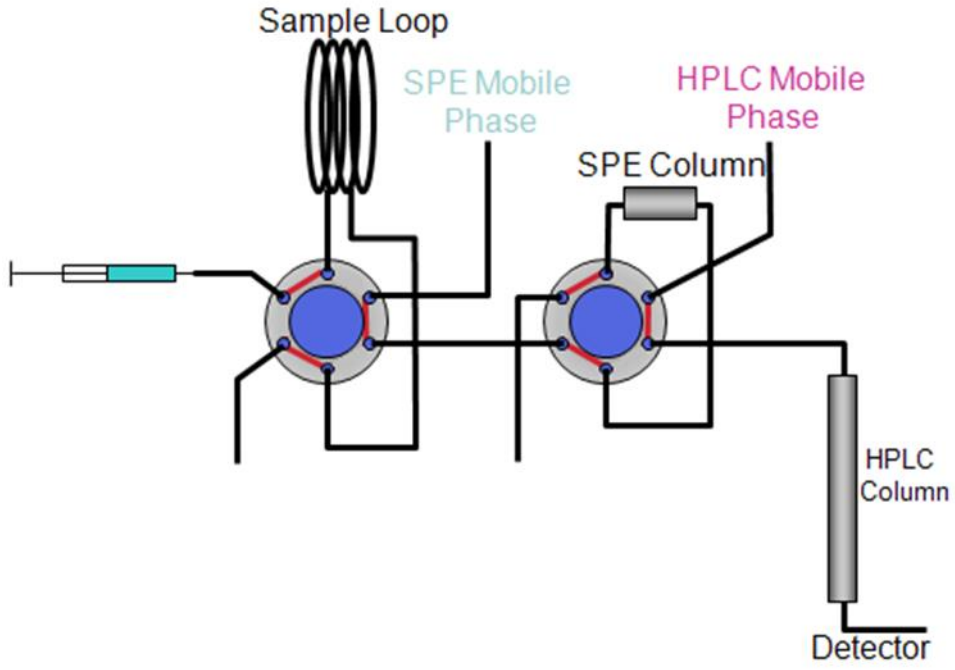

Figure 1: Schematic of in-line SPE and HPLC system. Valves are shown in sample inject position.

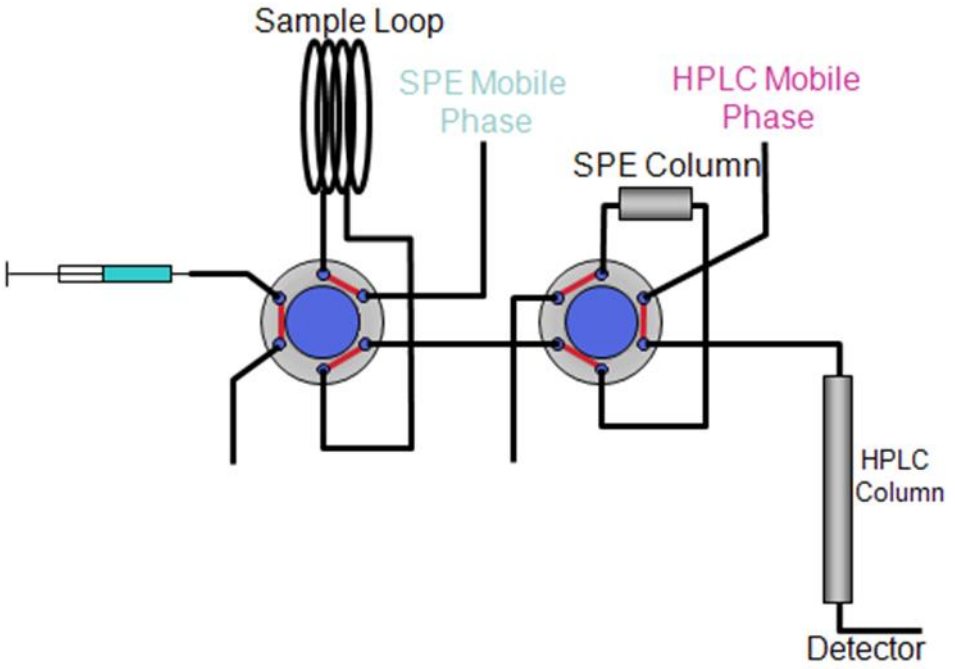

Figure 2: Schematic of in-line SPE and HPLC system. Valves are shown in SPE load position.

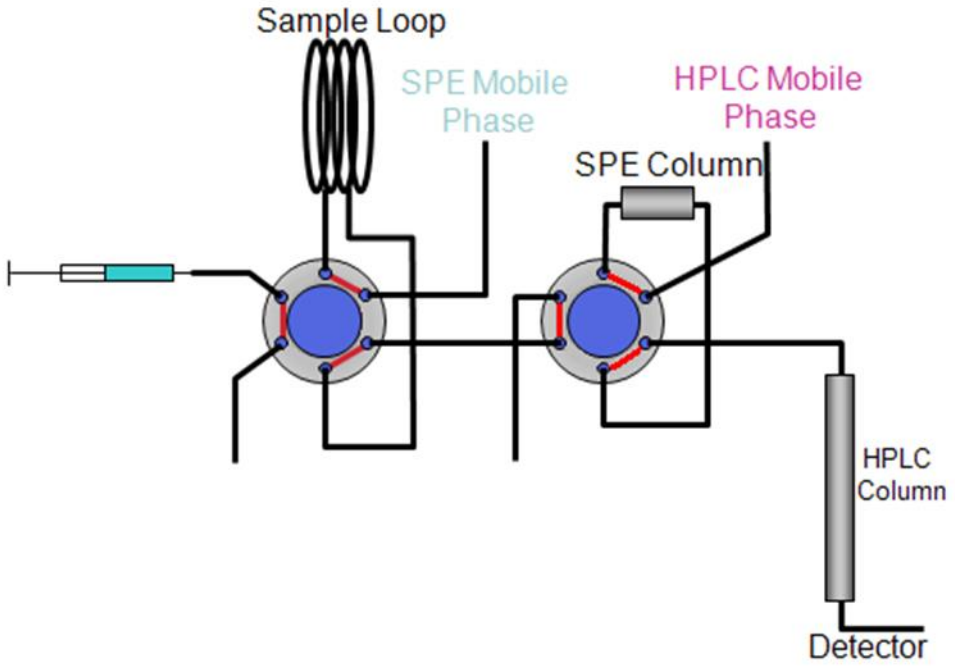

Figure 3: Schematic of in-line SPE and HPLC system. Valves are shown in SPE elution position.

Diprenorphine has a logP value of 2.57, so it is important to select the appropriate SPE and HPLC stationary phase which will retain [^{11}C]diprenorphine as well as the less lipophilic radio-metabolites such as [^{11}C]diprenorphine-3-glucuronide (logP value of 0.69). The metabolism of diprenorphine has been studied previously with different radiolabelled analogues of the molecule (Figure 4). Diprenorphine has been labelled with ^{11}C at the C17 position of the molecule[11] (*N*-[^{11}C]diprenorphine), however it has been suggested that diprenorphine is rapidly metabolised via N-dealkylation[12] resulting in the loss of the radiolabelled moiety. More recently an automated synthesis of an ^{18}F fluorinated analogue, 6-*O*-[2-[^{18}F]fluoroethyl)-6-*O*-desmethyldiprenorphine ([^{18}F]diprenorphine), was described[13]. [^{18}F]diprenorphine was shown to have similarities in the pharmacokinetics and receptor binding properties to [6-*O*-methyl-^{11}C]diprenorphine. However [^{18}F]diprenorphine showed lower brain uptake and rapid metabolism, with the radio-metabolites accounting for 20% of the radioactive signal in mouse brain 30 minutes after administration of the tracer[13]. The position of the ^{11}C radiolabel at the C6 position means that it is less susceptible to metabolism and the molecule is less rapidly metabolised compared to [^{18}F]diprenorphine[13].

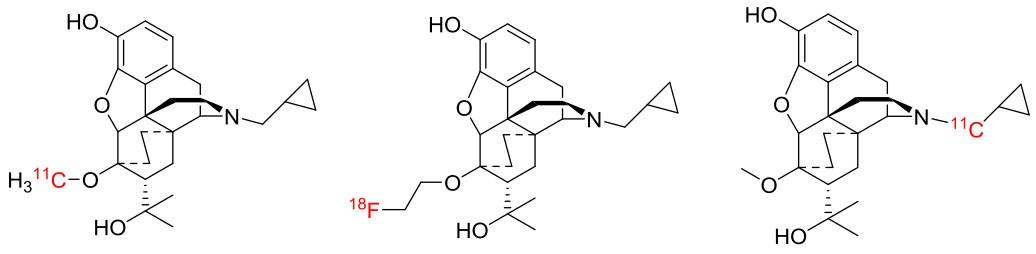

Figure 4: Radiolabelled analogues of diprenorphine.

Predicting radiotracer stability and metabolism *in vivo* can be challenging, however experiments using pooled human liver microsomes to 'digest' the radiotracer can be used to give an insight into what metabolites of the radiotracer might be expected *in vivo.* Bio-transformations are evoked by exposing [^{11}C]diprenorphine to pooled human liver microsomes, a source of the cytochrome P450 enzyme, and uridine glucuronosyl transferase (UGT) enzymes, both of which are important enzymes involved in the expulsion of foreign chemicals/drugs in the body. In addition computational programs can be used to predict the most likely chemical transformations that occur on a molecule during phase 1 or phase 2 metabolism. These predictions are made using specialised computer software such as with Meteor Nexus metabolite prediction software.

A method to accurately and reproducibly measure [^{11}C]diprenorphine metabolites using in line SPE and HPLC analysis has been developed. The metabolites of [^{11}C]diprenorphine from clinical scans have been compared with *in silico* predictions, as well as simulated metabolism of [^{11}C]diprenorphine using pooled human liver microsomes. The major radio-metabolite of [^{11}C]diprenorphine has also been identified by matrix-assisted laser desorption/ionisation mass spectroscopy (MALDI-MS) as [^{11}C]diprenorphine-3-glucuronide.

Materials and Equipment

Diprenorphine standards were purchased from Tocris Bioscience (Oxfordshire, U.K). Pooled human liver microsomes, Bovine serum albumin, UGT reaction solution A and UGT reaction solution B were all purchased from BD Biosciences (U.S). Sodium dihydrogen phosphate buffer, HPLC grade methanol and sodium hydroxide were purchased from Sigma Aldrich Company LTD (Dorset,

U.K). 0.45 µm PTFE syringe filters were purchased from Pall Life Sciences (Portsmouth, UK).

HPLC analysis was performed on a Shimadzu Prominence HPLC system running Laura 3 software from LabLogic (South Yorkshire, UK) and LC solutions from Shimadzu LTD, UK. The HPLC system was run with a CBM-20A controller, a LC-20AB solvent delivery system, an SPD-20A absorbance detector and SIL-20A auto sampler. A dual BGO coincidence detection and a flow-count radio HPLC detection system were both purchased from Bioscan (Washington DC, US). An ACE 5 C18 HL HPLC column was used and purchased from Hichrom (Berkshire, UK).

A PK121R centrifuge was purchased from Thermo Fisher Scientific LTD (Massachusetts, US) and a 1470 Automatic Gamma Counter (AGC) was purchased from PerkinElmer (Massachusetts, US).

Shim-Pack MAYI-C4 SPE cartridges were purchased from Shimadzu LTD, UK, Isolute PH SPE packing material was purchased from Biotage (Cardiff, UK) and C18 SPE packing material was purchased from Waters LTD (Hertfordshire, UK). Empty SPE column assemblies and fitting were purchased from Phenomenex (Macclesfield, UK).

Methods

[6-*O*-methyl-^{11}C]Diprenorphine production

[^{11}C]diprenorphine was synthesised according to a previously reported method[10] with some adaptations made to the radiochemistry and automated on a GE TRACERlab FX_{FE} radiochemistry system[14]. The product was formulated for human administration and produced in line with good manufacturing practice (GMP) guidelines.

[6-*O*-methyl-^{11}C]Diprenorphine metabolite analysis for PET scans.

[^{11}C]diprenorphine metabolites were analysed in discrete blood samples by way of in-line SPE followed by HPLC analysis. Discrete blood samples were spun down in a centrifuge at 4000 g for 2 minutes at 20 ˚C. Following this, 2 mL of the plasma layer was extracted and added to 3 mL of sodium dihydrogen phosphate buffer (NaH_2PO_4, 5 mM) which was pre-spiked with stable diprenorphine (15 µL of 1 mg/ml solution). The sample was then loaded onto a 5 mL stainless steel loop and

transferred in NaH_2PO_4 (5 mM) at a flow rate of 1 mL/min over a period of 5 minutes onto a pre-packed stainless steel SPE column (3 x 0.48 cm) containing a C18 bulk packing material. It should be noted that SPE columns packed with other stationary phases were used for different experiments. The SPE column was then washed for a further 3.5 minutes with NaH_2PO_4 at 1 mL/min. The liquid from the SPE load and SPE washing steps containing plasma proteins and the most polar metabolites was collected in a pre-weighed vial containing sodium hydroxide (NaOH, 50 µL). 5 mL aliquots of the SPE breakthrough were then taken, weighed and counted in a well counter. The SPE column was then eluted in the reverse direction onto an ACE-5 C18 HL HPLC column with methanol : NaH_2PO_4 (60 : 40) with the methanol : NaH_2PO_4 changing to 80 : 20 over the first 2.5 minutes, HPLC eluent was monitored for UV absorbance at 254 nm. The HPLC eluent was collected into fractions (1.6 mL and 2.4 mL) which were counted in a 10 well automatic gamma counter (AGC) in which one position was left clear for background corrections. For this study each subject underwent 2 PET scanning sessions conducted on separate days.

In order to assess the suitability of the SPE column being used, hot recoveries of the whole system were performed. This was done by making an injection onto the system which consisted of plasma (2 mL), NaH_2PO_4 (5 mM, 3.2 mL), a spike of stable diprenorphine and [^{11}C]diprenorphine. A 50 µL aliquot of the injection sample was taken and added to 1 mL of water which was weighed and then counted in the well counter. The recovery sample was then injected on to the whole system (SPE and HPLC) and was processed as described above. As well as collecting the SPE breakthrough, the SPE washes were also collected when performing recovery checks. In each case 5 mL aliquots of both SPE breakthrough and SPE washes were taken, weighed and counted in the well counter. Similar to above, the HPLC eluent was collected into fractions (1.6 mL and 2.4 mL) which were counted in a 10 well AGC with one position was left clear for background corrections. Measurement from the AGC and the well counter were processed and recoveries were calculated by comparing the radioactivity in the injection to the decay corrected activities in the SPE breakthrough aliquots, SPE wash aliquots and AGC fractions.

Production of [6-*O*-methyl-^{11}C]diprenorphine metabolites by means of digest, using pooled human liver microsomes

[^{11}C]diprenorphine metabolites were generated by performing a digest using pooled human liver microsomes. To a centrifuge tube containing pooled human liver microsomes (25 µL, approximately 0.5 mg) UGT reaction mixture solution A (200 µL, containing 25 mM UDPGA) and UGT reaction mixture solution B (82 µL, containing 5X-UGT assay buffer with alamethicin) was added. [^{11}C]diprenorphine and stable diprenorphine (10 µL of 1 mg/mL) were added to the assay before water (175 µL) and bovine serum albium (175 µL) were added. The digestion was then incubated in a water bath (37 ˚C) for 45 minutes to 1 hour after which the digestion was terminated with the addition of acetonitrile (500 µL). The reaction mixture was then spun at 16,060 g for 5 minutes at 4 ˚C in after which the reaction mixture was separated from the microsome pellets. Next the reaction mixture was filtered through an Acrodisc CR 4 mm syringe filter with a 0.45 µM PTFE membrane before being analysed via in-line SPE and HPLC.

Results

In Silico Analysis of [6-*O*-methyl-^{11}C]diprenorphine metabolites

A computational analysis of the metabolism of [^{11}C]diprenorphine was performed using Meteor Nexus software (from Lhasa LTD, Leeds, UK). Meteor Nexus is a knowledge-based computational software used to predict molecular metabolism. The software predicted that diprenorphine would undergo oxidative N-dealkytion via the family of CYP450 enzymes as part of phase 1 metabolism. The Nexus software also predicted oxidative O-alkylation of diprenorphine, again by means of the enzyme family CYP450 and as part of phase 1 metabolism. Another predicted metabolite of diprenorphine was formed from the glucuronidation of the aromatic alcohol via a uridine 5'-diphospho-glucuronosyltransferase (UGT) enzyme as a result of phase 2 metabolism to diprenorphine-3-glucuronide. The metabolites predicted by Meteor are depicted in Figure 5.

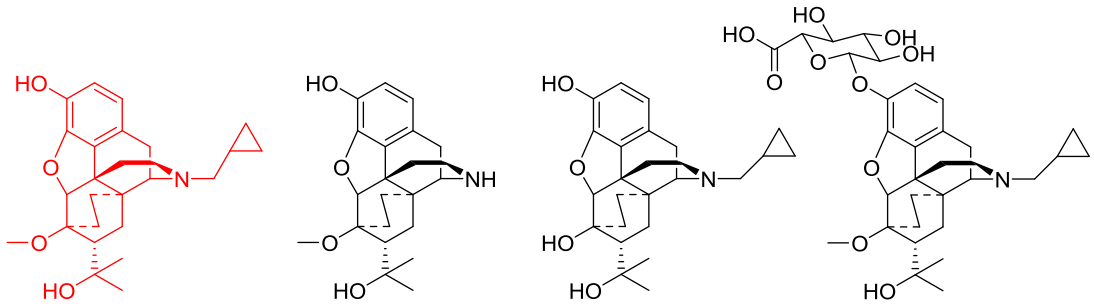

Formula: $C_{26}H_{35}NO_4$
Molecular Weight: 425.57
Log P: 2.57
CLogP: 2.6621

Formula: $C_{22}H_{29}NO_4$
Molecular Weight: 371.48
Log P: 1.47
CLogP: 1.4131

Formula: $C_{25}H_{33}NO_4$
Molecular Weight: 411.54
Log P: 2.21
CLogP: 1.8687

Formula: $C_{32}H_{43}NO_{10}$
Molecular Weight: 601.69
Log P: 0.69
CLogP: -1.5934

Figure 5: Metabolites of diprenorphine (including LogP values) predicted by Meteor Nexus. From l-r, diprenorphine (parent), product of oxidative N-dealkylation (phase 1 metabolism), product of oxidative O-dealkylation (phase 1 metabolism) and diprenorphine-3-glucuronide (via phase 2 metabolism).

SPE column loading and elution

A stainless SPE column (3 x 0.48 cm) was packed with C18 stationary phase and the loading and elution experiments were performed by placing the SPE column between dual BGO coincidence detectors. The purpose of this experiment was to assess the ability of the SPE material to trap [^{11}C]diprenorphine, to retain [^{11}C]diprenorphine during washing of the SPE and to elute [^{11}C]diprenorphine efficiently. During the SPE washing stage the observed radioactivity signal should plateau and level off. This is then followed by the elution of the [^{11}C]diprenorphine from the SPE. During this phase the radioactivity signal should be observed dropping to an area around the background levels as [^{11}C]diprenorphine leaves the SPE and is no longer detected by the BGO. An injection of [^{11}C]diprenorphine in plasma was loaded onto the SPE column as described above and the data was processed on the Laura 3 software. A typical radioactivity trace can be seen in Figure 6 showing the SPE loading washing and elution steps.

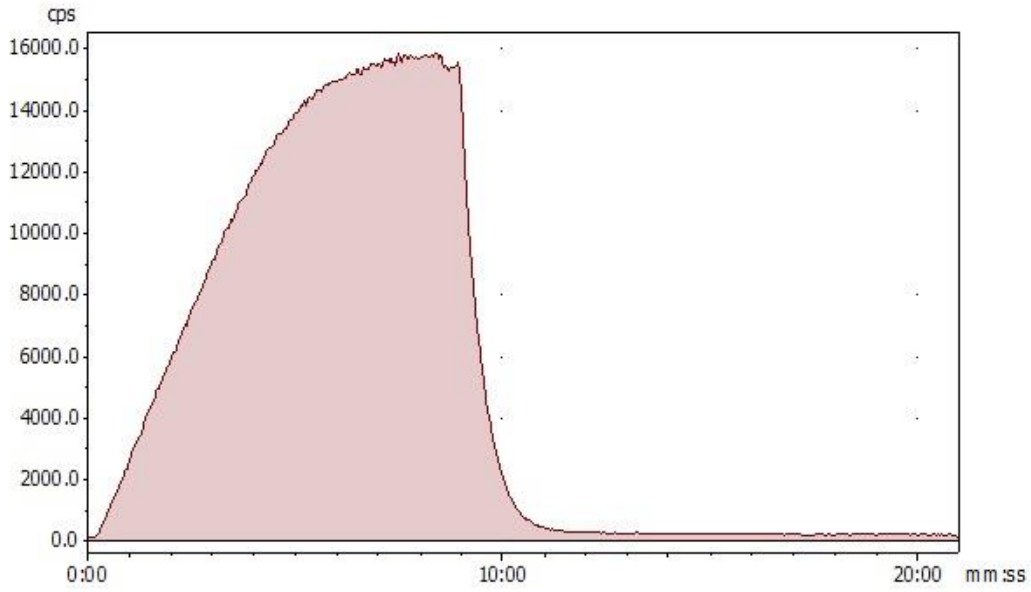

Figure 6: Radioactivity trace of C18 SPE column (300 x 48 mm) placed between dual BGO detectors during [^{11}C]diprenorphine loading, washing and elution.

[6-*O*-methyl-^{11}C]Diprenorphine metabolite analysis for PET

Arterial blood samples were taken from patients at 5 minutes, 10 minutes, 20 minutes, 30 minutes, 40 minutes and 60 minutes post [^{11}C]diprenorphine injection. The blood samples were processed as detailed in the methods section and analysed by in-line C18 SPE and HPLC analysis. Figure 7 shows the profile of [^{11}C]diprenorphine, the major metabolite [^{11}C]diprenorphine-3-glucuronide and of the SPE breakthrough at various time points post injection. The data shows pooled averages for each time point for 55 [^{11}C]diprenorphine PET scans.

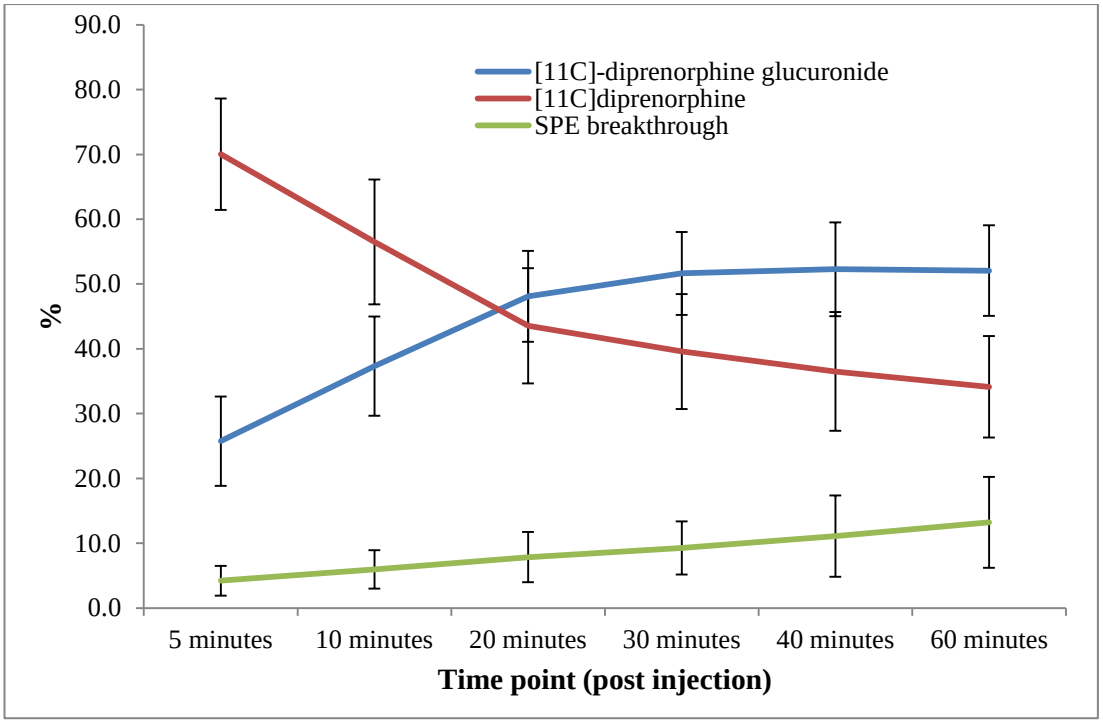

Figure 7: Metabolite profiles of [^{11}C]diprenorphine, [^{11}C]diprenorphine-3-glucuronide and SPE breakthrough. Data is based on pooled averages from 55 scans.

Recoveries of various SPE stationary phases

Various SPE stationary phases were investigated to determine which phase would be optimal for trapping and eluting both parent and metabolite molecules with minimal loss. Three stationary phases were considered, a C4 phase (Shim-Pack MAYI-C4), a C18 phase and a phenyl stationary phase. The C18 and the phenyl stationary phases were packed into stainless steel column assemblies, whilst the MAYI C4 material was pre-packed. Recoveries on the whole system (SPE and HPLC) were performed as described in the methods section, the results are summarised in Table 1.

SPE packing material	Average [^{11}C]diprenorphine recovery (%)	Average SPE breakthrough (%)	n =
Phenyl (Isolute Ph)	76.2 ± 7.4	0.6 ± 0.3	8
C4 (Shimadzu MAYI)	98.7 ± 2.9	3.9 ± 2.6	6
C18 (Waters)	93.9 ± 4.5	1.4 ± 0.5	86

Table 1: [^{11}C]diprenorphine recoveries for different SPE column stationary phases.

Discussion

In Silico Analysis of [6-*O*-methyl-^{11}C]diprenorphine metabolites

The chemical structures of the metabolites of diprenorphine which were predicted by Meteor Nexus metabolite prediction software can be seen along with their logP values in Figure 5. It is clear to see that the logP values for the metabolites are all lower than the logP of the parent diprenorphine molecule (2.57). We would expect that the metabolites of diprenorphine would elute before the parent on a C18 phase HPLC column and this is what we do observe. The computer software predicts the loss of the cyclopropyl moiety from the molecule which has long been suspected as a major metabolite of diprenorphine[12]. The software also predicted a loss of a methyl group form from the 6-hydroxy position of diprenorphine. If this was to happen with [^{11}C]diprenorphine we would lose the ^{11}C radiolabel. The final predicted structure is glucuronidation of diprenorphine at the 3-hydroxy position to produce [^{11}C]diprenorphine-3-glucuronide. We would anticipate that glucuronidation would occur at this position as it is the more acidic and reactive hydroxyl group.

[^{11}C]diprenorphine metabolites were generated using a digestion method with hepatic microsomes and isolated as described in the methods and the sample was analysed by MALDI-MS. The analyte (0.5 µL) was spotted onto a plate along with a matrix of α-cyano-4-hydroxycinnamic acid (CHCA), in 1:1:0.05 (water:acetonitrile:trifluoroaceticacid). The results showed 3 peaks of note, the major peak in the analysis at m/z 426 represents [diprenorphine+H]$^+$ and the peak at m/z 849 is the diprenorphine dimer. The peak at m/z 602 is diprenorphine glucuronide, thought to be the major metabolite.

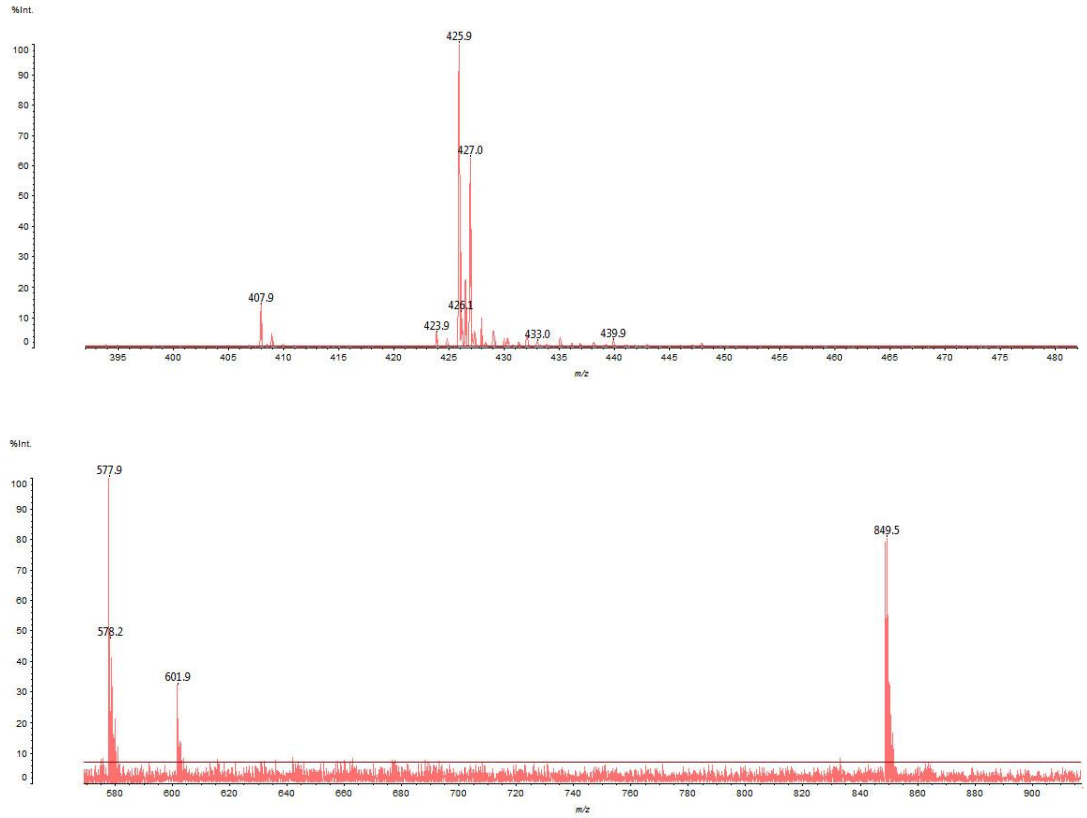

Figure 8: MALDI MS spectrum of diprenorphine digest showing peaks for parent diprenorphine (m/z 426), diprenorphine dimer (m/z 849) and diprenorphine glucuronide (m/z 602).

We have also shown good agreement between the predicted *in silico* metabolism of diprenorphine and the in vivo metabolism of [^{11}C]diprenorphine produced by hepatic microsome digestion. The Meteor software predicted the formation of diprenorphine-3-glucuronide via phase 2 metabolism and the UGT enzyme. We confirmed this was the case by performing a digestion of [^{11}C]diprenorphine with hepatic microsomes and confirmed the formation of [^{11}C]diprenorphine-3-glucuronide by MALDI-MS analysis. By identifying the major metabolite of [^{11}C]diprenorphine we can start to answer important questions such as will [^{11}C]diprenorphine-3-glucuronide cross the blood brain barrier, and if it does will it compete with [^{11}C]diprenorphine for available opioid receptor sites? The logP of [^{11}C]diprenorphine-3-glucuronide (0.69) suggests that it would find it difficult to traverse the blood brain barrier. The pharmacology of [^{11}C]diprenorphine-3-glucuronide is unclear, however we can compare how other glucuronides of opiates act on opioid receptors. For example morphine-3-glucuronide has been shown to have a low affinity at μ-receptors[15] whereas buprenorphine-3-glucuronide was

reported to have some biological activity which could contribute to the total pharmacology of buprenorphine[16]. More work needs to be completed to analyse the blood brain barrier permeability and affinity diprenorphine-3-glucuronide may have on opioid receptors.

SPE column loading and elution

Figure 6 shows a decay corrected radioactivity trace from a C18 SPE column placed between a dual BGO coincidence detector setup to observe the SPE loading and elution. [^{11}C]diprenorphine is seen to be loading onto the C18 SPE for the first 5 minutes after injection onto the system. Following this, there is a plateau showing that [^{11}C]diprenorphine is being held on the SPE column and is not moving through the SPE. At 8.5 minutes the 2 position 6-way valves switch to allow the HPLC eluent to flow through the C18 SPE column in the reverse direction eluting the [^{11}C]diprenorphine from the C18 SPE. This can be seen as the activity on the gamma trace drops down to background levels. The drop is rapid which depicts elution of [^{11}C]diprenorphine from the SPE.

[6-*O*-methyl-^{11}C]Diprenorphine metabolite analysis for PET

Figure 7 shows the profile of [^{11}C]diprenorphine, the major metabolite [^{11}C]diprenorphine-3-glucuronide and of the SPE breakthrough at various time points post [^{11}C]diprenorphine injection. From Figure 7 we can see that the percentage of [^{11}C]diprenorphine at 5 minutes post injection is around 70 % and [^{11}C]diprenorphine-3-glucuronide accounts for 25 % of the radioactivity at this time point. As we would expect, the percentage of [^{11}C]diprenorphine falls at later time-point finally reaching 34 % at 60 minutes and the percentage of [^{11}C]diprenorphine-3-glucuronide increases until a plateau of 52 % is reached at 30 minutes. The amount of [^{11}C]diprenorphine-3-glucuronide at 60 minutes post injection remains at 52 % The SPE breakthrough accounts for 4 % of the activity at 5 minutes post injection which increases to 13 % at 60 minutes. This fraction contains the most polar metabolites which are not retained by the SPE and are less likely to cross the blood brain barrier.

Recoveries of various SPE stationary phases

Table 1 shows [^{11}C]diprenorphine recovery measurements for the SPE stationary phases tested. We began by investigating the C4 (MAYI) pre-packed SPE

column which is designed for biological sample pre-treatment. The MAYI SPE cartridges have a packing material in which the interior of the pore is modified with C4 groups and the outer silica surface is coated with a hydrophilic polymer. Plasma proteins should be unable to access the pore and do not adhere to the polymer coating making them easy to elute whilst low molecular weight molecules (such as diprenorphine) will enter the pores and be retained by the inner pore surface. From the results in Table 1 we can see that on average we received good [^{11}C]diprenorphine recoveries at 98.7 % (n = 6). However we found that a significant amount of the parent was breaking through the C4 SPE column (3.9 % ± 2.6 %). We decided to investigate other SPE stationary phases and so moved our attention to the phenyl reverse phase packed in-house, into stainless steel SPE column assemblies a set-up which has been used previously for [^{11}C]diprenorphine PET studies. A low average percentage of [^{11}C]diprenorphine recovery was observed with this phenyl stationary phase (76.2 % ± 6.8%, n = 8). Interestingly this SPE stationary phase has been used previously for a [^{11}C]diprenorphine PET study where it was reported that > 98 % of total plasma activity was retained by the SPE[6]. However when the phenyl stationary phase was used it was discovered that the recoveries were low for a similar in line SPE HPLC set-up. The stationary phenyl phase should be more retentive of the lipophilic diprenorphine molecule compared to the C4 phase however this was not the case. The phenyl reverse phase did have a lower average percentage of SPE breakthrough with 0.6 % ± 0.3 % compared to the 3.9 % ± 2.6 % for the C4 phase. Finally we studied the properties of a C18 stationary phase again packed in-house. The C18 stationary phase showed good recoveries with an average of 93.9 % ± 4.5 % (n = 86) of the radioactivity recovered and only 1.4 % ± 0.5 % of radioactivity breaking through the SPE (it should be noted that this is for a much larger data set of n = 86 compared to the other SPE stationary phases). If we compare the percentage of SPE breakthrough in plasma for the C18 SPE column with the MAYI C4 SPE column we can see that much more of the radioactivity is retained by the C18 phase compared to the C4 phase which may suggest that the parent ([^{11}C]diprenorphine) could be breaking through the C4 cartridge. This is reinforced by the fact that C4 phase is less retentive than C18 stationary phase of lipophilic molecules. Diprenorphine with a logP value of 2.57 is not retained as well on the C4 material as it is on the C18 material.

Once it was clear that [11C]diprenorphine was well retained by the C18 stationary phase the effect of altering the length of the C18 SPE column was observed. The SPE column length was decreased from 500 mm to 300 mm. The shorter column was shown to be the optimal size for efficient loading and elution of [^{11}C]diprenorphine (as seen in Figure 6). Also a major benefit of the shorter SPE was the time which was saved in cleaning the SPE cartridge between injections which is an important factor given the time constraints of the short half-life of ^{11}C ($t_{½}$ = 20.38 mins).

Conclusion

A method is described to measure the metabolites of the PET radiotracer [^{11}C]diprenorphine via an in-line SPE method followed by HPLC analysis. After assessing various stationary phases of C4, phenyl and C18 we concluded that the C18 phase packed into a stainless column assembly (300 mm x 48 mm) were the best of the conditions investigated. This conclusion was made by investigating the loading, retention and subsequent elution of [^{11}C]diprenorphine from the SPE as well as performing experiments to measure the recovery of [^{11}C]diprenorphine.

With this method of [^{11}C]diprenorphine analysis, the metabolite profiles for the same subject over multiple [^{11}C]diprenorphine scans was consistent and as such it may be possible to apply a single set of metabolite data for a participant over multiple scans. As expected, we do still see differences in the metabolite profiles in different subjects. This shows the reliability and reproducibility of this method for [^{11}C]diprenorphine metabolite analysis, and we believe that our method should be the method of choice for [^{11}C]diprenorphine PET scanning.

References

[1] G. Henriksen, F. Willoch, P. S. Talbot, H.-J. Wester, *Drug Development Research* **2006**, *67*, 890.

[2] J. R. Lever, *Current Pharmaceutical Design* **2007**, *13*, 33.

[3] A. Hammers, M.-C. Asselin, R. Hinz, I. Kitchen, D. J. Brooks, J. S. Duncan, M. J. Koepp, *Brain* **2007**, *130*, 1009.

[4] F. Willoch, F. Schindler, H. J. Wester, M. Empl, A. Straube, M. Schwaiger, B. Conrad, T. R. Tölle, *Pain* **2004**, *108*, 213.

[5] R. F. Dannals, *Journal of Labelled Compounds and Radiopharmaceuticals* **2013**, *56*, 187.

[6] A. K. P. Jones, V. J. Cunningham, S.-K. Ha-Kawa, T. Fujiwara, Q. Liyii, S. K. Luthra, J. Ashburner, S. Osman, T. Jones, *Journal of Neuroscience Methods* **1994**, *51*, 123.

[7] D. D. Dougherty, J. Kong, M. Webb, A. A. Bonab, A. J. Fischman, R. L. Gollub, *Behavioural Brain Research* **2008**, *193*, 63.
[8] J. Maarrawi, R. Peyron, P. Mertens, N. Costes, M. Magnin, M. Sindou, B. Laurent, L. Garcia-Larrea, *Pain* **2007**, *127*, 183.
[9] J. J. Frost, H. S. Mayberg, B. Sadzot, R. F. Dannals, J. R. Lever, H. T. Ravert, A. A. Wilson, H. N. Wagner, Jr., J. M. Links, *Journal of Cerebral Blood Flow and Metabolism* **1990**, *10*, 484.
[10] S. K. Luthra, F. Brady, D. R. Turton, D. J. Brown, K. Dowsett, S. L. Waters, A. K. P. Jones, R. W. Matthews, J. C. Crowder, *Applied Radiation and Isotopes* **1994**, *45*, 857.
[11] S. K. Luthra, V. W. Pike, F. Brady, *Journal of the Chemical Society - Series Chemical Communications* **1985**, *NO. 20*, 1423.
[12] C.-Y. Shiue, L.-Q. Bai, R.-R. Teng, C. D. Arnett, S. L. Dewey, A. P. Wolf, D. W. McPherson, J. S. Fowler, J. Logan, M. J. Holland, E. J. Simon, *International Journal of Radiation Applications and Instrumentation. Part B. Nuclear Medicine and Biology* **1991**, *18*, 281.
[13] H.-J. Wester, F. Willoch, T. R. Tolle, F. Munz, M. Herz, I. Oye, J. Schadrack, M. Schwaiger, P. Bartenstein, *Journal of Nuclear Medicine* **2000**, *41*, 1279.
[14] M. Fairclough, C. Prenant, G. Brown, A. McMahon, J. Lowe, A. Jones, *Journal of Labelled Compounds and Radiopharmaceuticals* **2014**, *57*, 388.
[15] S. E. Bartlett, M. T. Smith, *Life Sciences* **1995**, *57*, 609.
[16] S. M. Brown, M. Holtzman, T. Kim, E. D. Kharasch, *Anesthesiology* **2011**, *115*, 1251.

Publication 3 (page 138)

CHAPTER 4: Striatal opioid receptor availability predicts acute and chronic pain perception in arthritis: evidence for opioid adaption to chronic pain.

Accepted for Publication in PAIN

Striatal opioid receptor availability predicts acute and chronic pain perception in arthritis: evidence for opioid adaption to chronic pain.

Abbreviated title: Opioid adaptation to chronic pain

Authors

Christopher A Brown [1], Julian Matthews [2], Michael Fairclough [2], Adam McMahon [2], Elizabeth Barnett [2], Ali Al-Kaysi [3], Wael El-Deredy [4], Anthony KP Jones [5]

[1] CamPain group, Department of Anaesthesia, University of Cambridge, Cambridge, United Kingdom, CB2 0QQ

[2] Wolfson Molecular Imaging Centre, University of Manchester, Manchester, United Kingdom, M20 3LJ

[3] Department of Anaesthesia, Southport and Ormskirk Hospitals, Southport, Merseyside, United Kingdom, PR8 6PN

[4] School of Psychological Sciences, University of Manchester, Manchester, United Kingdom, M13 9PL; School of Biomedical Engineering, University of Valparaiso, Chile

[5] Human Pain Research Group, Institute of Brain, Behaviour and Mental Health, University of Manchester, Salford, United Kingdom, M6 8HD

Abstract

The experience of pain in humans is modulated by endogenous and exogenous opioids. Better understanding of how the opioid system adapts to chronic pain may shed light on the sustainability of treatments that alter opioid physiology and pharmacology. We present evidence that chronic pain in arthritis causes adaptive up-regulation of opioid receptors (OpRs) in the striatum. Using Positron Emission

Tomography (PET) and the radiotracer ^{11}C-diprenorphine (a non-selective opioid receptor antagonist), patients with arthritis pain (n = 17) and healthy controls (n = 9) underwent whole-brain PET scanning to calculate parametric maps of opioid receptor availability. Within the arthritis group, greater opioid receptor availability was found in the striatum (including the caudate) of patients reporting greater levels of recent chronic pain. In both patients and healthy controls greater opioid receptor availability in the caudate (after correcting for levels of chronic pain) was associated with higher pain threshold, suggesting that greater striatal opioid receptor availability normally reduces the perception of nociceptive input. Conversely, patients with arthritis pain had overall less opioid receptor availability within the striatum, consistent with greater occupation of opioid receptor sites by endogenous opioids. Together with supporting evidence from animal studies, these findings are consistent with the view that chronic pain results in an adaptive upregulation of opioid receptor availability. This may provide an explanation for individual variability in resiliency to chronic pain and therapeutic response. Further clinical studies are required to establish the pharmacological basis for these effects and their implications for chronic pain therapy.

Acknowledgements

The authors declare no competing financial interests. The study was funded by a project grant from the Medical Research Council in the United Kingdom. We extend our gratitude to all staff at the Wolfson Molecular Imagine Centre who were essential for the success of this project, in particular: Professor Karl Herholz and Dr Peter Talbot who helped with the initial concept and design, and the radiographers, radiochemists and blood lab for helping to implement the study. We also wish to thank the consultant anaesthetists who aided in the collection of blood data, and especially to our research nurse Ann Lenton who was crucial for patient recruitment.

Introduction

Musculoskeletal pain is one of the most common reasons for primary care consultation and is most frequently reported by patients with arthritis[1]. However, there is no clear correlation between pain and structural joint damage in osteoarthritis[2] or between the technical success of the total joint replacement and pain relief[3]. The physiological basis of this variability in pain and treatment

outcomes is uncertain. One possibility is natural variability in pain control mechanisms in the central nervous system (CNS).

The ascending spinothalamic pathways that mediate pain terminate in multiple thalamic nuclei, with the main cortical targets being the posterior insula, medial parietal operculum (covering the insula) and mid-cingulate cortex[4]. However, conscious experiences of pain require further cortical activity in 'second-order' pain processing regions such as the anterior cingulate and anterior insulae that produce context-dependent responses to pain[4]. Together with prefrontal cortex, these pain processing regions project to the basal ganglia including the striatum, which also receives afferent nociceptive inputs from the spinal cord via the globus pallidus[5]. The striatum, including the caudate, putamen and nucleus accumbens, are the most densely populated regions for opioid receptors in the brain[6-8], and are thought to be important for opioid-mediated endogenous analgesia[9, 10], for example as part of the placebo analgesic effect[11].

The endogenous opioid system is poorly characterised in patients with arthritis. Positron Emission Tomography (PET) receptor binding studies enable assessment of the endogenous opioid system via radiotracers that bind to opioid receptors (OpRs), such as carbon-11 labelled diprenorphine ([^{11}C]-DPN), an antagonist that binds equally well to mu, delta and kappa OpRs[12, 13]. Experimental noxious stimulation in humans decreases the binding, and therefore availability, of opioid radiotracers in a number of pain modulatory brain regions, including the thalamus, striatum, anterior cingulate, insula and prefrontal cortices[14-16]. Reduced OpR availability in the human brain has been associated with rheumatoid arthritis[17], chronic neuropathic pain[18-22] and fibromyalgia[23], but the relationship of these findings to acute and chronic pain perception remains largely obscure.

Here we used PET with [^{11}C]-DPN to assess OpR availability patients with arthritis and healthy controls, to identify relationships between OpR availability and the level of perceived acute and chronic pain. Our analysis revealed associations between the striatum and the perception of both acute and chronic pain, which we discuss in terms of adaptive upregulation of OpR binding sites in chronic pain states.

Materials and Methods

The research study was approved by Stockport NHS Research Ethics Committee (reference 09/H1012/44) and permission granted by ARSAC (radiation protection agency).

Participants

17 patients (12 females) and nine healthy control participants (3 females) were recruited into the study. All participants gave written informed consent. The characteristics of the participants are shown in Table 1. Patients were recruited from primary and secondary care in Greater Manchester, while healthy control participants were recruited from an existing database of research volunteers, and from primary care in Greater Manchester. 15 participants had a diagnosis of Osteoarthritis (OA) while 2 had a diagnosis of Rheumatoid Arthritis (RA). All patients had experienced chronic pain for at least the past three months. OA and RA patients fulfilled the American College of Rheumatology (ACR) criteria for the diagnosis of OA[24] and RA[25]. No control participants were experiencing any chronic pain or other recurrent health problems. Exclusion criteria for both groups included age of <35 years, and medical records showing a history of neurological disorder, morbid psychiatric disorder (including major depression and anxiety-related disorders confirmed by a psychiatrist), organ failure or cardiovascular disease. It was expected that patients would be recruited with sub-clinical levels of anxiety and depression that are normal for chronic pain populations.

Any patients taking opioid analgesic medication, of which there were two, were asked to withdraw prior to scanning. The timing of this withdrawal was determined on a case-by-case basis, but was started no more than 2 weeks prior, and completed not later than 2 days prior, to each scanning session. Any paracetamol or NSAIDs were withdrawn at least 24 hrs prior to scanning.

MRI data acquisition and pre-processing

A T_1-weighted MRI brain scan was acquired for the purpose of excluding structural abnormality, co-registration and spatial normalization of PET images. Scanning was performed on a Philips Achieva 1.5 Tesla scanner at the Wolfson Molecular Imaging Centre using a 3-D magnetization prepared rapid gradient echo sequence (MPRAGE;

TR 8.6 ms, TE 4.0 ms, FOV 240 mm^2, Matrix 256 × 256, reconstructed voxel size 0.94 × 0.94 × 1.2, 170 slices) and clinically reported before each subject's PET scan.

MRIs were segmented into white matter, grey matter and cerebrospinal fluid using Statistical Parametric Mapping (SPM8, Wellcome Department of Imaging Neuroscience, Institute of Neurology, UCL, London, UK) running on Matlab version 7.10 (The Mathworks Inc., Natick, MA, USA).

Questionnaire assessments

Patients (but not healthy controls) completed an assessment of clinical pain as experienced over the last week, prior to PET scanning. Clinical pain was measured using the short-form McGill Pain Questionnaire (MPQ)[26], which has subscales for sensory and affective pain.

Positron Emission Tomography (PET) scans

A cannula was inserted into a radial artery of the non-dominant forearm after a satisfactory modified Allen's test and local anaesthesia, for sampling of arterial blood during the scan. An intra-venous cannula was inserted into the dominant forearm for radiotracer injection.

Patients were scanned using a Siemens/CTI High Resolution Research Tomograph (HRRT; CTI/Siemens Molecular Imaging, TN, USA [27]) PET scanner at the Wolfson Molecular Imaging Centre, capable of 2.5 mm resolution. This is a dedicated brain PET scanner comprising eight flat panel detectors, with transaxial and axial FOVs of 31.2 and 25.2 cm, respectively. Depth-of-interaction information was provided by a dual-layer scintillator phoswich detector (10 mm LSO, 10 mm LYSO). Point source resolution varied across the field of view from approximately 2.3 to 3.2 mm (full-width-at-half-maximum; FWHM) in the transaxial direction and from 2.5 to 3.4 mm in the axial direction.

Participants were positioned supine with their transaxial planes parallel to the line intersecting anterior and posterior commissure (AC–PC line). Head position was measured and equated as best as possible in both PET sessions. Head movement during scanning was discouraged by applying gentle pressure to the nasion via a padded attachment to the head holder. Patients wore a customized neoprene cap with a reflective tool attached to the vertex that was used to continuously assess head motion using a Polaris Vicra infrared motion detector (Northern Digital, Ontario,

Canada). Prior to further scanning, a 6 min transmission scan was performed for attenuation correction, facilitated by a ^{137}Cs transmission point source[28].

Regional cerebral blood flow (rCBF) was measured to allow for assessment of the relationship of [^{11}C]-DPN binding results to rCBF. Following the transmission scan and immediately prior to the [^{11}C]-DPN scan, 510 MBq to 645 MBq (target dose: 600MBq) of ^{15}O-labelled water ($H_2{}^{15}O$) was administered, with the dynamic PET data collected into 26 frames (variable background frame, 10x5s, 6x10s, 3x20s, 6x30s). The injections were administered using an automatic radio water generator (HIDEX Inc., Turku, Finland) with the injection sequence consisting of a 15 second flush of cold saline, a 15 second injection of saline containing the $H_2{}^{15}O$, and a 75 second flush of cold saline to ensure all the activity is administered. The rate of injection was 5 mL min^{-1} with 17.5 mL of saline administered in total. Commencing 1 min prior to injection and continuing until 6 min post injection, arterial blood was continuously withdrawn at a rate of 5 mL min^{-1} with continuous radioactivity measurements made using a bespoke Bismuth Germanate (BGO) detector[29]. In addition, three discrete 1 ml blood samples were taken at 4, 5 and 6 min after injection with the radioactivity concentration measured using a bespoke calibrated NaI well counter and which was subsequently used to calibrate the continuous blood data.

This was followed by an i.v. smooth bolus subpharmacological tracer dose of [^{11}C]-DPN injected over 20 s, followed by a 20 s saline flush. [^{11}C]-DPN was initially synthesized in situ at the Wolfson Molecular Imaging Centre using the methylation method[30]. Characteristics of [^{11}C]-DPN doses are shown in table 2. A 90-minute continuous acquisition in list mode followed injection. The emission data were rebinned into 32 frames of increasing duration (variable length background frame, 3×10s, 7×30s, 12×120s, 6×300s, 3×600s). Randoms correction was performed using smoothed delayed coincidences[31]. Scatter correction was calculated via simulation[32]. Both corrections were applied within the image reconstruction procedure using an ordinary Poisson algorithm.

As with the $H_2{}^{15}O$ scan, continuous measurements of the radioactivity in arterial blood were conducted from one minute prior to injection until 10 minutes after injection with blood withdrawn at a rate of 5 mL min^{-1}. Further intermittent discrete arterial blood sampling took place for cross-calibration and to determine the partition

of blood radioactivity between plasma and whole blood (erythrocytes) at 5, 7.5, 10, 15, 20, 30, 40, 50, 60, 75 and 90 mins, using a NaI calibrated well counter. The samples at 5, 7.5 and 10 min were taken from a 3-way tap immediate post the BGO detector whilst the remaining samples were taken through a short extension line attached to the cannula and immediately following the withdrawal and discard of 2 mL of blood. Separate samples were taken to determine the concentration of unmetabolised [^{11}C]-DPN, following the HPLC method described previously[18, 30], with samples withdrawn at 5, 10, 20, 30, 40, 60, and 75 mins.

Derivation of arterial input function

The input function of parent [^{11}C]-DPN in arterial blood plasma was derived as follows. To obtain the time-course of whole blood radioactivity over time, the continuous blood data from the first 10 min of the [^{11}C]-DPN scan was firstly calibrated against radioactivity measured in discrete blood samples (via a well counter) at corresponding time points. This initial time-course was then spliced with an interpolation of the discrete blood radioactivity data over the remainder of the scan to obtain the full time-course. From the discrete blood samples, the plasma-over-blood ratio was calculated and linearly fitted. Using the radio-HPLC data, the percentage of radioactivity attributed to the parent radiotracer in plasma was fitted as an exponential function in which time zero was restricted to unity. Input functions were then derived by multiplying (a) the time course of radioactivity in whole blood, (b) the linear function describing the plasma-over-blood ratio over time, and (c) the exponential function describing the parent fraction in plasma over time.

[^{11}C]-DPN and $H_2{}^{15}O$ PET image reconstruction

PET images were reconstructed to a 256 × 256 × 207 matrix (isotropic voxel size of 1.21875 mm^3) using an iterative Ordinary Poisson Ordered Subset Expectation Maximization algorithm (OP-OSEM; 12 iterations). The reconstruction was performed using the HRRT user community software with the default resolution kernel[33]. Following reconstruction, the dynamic images were trimmed, calibrated and stored as Analyze 7.5 formatted images. The calibration factor was determined using a uniform head-sized phantom which is scanned periodically (~every 2 weeks).

Derivation of ^{11}C-DPN Volume of Distribution (VD_{DPN}) and $K1_{DPN}$

Parametric images of the [^{11}C]-DPN volume-of-distribution (VD_{DPN}) and the [^{11}C]-DPN rate of uptake from blood to tissue ($K1_{DPN}$) were calculated using spectral analysis[34] and implemented using the non-negative least squared algorithm (conventional spectral analysis[35]). Inputs to this analysis were the dynamic PET images and the arterial input function, both uncorrected for decay of ^{11}C. The fast frequency boundary was set to 0.02 s−1 and the slow frequency boundary to 0.0008 s−1. The slow frequency boundary was informed by two considerations: (a) the slowest possible kinetics of [^{11}C]-DPN, which is limited by the physical decay constant of the isotope (0.0005663 s−1), deriving from the half-life of ^{11}C (20.4 min), (b) data evaluating the image quality, reproducibility and reliability of [^{11}C]-DPN VD images across a range of slow frequency boundaries, which identified 0.0008 s−1 as being superior to lower cut-offs that were closer to the decay constant of ^{11}C[36]. The spectra were spaced logarithmically and the magnitude normalised so that the weighted columns summed to unity. Individual data points were weighted according to the reciprocal of the variance, as estimated from the frame duration over the total image concentration. A delay, which was fixed over the entire image volume, was estimate by fitting the same spectral analysis model to a TAC from a ROI over the entire image volume and varying the delay using a golden line search algorithm to determine the delay that minimised the weighted least squared error.

Derivation of regional cerebral blood flow (rCBF)

Parametric images of the $H_2{}^{15}O$ kinetic parameter $K1_{H2O}$ (ml min-1 ml-1), a measure of rCBF, were obtained using a one-tissue compartment model in which $K1_{H2O}$ is the rate of uptake of $H_2{}^{15}O$ from blood to brain. An input function of total radioactivity in whole blood was used that was calculated by scaling the continuous blood data, as with the [^{11}C]-DPN blood data. Reconstructed $H_2{}^{15}O$ PET images were initially smoothed with a 4mm FWHM Gaussian kernel prior to kinetic modeling using the Generalized Linear Least Squares (GLLS) algorithm.

VDDPN, K1DPN and K1H2O image pre-processing

Pre-processing of parametric images was performed using SPM8 (Statistical Parametric Mapping, Wellcome Department of Cognitive Neurology, London, UK). Each PET image were co-registered onto the corresponding T1-weighted MRI image using rigid-body transformation derived from the normalized mutual information

measure of image matching[37]. Next, MRI images were spatially normalised into the International Consortium for Brain Mapping (ICBM) standardized space (Montreal Neurological Institute, Montreal, Canada) using nonlinear basis functions, with the same transformation characteristics then applied to the co-registered parametric PET images.

Calculation of global $K1_{DPN}$

Kinetic modelling of [^{11}C]-DPN using spectral analysis is based on a compartmental model in which delivery of the radiotracer (represented by the parameter $K1_{DPN}$) to brain tissues is modelled separately to specific binding (represented by VD_{DPN}) and non-specific binding (to other cellular molecules). However, $K1_{DPN}$ would be expected to change along with blood flow as a result of differences in pain state. In particular, delivery effects may act as a confounder of the positive relationship between chronic pain perception and radiotracer binding: it would be expected that chronic pain would increase blood flow to the brain and increase the concentration of radiotracer in regions of interest. We controlled for radiotracer delivery effects within the statistical analysis by removing any variance in VD_{DPN} that could be accounted for by global $K1_{DPN}$ (the parameter estimating radiotracer delivery). While a reliance on global values of $K1_{DPN}$ might not be ideal we determined that *regional* $K1_{DPN}$ did not correlate with regional VD_{DPN} as a result. The weighted average of $K1_{DPN}$ values in grey matter across the whole brain were therefore calculated for each scan. $K1_{DPN}$ values in grey matter were initially identified using a grey matter mask on $K1_{DPN}$ images.

Analysis of head motion data

Head motion is a nuisance variable that could potentially cause unwanted between-subject and/or between-group variability in VD_{DPN} values. We therefore controlled for head motion in statistical tests. Quantitative head motion data was collected from the Vicra system, but the raw data was considered unreliable due to the observation that the head was able to move to a small extent within the neoprene cap worn by the participant to mount the head motion sensors. Analysis of head motion data was therefore performed in semi-quantitative manner, in that it relied on some qualitative assessment to achieve an ordinal score of total motion.

Head motion data consisted of both translational and rotational movements, each represented by three separate time-courses for each dimension of movement. Using visual inspection of this data, each [^{11}C]-DPN scan was scored separately for (a) intra-scan motion taking place over two or more dynamic frames of the PET data, (b) motion taking place between the transmission scan and the [^{11}C]-DPN scan, (c) the magnitude of infrequent intra-frame discrete motion events (d) the magnitude of frequent intra-frame motion events (Table 3). Separate scales were used to score each item for the degree of motion observed to account for the likely impact of that motion on the quality of the PET data. Movements of less than 1 mm translation, or 1 degree of rotation (which roughly equates to a 1 mm movement of superficial cortical regions), were considered inconsequential due to the resolution of the PET camera at 2.5 mm. Intra-frame motion events were scored higher (and higher again with greater frequency) than motion events spanning across two or more dynamic frames of PET data, because the latter were at least partially corrected during reconstruction. Scores for each type of motion were summed to create an overall motion severity score for each scan. Two researchers scored the head motion data independently and these scores were meaned.

Assessment of acute thermal pain threshold

The order of PET and thermal pain threshold assessments were randomised between participants and occurred on different days within four weeks of each other. Acute pain was induced using a CO_2 laser (150ms duration, beam diameter of 15mm), which specifically activates nociceptors in the skin[38], applied to the dorsal surface of the subjects' right forearm. Between stimuli, the laser was moved randomly over an area 3cm x 5cm to avoid habituation, sensitization or skin damage, with stimuli occurring at 10 s intervals. Subjects wore protective laser safety goggles.

To determine pain threshold, the Method of Levels was used. Participants were instructed to attend to the intensity of each laser stimulus and to rate it using a 0-10 numerical rating scale (NRS), which was anchored such that a level 4 indicated pain threshold, 7 indicated moderate pain, and 10 indicated unbearable pain. Laser stimuli were gradually increased in steps of 0.3 W cm-2 stimulus irradiance, from zero up to a subjective intensity of 7/10, and repeated three times. Pain threshold was

considered as the mean stimulus energy, over the first three ramps, required to elicit a response of 4/10.

Statistical analyses

Statistical analyses were conducted on [^{11}C]-DPN VD images on a voxel-by-voxel basis across the whole brain using SPM8 software. Before whole-brain analyses, smoothing of images was performed using a three-dimensional Gaussian kernel of 8 mm.

Whole-brain regression analyses were conducted within the patient group (n = 17) to identify regions correlating with sensory and affective dimensions of pain (Short-Form McGill Pain Questionnaire, sensory and affective subscales). In all tests, a number of covariates controlled for nuisance variables: subjects' age (years), subjects' sex (binary), subjects' weight (kg), [^{11}C]-DPN dose injected (MBq), global $K1_{DPN}$ (min^{-1}), head motion scores, and mean NRS ratings of pain reported across the whole scan. For all whole-brain comparisons, results are reported at uncorrected probability thresholds of $p < 0.001$ with a minimum cluster size of 50 voxels, and results are considered statistically significant after voxel-level correction for multiple comparisons using the Family-Wise Error rate set to 0.05.

Further analyses were conducted on regions-of-interest (ROIs) whose values were obtained as follows. From each scan, VD_{DPN} values were extracted from ROIs in which supra-threshold clusters (after FWE correction) were found. The ROIs were defined by anatomical labels within a previously published probabilistic atlas of the human brain[39]. A weighted average of VD_{DPN} values within ROIs was calculated. $K1_{DPN}$ and $K1_{H2O}$ values were obtained from ROIs in the same way.

ROI analyses sought to identify group differences and correlations with pain threshold. Firstly, ROIs from the patient (n = 17) and healthy control (n = 9) groups were statistically compared using an independent samples t-test with significance threshold of $p < 0.05$, after corrections had been made to the mean VD_{DPN} within each ROI by controlling for variance related to nuisance variables. The same nuisance variables were used as in the whole-brain analysis described above. Secondly, ROI data from each group separately, and also from the pooled data across both groups, were correlated with pain threshold as assessed by the acute laser

stimuli. Mean ROI values were first corrected for nuisance variables as described above, with an additional variable being each subjects' 0 – 10 NRS rating of acute laser pain intensity. Pearson's produce-moment correlation coefficient was obtained and results were considered statistically significant at $p < 0.05$.

To test for whether rCBF explained any of the variances in the VD_{DPN} data after correction for $K1_{DPN}$, mean $K1_{H2O}$ within ROIs were tested for correlation with both mean VD_{DPN} within the same ROIs, and predictor variables of interest showing statistically significant relationships with VD_{DPN} (namely, McGill sensory and affective pain scores and acute pain threshold). $K1_{H2O}$ for the patient (n = 14) and control (n = 8) groups were also compared by independent samples t-test in the same way as for the VD_{DPN} data.

Results

Participant characteristics and group comparisons

Data for group comparisons of sex, age, weight, radiotracer doses, intra-scan pain ratings, head motion during scanning and acute laser thermal pain thresholds are shown in Table 1. There was a larger proportion of females in the patient group (that was not statistically significant), and patients were significantly older than healthy controls. The dose of [^{11}C]-DPN injected, and the weight of participants (which may impact on radiotracer concentrations reaching the brain) did not significantly differ between groups, while the dose of water injected to assess rCBF was overall greater in patients than controls. On average, patients reported being in greater pain than controls during scanning, but the results were not statistically significant suggesting that efforts to make patients comfortable were at least partially successful. However, patients on average showed more than twice as much head motion during scanning, although this did not reach statistical significance compared to the healthy group. Lastly, while patients may scale pain differently due to their prior experience of chronic pain, we found no evidence of a difference in pain thresholds between groups.

Effect of chronic pain perception on opioid receptor availability

Whole-brain SPM regression analysis (Figure 1a and 1b, Table 4) revealed that in chronic pain patients, McGill sensory pain scores, for their chronic pain over the previous week, significantly and positively predicted opioid receptor availability at

the cluster level in the caudate nucleus, continuous with the nucleus accumbens and the subcallosal area. The right mid-insula showed the same effect at just below the level of significance. As the data were corrected for head motion in this statistical model, the greater VD values could not be ascribed to this factor. Also, having corrected for delivery effects in the analysis using the kinetic parameter K1, the mean VD values were not correlated with rCBF in the caudate ($r = 0.27$, $p = 0.35$), nor was rCBF related to chronic pain perception (Table 5), suggesting that the relationship between chronic pain perception and VD in the region of interest was not driven by greater blood flow in patients experiencing greater chronic pain.

As confirmation that the main result in the caudate was not related to modification of the endogenous opioid system by recent use of opioid medication, ROI analysis on the whole caudate was found to be comparable for the whole patient group ($n = 17$, $r = 0.691$, $p = 0.002$) and for a restricted patient group that excluded those withdrawn from opioid medication for the purpose of scanning ($n = 15$, $r = 0.687$, $p = 0.005$).

Analysis on a further striatal ROI (putamen, Table 5), in which mean VD values were taken over each ROI bilaterally, also revealed significant associations between chronic pain perception and opioid receptor availability. Testing the same ROIs against patients' affective pain perception (McGill affective pain scores) yielded a significant positive relationship within the caudate nucleus and subcallosal area only.

Opioid receptor availability as a predictor of pain threshold

Opioid receptor availability was found to be a positive predictor of laser heat pain threshold in both the caudate and subcallosal area (Table 5), with the strongest effect in the caudate (Figure 1c). Effects were close to significance in the putamen and insula, but not in nucleus accumbens. The strength of the effect was also greater (for caudate and subcallosal area) in the pooled data over both groups, with individual groups showing weaker relationships (leading to effects above the threshold of significance in the subcallosal area) consistent with the fewer degrees of freedom when considering individual groups. The analysis considered variance in opioid receptor availability that was not explained by chronic pain perception by including the latter as a nuisance variable.

Pain thresholds were also related to rCBF in the caudate nucleus, but on further assessment rCBF was not related to diprenorphine VD values in the caudate ($r =$

0.21, p = 0.36), and so the relationship between the OpR binding and rCBF results remain obscure.

Group differences in opioid receptor availability

Group comparison of mean VD values in ROIs revealed overall lower opioid receptor availability in the caudate nucleus in patients relative to controls (Table 5). While opioid receptor availability was also lower in patients in the subcallosal area and nucleus accumbens, these effects did not reach significance. There were no group differences in any other ROIs. There were no group differences in rCBF in the caudate nucleus.

Discussion

Three key findings emerge from this study: Firstly, that the perception of higher levels of chronic pain in arthritis predicts greater opioid receptor availability across pain modulatory regions of the basal ganglia, and particularly strongly within the caudate, nucleus accumbens and subcallosal area. This is the first time this has been reported in patients with arthritic pain. Secondly, overall caudate OpR availability is reduced in arthritis patients relative to healthy controls, consistent with greater occupation by endogenous opioid peptides. Thirdly, when OpR availability in the caudate was considered independently of chronic pain perception, it was positively associated with acute thermal pain threshold (in both patients and controls).

Our analyses were strengthened by controlling for radiotracer delivery effects and head motion, two factors that are likely to be both responsive to pain states and have an influence on PET radioligand results. Our results have implications for the understanding of the functioning of the opioid system in chronic pain states.

OpR availability and opioid tone in acute and chronic pain

The positive relationship between OpR availability and chronic pain perception could result either from a greater density of OpRs on neuronal cellular membranes (e.g. due to increased trafficking or upregulation), reduced opioid ‘tone’ (release of EOPs), or both. With our methodology we could not directly measure opioid tone and OpR density independently. However, a number of considerations suggest that the association found is due to increased OpR density, rather than reduced competition for binding sites.

There is evidence from animal studies that delta and kappa-OpRs in the brain and spinal cord can be up-regulated in response to mu-OpR agonism. Electron microscopy studies of the subcellular localization of delta-OpRs have shown that under normal conditions, the majority of delta-OpRs are localized to intracellular sites rather than neuronal plasma membranes[40, 41]. For mu-OpRs there is only evidence of up-regulation in response to *reduced* neurotransmitter binding, just as the normal adaptation to *greater* binding (e.g. in response to morphine[42]) is receptor down-regulation. However, prolonged and selective stimulation of mu-OpRs can cause trafficking of delta-OpRs to plasma membranes *in vivo*[43], including mouse basal ganglia[44], thereby increasing the anti-nociceptive potency of delta-OpR agonists[45, 46]. This may account for the greater antinociceptive effects of delta-selective agonists than non-selective agonists in chronic pain states. Repeated administration of mu-agonists also up-regulates expression of the kappa-OpRs in the brain[47]. Animal models of chronic inflammatory pain have shown an increase in cell membrane expression of delta-OpRs both postsynaptically[48] and presynaptically[49] in the dorsal spinal cord ipsilateral to the site of injury. One view is that stimulus-evoked translocation of delta-OpRs to neuronal plasma membranes has evolved as part of a homeostatic mechanism to maintain control of nociceptive transmission[50].

Our analysis shows that the variances in OpR availability in the caudate nucleus explained by acute pain threshold were present in both chronic pain patients and healthy controls, and were not dependent on chronic pain perception. These variances can therefore be explained by natural variability in OpR density (likely at either mu-OpRs or kappa-OpRs[6]) that is independent of the presence of arthritic disease and chronic pain symptoms. A greater density of OpRs would be expected to increase the sensitivity of post-synaptic neurons to opioid-mediated inhibition in response to pain, thereby increasing 'gain' in the system.

Opioid tone is highly dependent on current pain state, as illustrated by the fact that induction of acute pain for a short time during PET scanning procedures can be enough to cause a reduction in OpR availability as a result of endogenous opioid release and competitive binding to OpRs[16]. Yet, our data showing a positive association between OpR availability and prior chronic pain perception was statistically independent of intra-scan pain perception. This does not favour the

explanation that competition for OpR binding by endogenous ligands induced pain intra-scan pain was causing the positive correlation between OpR availability and prior chronic pain state.

Group differences

Patients were made as comfortable as possible during scanning, but inevitably a small number of patients did experience some discomfort that led to the higher mean and variance in intra-scan pain scores in the patient group relative to controls. It is also reasonable to suppose that patients scaled their intra-scan discomfort differently from healthy controls (on the basis of their chronic pain experience), such that small amounts of pain rated by patients might equate to larger amounts if experienced by healthy controls. Hence our intra-scan pain ratings are potentially an under-estimation in the patient group. Therefore, the finding of overall lower OpR availability in patients vs. controls may be a result of competition for OpR binding by the release of endogenous ligands as a result of pain being experienced during scanning. This is consistent with previous studies which have provided evidence consistent with chronic neuropathic pain[18-22] and inflammatory arthritic pain[17] resulting in release of EOPs reflected by reduced OpR availability.

Striatal relationships to chronic pain perception

The functional roles of the different nuclei of the striatum in pain perception and behaviour are far from well understood. The striatum is best known for its involvement in dopaminergic mechanisms of motor learning (dorsal striatum) and motivation/reward (ventral striatum). There is evidence for a relationship between dopamine receptor binding in the ventral striatum (nucleus accumbens) with affective responses to pain[51]. Ventral striatal reward mechanisms may therefore be directly implicated in driving the affective component of pain. However, our data showing a stronger correlation of OpR availability with the sensory than the affective components of pain cast doubt on this hypothesis, and suggest that the ventral striatum may have a more general motivational function in driving behavioural responses to pain. This is consistent with previous work demonstrating that stimulation of the caudate in monkey reduces behavioural reactivity to acute pain[52].

The striatal dopamine and opioid systems have previously been shown to be abnormal in chronic pain syndromes. Patients with fibromyalgia and orofacial pain

syndromes[53, 54] have an abnormal dopamine response to pain in the caudate and putamen[55]. Furthermore, there is evidence of increased gray matter density in the striatum in a number of chronic pain conditions including fibromyalgia[56], chronic low back pain[57], and chronic vulvar pain[58]. It is not yet clear how these abnormalities relate to the endogenous opioid system or to pain perception. Abnormalities in both dopaminergic and opioidergic neurotransmission in the striatum in chronic pain patients might reflect motivational and motor processes such as the learning or expression of habitual responses to pain[59].

Opioidergic abnormalities: cause or consequence of chronic pain?

We make the case, based on animal research, for an adaptive up-regulation of OpRs in response to chronic pain as part of a homeostatic mechanism. Patients who fail to adequately up-regulate OpRs in response to chronic pain may be at risk of a more extreme and/or refractory phenotype. Patients with lower OpR availability may have lower pain thresholds and be more susceptible to a chronic pain condition. Hence, it is tempting to assert that maintaining a lower striatal OpR availability in patients with chronic pain represents a physiological vulnerability to developing or maintaining states of chronic pain. However, while other studies of OpR availability in chronic pain patients have not assessed pain thresholds, we found no difference between pain thresholds in patients and control subjects. This makes it more challenging to make an argument for lower OpR availability in chronic pain patients being a contributing factor to chronic pain rather than an adaptive change with greater occupation of endogenous opioids. However, larger and longitudinal studies may be needed to clarify this relationship.

Conclusions

Our data is consistent with animal data showing that chronic pain states upregulate OpRs and suggest that same occurs in humans in response to chronic arthritic pain. We suggest that this may be part of a homeostatic regulatory mechanism that reduces excessive nociceptive processing. This is important because it may explain individual resilience and vulnerability to chronic arthritic pain and the variable response to pharmacological (e.g. synthetic opiates) and non-pharmacological interventions (e.g. exercise). Further sequential studies are needed to examine the benefits and pitfalls of current therapeutic approaches to chronic pain in terms of

their effects on OpR availability in the brain and the potential for increasing resilience to developing chronic pain in the first place.

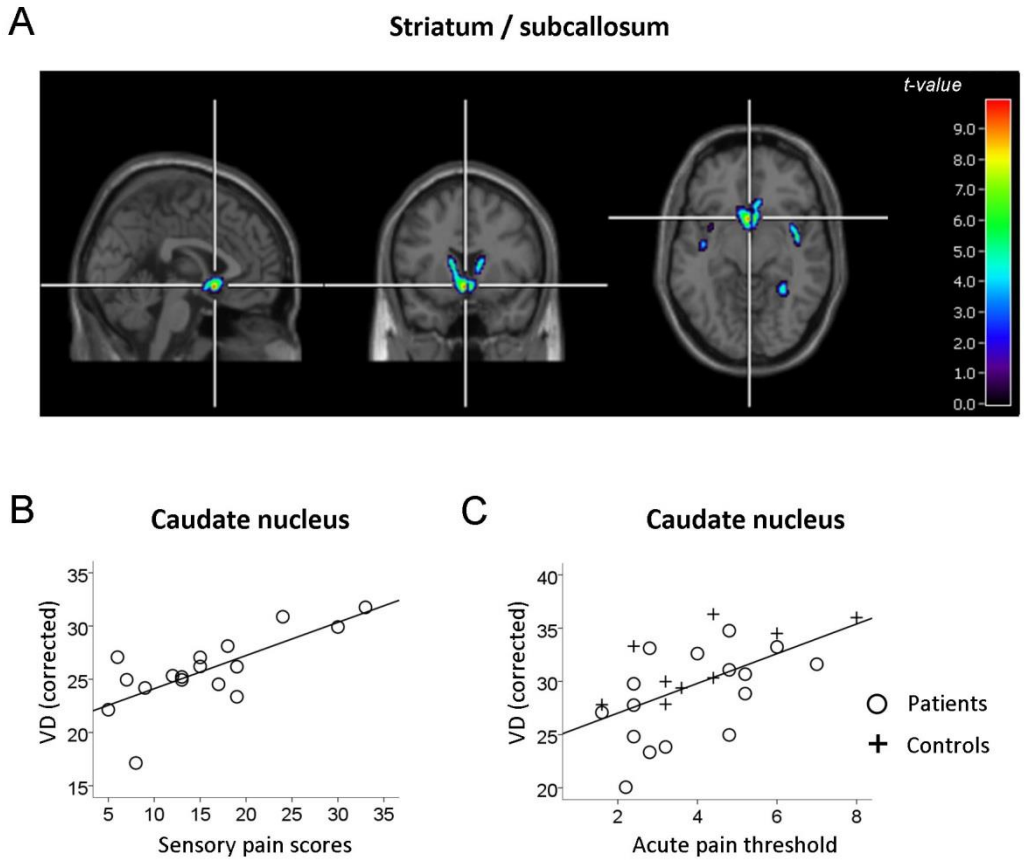

Figure 1

Relationship of ^{11}C-DPN binding to chronic pain perception and acute pain thresholds. The Volume of Distribution (VD), as a proxy of ^{11}C-DPN binding, was adjusted for a number of nuisance variables in each analysis (see Methods). (a) Whole-brain SPM regression analysis of McGill sensory pain scores as a predictor of ^{11}C-DPN binding (patients only, *n* = 17). Images are displayed at a voxel threshold of $p < 0.001$ uncorrected and a cluster threshold equating to the size of the significant cluster. (b) For illustrative purposes, subsequent extraction of mean VD values from the caudate nucleus was corrected for the same nuisance variables and plotted against McGill sensory pain scores. (c) Pain threshold (laser energy in W cm-2 required to elicit the lowest pain sensation) regressed on VD values (mean across all voxels in the caudate ROI) after correction for nuisance variables. Regression line illustrates fits for the pooled data across groups (patients and controls, *n* = 26).

Table 1: Group characteristics

	***n* total**	***n* females**	**Age (Years)**	**Weight (Kg)**	**DPN dose injected (MBq)**	**H2O dose injected (MBq)**	**Head motion**	**Intra-scan pain ratings**	**Thermal pain threshold (W cm^{-2})**
Arthritis patients	17	12	57.5 (12.1)	83.1 (21.0)	490.0 (62.3)	606.7 (22.3)	3.6 (3.3)	2.5 (2.0)	3.9 (1.5)
Healthy controls	9	3	45.4 (7.5)	78.8 (16.2)	505.0 (33.0)	583.4 (30.7)	1.6 (1.8)	1.5 (1.4)	4.0 (1.9)
Independent samples test p statistic		0.08	*0.004*	0.59	0.26	0.07	0.1456†	0.18	0.76

Values are means (with standard deviation). Equal variances not assumed. All test are parametric t-tests except for † indicating non-parametric Wilcoxon rank sum test

Table 2: Descriptive statistics of [^{11}C]-DPN doses injected

	Radio-chemical purity (%)	Dose injected (MBq)	Specific Activity (GBq/μmol)	Mass injected (μg)	Mass injected (μg/kg)
Min	93.2	276.1	116.6	0.8	0.011
Max	100.0	565.2	525.9	5.1	0.100
Mean	96.4	484.7	254.9	2.4	0.033
Median	96.0	506.2	238.4	2.3	0.029

Table 3: Scoring system for semi-quantitative derivation of head motion scores

		Inter-frame motion over the whole scan	Motion relative to transmission scan	Infrequent discrete intra-frame motion	Frequent discrete intra-frame motion
Magnitude of motion	< 1mm/degree	0	0	0	0
	1-2mm/degrees	1	1	2	3
	2-5mm/degrees	2	2	3	4
	> 5mm/degrees	3	3	4	5

Table 4: Brain regions correlating with McGill Pain Questionnaire (sensory subscale) scores.

Cluster		cluster significance p(FWE)	cluster size (voxels)	Maximal voxel (MNI, mm) x	y	z
Caudate / accumbens / subcallosal area	L, R	0.00	499	0	10	-10
Insula (middle section)	R	0.07	198	42	-4	-4
Temporal lobe (posterior)	R	0.15	155	18	-42	0
Temporal lobe (posterior) / parietal lobe (inferiolateral)	R	0.23	130	46	-34	16
Frontal gyrus (superior)	L	0.37	102	-14	34	48
Insula (middle section)	R	0.54	80	-42	-14	-6
Frontal gyrus (superior)	R	0.56	77	16	44	40
Occipital lobe (lateral)	L	0.60	73	-44	-76	0
Parietal lobe (inferiolateral)	R	0.70	62	52	-28	38
Frontal gyrus (superior)	L	0.80	51	-12	-10	48

p(FWE): probability of incorrectly rejecting the null hypothesis after family-wise error correlation for multiple comparisons; MNI: Montreal Neurological Institute coordinate system.

Table 5: Statistics relating to random and fixed effect analyses on ROIs

	McGill sensory pain		McGill affective pain		Acute pain threshold						Group	
	Arthritis patients		*Arthritis patients*		*Groups pooled*		*Arthritis patients*		*Healthy controls*		*Patients vs. controls*	
	r	***p***	***r***	***p***	***r***	***p***	***r***	***p***	***r***	***p***	***t***	***p***
Diprenorphine data												
n	17		17		26		17		9		17, 9	
Caud	0.691	*0.002*	0.587	*0.013*	0.596	*0.002*	0.572	*0.021*	0.735	*0.024*	-2.107	*0.047*
Subcal	0.779	*0.001*	0.536	*0.026*	0.424	*0.035*	0.49	0.054	0.339	0.373	-1.728	0.098
NuAcc	0.691	*0.002*	0.356	0.160	0.300	0.146	0.431	0.096	0.044	0.911	-1.452	0.160
Ins	0.653	*0.003*	0.284	0.269	0.377	0.063	0.454	0.077	0.247	0.521	-1.648	0.113
Puta	0.567	*0.018*	0.197	0.449	0.382	0.060	0.476	0.063	0.204	0.598	-1.770	0.090
Water data												
n	14		14		22		14		8		14, 8	
Caud	0.282	0.329	0.208	0.475	0.524	0.012	0.314	0.274	0.701	0.053	-1.013	0.339

Significant effects are italicized. Caud: Caudate Nucleus; Subcal: Subcallosal area; NuAcc: Nucleus Accumbens; Ins: Insula; Puta: Putamen; r: Pearson's product moment correlation coefficient; p: probability of incorrectly rejecting the null hypothesis.

References

[1] A. D. Woolf, B. Pfleger, *Bulletin of the World Health Organisation* **2003**, *81*, 646.

[2] J. Bedson, P. R. Croft, *BMC Musculoskeletal Disorders* **2008**, *9*.

[3] A. Nilsdotter, I. Petersson, E. Roos, L. Lohmander, *Annals of the Rheumatic Diseases* **2003**, *62*, 923.

[4] L. Garcia-Larrea, R. Peyron, *Pain* **2013**, *154 Suppl 1*, S29.

[5] J. M. Braz, M. A. Nassar, J. N. Wood, A. I. Basbaum, *Neuron* **2005**, *47*, 787.

[6] A. J. Cross, C. Hille, P. Slater, *Brain Research* **1987**, *418*, 343.

[7] A. K. Jones, L. Y. Qi, T. Fujirawa, S. K. Luthra, J. Ashburner, P. Bloomfield, V. J. Cunningham, M. Itoh, H. Fukuda, T. Jones, *Neuroscience Letters* **1991**, *126*, 25.

[8] U. Baumgartner, H. G. Buchholz, A. Bellosevich, W. Magerl, T. Siessmeier, R. Rolke, S. Hohnemann, M. Piel, F. Rosch, H. J. Wester, G. Henriksen, P. Stoeter, P. Bartenstein, R. D. Treede, M. Schreckenberger, *Neuroimage* **2006**, *30*, 692.

[9] E. H. Chudler, W. K. Dong, *Pain* **1995**, *60*, 3.

[10] R. W. Gear, K. O. Aley, J. D. Levine, *The Journal of Neuroscience* **1999**, *19*, 7175.

[11] D. J. Scott, C. S. Stohler, C. M. Egnatuk, H. Wang, R. A. Koeppe, J. K. Zubieta, *Archives of General Psychiatry* **2008**, *65*, 220.

[12] A. K. P. Jones, S. K. Luthra, V. W. Pike, S. Herold, F. Brady, *The Lancet* **1985**, *326*, 665.

[13] A. K. Jones, K. Friston, R. Dolan, *Baillieres Clinical Endocrinology and Metabolism* **1991**, *5*, 187.

[14] J. K. Zubieta, Y. R. Smith, J. A. Bueller, Y. Xu, M. R. Kilbourn, D. M. Jewett, C. R. Meyer, R. A. Koeppe, C. S. Stohler, *Science* **2001**, *293*, 311.

[15] B. Bencherif, P. N. Fuchs, R. Sheth, R. F. Dannals, J. N. Campbell, J. J. Frost, *Pain* **2002**, *99*, 589.

[16] T. Sprenger, M. Valet, H. Boecker, G. Henriksen, M. E. Spilker, F. Willoch, K. J. Wagner, H. J. Wester, T. R. Tolle, *Pain* **2006**, *122*, 63.

[17] A. K. Jones, V. J. Cunningham, S. Ha-Kawa, T. Fujiwara, S. K. Luthra, S. Silva, S. Derbyshire, T. Jones, *British Journal of Rheumatology* **1994**, *33*, 909.

[18] A. K. Jones, V. J. Cunningham, S. K. Ha-Kawa, T. Fujiwara, Q. Liyii, S. K. Luthra, J. Ashburner, S. Osman, T. Jones, *Journal of Neuroscience Methods* **1994**, *51*, 123.

[19] A. K. Jones, N. D. Kitchen, H. Watabe, V. J. Cunningham, T. Jones, S. K. Luthra, D. G. Thomas, *Journal of Cerebral Blood Flow and Metabolism* **1999**, *19*, 803.

[20] A. K. Jones, H. Watabe, V. J. Cunningham, T. Jones, *Eur J Pain* **2004**, *8*, 479.

[21] F. Willoch, F. Schindler, H. J. Wester, M. Empl, A. Straube, M. Schwaiger, B. Conrad, T. R. Tolle, *Pain* **2004**, *108*, 213.

[22] J. Maarrawi, R. Peyron, P. Mertens, N. Costes, M. Magnin, M. Sindou, B. Laurent, L. Garcia-Larrea, *Pain* **2007**, *127*, 183.

[23] R. E. Harris, D. J. Clauw, D. J. Scott, S. A. McLean, R. H. Gracely, J. K. Zubieta, *The Journal of Neuroscience* **2007**, *27*, 10000.

[24] R. Altman, G. Alarcón, D. Appelrouth, D. Bloch, D. Borenstein, K. Brandt, C. Brown, T. D. Cooke, W. Daniel, D. Feldman, R. Greenwald, M.

Hochberg, D. Howell, R. Ike, P. Kapila, D. Kaplan, W. Koopman, C. Marino, E. McDonald, D. J. McShane, T. Medsger, B. Michel, W. A. Murphy, T. Osial, R. Ramsey-Goldman, B. Rothschild, F. Wolfe, *Arthritis & Rheumatism* **1991**, *34*, 505.

[25] D. Aletaha, T. Neogi, A. J. Silman, J. Funovits, D. T. Felson, C. O. Bingham, 3rd, N. S. Birnbaum, G. R. Burmester, V. P. Bykerk, M. D. Cohen, B. Combe, K. H. Costenbader, M. Dougados, P. Emery, G. Ferraccioli, J. M. Hazes, K. Hobbs, T. W. Huizinga, A. Kavanaugh, J. Kay, T. K. Kvien, T. Laing, P. Mease, H. A. Menard, L. W. Moreland, R. L. Naden, T. Pincus, J. S. Smolen, E. Stanislawska-Biernat, D. Symmons, P. P. Tak, K. S. Upchurch, J. Vencovsky, F. Wolfe, G. Hawker, *Arthritis & Rheumatism* **2010**, *62*, 2569.

[26] R. Melzack, *Pain* **1987**, *30*, 191.

[27] H. W. de Jong, F. H. van Velden, R. W. Kloet, F. L. Buijs, R. Boellaard, A. A. Lammertsma, *Physics in Medical Biology* **2007**, *52*, 1505.

[28] C. Knoess, J. Rist, C. Michel, Z. Burbar, L. Eriksson, V. Panin, L. Byars, M. Lenox, K. Wienhard, W. D. Heiss, R. Nutt, in *Nuclear Science Symposium Conference Record, 2003 IEEE, Vol. 3*, **2003**, pp. 1936.

[29] A. S. Ranicar, C. W. Williams, L. Schnorr, J. C. Clark, C. G. Rhodes, P. M. Bloomfield, T. Jones, *Medical Progress Through Technology* **1991**, *17*, 259.

[30] M. Fairclough, C. Prenant, G. Brown, A. McMahon, J. Lowe, A. Jones, *Journal of Labelled Compounds and Radiopharmaceuticals* **2014**, *57*, 388.

[31] M. E. Casey, E. J. Hoffman, *Journal of Computer Assisted Tomography* **1986**, *10*, 845.

[32] C. C. Watson, M. E. Casey, C. Michel, B. Bendriem, in *Nuclear Science Symposium Conference Record, 2004 IEEE, Vol. 5*, **2004**, pp. 3008.

[33] C. Comtat, F. C. Sureau, M. Sibomana, I. K. Hong, N. Sjoholm, R. Trebossen, in *Nuclear Science Symposium Conference Record, 2008. NSS '08. IEEE*, **2008**, pp. 4120.

[34] M. Tadokoro, A. Jones, V. Cunningham, D. Sashin, S. Grootoonk, J. Ashburner, T. Jones, *Annals of Nuclear Medicine* **1993**, *7*, S50.

[35] V. J. Cunningham, T. Jones, *Journal of Cerebral Blood Flow and Metabolism* **1993**, *13*, 15.

[36] A. Hammers, M. C. Asselin, F. E. Turkheimer, R. Hinz, S. Osman, G. Hotton, D. J. Brooks, J. S. Duncan, M. J. Koepp, *Neuroimage* **2007**, *38*, 82.

[37] F. Maes, A. Collignon, D. Vandermeulen, G. Marchal, P. Suetens, *Medical Imaging, IEEE Transactions on* **1997**, *16*, 187.

[38] R. A. Meyer, R. E. Walker, V. B. Mountcastle, Jr., *IEEE Transactions on Biomedical Engineering* **1976**, *23*, 54.

[39] A. Hammers, R. Allom, M. J. Koepp, S. L. Free, R. Myers, L. Lemieux, T. N. Mitchell, D. J. Brooks, J. S. Duncan, *Human Brain Mapping* **2003**, *19*, 224.

[40] P. Y. Cheng, A. L. Svingos, H. Wang, C. L. Clarke, S. Jenab, I. W. Beczkowska, C. E. Inturrisi, V. M. Pickel, *The Journal of Neuroscience* **1995**, *15*, 5976.

[41] C. M. Cahill, K. A. McClellan, A. Morinville, C. Hoffert, D. Hubatsch, D. O'Donnell, A. Beaudet, *Journal of Comparative Neurology* **2001**, *440*, 65.

[42] J. E. Zadina, S. L. Chang, L. J. Ge, A. J. Kastin, *Journal of Pharmacology and Experimental Therapeutics* **1993**, *265*, 254.

[43] C. M. Cahill, A. Morinville, M. C. Lee, J. P. Vincent, B. Collier, A. Beaudet, *The Journal of Neuroscience* **2001**, *21*, 7598.

[44] A. L. Lucido, A. Morinville, L. Gendron, T. Stroh, A. Beaudet, *Journal of Molecular Neuroscience* **2005**, *25*, 207.
[45] J. Ma, Y. Zhang, A. E. Kalyuzhny, Z. Z. Pan, *Molecular Pharmacology* **2006**, *69*, 1137.
[46] A. A. A. Pradhan, C. Siau, A. Constantin, P. B. S. Clarke, *Neuroscience* **2006**, *141*, 947.
[47] X.-M. Wang, Y. Zhou, R. Spangler, A. Ho, J.-S. Han, M. J. Kreek, *Molecular Brain Research* **1999**, *66*, 184.
[48] C. M. Cahill, A. Morinville, C. Hoffert, D. O'Donnell, A. Beaudet, *Pain* **2003**, *101*, 199.
[49] L. Gendron, A. L. Lucido, F. Mennicken, D. O'Donnell, J.-P. Vincent, T. Stroh, A. Beaudet, *The Journal of Neuroscience* **2006**, *26*, 953.
[50] C. M. Cahill, S. V. Holdridge, A. Morinville, *Trends in Pharmacological Sciences* **2007**, *28*, 23.
[51] D. J. Scott, M. M. Heitzeg, R. A. Koeppe, C. S. Stohler, J.-K. Zubieta, *The Journal of Neuroscience* **2006**, *26*, 10789.
[52] C. G. Lineberry, C. J. Vierck, *Brain Research* **1975**, *98*, 119.
[53] N. Hagelberg, H. Forssell, S. Aalto, J. O. Rinne, H. Scheinin, T. Taiminen, K. Nagren, O. Eskola, S. K. Jaaskelainen, *Pain* **2003**, *106*, 43.
[54] N. Hagelberg, H. Forssell, J. O. Rinne, H. Scheinin, T. Taiminen, S. Aalto, S. Luutonen, K. Nagren, S. Jaaskelainen, *Pain* **2003**, *101*, 149.
[55] P. B. Wood, P. Schweinhardt, E. Jaeger, A. Dagher, H. Hakyemez, E. A. Rabiner, M. C. Bushnell, B. A. Chizh, *European Journal of Neuroscience* **2007**, *25*, 3576.
[56] T. Schmidt-Wilcke, R. Luerding, T. Weigand, T. Jürgens, G. Schuierer, E. Leinisch, U. Bogdahn, *Pain* **2007**, *132, Supplement 1*, S109.
[57] T. Schmidt-Wilcke, E. Leinisch, S. Gänßbauer, B. Draganski, U. Bogdahn, J. Altmeppen, A. May, *Pain* **2006**, *125*, 89.
[58] P. Schweinhardt, A. Kuchinad, C. F. Pukall, M. C. Bushnell, *Pain* **2008**, *140*, 411.
[59] N. D. Daw, D. Shohamy, *Social Cognition* **2008**, *26*, 593.

Publication 4 (page 164)

CHAPTER 5: Radiolabeling with fluorine-18 of a protein, interleukin-1 receptor antagonist.

Published in:

Applied Radiation and Isotopes, Volume 68, Issue 9, Pages: 1721-1727, 2010.

Radiolabeling with fluorine-18 of a protein, interleukin-1 receptor antagonist.

C. Prenant[a]*, C. Cawthorne[b], M. Fairclough[a], N. Rothwell[c], H. Boutin[c].

[a]*Wolfson Molecular Imaging Centre, University of Manchester, Manchester, UK.*

[b]*Academic Department of Radiation Oncology, The Christie NHS Foundation Trust, Manchester, UK.*

[c]*Faculty of Life Sciences, University of Manchester, Manchester, UK.*

*Corresponding author. Present address: Cyclopharma, CERRP, 1-3 rue Germaine Richier, Tours 37100, France. Tel.: +33247367651; Fax.: +33247498830.

E-mail address: cprenant@cyclopharma.fr (C. Prenant).

Abstract

IL-1RA is a naturally occurring antagonist of the pro-inflammatory cytokine interleukin-1 (IL-1) with high therapeutic promise, but its pharmacokinetic remains poorly documented. We describe in this report the radiolabeling of recombinant human interleukin-1 receptor antagonist (rhIL-1RA) with fluorine-18, to allow pharmacokinetic studies by positron emission tomography (PET). rhIL-1RA was labeled randomly by reductive alkylation of free amino groups (the ε-amino group of lysine residues or amino-terminal residues) using [^{18}F]fluoroacetaldehyde under mild reaction conditions. Radiosyntheses used a remotely controlled experimental rig within 100 min and the radiochemical yield was in the range of 7.1-24.2% (decay corrected, based on seventeen syntheses). We showed that the produced [^{18}F]fluoroethyl-rhIL-1RA retained binding specificity by conducting an assay on rat brain sections, allowing its pharmakokinetic study using PET.

Keywords: [^{18}F]rhIL-1RA; IL-1; inflammation; [^{18}F]fluoroacetaldehyde; PET.

Introduction

The pro-inflammatory cytokine IL-1 plays an important role in inflammation, angiogenesis and the immune response[1, 2] and has been implicated in neurodegenerative diseases[3-8]. Inhibition of IL-1 function by the naturally occurring, selective and potent antagonist IL-1RA has therapeutic promise in

preventing damage in a range of inflammatory and autoimmune disorders including rheumatoid arthritis[9] and psoriasis.

rhIL-1RA also demonstrated benefit in preclinical studies on experimentally induced ischemic, excitotoxic, and traumatic brain insults in rodents[10, 11] and potential in early clinical trials[12]. However, little is known about the biodistribution, pharmacokinetics and metabolism of rhIL-1RA so that brain penetration may be a key issue in its potential development as a therapeutic agent in brain traumatisms.

Pharmacokinetic modeling of rhIL-1RA administered intravenously in patients with subarachnoid haemorrhage (SAH)[13] reported that it crossed significantly, but slowly into the CSF. However, the CSF concentrations achieved were similar to or above those found to be neuroprotective in rodents[13]. A potential limitation of this work, as noted by the authors, is that the concentration of proteins in the CSF of patients may not reflect the concentration in the local brain environment.

Limited pharmacokinetics, tissue distribution and elimination studies of IL-1RA in rats using ^{35}S-IL-1RA has been reported[14]. Moreover, IL-1RA, radiolabelled with iodine-123, has been evaluated as a scintigraphic imaging marker of infection in a rabbit model but showed relatively poor imaging characteristics in term of both resolution and sensitivity[15]. In contrast, positron emission tomography (PET) has proved useful to study the pharmacokinetics and biodistribution of labeled peptides and proteins[16-18]. This led us to develop a radiolabeling method for rhIL-1RA, based on fluorine-18, for use with PET in order to better study the pharmacokinetics of this molecule with respect to brain uptake and metabolism.

Among the approaches investigated for fluorine-18 labeling of proteins using [^{18}F]fluoride, ^{18}F-acylation using 4-[^{18}F]fluorobenzoyl moiety[18, 19] and chemoselective reactions of 4-[^{18}F]fluorobenzaldehyde ([^{18}F]FB-CHO) with peptide functionalized with a hydrazine or a aminooxy group producing respectively oxime and hydrazone have been extensively used[20, 21]. The drawback of the labeling approaches using 4-[^{18}F]fluorobenzoyl moiety is the lengthy, time-consuming multi-step preparation, involving a HPLC purification, of the ^{18}F labelling agents. Peptide labeling approaches using the highly lipophilic [^{18}F]FB-CHO require the use of an organic co-solvent such as DMSO, furthermore preparation of [^{18}F]FB-CHO involves a step of purification using HPLC or solid phase extraction. Another

labeling method for IL-1RA was therefore attempted: reductive [^{18}F]fluoroethylation of free amino groups (ε-amino group of lysine residues or amino-terminal residues) using [^{18}F]fluoroacetaldehyde[22].

Reductive alkylation is a well-established method for the chemical modification of amino groups in proteins with minimal perturbation in their structure and function. The method is rapid and employs mild conditions, it has little effect on the physical chemical properties, only a slight change in the pKa of the ε-monoalkylamino groups which are generally slightly more basic than the corresponding primary amino groups[23]. Means (1997)[24] has shown that when using acetaldehyde only the corresponding monoalkylated lysine is produced. Moreover reductive alkylation of protein amino groups with small carbonyl compounds like formaldehyde or acetaldehyde cause a minimal disturbance of existing electrostatic interactions. Larger and generally more hydrophobic carbonyl compounds should, however, increase both the bulk and hydrophobicity of the amino group and reduce its ability to form hydrogen bonds[24].

The choice of the reducing agent is crucial, Jentoft and Dearborn (1979)[25] and Geoghegan et al. (1981)[26] have applied the reductive methylation to different proteins using [^{12}C], [^{13}C] and [^{14}C]formaldehyde and shown that using sodium cyanoborohydride instead of sodium borohydride prevent aldehydes or ketones reduction, inter or intramolecular bridges formation, disulfide bond reductions or labile peptide bonds cleavage. This method has been used for carbon-11 labelling with [^{11}C]formaldehyde of fibrinogen[27], and concanavalin A[28].

The mechanism for reductive [^{18}F]fluoroethylation of a free amino group of the IL-1RA involves the formation of an imine intermediate, the reduction of which yields the corresponding [^{18}F]fluoroethyllysine (Figure 1).

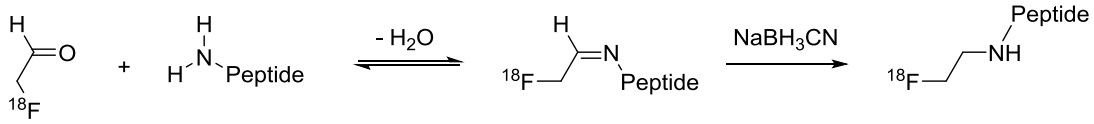

Figure 1: Reductive [^{18}F]fluoroethylation of the IL-1RA with [^{18}F]fluoroacetaldehyde.

Radiolabeling was carried out in a remotely controlled experimental rig. The hydrophilicity and high reactivity with amino groups of [^{18}F]fluoroacetaldehyde in reductive alkylation conditions makes it a good reagent for protein radiolabeling by targeting free amino groups producing *N*-[^{18}F]fluoroethyl derivatives. The small size

of the [^{18}F]fluoroethyl substituent is expected to have little impact on the rhIL-1RA integrity. Nevertheless as one of the nine lysine moieties on IL-1RA has been identified as important for receptor interaction[29], binding properties of the [^{18}F]IL-1RA were assayed using rat brain sections and autoradiography.

Materials and methods

Remotely controlled radiosynthesis set-up

The remotely controlled radiosynthesis experimental rig was set up in a lead-shielded fume-cupboard (Figure 2). The core of the radiosynthesis set up was comprised of three remotely controlled six-port/two-position electrically activated Valco valves (Thames Restek UK Ltd, UK). [^{18}F]Fluoroacetaldehyde production was carried out in Wheaton borosilicate screw-top V-vials, capacity 3.0 ml, with open-top cap and PTFE-faced silicon septum (Sigma-Aldrich, UK) using a home-made, temperature-regulated block heater, equipped with a magnetic stirrer and cooled with compressed air via a valve manually operated from outside the fume-cupboard. Reagents were added from outside the fume-cupboard via two shut-off, low-pressure, valves from Upchurch (Sigma-Aldrich, UK). The labeling of rhIL-1RA was carried out in a 1.5 ml microtube with attached screw cap (Sigma-Alrich, UK) using a digital block heater (Jencons Scientific, UK). The produced [^{18}F]rhIL-1RA was injected through a low protein-binding Pall Acrodisc® syringe filter (13 mm Diameter, 0.2 µm pore size) onto a 5 ml HiTrap™ desalting column (GE Healthcare, UK) for purification using a programmable syringe pump model ALADDIN-220 (World Precision Instruments, UK). Radioactivity in reaction vials was monitored using a Ratemeter Mini 900 (Thermo Electron Corporation, UK). [^{18}F]rhIL-1RA and other radioactive fractions collected after separation on the HiTrap column were measured on a Capintec CRC-15R.

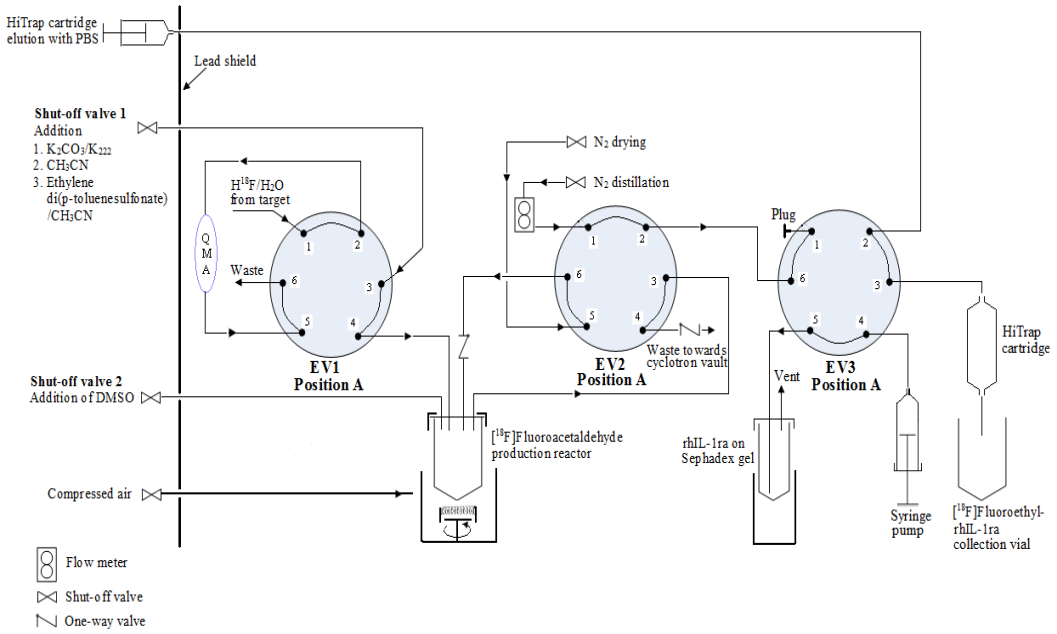

Figure 2: Remotely controlled radiosynthesis experimental rig for [^{18}F]rhIL-1RA production.

Chemicals

Solvents were purchased from Sigma-Aldrich and were used without further purification. The rhIL-1RA, Anakinra® (Kineret®), was kindly provided by Amgen (Thousand Oaks, CA, USA). Kineret® is a recombinant, methionylated, nonglycosylated synthetic form of the human interleukin-1 receptor antagonist (IL-1RA). It was provided as a solution formulated for injection consisting of 100 mg of Anakinra, 1.29 mg of sodium citrate, 5.48 mg sodium chloride, 0.12 mg disodium EDTA, and 0.70 mg polysorbate 80 in 1 mL water for injection, USP (pH 6.5 at room temperature). [^{18}F]Fluoride was produced via the $^{18}O(p,n)^{18}F$ nuclear reaction by 16.4 MeV proton bombardment of an isotopically enriched [^{18}O] water target (95–97% $H_2{}^{18}O$ water enrichment) using a GE PETtrace cyclotron.

Radiochemistry.

Production of [^{18}F]potassium fluoride.

The three electrovalves in the experimental rig (Figure 2) were set in position A at initial time of the synthesis, aqueous [^{18}F]fluoride solution (2 ml, 1.73-3.42 GBq) was sent from the cyclotron target onto a QMA cartridge, in the carbonate form. Electrovalve 1 was subsequently switched to position B and [^{18}F]KF was eluted from the QMA with 1.1 mg (8 µmol) potassium carbonate and 10 mg (26.5 µmol) of 4,7,13,16,21,24-hexaoxa-1,10-diazabicyclo[8,8,8]hexacosane (Kryptofix 222) in 0.5

ml water, added from shut-off valve 1, into the reactor. Electrovalve 1 was subsequently switched back to position A and 1ml of acetonitrile was added from shut-off valve 1. Temperature of the heater was set to 110°C and the mixture was then dried under nitrogen for 5 minutes. This drying step was repeated twice with 0.8 ml of acetonitrile after what the heater was cooled to 30°C.

[^{18}F]Fluoroethyltosylate.

A solution of ethylene di-*p*-toluenesulphonate, 5 mg (13.5 µmol) in 0.3 ml acetonitrile was added to the dried [^{18}F]potassium fluoride/Kryptofix complex through shut-off valve 1. Electrovalve 2 was subsequently switched to position B, the heater set to 90 °C and the mixture was heated for 8 min.

[^{18}F]Fluoroacetaldehyde.

The heater was subsequently cooled to 60 °C, electrovalve 2 switched to position A and acetonitrile was evaporated under nitrogen. Evaporation was completed within three minutes after what electrovalves 2 and 3 were switched to position B, anhydrous DMSO (0.2 ml) was added through shut-off valve 2 and the temperature of the heater was set to 150 °C. Around one minute after the heater had reached this temperature [^{18}F]fluoroacetaldehyde started to distil conveyed by nitrogen (7–8 ml/min).

[^{18}F]rhIL-1RA.

Distilled [^{18}F]fluoroacetaldehyde was trapped into a microtube containing the rhIL-1RA in suspension in a Sephadex® gel to avoid foaming of the protein solution. The gel was made by addition of 20µl (2mg) of a solution of the rhIL-1RA formulated for injection (100 mg/ml), and 40 µl of a 0.25 M solution of sodium cyanoborohydride in citrate buffer (citric acid, ~0.060 M, sodium hydroxide, ~0.16 M, pH = 6), onto dry Sephadex® G-50 (6 mg). After 8 minutes all the [^{18}F]fluoroacetaldehyde was distilled, as monitored by a radioactivity detector. The microtube was subsequently heated at 38 °C for 45 min after which time PBS (1 ml, pH 7.2) was added to the gel via the syringe pump. This addition was followed by the withdrawing of suspension via a programmed step on the syringe pump, after which electrovalve 3 was switched to position A. The reaction mixture was then injected by the syringe pump onto a HiTrap® column via a low-protein-binding filter for purification. After injection onto the column electrovalve 3 was switched back to

position A and the HiTrap® was eluted with PBS using a syringe from outside the fume-cupboard. The first 0.5 ml were sent to waste, [^{18}F]rhIL-1RA eluted within the following 2 ml fraction which was collected, weighted, the radioactivity measured and a sample (20 µl) analyzed for QC.

[^{18}F]rhIL-1RA was prepared within 100 min, from the time of the addition of the $^{18}F^-$, with 7.1-24.2% radiochemical yield (mean value 11.4 ± 4.1**%,** based on seventeen syntheses and decay corrected). [^{18}F]rhIL-1RA, 60.31 to 310.8 MBq (uncorrected for decay) was thus collected as a 2 mL fraction. The specific activity ranged from 913.15 to 5040.20 MBq/µmol. From 2 mg of initial rhIL-1RA, 1.1 to 1.9 mg was recovered as a mixture of labeled and unlabelled protein.

Quality Control

SE-HPLC

QC analyses of rhIL-1RA and [^{18}F]rhIL-1RA were made by size exclusion high-performance liquid chromatography (SE-HPLC) performed on a HPLC Shimadzu prominence system operated using a LabLogic software Laura 3 and configured with a CBM-20A controller, an LC-20AB solvent delivery system and a SPD-20A dual wavelength absorbance detector set at 254 and 235 nm. The system was equipped with a Superdex® Gel Filtration Column Peptide HR10/300 GL (GE Healthcare, UK) eluted with PBS at a 1 ml/min flow-rate. Radioactivity was monitored with a radio-HPLC Bioscan Flowcount B-FC 3100 detector.

SDS PAGE

Fifteen percent acrylamide gels were cast with a 4% acrylamide stacking gel using a Mini Protean III system (Bio-Rad). 5µl Prestained Precision Plus Protein Standards (BioRad, UK, Catalogue number 161-0375) were loaded into lane one and a sample of ca 50 ng of mixed radiolabelled and unlabelled protein from the 1.6-1.8 mg recovered fraction of rhIL-1RA diluted in 2X Laemlli Buffer (4% sodium dodecyl sulphate (SDS), 20% Glycerol, 120mM Tris.Cl pH 6.8, 0.01% Bromophenol blue, 10% 2-mercaptoethanol) was loaded into lane 2. They were run at 30mA until the dye appeared at the bottom at which point they were removed and fixed by immersion in 45% deionised water, 45% methanol and 10% acetic acid. Gels of radiolabelled rhIL-1RA were then photographed, sealed in clingfilm and placed into an imaging cassette. Autoradiography was performed using a Fujifilm Bio-Imaging

Analyzer BAS-1800II (FujiFilm U.K. Ltd., U.K) and data were analysed using Advanced Image Data Analyzer software (Raytest, Straubenhardt, Germany). Radiolabelled protein was sized by overlaying the photograph onto the autoradiogram. Gels of unlabelled rhIL-1RA were stained with Coomassie Brilliant Blue (PhastGel™ Blue R, GE Healthcare, UK).

In vitro binding of [^{18}F]rhIL-1RA to IL-1 receptor.

An *in vitro* assay was performed to investigate the ability of the produced [^{18}F]rhIL-1RA to bind to the IL-1 receptors. The assay was conducted using rat brain slices (n = 3; 9-11 brain sections per rat). Binding of the labeled protein was detected by autoradiography.

Brain sample preparation

Adult, male, Sprague-Dawley rats (250-300 g body-weight) were used to perform autoradiography experiments. The animals were housed in a controlled environment of 12 h light/dark cycle (08:00/20:00 h) at 22 °C. Transient focal cerebral ischemia (60 min) was induced in rats by the intraluminal thread method, as described previously[30]. 7 days post-MCAO, rats were killed by anaesthetic overdose with Isoflurane and decapitated. Brains were removed quickly and frozen in cooled (-40°C) isopentane. Coronal brain sections were cut serially (20µm at 1.2mm intervals between each level) on frozen brains by cryostat. All procedures were performed in accordance with UK legislation under the 1986 Animals (Scientific Procedures) Act and by approved protocols (Home Office Project License Number 40/3076).

Binding assay.

Specific binding of [^{18}F]rhIL-1RA was determined by comparing the level of total binding (specific and non-specific binding) and the level of non-specific binding in matched rat brain sections. To determine total binding, slices of healthy rat brains were pre-incubated in 10 mM phosphate buffer saline (PBS) at 4°C for 5 min, then incubated in solutions of different concentrations of the [^{18}F]rhIL-1RA (10, 20 and 40 nM in PBS, 10 mM, at room temperature). After 30 min incubation, the slices were washed three times 3 min in PBS, to remove unbound radiolabelled protein, then quickly rinsed in cold distilled water, before exposition to PhosphorImager plates overnight. To determine non-specific binding, a second set of brain sections were treated as described above but in a solutions containing [^{18}F]rhIL-1RA (10, 20

and 40 nM) and one thousand-fold excess (i.e. 10 to 40 µM) of non-radiolabelled rhIL-1RA. Radiolabelled rhIL-1RA that was not displaced by non-radiolabelled rhIL-1RA accounted for the non-specifically bound. Specific binding was calculated by subtracting the non-specific from total binding of [^{18}F]rhIL-1RA.

Result and discussion

Although targetting randomly ε-amino groups of lysine moieties could be considered as the drawback of this labeling approach, with [^{18}F]fluoroacetaldehyde the size of the added [^{18}F]fluoroethyl substituent is small and should have little effect on the physical chemical properties and the structure of the protein allowing PET pharmacokinetic studies. In addition to its small size [^{18}F]fluoroacetaldehyde presents following advantages: first it is easily produced via a fast and simple procedure in a two-step, one-pot reaction using oxidation with DMSO of [^{18}F]fluoroethyltosylate, second it is simply extracted continuously by distillation from the reaction mixture sparing a purification step using HPLC or solid phase extraction and finally the highly hydrophilic aldehyde is efficiently trapped in a small volume of water (<100µl). Furthermore the mild labeling conditions, citrate buffer pH 6 and low temperature (38°C), make the purification of the radiolabelled protein straightforward. Purification of the [^{18}F]rhIL1-ra was thus simply made by eluting the reaction mixture through a HiTrap desalting column. Analysis of the crude synthesis mixture by SE-HPLC using the radioactivity detector before purification on the HiTrap cartridge showed that it contained [^{18}F]rhIL-1RA (R_t = 12.2 min), unreacted [^{18}F]fluoroacetaldehyde (R_t = 20 min) and a minor unidentified radioactive impurity (R_t = 24.2 min) (Figure 3). [^{18}F]rhIL-1RA accounted for 28-35% of the total radioactivity of the analyte of the synthesis mixture (yield based on three analyses). Identification of the second peak as [^{18}F]Fluoroacetaldehyde was made by comparing the retention time with standard fluoracetaldehyde prepared as previously described[22]. The unidentified radioactive impurity may have resulted from [^{18}F]fluoroacetaldehyde reduction to [^{18}F]fluoroethanol or the reaction of free cyanide ion released from sodium cyanoborohydride with [^{18}F]fluoroacetaldehyde to produce the cyanohydrin, lactonitrile[31]. Both small molecules were sufficiently retained on the HiTrap column to allow the protein to be eluted as a pure compound under monomeric and dimeric form with a radiochemical purity, for the mixed two forms, over 95% in a small volume (2 ml). QC SE-HPLC analysis of the [^{18}F]rhIL-

1RA, UV absorbance trace as well as the radioactivity trace (Figure 4) showed two poorly resolved peaks. On the UV absorbance trace, the small peak at retention time 10.0 min preceding a larger one at retention time 11.8 min, suggested the presence of a dimer. SDS-PAGE analysis of the labeled rhIL-1RA (Figure 5) confirmed the presence of a minor dimeric fraction (faint band at approximately 35 kD), but most of the radioactivity migrated to a position consistent with a 17 kDa protein. Similarly, the SE-HPLC chromatogram of the reference rhIL-1RA showed two peaks (data not shown) nevertheless only a monomeric molecular weight was seen by SDS-PAGE (data not shown).

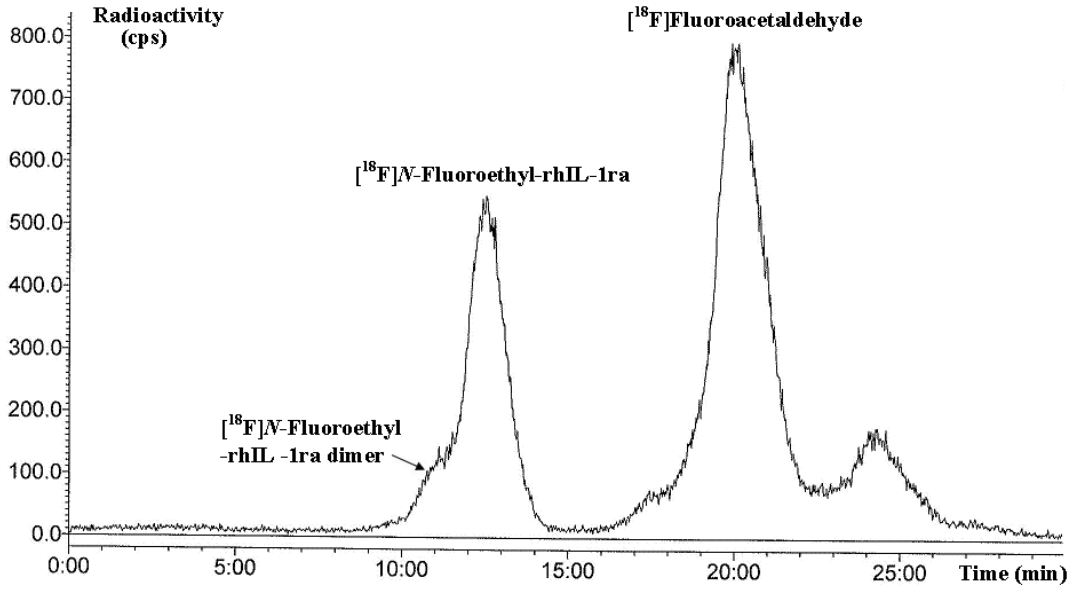

Figure 3: Radio-SE-HPLC analysis of the crude synthesis mixture. [^{18}F]rhIL-1RA (R_t = 12.2 min), [^{18}F]fluoroacetaldehyde (R_t = 20 min), unidentified radioactive impurity (R_t = 24.6 min).

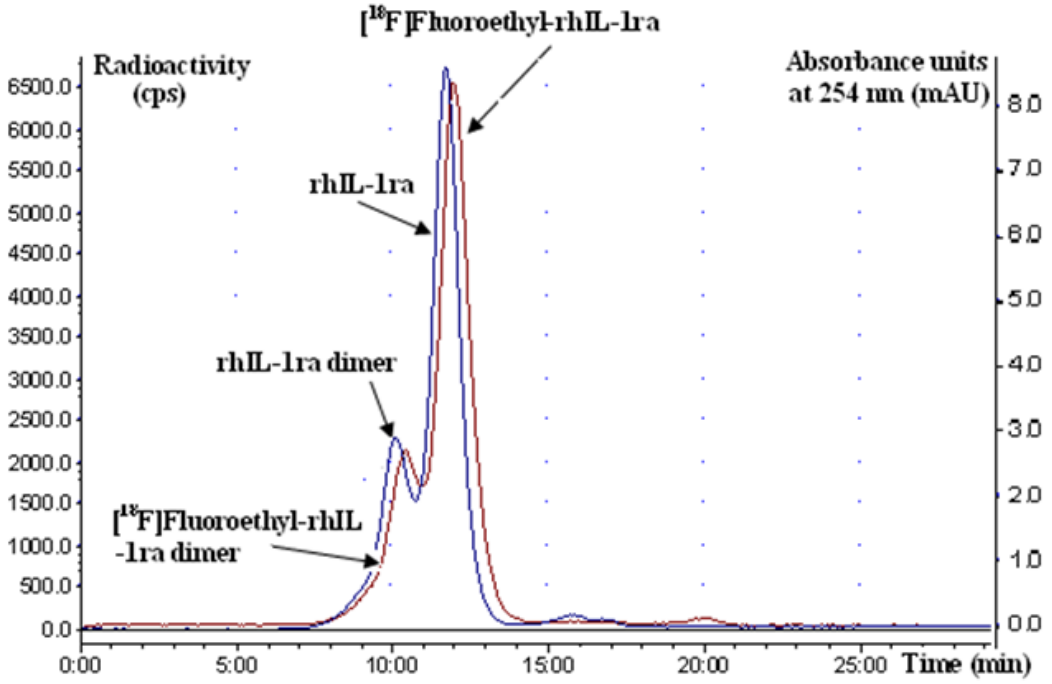

Figure 4: QC of the purified [^{18}F]rhIL-1RA, SE-HPLC uv-trace and radio-trace.

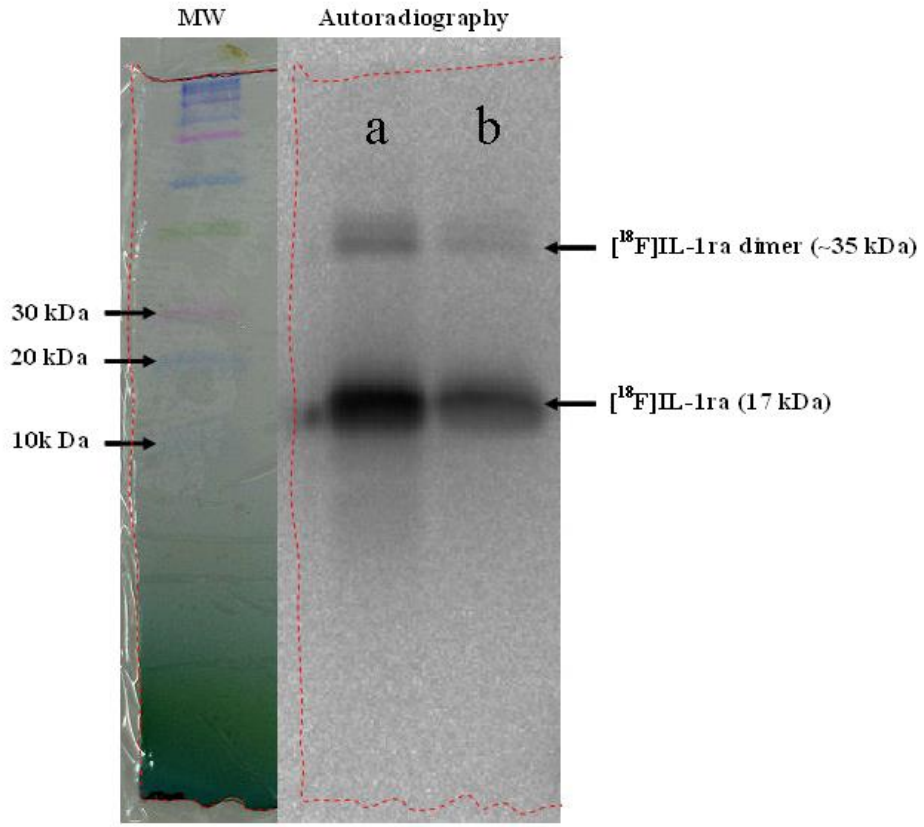

Figure 5: PAGE analysis of the purified [^{18}F]rhIL-1RA (MW: molecular weight references loaded in the same lane than [^{18}F]rhIL-1RA (a)) and autoradiography (a: 1.1 µg of rhIL-1RA = 17.8 kBq in 20µl; b: 0.1 µg of rhIL-1RA = 2.2 kBq in 20µl).

At relatively high concentrations (i.e. 100 mg/ml), rhIL-1RA exists in a monomer-dimer equilibrium[32-35]. Chang et al. (1996)[32] have also shown that an irreversible dimer formed, that amounted to 8% of the total soluble protein, during storage for two months at 30 °C and this irreversible dimer was mostly dissociated during SDS-PAGE. Our radiolabeling method was applied to other proteins without producing dimerization (data not shown), thus we cannot exclude the possibility that production of the dimer was caused during storage of the rhIL-1RA solution and the non-visualisation of unlabelled rhIL-1RA dimer by SDS-PAGE/Coomassie staining was due to a lack of sensitivity of this technique.

Since expression of IL-1 receptors has been reported before in rat and mouse brains[36-38], we choose to use autoradiography on rat brain sections to test whether we could observe any specific binding (displaceable) of our [^{18}F] radiolabelled IL-1RA. Specificity of binding was determined by displacement of the bound [^{18}F]rhIL-1RA by an excess of unlabelled rhIL-1RA on rat brain sections as measured by autoradiography (Figure 6 a). Comparison of the total binding (Tot) and non-specific binding (NS) indicated that specific binding (Spe) of the radiolabelled [^{18}F]rhIL-1RA to IL-1 receptors accounted for 24 to 29% of total binding (Figure 6 b). Aware of the high concentrations of [^{18}F]rhIL-1RA (mixed with unlabelled) used for autoradiography when compared to the reported K_d of IL-1RA for the IL-1 receptors, we have tried to assess specific binding with lower concentrations of [^{18}F]rhIL-1RA (1nM) using autoradiography and binding on cell membranes preparation; unfortunately due to the relatively short half-life of fluorine-18 (when compared with iodine-125 for example), we could not detect any reliable signal on the PhosphorImager plates or by γ-counting. Clearly, fluorine-18 labeling of protein would not be the most convenient and appropriate technique to assess *in vitro* binding of a tracer to receptors expressed at very low levels such as the IL-1 receptors. In this study, exemplifying this new radiochemistry, the main aim of labeling rhIL-1RA was more to develop a tool to assess the biodistribution and metabolisms of IL-1RA than its *in vitro* binding, especially when considering the high level of non-specific binding observed here.

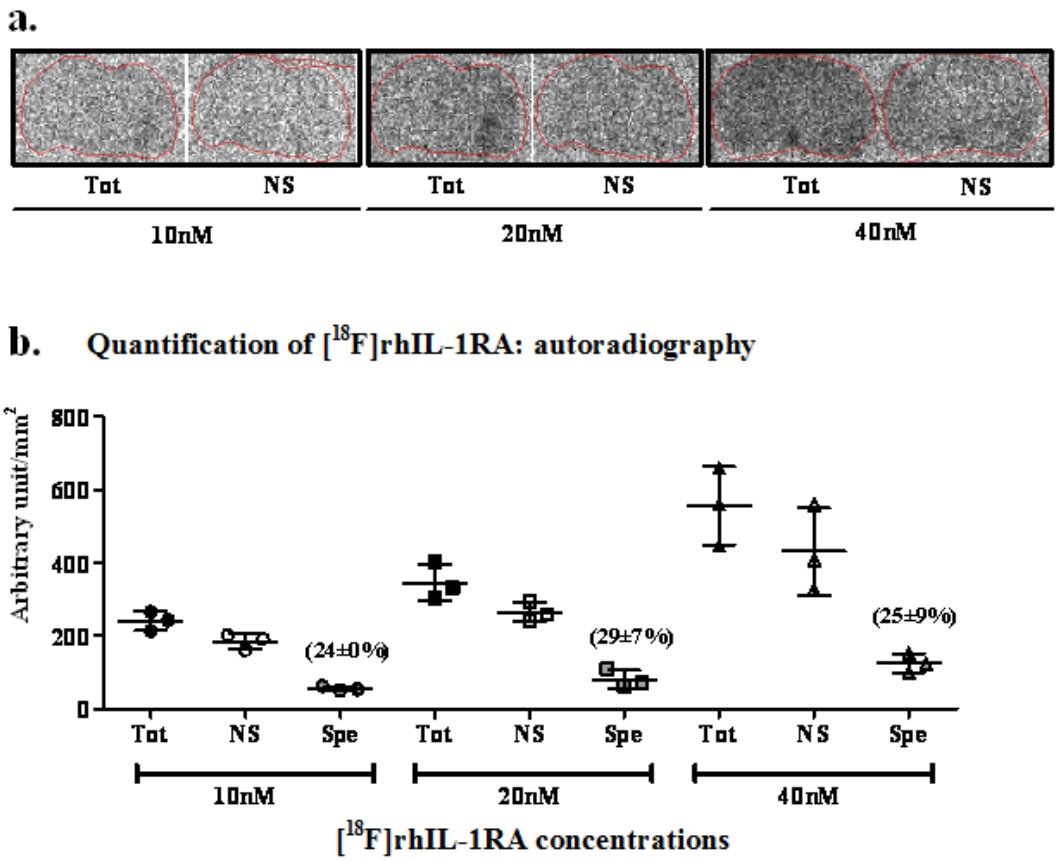

Figure 6: (a) Representative examples of autoradiography of rat brain slices by incubation with 10nM, 20nM and 40nM of [^{18}F]rhIL-1RA (mixture of [^{18}Frh]IL-1RA, [^{19}F]rhIL-1RA and precursor rhIL-1RA. Non-specific binding (NS) was assessed by incubating the brain sections with [^{18}F]rhIL-1RA (10, 20, 40nM) together with an excess of unlabelled rhIL-1RA (10, 20 and 40µM). (b) Specific binding (indicated as percentage of total binding in brackets, mean ± SD) of various concentrations of [^{18}F]rhIL-1RA on rat brain sections.

Conclusion

We describe here a simple method for radiolabeling of rhIL-1RA using [^{18}F]fluoroacetaldehyde. Radiosynthesis and purification, using a HiTrap® desalting column, were carried out in a remotely controlled experimental rig within 100 min. The radiochemical yield was in the range of 7.1-24.2% (mean value 11.4 ± 4.1%, decay-corrected, based on seventeen syntheses). Starting from 1.73-3.42 GBq (64-126 mCi) of fluorine-18, 60.31-310.80 MBq (1.63-8.40 mCi) of [^{18}F]rhIL-1RA were produced**.** Moreover we showed that [^{18}F]rhIL-1RA retained binding potency in a rat brain binding assay. Therefore this method allowed us to produce [^{18}F]rhIL-1RA on a small scale with sufficient radiochemical purity and specific activity to enable pharmacokinetic studies in small animals using PET and the investigation of the

relevance of rhIL-1RA as a therapeutic agent in brain traumatisms. Moreover, this radiolabeling technique can be applied to any peptide and protein with lysine moieties available for reaction with [^{18}F]fluoroacetaldehyde; thus providing another method for the radiolabeling of proteins of interest/therapeutic agents, for the assessment of both their pharmacokinetics and biodistribution or their use as imaging biomarkers.

Acknowledgements

The authors would like to thanks AMGEN for providing the rhIL-1RA (Kineret®) (MTA 200613204-001). C. Prenant, M. Fairclough and this project were funded by the Wolfson Molecular Imaging Centre, University of Manchester. C. Cawthorne was funded by Cancer Research UK (Grant C153/A4331). N. Rothwell and H. Boutin are funded by the Medical Research Council (UK).

References

[1] C. A. Dinarello, *The FASEB Journal* **1988**, *2*, 108.
[2] C. A. Dinarello, *Cytokine Growth Factor Reviews* **1997**, *8*, 253.
[3] S. M. Allan, N. J. Rothwell, *Philosophical Transactions B* **2003,** *358*, 1669.
[4] S. M. Allan, P. J. Tyrrell, N. J. Rothwell, *Nature Reviews Immunology* **2005**, *5*, 629.
[5] A. Basu, J. K. Krady, S. W. Levison, *Journal of Neuroscience Research* **2004**, *78*, 151.
[6] H. C. Emsley, C. J. Smith, C. M. Gavin, R. F. Georgiou, A. Vail, E. M. Barberan, K. Illingworth, S. Scarth, V. Wickramasinghe, M. E. Hoadley, N. J. Rothwell, P. J. Tyrrell, S. J. Hopkins, *BMC Neurology* **2007**, *7*, 5.
[7] H. C. Emsley, C. J. Smith, P. J. Tyrrell, S. J. Hopkins, *Neurocritical Care* **2008**, *9*, 125.
[8] S. M. Lucas, N. J. Rothwell, R. M. Gibson, *British Journal of Pharmacology* **2006**, *147 Suppl 1*, S232.
[9] D. E. Furst, *Clinical Therapeutics* **2004**, *26*, 1960.
[10] E. Pinteaux, N. J. Rothwell, H. Boutin, *Glia* **2006**, *53*, 551.
[11] O. Touzani, H. Boutin, J. Chuquet, N. Rothwell, *Journal of Neuroimmunology* **1999**, *100*, 203.
[12] H. Emsley, C. Smith, R. Georgiou, A. Vail, S. Hopkins, N. Rothwell, P. Tyrrell, *Journal of Neurology, Neurosurgery, and Psychiatry* **2005**, *76*, 1366.
[13] S. R. Clark, C. J. McMahon, I. Gueorguieva, M. Rowland, S. Scarth, R. Georgiou, P. J. Tyrrell, S. J. Hopkins, N. J. Rothwell, *Journal of Cerebral Blood Flow and Metabolism* **2008**, *28*, 387.
[14] D. C. Kim, B. Reitz, D. F. Carmichael, D. C. Bloedow, *Journal of Pharmaceutical Sciences* **1995**, *84*, 575.
[15] C. J. van der Laken, O. C. Boerman, W. J. Oyen, M. T. van de Ven, J. W. van der Meer, F. H. Corstens, *European Journal of Nuclear Medicine and Molecular Imaging* **1998**, *25*, 347.

[16] J. R. Grierson, K. J. Yagle, J. F. Eary, J. F. Tait, D. F. Gibson, B. Lewellen, J. M. Link, K. A. Krohn, *Bioconjugate Chemistry* **2004**, *15*, 373.
[17] R. Haubner, H.-J. Wester, W. A. Weber, C. Mang, S. I. Ziegler, S. L. Goodman, R. Senekowitsch-Schmidtke, H. Kessler, M. Schwaiger, *Cancer Research* **2001**, *61*, 1781.
[18] G. Kramer-Marek, D. O. Kiesewetter, L. Martiniova, E. Jagoda, S. B. Lee, J. Capala, *European Journal of Nuclear Medicine and Molecular Imaging* **2008**, *35*, 1008.
[19] S. M. Okarvi, *European Journal of Nuclear Medicine and Molecular Imaging* **2001**, *28*, 929.
[20] Z. Cheng, O. P. De Jesus, M. Namavari, A. De, J. Levi, J. M. Webster, R. Zhang, B. Lee, F. A. Syud, S. S. Gambhir, *Journal of Nuclear Medicine* **2008**, *49*, 804.
[21] H. J. Wester, M. Schottelius, in *PET Chemistry, Vol. 64* (Eds.: P. A. Schubiger, L. Lehmann, M. Friebe), Springer Berlin Heidelberg, **2007**, pp. 79.
[22] C. Prenant, J. Gillies, J. Bailey, G. Chimon, N. Smith, G. C. Jayson, J. Zweit, *Journal of Labelled Compounds and Radiopharmaceuticals* **2008**, *51*, 262.
[23] G. E. Means, R. E. Feeney, *Analytical Biochemistry* **1995**, *224*, 1.
[24] G. E. Means, *Methods in Enzymology* **1977**, *47*, 469.
[25] N. Jentoft, D. G. Dearborn, *Journal of Biological Chemistry* **1979**, *254*, 4359.
[26] K. F. Geoghegan, J. C. Cabacungan, H. B. Dixon, R. E. Feeney, *International Journal of Peptide and Protein Research* **1981**, *17*, 345.
[27] M. G. Straatmann, M. J. Welch, *The Journal of Nuclear Medicine* **1975**, *16*, 425.
[28] G. Berger, M. Mazière, C. Prenant, J. Sastre, D. Comar, *The International Journal of Applied Radiation and Isotopes* **1984**, *35*, 81.
[29] R. J. Evans, J. Bray, J. D. Childs, G. P. Vigers, B. J. Brandhuber, J. J. Skalicky, R. C. Thompson, S. P. Eisenberg, *Journal of Biological Chemistry* **1995**, *270*, 11477.
[30] E. Z. Longa, P. R. Weinstein, S. Carlson, R. Cummins, *Stroke* **1989**, *20*, 84.
[31] M. J. Gidley, J. K. Sanders, *Biochemical Journal* **1982**, *203*, 331.
[32] B. S. Chang, R. M. Beauvais, T. Arakawa, L. O. Narhi, A. Dong, D. I. Aparisio, J. F. Carpenter, *Biophysical Journal* **1996**, *71*, 3399.
[33] S. Roy, R. Jung, B. A. Kerwin, T. W. Randolph, J. F. Carpenter, *Journal of Pharmaceutical Sciences* **2005**, *94*, 382.
[34] J. R. Alford, B. S. Kendrick, J. F. Carpenter, T. W. Randolph, *Journal of Pharmaceutical Sciences* **2008**, *97*, 3005.
[35] J. R. Alford, S. C. Kwok, J. N. Roberts, D. S. Wuttke, B. S. Kendrick, J. F. Carpenter, T. W. Randolph, *Journal of Pharmaceutical Sciences* **2008**, *97*, 3035.
[36] P. Parnet, S. Amindari, C. Wu, D. Brunke-Reese, E. Goujon, J. A. Weyhenmeyer, R. Dantzer, K. W. Kelley, *Brain Research Molecular Brain Research* **1994**, *27*, 63.
[37] R. A. French, R. W. VanHoy, R. Chizzonite, J. F. Zachary, R. Dantzer, P. Parnet, R. M. Bluthe, K. W. Kelley, *Journal of Neuroimmunology* **1999**, *93*, 194.
[38] W. J. Friedman, *Experimental Neurology* **2001**, *168*, 23.

Publication 5 (page 180)

CHAPTER 6: A new Technique for The Radiolabelling of Mixed Leukocytes with Zirconium-89 for Inflammation Imaging with Positron Emission Tomography

Submitted for Publication

A new Technique for The Radiolabelling of Mixed Leukocytes with Zirconium-89 for Inflammation Imaging with Positron Emission Tomography

M. Fairclough[1], C. Prenant[1], B. Ellis[2], H. Boutin[1], A. McMahon[1], G. Brown[1], P. Locatelli[3] and A. Jones[4]*

1. Wolfson Molecular Imaging Centre, Manchester, UK. 2. Central Manchester University Hospital, NHS Foundation Trust, UK. 3. Materials Science Building, University of Manchester, Manchester, UK. 4. Clinical Sciences Building, Salford Royal NHS Foundation Trust, Manchester, UK

**Correspondence to: M. Fairclough, Wolfson Molecular Imaging Centre, The University of Manchester, 27 Palatine Road, Manchester M20 3LJ, UK. Tel.: +44(0)1612750034*

E-mail: michael.fairclough@manchester.ac.uk

Abstract

PURPOSE: Mixed leukocyte (white blood cells [WBCs]) trafficking using positron emission tomography (PET) is receiving growing interest to diagnose and monitor inflammatory conditions. PET, a high sensitivity molecular imaging technique, allows precise quantification of the signal produced from radiolabelled moieties.

PROCEDURES: Chitosan nanoparticles (CN) were used to deliver radiometals into WBCs. Experiments were carried out using mixed WBCs freshly isolated from whole human blood.

RESULTS: WBCs labelling efficiency was higher with [^{89}Zr]-loaded-CN (76.8% ± 9.6% (n=12)) than with [^{64}Cu]-loaded-CN (26.3% ± 7.0 % (n=7)). [^{89}Zr]-labelled WBCs showed an initial loss of 28.4% ± 5.8% (n=2) of the radioactivity after 2 hours. This initial loss was then followed by a plateau as [^{89}Zr] remains stable in the cells.

CONCLUSIONS: WBCs labelling with [^{89}Zr]-loaded-CN showed a fast kinetic of cell uptake, high labelling efficiency and a relatively good retention of the radioactivity. This method has potential application for PET imaging of inflammation.

Keywords: PET, zirconium-89, copper-64, Inflammation Imaging, White Blood Cell Trafficking

Introduction

Different imaging modalities have been applied to image inflammation. Magnetic resonance imaging (MRI) and ultrasound imaging have provided some promising methods of assessing synovitis in joints[1] but have failed to provide quantitative methods of measuring inflammation.

Radiolabeled leukocyte scintigraphy with Single-Photon Emission Computed Tomography (SPECT) using Technetium-99m and Indium-111 chelates are the most widely used clinical procedures for the assessment of inflammatory diseases[2]. Molecular imaging technologies such as SPECT and Positron Emission Tomography (PET) are well suited for tracking the migration of leukocytes to inflammation foci *in vivo*. However the sensitivity of PET (10^{-11}–10^{-12} M) is at least 1–2 orders of magnitude higher than single photon imaging systems (10^{-10} M)[3] and PET is more attractive for the quantification of the regional signal from migrated cells. Therefore, *in vivo* imaging of leukocyte trafficking using PET is receiving growing interest for applications in immunological studies to ***i)*** track the selective recruitment of specific immune cells during pathogenesis, ***ii)*** detect probable infectious/inflammatory foci and ***iii)*** devise rational therapeutic strategies[4] and carry out longitudinal studies.

Different approaches have been developed for tracking radiolabelled leukocytes *in vivo* with PET using the positron emitting isotopes copper-64 ([^{64}Cu], $t_{1/2}$ = 12.7 h) and fluorine-18 ([^{18}F], $t_{1/2}$ = 109.7 min). Cationic [^{64}Cu]$^{2+}$ requires a chelate to transport it into cells, ^{64}Cu-pyruvaldehyde-bis(N^4-methylthiosemi-carbazone) (PTSM), [^{64}Cu]-polyethylenimine (PEI) and [^{64}Cu] loaded magnetic nanoparticles have been reported for WBC labelling[3-5]. [^{64}Cu]-PTSM proved to be superior to [^{18}F]-FDG-labelled leukocytes with a higher and more reproducible labelling efficiency[6]. Furthermore the short physical half-life of [^{18}F] is not suitable for long term observations and non-specific uptake was observed with [^{18}F]-FDG-labelled leukocytes partly due to high efflux of [^{18}F] after injection[7]. In addition carbon-11 ([^{11}C], $t_{1/2}$ = 20.3 min) has been utilised for macrophage imaging in rheumatoid synovitis[8]. The PET tracer [^{11}C]PK11195, a substrate for the peripheral benzodiazepine receptor which can be found on macrophage was used. The

constraints of the short physical half-life of [^{11}C] means that this method of imaging macrophages is restricted to static scans of joints and is not appropriate for trafficking of macrophages.

The positron emitter Zirconium-89 ([^{89}Zr], t ½ = 78.4h), has emerged as a suitable radioisotope for imaging processes with longer pharmacokinetics with PET[9-12] due to its physical decay properties. [^{89}Zr] has had successful applications in immune-PET imaging[10-15] as well as applications in antibody labelling for preclinical PET scanning, and is ideally suited for cell trafficking over long periods of time[9], [^{89}Zr] labelled dextran nanoparticles have been used for *in vivo* macrophage imaging[16]. In comparison to [^{64}Cu], [^{89}Zr] has a longer physical half-life as well as a higher positron emission branching ratio of 22.3% compared to 17.5% for [^{64}Cu]. Furthermore the relatively low energy of the emitted positron (E_{ave} β^+ = 396 keV) results in high resolution [^{89}Zr] images comparable to those observed with [^{64}Cu]. Desferrioxamine B (DFO) is the most successfully employed chelator of [^{89}Zr]$^{4+}$ metal ions owing to its high affinity for the metal[11, 12]. Nevertheless the hydrophilic property of DFO makes it unsuitable for carrying [^{89}Zr] into cells across the lipophilic membrane. More recently [^{89}Zr]-Oxinate$_4$ has been used to for *in vivo* cell trafficking with PET[17]. This technique showed a radiolabelling yield comparable to that with indium-111 SPECT, as well as a high retention of [^{89}Zr] in cells, however further evaluation of cytotoxicity effects is required[17].

Chitosan, a biocompatible and non-antigenic co-polymer of glucosamine and *N*-acetylglucosamine with metal ion chelating properties[18] is an appropriate carrier of [^{89}Zr] for cell labelling. Chitosan has been reported to show potential as a carrier for drug and gene delivery to cells[19-30], and chitosan-based formulations have been prepared for drug delivery systems. Chitosan is widely available, inexpensive and can be obtained in a wide variety of molecular weight distributions as well as at differing degrees of deacetylation (DD).

The free amino (depending on DD) and hydroxyl groups of chitosan allows for conjugation with peptides and proteins or the incorporation of inorganic materials including metal ions[18]. Both chitosan polymer and CN have acquired great interest in various fields including wound dressing[21, 31] and tissue engineering[20] applications which are made possible by the biocompatibility, biodegradability and

non-toxicity properties offered by chitosan[21, 22, 32]. Furthermore various chitosan composites have been investigated for biomedical applications[33-36] and molecular imaging[37, 38]. The preparation of chitosan quantum dot composites for drug or gene delivery with optical imaging utility has been reported[34, 39, 40] and biocompatible carboxymethyl-chitosan (CMCS)-coated super paramagnetic iron oxides have been prepared to visualise human stem cells with MRI[37, 41]. Also RGD peptide delivery systems have been prepared from glycol CN for use as an antiangiogenic model drug in cancer therapy[37, 42].

CN can be constructed from chitosan polymer by microemulsification or complex coacervation however both methods require harsh processing conditions and organic solvents or toxic reagents[43]. Alternatively ionotropic gelation[25-27, 43, 44] can be used which involves cross-linking chitosan polymer chains with a poly anion. This is carried out in mild and aqueous conditions which could potentially be exploited for delivery of PET radioisotopes into circulating leukocyte cells. CN have been shown to penetrate cells by a number of endocytosis and pinocytosis uptake pathways[19]. Compared to other cationic polymers used for cell transfection such as PEI[45], chitosan is reported to display less cytotoxicity while maintaining cell viability[46].

Described in this work is a new technique to radiolabel mixed human leukocytes with [^{89}Zr] and [^{64}Cu] using CN as carrier. The radiometals are directly compared for their affinity for CN, uptake into cells and cell retention. Previously, [^{89}Zr] labelled dextran nanoparticles have been used for macrophage imaging[16] however the reported method required the use of epichlorohydrin as a reticulating agent to form the nanoparticles. This was followed by coupling the nanoparticles to DFO in order to complex [^{89}Zr] and finally an amino end-capping step. The method reported here is much less complex in terms of building the CN and requires neither the use of toxic organic reagents to construct the nanoparticles nor coupling to DFO or any other complexing agent. This method for radiolabelling mixed leukocytes can be translated to a preclinical model of inflammation to assess its potential for future clinical assessment of inflammatory disease.

Materials and Methods

Materials and Equipment

[^{89}Zr] oxalate was purchased from Perkin Elmer (Italy)/BV cyclotron (Netherlands), [^{64}Cu] copper chloride was purchased from Cambridge University; Chitosan 15 kDa (> 85% degree of deacetylation) was purchased from Tebu-bio (France) chitosan 50 – 190 kDa (85% degree of deacetylation) and chitosan 190 – 310 kDa (85% degree of deacetylation) were purchased from Sigma Aldrich (UK). Acetic acid, sodium hydroxide, pentasodium tripolyphosphate (TPP) were all purchased from Sigma Aldrich (UK) and were used without any further purification. An Edwards Modulyo 4K Freeze dryer (UK) was used to freeze dry CN.

Acid Citrate Dextrose (formula A) was purchased from Huddersfield Pharmacy Manufacturing Unit (UK) and HESPAN 6% solution (hydroxyethyl starch) was purchased from Grifols (UK). Hank's balanced salt solution, Trypan blue solution (0.4% w/v) and Haemocytometer were all acquired from Sigma Aldrich (UK).

A PK121R multispeed refrigerated centrifuge from Thermo Scientific (UK) was used along with a Micro Centaur centrifuge (MSE, UK). For radiolabelling of CN, uptake and retention of [^{89}Zr]/[^{64}Cu]-loaded CN into leukocyte cells a Thermo Shaker PHMT (from Grant Instruments UK) was used to heat and agitate the solutions. A Vortex Genie-2 which was obtained from Scientific Instruments (US), was used to re-suspend solutions where necessary. The procedure for separation of mixed leukocytes from whole blood was performed in a SafeFlow 1.2 safety cabinet from Bioair Instruments (Italy). Measurements of radioactive samples were performed with an Isomed 2000 dose calibrator from MED (Germany) and a 1470 Wizard Automatic Gamma Counter from Perkin Elmer (UK). Scanning Electron Microscopy Images were taken using a Phillips XL30 FEG SEM and an Olympus BX51 microscope (Japan) was used to view cells for the cell viability assay.

Chitosan nanoparticle construct

Chitosan (15 kDa, > 85% degree of deacetylation, 0.3 g) was solubilised in a 1% acetic acid solution (60 mL) and was left to stir for 1 hour. The pH of the chitosan solution was then adjusted to 4.7 with the addition of sodium hydroxide (0.2 M). A solution of sodium tripolyphosphate (50 mg in 20 mL of deionised water) was added in a drop-wise manner to the chitosan solution with stirring. CN formed

instantaneously on addition of the poly anion. CN were isolated by centrifugation at 3,025 g for 30 minutes at 4 ˚C, the supernatant was removed and the nanoparticles were washed with deionised water and centrifugation was repeated. The supernatant was removed and the nanoparticles were isolated as a gel and placed in a desiccator for 3 hours. CN where stored at 2-4 ˚C as this temperature was reported to have no effect on size and physical stability of the particles[47], and the particles were characterised via scanning electroscope microscopy (SEM). In order to assess the amount of dry chitosan in the chitosan nanoparticle gel, samples were freeze-dried to remove water. Following the free dry process the dry residue was weighed to determine the content of chitosan.

Isolation of mixed human leukocytes

Each experiment was carried out using mixed white blood cells (WBC) freshly isolated from whole blood following erythrocyte sedimentation according to a reported procedure[48, 49]. Venous blood (51 mL) taken from healthy volunteers and was drawn into syringes containing acid-citrate dextrose (ACD) in a proportion of 1.5 parts to 8.5 parts of whole blood. The contents were mixed well and dispensed into two 50 mL Falcon tubes. Next 3 mL of 6% hydroxy ethyl starch (Hespan) was added to each tube and the contents mixed slowly to avoid the formation of air bubbles. The Falcon tubes were maintained in an upright position for 60 minutes to allow red blood cells to settle. The leukocyte-rich platelet-rich plasma (LRPRP) supernatant was then carefully removed and centrifuged at 150 g for 5 minutes at room temperature to obtain a supernatant of platelet-rich plasma (PRP) and a pellet of mixed leukocytes. The PRP supernatant was removed and the mixed leukocyte pellet was re-suspended in saline (2 mL). Next the PRP was centrifuged at 1500 g for 10 minutes at room temperature to obtain cell free plasma (CFP) which was removed and retained for washing and re-suspending cells following the radiolabelling process.

Radiolabelling of chitosan nanoparticles with [^{89}Zr] and [^{64}Cu]

Approximately 15-20 mg of the chitosan nanoparticle gel was re-suspended in deionised water (300 µL) in a 1.5 mL Eppendorf vial. [^{89}Zr] (in oxalic acid) or [^{64}Cu] (as aqueous [^{64}Cu] chloride ([^{64}Cu]Cl_2)) was added to the Eppendorf vial (approximately 400 kBq) before being placed in a thermo-shaker and incubated at 1400 rpm at room temperature for 45 minutes. Following incubation the mixture was

centrifuged at 11,600 g for 10 minutes to leave a supernatant containing free [^{89}Zr]-oxalate or [^{64}Cu]Cl_2 and a pellet containing [^{89}Zr] or [^{64}Cu] loaded CN. Next the [^{89}Zr] or [^{64}Cu] loaded CN were washed with water (300 µL) and centrifugation was repeated to remove any free [^{89}Zr] or [^{64}Cu]. The radioactivity in the supernatants and pellet were then counted in a gamma counter and the radiolabelling efficiency is expressed as percentage of the ratio between radioactivity associated with the CN and total radioactivity.

Uptake and retention of [^{89}Zr]- or [^{64}Cu]- loaded chitosan nanoparticles into mixed human Leukocytes

The [^{89}Zr]- or [^{64}Cu]-loaded CN were re-suspended in saline (200 µL) and the re-suspended mixed leukocytes (200 µL in saline) were added to the solution and gently mixed. The mixture was then incubated in a thermo-shaker at 37 ˚C, at 1400 rpm for 15 minutes. Following incubation, leukocyte radiolabelling was terminated by the addition of CFP (1 mL). The radiolabelled leukocytes were separated from the mixture by centrifugation at 150 g for 5 minutes to leave a pellet of [^{89}Zr]- or [^{64}Cu]-labelled leukocytes. The radioactivity in the supernatant and the pellet were counted in a gamma counter. Radiolabelling efficiency is expressed as a percentage of the ratio between radioactivity associated with the leukocytes and total radioactivity.

To assess cell retention of the radioactivity, a sample of leucocytes labelled with [^{89}Zr]- or [^{64}Cu]-loaded CN were re-suspended in CFP and allowed to incubate for 24 hours at 37 ˚C. At intervals of 1, 2, 3, 4 and 24 hours the mixture was centrifuged at 150 g for 5 minutes, the supernatant was removed and the pellet containing [^{89}Zr]- or [^{64}Cu]-labelled leukocytes was re-suspended in fresh CFP. Removed CFP fractions and leukocyte pellets were measured for radioactivity in a gamma counter and the radioactivity efflux rate determined.

Measurement of Cell Viability by Trypan Blue exclusion assay

To measure the viability of cells the Trypan Blue exclusion assay was used. The cell pellet was initially re-suspended in Hank's balanced salt solution (9.5 g/L, 500 µL). Next 50 µL of the cell suspension was added to a falcon tube containing a further 4 mL of Hank's balanced salt solution and 0.4% (w/v) Trypan Blue Solution (500 µL) was added. The solution was mixed and a Pasteur pipette was used to load

the mixture onto a haemocytometer, viable and non-viable cells were then counted in the haemocytometer under a microscope.

Results

Chitosan Nanoparticle construct

Analysis by scanning electron microscope (SEM) of nanoparticles generated from 15 kDa chitosan (Figure 1) showed particles with spherical shape and a size distribution ranging from 57 – 153 nm in diameter.

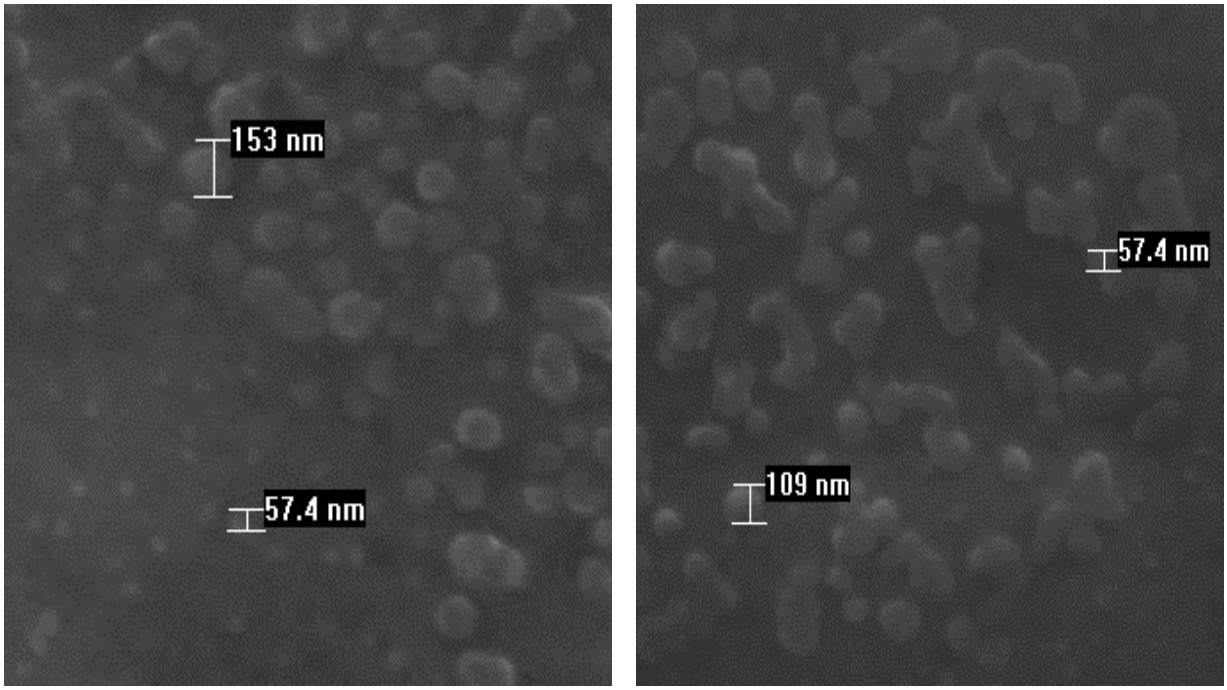

Figure 1: SEM image of CN

Radiolabelling of Chitosan Nanoparticles with [^{89}Zr] and [^{64}Cu]

Results show that CN bind both [^{89}Zr] and [^{64}Cu] very efficiently averaging slightly more than 70% of radiometal uptake after 45 minutes (Table 1 and 2 respectively). The highest labelling efficiency with [^{89}Zr] was observed with nanoparticles built from 190 – 310 kDa (MMW). The labelling efficiency was consistent over all size distributions of CN tested for [^{64}Cu] radiolabelling.

CN	15 kDa	LMW (50 - 190 kDa)	MMW (190 - 310 kDa)
[^{89}Zr] uptake (%)	73.8 ± 18.8 (n=30)	72.8 ± 24.4 (n=8)	90.3 ± 14.8 (n=8)

Table 1: Binding efficiency of [^{89}Zr] to CN produced from various weight distributions of chitosan polymer.

CN	15 kDa	LMW (50 - 190 kDa)	MMW (190 - 310 kDa)
[^{64}Cu] uptake (%)	70.7 ± 16.2 (n=17)	73.5 ± 5.3 (n=3)	71.9 ± 2.3 (n=3)

Table 2: Binding efficiency of [^{64}Cu] to CN produced from various weight distributions of chitosan polymer.

Uptake and retention of [^{89}Zr]-or[^{64}Cu]-Loaded Chitosan Nanoparticles into mixed human Leukocytes

Leukocyte uptake of [^{89}Zr]-loaded CN was measured as a function of incubation time (figure 2). A high initial uptake 82.7% ± 1.9% was followed by a decrease and eventually a plateau at 65.5% ± 13.1% uptake after 30 minutes to 60 minutes incubation (63% uptake).

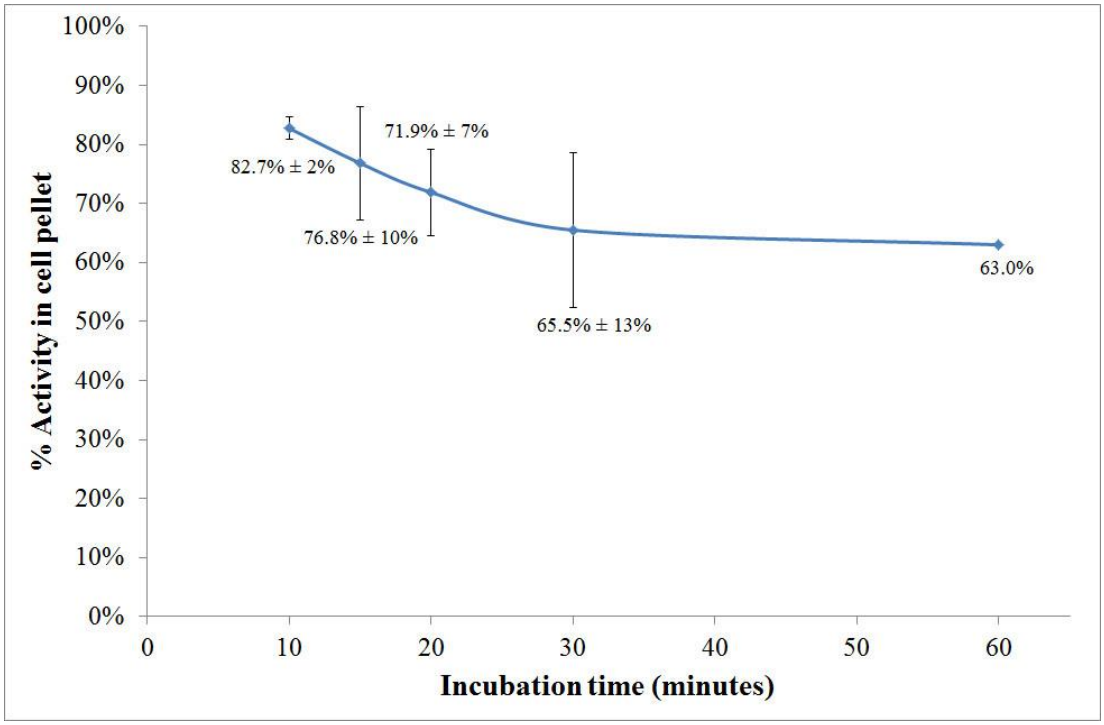

Figure 2: Uptake of [^{89}Zr] labelled CN into mixed human leukocytes cells.

Retention of [^{89}Zr] by the mixed leukocytes was subsequently measured over a period of 24 hours (figure 3).

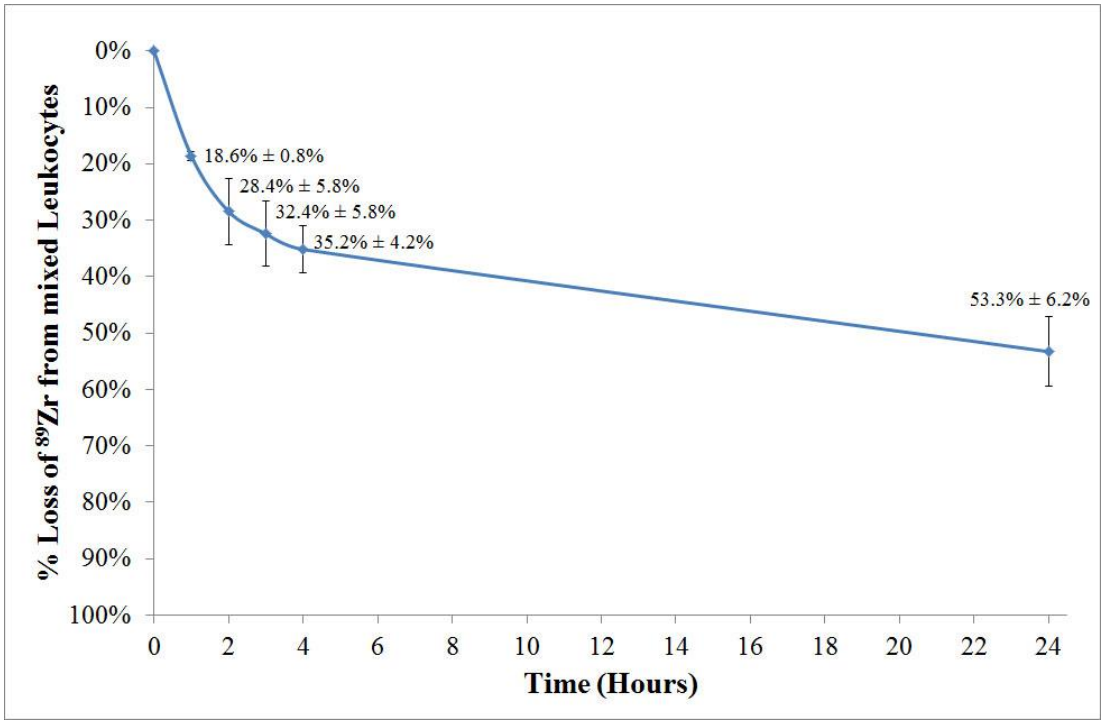

Figure 3: Efflux of [^{89}Zr] from mixed leukocyte cells over 24 hour period (all values are decay corrected to time = 0 hours).

Similarly, cell uptake of [^{64}Cu]-loaded CN and the retention of the radioactivity into the cells was investigated. The uptake efficiency of [^{64}Cu]-loaded CN was significantly lower than was observed for its [^{89}Zr] counterpart as can be seen in figure 4. [^{64}Cu] uptake reached a maximum of 26.3% ± 7.0% (n=7) after 20 minutes incubation time which decreased to 22.6% ± 4.6% (n=3) after 30 minutes incubation.

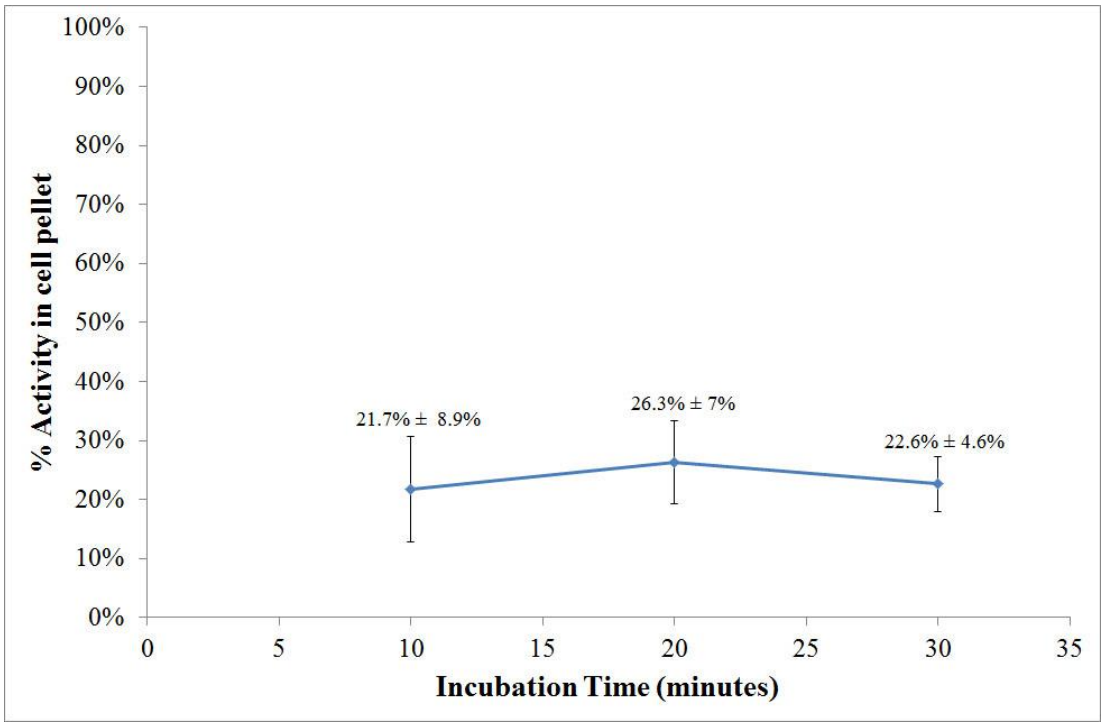

Figure 4: Uptake of [^{64}Cu] labelled CN into mixed human leukocyte cells.

Efflux of [^{64}Cu] from leukocytes was observed after 20 minutes incubation of [^{64}Cu]-loaded CN with mixed leukocytes over a period of 3 hours. Figure 5 shows that the [^{64}Cu] is expelled from the leukocyte cells to a greater extent and at a much faster rate when compared with [^{89}Zr]. More than 90% of the radioactivity was expelled from the cells after 2 hours.

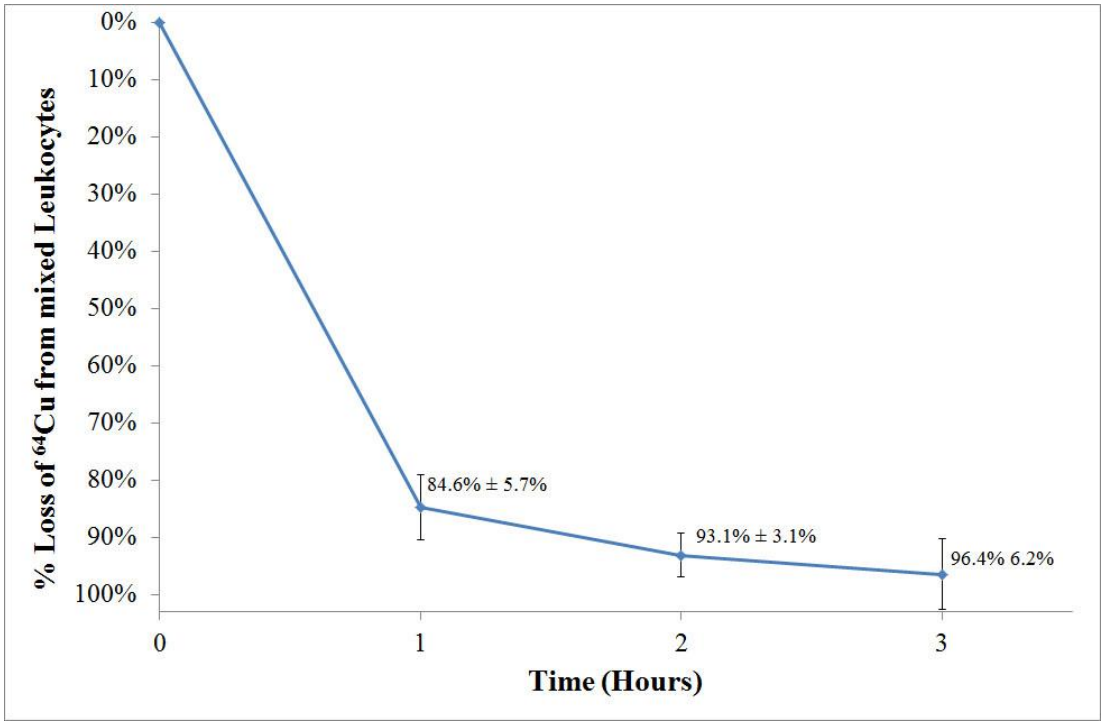

Figure 5: Efflux of [^{64}Cu] from mixed leukocyte cells over 3 hour period (all values are decay corrected to time = 0 hours).

Viability of cells was studied by Trypan Blue exclusion method for [^{89}Zr]-loaded CN only. Immediately following the radiolabelling of mixed leukocytes 61% of the cells remained viable. Following exposure of leukocyte cells to 4.6 mg of CN the amount of viable cells decreased from 99% to 87%. After exposure to 10 mg of CN the amount of viable cells decreased to 81%. Using 20 mg of CN resulted in a cell viability of 70%.

Discussion

Chitosan Nanoparticle construct

Chitosan nanoparticle formation by ionotropic gelation results from the electrostatic interaction between the protonated tertiary amine groups of chitosan and the charged groups of TPP. The size and surface charge of the nanoparticles formed is dependent upon the molecular weight and degree of deacetylation of chitosan, the weight ratio of chitosan to TPP as well as the pH of the solutions[25, 26, 50-53]. The fast kinetics of the formation of an opalescent solution containing CN slows the diffusion of the reactants into the solution and prevents the progress of further nanoparticle formation. From freeze-dried CN we evaluated that only a fraction (26%, n=3) of the chitosan polymer formed into nanoparticles. On assessment of the freeze-dried CN

generated from MMW and LMW chitosan, it was discovered that they were difficult to re-suspend in saline solution. In addition, separation of freeze dried CN and mixed leukocyte cells by centrifugation proved to be problematic in solutions which contained both materials and co-precipitation was observed. In order to make the nanoparticles more soluble, methylation of chitosan polymer at the amine functionality which leads to quaternisation at the position was attempted using a method described previously[46]. It was expected the permanent quaternisation (completed with methyl iodide and under basic conditions) would increase the water solubility of chitosan and that the resulting increase in cationic character could ultimately lead to interactions with the negatively charged surface of cells. However the decreased number of free amine moieties resulted in low binding affinities of the tri-methylated chitosan to the radio-metals (data not shown).

Nanoparticles with higher stability and water-solubility were generated from lower molecular weight chitosan polymer (15 kDa). These CN were less prone to agglomeration and were easily re-suspended following centrifugation. As a result nanoparticles formed from 15 kDa chitosan polymers were used in gel form in all further experiments.

Refinement of the purification process of CN may be possible. Centrifugation may not be the best option as CN may be collected together with free polyanion (TPP) Which has metal-chelation properties and may contribute to the chelation of [^{89}Zr] and [^{64}Cu]. Other possible methods of purification such as dialysis may offer a more efficient separation of CN from free TPP. However the effect on the size and charge of the collected CN should be assessed as this could have an effect on the mechanism of uptake of the nanoparticles by mixed leukocyte cells.

Radiolabelling of Chitosan Nanoparticles with [^{89}Zr] and [^{64}Cu]

The metal binding efficiency of CN is not necessarily correlated to the molecular mass of chitosan used to prepare the nanoparticles. However CN prepared from MMW chitosan showed the highest affinity for [^{89}Zr] with 90.3% ± 14.8% uptake (table 1). The higher uptake of [^{89}Zr] by CN built from MMW chitosan suggests that these nanoparticles have more chelating sites available for the zirconium ions to bind. Interestingly these nanoparticles did not show similar high affinity for [^{64}Cu] (71.9% ± 2.3%). However these nanoparticles were not selected

for further experiments due to the difficulty in re-suspending them in saline solution as well as the problems of separating them from mixed leukocytes by centrifugation which would often lead to co-precipitation. The content of dry CN in 20 mg of CN gel was determined to be around 0.6 mg after freeze-drying of the gel and weighing the solid CN which remained following the freeze drying process. It was found that 5 mg of CN gel, corresponding to 0.15 mg of CN, was able to load 3.7 MBq of [^{89}Zr], resulting in a specific radioactivity of 24.7 MBq/mg CN.

Uptake and retention of [^{89}Zr]- or [^{64}Cu]-Loaded Chitosan Nanoparticles into mixed human Leukocytes

The graph shown in figure 2 suggests a two-step process for the mechanism of uptake of [^{89}Zr]-loaded CN through the cell membrane via pinocytosis[19] rather than by phagocytosis. A similar mechanism to that reported by Lesniak *et al* for the cell uptake of carboxylated polystyrene and silica nanoparticles[54] may be occurring here. An initial step in which the cationic nanoparticles adhere reversibly to the negatively charged cell membrane by electrostatic interaction, followed by internalisation into the cell via a slower process. The initial fast uptake of [^{89}Zr]-loaded CN into the cells (as seen in figure 2) may be the result of an accumulation of the [^{89}Zr]-CN at the cell membrane through a weak adhesive contact after the initial mixing with the leukocytes using a vortex for 30 seconds followed by dissociation and dispersion until an equilibrium is reached. Leukocytes were radiolabelled in saline rather than a plasma medium to avoid any potential binding of the [^{89}Zr] or [^{64}Cu] to plasma proteins which would result in lower labelling efficiencies.

Efflux of the radioactivity from the cells reached 28.4% (± 5.8%) loss of [^{89}Zr] after 2 hours and was followed by a slow release afterwards (figure 3). After 24 hours around 50% of the radioactivity was still associated with the cells. We can infer from the results shown in figures 2 and 3 that only a fraction of the [^{89}Zr]-loaded CN are internalised after 15 minutes incubation and a fraction is still bound to the cell membrane. The loss of radioactivity from this point is likely to be due to competition between plasma proteins in the cell free plasma (CFP) and the cell membrane bound CN for the [^{89}Zr].

Due to the size and shape of the CN (< 0.5 µm) and their ability to interact with the cell membrane resulting from their surface charge, it is likely that cellular

internalisation involves an endocytosis pathway[55]. These results reflect fast initial adhesion of [^{89}Zr] or [^{64}Cu]-loaded CN to the cell membrane followed by partial removal leading to only a fraction of nanoparticles being internalised into the cell.

[^{64}Cu]-loaded CN showed a much poorer uptake into leukocytes cells compared to its [^{89}Zr] counterpart. In addition the efflux of [^{64}Cu] from cells was much more rapid with more than 90% of the [^{64}Cu] being expelled from the cell after 2 hour incubation in CFP. Similarly to the situation with the [^{89}Zr]-loaded CN, the loss could be attributed to the competition between components in the CFP and the leukocyte membrane bound [^{64}Cu]-loaded CN. The rapid loss of radioactivity from the cells might be a result of the greater affinity of components of the CFP for copper rather than zirconium. Copper as a trace element is found in humans and is important in various physiological processes; as such human plasma contains specific copper transporter proteins such as ceruloplasmin or transcuprein[56].

The cytotoxicity effect of unlabelled CN on mixed leukocytes was also studied. Interestingly we found that increased exposure to chitosan nanoparticle gel had a negative effect on the viability of leukocyte cells which is the opposite result to that reported by Kean *et al*[46]. This implies that there is indeed a correlation between the amounts of chitosan nanoparticle and the viability of leukocyte cells.

Conclusion

We report a simple and reproducible method for radiolabelling mixed human leukocytes with [^{89}Zr]. This new technique will allow for the quantitative imaging of inflammation using positron emission tomography (PET). With this method, which utilises CN as a delivery system of the PET isotope into the cells, we have demonstrated a fast uptake of [^{89}Zr] into leukocyte cells with a slow rate of efflux thereafter. Chitosan is an attractive carrier owing to its low cytotoxicity, biocompatibility and biodegradability which has been previously demonstrated. However, a correlation between the amount of CN used and the viability of leukocyte cells was discovered, with higher amounts of CN reducing the viability of cells. A method of chitosan nanoparticle generation which uses less native chitosan and which uses a different method of purification is currently being investigated to overcome this situation and to reduce the amount of free TPP in the nanoparticle formulation.

Radiolabelling of mixed human leukocyte cells with [^{64}Cu] was also directly compared to [^{89}Zr] radiolabelling. A lower uptake of [^{64}Cu] into leukocyte cells was observed as well as a high efflux of the [^{64}Cu] from the cell. The results suggest that [^{89}Zr] is the superior radiometal to use for human inflammation scanning. The uptake mechanism of [^{89}Zr]/[^{64}Cu]-loaded CN into cells is unclear. There is a possibility of phagocytic engulfment[4] but the most likely method of internalisation is via an endocytosis or pinocytosis mechanism based on the size, shape and surface charge of the CN. Our method of radiolabelling WBC's with long lived PET isotopes is made more attractive due to its ease of use compared to other reported methods[16] which require the addition of an organic reticulating agent and coupling of a metal complexing agent. Our technique requires neither the use of toxic organic reagents to construct the nanoparticles nor coupling to a complexing agent. This technique is suitable for measuring and monitoring the regional signal from migrated radiolabelled white blood cells to pathological tissue in infectious and inflammatory diseases such as inflammatory arthritis. It offers the potential for superior quantification and sensitivity compared to current methods such as Single-Photon Emission Computed Tomography (SPECT). This represents the first essential steps towards the development of a generic PET technique for quantitative imaging of inflammation in the clinic with potential for applications to monitor other types of cell traffic such as stem cells.

Acknowledgements

We gratefully acknowledge the support provided by the NIHR Manchester Musculoskeletal Biomedical Research Unit.

References

[1] M. Karsdal, T. Woodworth, K. Henriksen, W. Maksymowych, H. Genant, P. Vergnaud, C. Christiansen, T. Schubert, P. Qvist, G. Schett, A. Platt, A.-C. Bay-Jensen, *Arthritis Research & Therapy* **2011**, *13*, 215.

[2] C. J. Palestro, C. Love, K. Bhargava, K., *Quarterly Journal of Nuclear Medicine and Molecular Imaging* **2009**, *53*, 105

[3] N. Adonai, K. N. Nguyen, J. Walsh, M. Iyer, T. Toyokuni, M. E. Phelps, T. McCarthy, D. W. McCarthy, S. S. Gambhir, *Proceedings of the National Academy of Sciences of the United States of America* **2002**, *99*, 3030.

[4] A. Pala, M. Liberatore, P. D'Elia, F. Nepi, V. Megna, M. Mastantuono, A. Al-Nahhas, D. Rubello, M. Barteri, *Molecular Imaging and Biology* **2011**, 1.

[5] Z.-B. Li, K. Chen, Z. Wu, H. Wang, G. Niu, X. Chen, *Molecular Imaging and Biology* **2009**, *11*, 415.
[6] K. K. Bhargava, R. K. Gupta, K. J. Nichols, C. J. Palestro, *Nuclear Medicine and Biology* **2009**, *36*, 545.
[7] C. Wu, G. Ma, J. Li, K. Zheng, Y. Dang, X. Shi, Y. Sun, F. Li, Z. Zhu, *Clinical Imaging* **2013**, *37*, 28.
[8] C. J. van der Laken, E. H. Elzinga, M. A. Kropholler, C. F. M. Molthoff, J. W. van der Heijden, K. Maruyama, R. Boellaard, B. A. C. Dijkmans, A. A. Lammertsma, A. E. Voskuyl, *Arthritis & Rheumatism* **2008**, *58*, 3350.
[9] G. Fischer, U. Seibold, R. Schirrmacher, B. Wängler, C. Wängler, *Molecules* **2013**, *18*, 6469.
[10] M. A. Deri, B. M. Zeglis, J. S. Lewis, *Nuclear Medicine and Biology* **2013**, *40*, 3
[11] L. Perk, M. Vosjan, G. Visser, M. Budde, P. Jurek, G. Kiefer, G. van Dongen, *European Journal of Nuclear Medicine and Molecular Imaging* **2010**, *37*, 250.
[12] M. J. W. D. Vosjan, L. R. Perk, G. W. M. Visser, M. Budde, P. Jurek, G. E. Kiefer, G. A. M. S. van Dongen, *Nature Protocols* **2010**, *5*, 739.
[13] P. K. E. Borjesson, Y. W. S. Jauw, R. Boellaard, R. de Bree, E. F. I. Comans, J. C. Roos, J. A. Castelijns, M. J. W. D. Vosjan, J. A. Kummer, C. R. Leemans, A. A. Lammertsma, G. A. M. S. van Dongen, *Clinical Cancer Research* **2006**, *12*, 2133.
[14] T. K. Nayak, M. W. Brechbiel, *Bioconjugate Chemistry* **2009**, *20*, 825.
[15] P. K. E. Börjesson, Y. W. S. Jauw, R. de Bree, J. C. Roos, J. A. Castelijns, C. R. Leemans, G. A. M. S. van Dongen, R. Boellaard, *Journal of Nuclear Medicine* **2009**, *50*, 1828.
[16] E. J. Keliher, J. Yoo, M. Nahrendorf, J. S. Lewis, B. Marinelli, A. Newton, M. J. Pittet, R. Weissleder, *Bioconjugate Chemistry* **2011**, *22*, 2383.
[17] P. Charoenphun, L. K. Meszaros, K. Chuamsaamarkkee, E. Sharif-Paghaleh, J. R. Ballinger, T. J. Ferris, M. J. Went, G. E. Mullen, P. J. Blower, *European Journal of Nuclear Medicine and Molecular Imaging* **2014**.
[18] A. J. Varma, S. V. Deshpande, J. F. Kennedy, *Carbohydrate Polymers* **2004**, *55*, 77.
[19] H. Y. Nam, S. M. Kwon, H. Chung, S.-Y. Lee, S.-H. Kwon, H. Jeon, Y. Kim, J. H. Park, J. Kim, S. Her, Y.-K. Oh, I. C. Kwon, K. Kim, S. Y. Jeong, *Journal of Controlled Release* **2009**, *135*, 259.
[20] T. Kean, M. Thanou, *Advanced Drug Delivery Reviews* **2010**, *62*, 3.
[21] R. Jayakumar, D. Menon, K. Manzoor, S. V. Nair, H. Tamura, *Carbohydrate Polymers* **2010**, *82*, 227.
[22] H. Peniche, C. Peniche, *Polymer International* **2011**, *60*, 883.
[23] M. Garcia-Fuentes, M. J. Alonso, *Journal of Controlled Release* **2012**, *161*, 496.
[24] M.-C. Chen, F.-L. Mi, Z.-X. Liao, C.-W. Hsiao, K. Sonaje, M.-F. Chung, L.-W. Hsu, H.-W. Sung, *Advanced Drug Delivery Reviews* **2013**, *65*, 865.
[25] H.-l. Zhang, S.-h. Wu, Y. Tao, L.-q. Zang, Z.-q. Su, *Journal of Nanomaterials* **2010**, *2010*.
[26] P. Calvo, C. Remuñán-López, J. L. Vila-Jato, M. J. Alonso, *Journal of Applied Polymer Science* **1997**, *63*, 125.
[27] L. Qi, Z. Xu, X. Jiang, C. Hu, X. Zou, *Carbohydrate Research* **2004**, *339*, 2693.

[28] V. Dodane, V. D. Vilivalam, *Pharmaceutical Science & Technology Today* **1998**, *1*, 246.
[29] W. Tiyaboonchai, *Naresuan University Journal* **2003**, *11*, 51.
[30] T. Ishii, Y. Okahata, T. Sato, *Biochimica et Biophysica Acta (BBA) - Biomembranes* **2001**, *1514*, 51.
[31] P. Baldrick, *Regulatory Toxicology and Pharmacology* **2010**, *56*, 290.
[32] S. Bagheri-Khoulenjani, S. M. Taghizadeh, H. Mirzadeh, *Carbohydrate Polymers* **2009**, *78*, 773.
[33] L. Casettari, D. Vllasaliu, J. K. W. Lam, M. Soliman, L. Illum, *Biomaterials* **2012**, *33*, 7565.
[34] S. Hein, K. Wang, W. F. Stevens, J. Kjems, *Materials Science and Technology* **2008**, *24*, 1053.
[35] H. Sashiwa, S.-i. Aiba, *Progress in Polymer Science* **2004**, *29*, 887.
[36] W. Yang, T. Mou, W. Guo, H. Jing, C. Peng, X. Zhang, Y. Ma, B. Liu, *Bioorganic & Medicinal Chemistry Letters* **2010**, *20*, 4840.
[37] P. Agrawal, G. J. Strijkers, K. Nicolay, *Advanced Drug Delivery Reviews* **2010**, *62*, 42.
[38] K. Sonaje, E.-Y. Chuang, K.-J. Lin, T.-C. Yen, F.-Y. Su, M. T. Tseng, H.-W. Sung, *Molecular Pharmaceutics* **2012**, *9*, 1271.
[39] W. B. Tan, S. Jiang, Y. Zhang, *Biomaterials* **2007**, *28*, 1565.
[40] L. Linlin, C. Dong, Z. Yanqi, D. Zhengtao, R. Xiangling, M. Xianwei, T. Fangqiong, R. Jun, Z. Lin, *Nanotechnology* **2007**, *18*, 405102.
[41] Z. Shi, K. G. Neoh, E. T. Kang, B. Shuter, S.-C. Wang, C. Poh, W. Wang, *ACS Applied Materials & Interfaces* **2008**, *1*, 328.
[42] J.-H. Kim, Y.-S. Kim, K. Park, E. Kang, S. Lee, H. Y. Nam, K. Kim, J. H. Park, D. Y. Chi, R.-W. Park, I.-S. Kim, K. Choi, I. Chan Kwon, *Biomaterials* **2008**, *29*, 1920.
[43] K. Nagpal, S. K. Singh, D. N. Mishra, *Chemical and Pharmaceutical Bulletin* **2010**, *58*, 1423.
[44] K. A. Janes, P. Calvo, M. J. Alonso, *Advanced Drug Delivery Reviews* **2001**, *47*, 83.
[45] D. Fischer, Y. Li, B. Ahlemeyer, J. Krieglstein, T. Kissel, *Biomaterials* **2003**, *24*, 1121.
[46] T. Kean, S. Roth, M. Thanou, *Journal of Controlled Release* **2005**, *103*, 643.
[47] M. L. Thakur, J. P. Lavender, R. N. Arnot, D. J. Silvester, A. W. Segal, *Journal of Nuclear Medicine* **1977**, *18*, 1014.
[48] B. Ellis, in *Sampson's Book of Radiopharmacy* (Ed.: T. Theobold), **2011**, pp. 421.
[49] M. A. Al-Janabi, A. K. Jones, K. Solanki, R. Sobnack, J. Bomanji, A. A. Al-Nahhas, D. V. Doyle, K. E. Britton, E. C. Huskisson, *Nuclear Medicine Communications* **1988**, *9*, 987.
[50] A. Nasti, N. Zaki, P. Leonardis, S. Ungphaiboon, P. Sansongsak, M. Rimoli, N. Tirelli, *Pharmaceutical Research* **2009**, *26*, 1918.
[51] A. Rampino, M. Borgogna, P. Blasi, B. Bellich, A. Cesàro, *International Journal of Pharmaceutics* **2013**, *455*, 219.
[52] H. Zhang, M. Oh, C. Allen, E. Kumacheva, *Biomacromolecules* **2004**, *5*, 2461.
[53] Q. Gan, T. Wang, C. Cochrane, P. McCarron, *Colloids and Surfaces B: Biointerfaces* **2005**, *44*, 65.

[54] A. Lesniak, A. Salvati, M. J. Santos-Martinez, M. W. Radomski, K. A. Dawson, C. Åberg, *Journal of the American Chemical Society* **2013**, *135*, 1438.
[55] I. Canton, G. Battaglia, *Chemical Society Reviews* **2012**, *41*, 2718.
[56] R. Hueting, *Journal of Labelled Compounds and Radiopharmaceuticals* **2014**, *57*, 231.

Publication 6 (page 201)

CHAPTER 7: An optimised method to prepare Zirconium-89 Radiolabelled chitosan nanoparticles as an application for leukocyte trafficking with Positron Emission Tomography

Prepared for Publication

An optimised method to prepare zirconium-89 radiolabelled chitosan nanoparticles as an application for leukocyte trafficking with positron emission tomography.

M. Fairclough[1], B. Ellis[2], H. Boutin[1], A. Jones[3] A. McMahon[1], G. Brown[1], A. Gennari[4] and C. Prenant[1]*

1. Wolfson Molecular Imaging Centre, Manchester, UK. 2. Central Manchester University Hospital, NHS Foundation Trust, UK. 3. Clinical Sciences Building, Salford Royal NHS Foundation Trust, Manchester, UK. 4. Institute of Inflammation and Repair, University of Manchester, Manchester, UK.

**Correspondence to: M. Fairclough, Wolfson Molecular Imaging Centre, The University of Manchester, 27 Palatine Road, Manchester M20 3LJ, UK. Tel.: +44(0)1612750034*

E-mail: michael.fairclough@manchester.ac.uk

Abstract

Mixed leukocyte (white blood cells [WBC]) trafficking using positron emission tomography (PET) is receiving growing interest to diagnose and monitor inflammatory conditions. PET is a high sensitivity molecular imaging technique that allows precise quantification of the signal produced from the radiolabelled moiety. We have evaluated a new methods for labelling WBC with zirconium-89 (^{89}Zr, $t_{1/2}$ = 78.41 hours) using chitosan nanoparticles (CN) as the carrier for delivery of the radiometal into the leukocytes. In our current work we report an optimised method for the preparation of CN via a mechanism of ionotropic gelation. We recently reported on the use of CN to carry ^{64}Cu and ^{89}Zr into leukocytes for trafficking with PET[1]. In this report we described an optimised method for CN generation and radiometal loading. The method of CN generation described here has the advantage of more reproducibility in CN properties as well as the size distribution of nanoparticles.

Introduction

Chitosan is a linear polysaccharide consisting of randomly distributed β-1-4-linked d-glucosamine and *N*-acetyl-d-glucosamine units and has metal chelating properties[2]. The polymer is commercially available and can be obtained at various molecular weights and with different degrees of deacetylation (DD). Recently, chitosan has received growing interest from the scientific community and has found applications in a number of fields including, but not limited to, drug and gene

delivery systems[3-5], wound dressing and as scaffolds for tissue engineering[6]. These applications are made possible due to the bio-compatibility, bio-degradability and apparent low toxicity of chitosan[7]. It is these properties, as well as the metal chelating properties, which have drawn our attention to the use of chitosan nanoparticles (CN) as a carrier of the PET radiometal, ^{89}Zr, into mixed leukocyte cells for cell trafficking. *In-vivo* imaging of leukocyte cells with PET has applications in immunological studies to track the selective recruitment of specific immune cells during pathogenesis, to detect probable infectious/inflammatory foci and also to devise rational therapeutic strategies and carry out longitudinal studies.

Nanoparticles can be formed from chitosan polymer by crosslinking the linear polymer chains using a polyanion such as pentasodium tripolyphosphate (TPP) via a mechanism of ionotropic gelation[8-10]. Ionotropic gelation is an attractive mechanism for CN formation owing to the mild and aqueous conditions used in comparison to other mechanisms such as microemulsification or complex coacervation[10]. The size and surface charge of CN is very adaptive to changes of concentration and ratio of chitosan to polyanion and of the cross-linking agent, to pH changes and to the method of CN purification.

In this short note we describe the optimisation of the preparation of CN to be used as a carrier of ^{89}Zr into human leukocyte cells. This is followed by an investigation of the affinity of CN for ^{89}Zr and the subsequent uptake and retention of ^{89}Zr-loaded CN into mixed human leukocyte cells. The radiolabelling of leukocytes with ^{89}Zr-loaded CN is described here, but the versatility of this method means that it could also be transferable to radiolabelling of similar cell types.

Experimental

CN preparation

Chitosan (15 kDa, > 85% degree of deacetylation, 14 mg) was solubilised in HCl (4.6 mM, 20 mL) to form a 0.7 mg/ml solution, and was left to stir for 24 hours. The pH of the chitosan solution was then adjusted to 5 with the addition of sodium hydroxide (0.1 M). Meanwhile, a 1mg/ml solution of TPP was made (10 mg TPP in 10 mL of deionised water) and both the TPP and the chitosan solutions were filtered via a 0.22 µm filter. Next, 80 µL of the TPP solution was added to 917 µL of the chitosan solution (chitosan**:**TPP ratio of 8**:**1, w/w) to form nanoparticles, and the

mixture was allowed to stir for 30 minutes. The solution of CN were then transferred to Pur-A-Lyzer Maxi 12000 dialysis tubes (12 kDa molecular weight cut-off) and were dialysed against de-ionised water for 24 hours to remove all of the TPP cross-linking agent. The CN solution was then recovered and stored at 2-4 ºC (as this temperature was reported to have no effect on size and physical stability of the particles[11]) CN were characterised for size and zeta potential by dynamic light scattering (DLS) using a Malvern Zetasizer nano-series.

Isolation of mixed human leukocytes

Each experiment was carried out using mixed white blood cells (WBC) freshly isolated from whole blood following erythrocyte sedimentation according to a reported procedure[1, 12].

Results and Discussion

CN properties

The size and zeta potential (ζ) of CN prepared from 15 kDa chitosan polymer were analysed by dynamic light scattering (DLS). The results showed an average CN size of 342.7 nm in diameter, with a polydispersity index (pdi) of 0.376 as seen in Figure 1. The pdi results are consistent with those reported previously[13, 14] and our pdi value is actually lower than that reported by Papadimitriou *et al*.

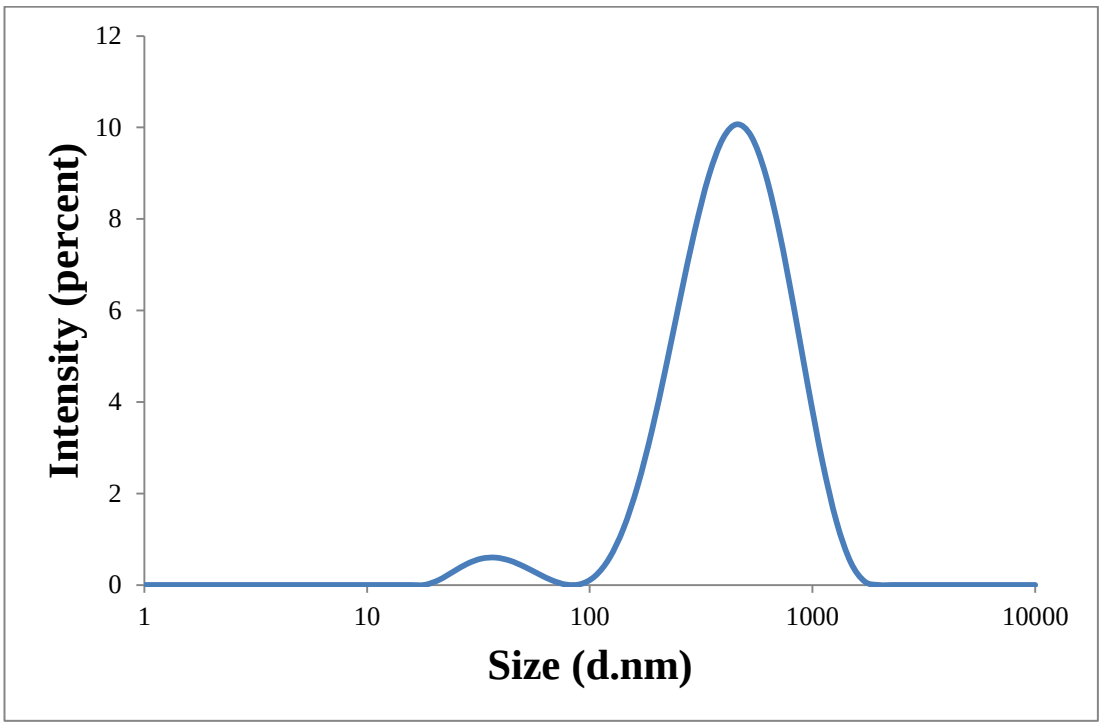

Figure 1: CN diameter measured by DLS.

The ζ-potential of CN was also measured and was found to be +45.7 ± 3.96 mV as can be seen in Figure 2.

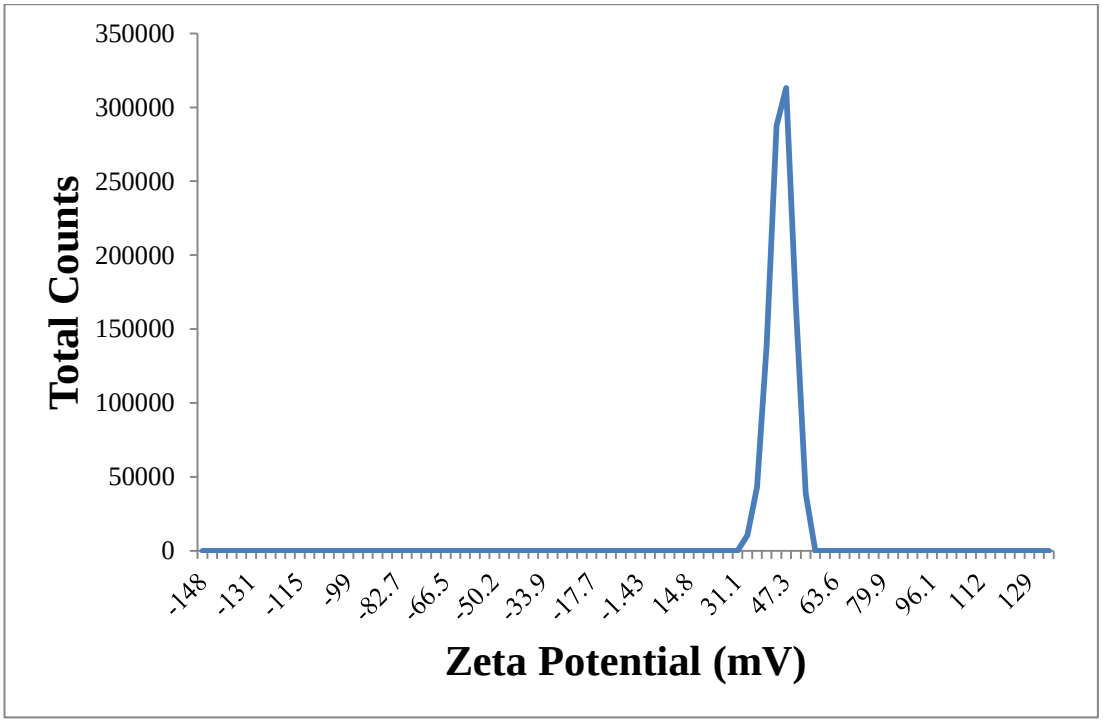

Figure 2: CN zeta potential measurement.

CN were prepared from different chitosan**:**TPP ratios and the size and ζ-potential of the CN were assessed as seen in Figure 3 and Figure 4 respectively.

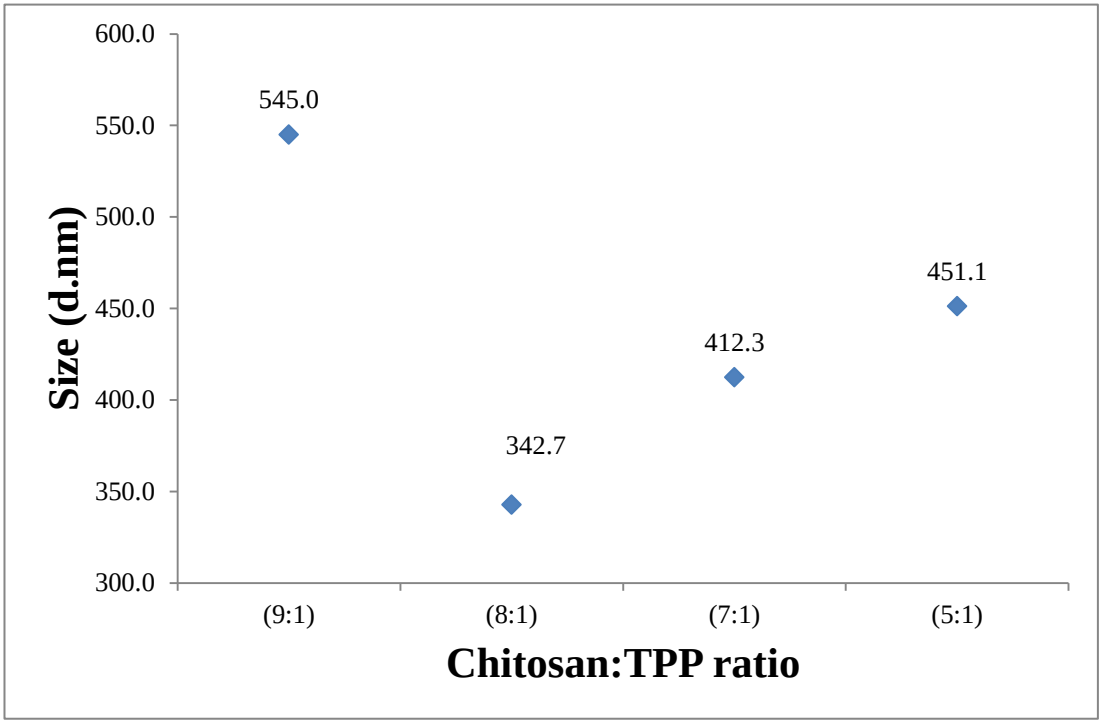

Figure 3: The effect of different chitosan:TPP ratio on CN size.

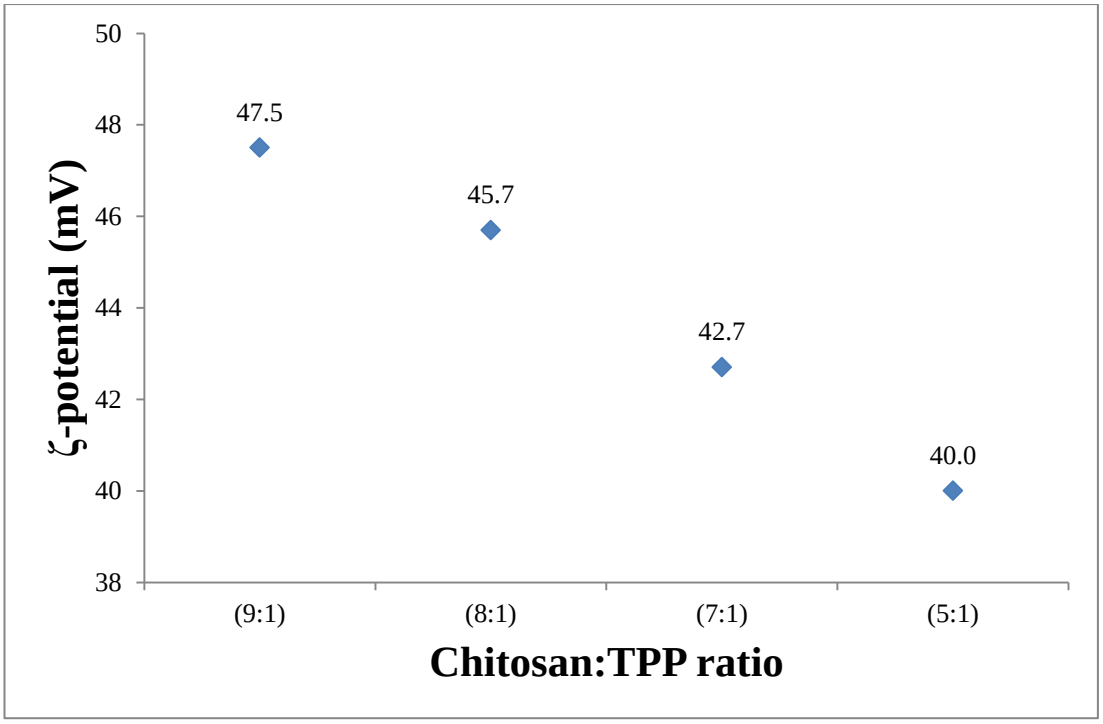

Figure 4: The effect of different chitosan:TPP ratio on CN ζ-potential.

Figure 3 shows the trend in CN size as the chitosan:TPP ratio is altered. At a 9:1 ratio the average size is 545.0 nm and this decreases to 342.7 nm at an 8:1 ratio of chitosan:TPP. As the ratio changes to 6:1 and then 5:1 an increase to the size of CN is seen from 412.3 nm to 451.1 nm. Figure 4 shows the trend in ζ-potential of CN as the chitosan:TPP ratio changes. There is a clear trend as the ratio of chitosan:TPP becomes smaller the ζ-potential of CN produced becomes lower dropping from 47.5 mV at a 9:1 chitosan:TPP to 40.0 mV at a 5:1 chitosan:TPP. Using this data it was decided that an 8:1 chitosan:TPP would be used to construct CN. This produces CN at a size which allows uptake by cells and maintains a positive surface charge for the electrostatic attraction of CN to cell surfaces. The pdi values of the CN built from 9:1 and 7:1 chitosan:TPP where larger (0.437 and 0.407) than the pdi reported for those produced with a 8:1 ratio (0.376). This suggests that CN produced from 8:1 chitosan:TPP where less polydisperse than other batches.

Being able to control the size and surface charge of CN is important as it gives a good insight into how the CN are taken up by cells. There are a number of endocytosis mechanisms which can occur in a typical eukaryotic cell, and these mechanisms can be dependent on the size of the particle being taken up by the cell[15]. By controlling the size of the CN we are able to predict more accurately by

which endocytosis mechanism they are taken up into the cell. It is also important that the CN have a positive ζ-potential, as it is this positive charge which initially attracts the CN to the negatively charged surface of the cell. Following this initial electrostatic interaction a cell internalisation step, either by phagocytosis or endocytosis takes place.

Using dialysis to purify the CN ensures that no TPP is left in the CN formulation. Previously, centrifugation has been used to purify CN[14, 16], however the disadvantage of purification in this way is that all components including CN, native chitosan and TPP cross-linking agent are collected. This means that there is little control of what is being collected and that the physical properties of CN can, as a result, be variable. Furthermore, the nature of our previous method of CN production was the fast production of a gel which prevented the diffusion of any further chitosan and TPP into the nanoparticles therefore terminating the CN production.

Affinity of ^{89}Zr for CN

CN (300 µL) were incubated with ^{89}Zr (approximately 17 MBq as ^{89}Zr-oxalate) in a Thermo-shaker at room temperature for 45 minutes. Following incubation the ^{89}Zr-loaded CN were separated from free ^{89}Zr by centrifugation and washed twice with deionised water. The supernatant (containing free ^{89}Zr) and the pellet of ^{89}Zr-loaded CN were measured for radioactivity. The amount of ^{89}Zr associated with the CN after incubation and washing was 31 % ± 6 % (n = 15).

Uptake and Retention of ^{89}Zr-loaded CN in mixed leukocytes

^{89}Zr-loaded CN were re-suspended in saline (200 µL) and re-suspended mixed leukocytes (200 µL in saline) were added to the mixture with gentle mixing. The mixture was then incubated in a thermo-shaker at 37 ˚C, at 1400 rpm for 30 minutes, 1 hour, 2 hours, 3 hours and 24 hours. Following incubation, leukocyte radiolabelling was terminated at each time interval by the addition of cell free plasma (CFP, 1 mL). The radiolabelled leukocytes were separated from the mixture by centrifugation (150 g for 5 minutes) to leave a pellet of ^{89}Zr labelled leukocytes. The radioactivity in the supernatant and the pellet were counted in a gamma counter. Radiolabelling efficiency is expressed as a percentage of the ratio between radioactivity associated with the leukocytes and total radioactivity.

To assess cell retention of ^{89}Zr, a sample of leukocytes labelled with ^{89}Zr-loaded CN was re-suspended in CFP and allowed to incubate for 24 hours at 37 ˚C. At intervals of 1, 2, 3, and 24 hours the mixture was centrifuged (150 g for 5 minutes) and the supernatant was removed and the pellet containing ^{89}Zr-labelled leukocytes was re-suspended in fresh CFP. Removed CFP fractions and leukocyte pellets were measured for radioactivity in a gamma counter and the radioactivity efflux rate determined. The results for both uptake and efflux of ^{89}Zr in leukocytes cell can be seen in Figure 5.

Figure 5 shows that the uptake of our ^{89}Zr-loaded CN seems to occur in two phases, similar to that reported by Lesniak *et al*., for the internalisation of carboxylated polystyrene and silica nanoparticles in epithelial cells[17]. In an initial step there is an electrostatic interaction between the positive charge on the surface of the CN and the negatively charged cell membrane of the leukocyte cells. In a second step, the ^{89}Zr-loaded CN, are internalised by a mechanism of endocytosis or phagocytosis. Figure 5 demonstrates a relatively fast loss of ^{89}Zr from the cell which shows the release of ^{89}Zr-loaded CN from the cell membrane whilst the remaining ^{89}Zr-loaded CN are internalised by the cell in a slower process which is demonstrated by the uptake plot of Figure 5. There may be some competition for the ^{89}Zr from plasma proteins with chelating properties and this may well account for the loss of ^{89}Zr from the cell membrane.

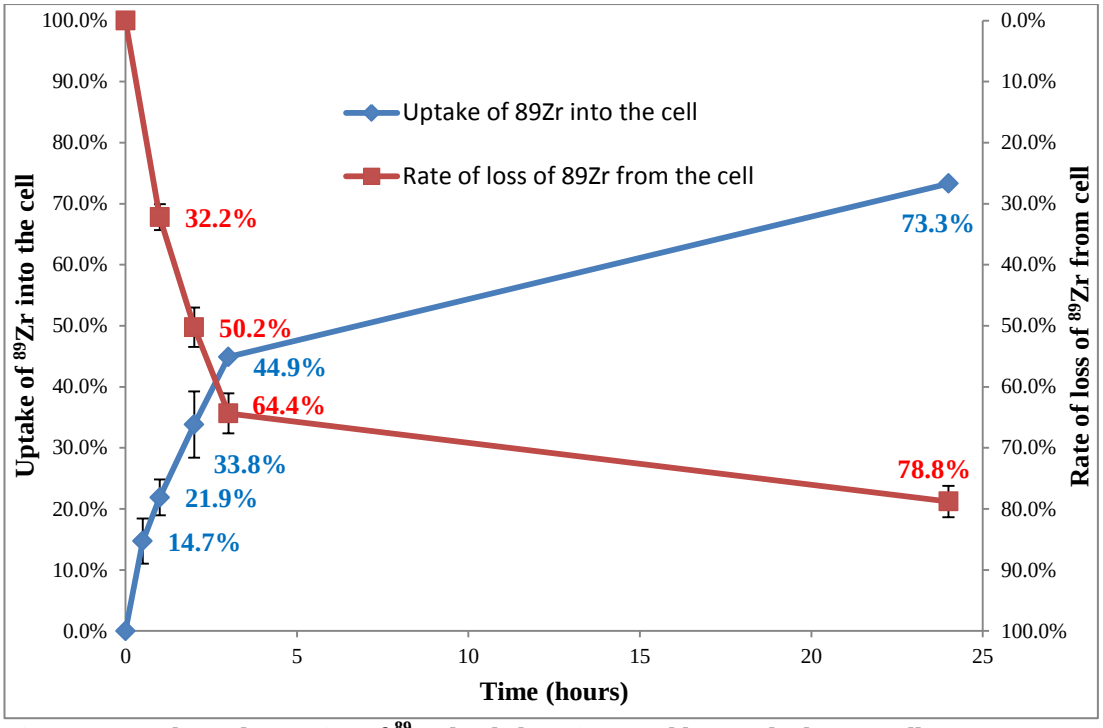

Figure 5: Uptake and retention of ^{89}Zr-loaded CN in mixed human leukocyte cells.

Conclusions

Described in this work is the optimisation of the preparation of CN to be used as a carrier of ^{89}Zr into human leukocyte cells. The versatility of this radiolabelling method means that it may also be applied to the radiolabelling of other cell types which have the capability of phagocytosis and endocytosis. With CN produced by this method a two-step mechanism of ^{89}Zr-loaded CN uptake by leukocytes was shown. A cell membrane interaction is followed by a slower internalisation step. ^{89}Zr-labelled leukocyte cells can then be used with PET for cell trafficking in inflammation imaging. This method of CN preparation uses a low concentration of both the chitosan and TPP which will therefore lower any possible cytotoxicity effects. Also, a large ratio of chitosan:TPP (8:1) along with purification by dialysis is used to reproducibly and reliably construct CN of 342.7 nm in diameter (pdi = 0.376) with a ζ-potential of +45.7 ± 3.96 mV.

CN offer a way to radiolabel mixed leukocyte cells with the PET isotope ^{89}Zr for inflammation imaging. By controlling the conditions of CN production we can reproduce the physical properties (such as diameter and surface charge) of the CN and we have shown that these ^{89}Zr-loaded CN can be used to radiolabel mixed human leukocytes. The relative stability of ^{89}Zr in leukocyte cells from 3 hours to 24 hours (Figure 5) is encouraging for PET imaging of leukocyte cells. Additionally the

versatility of this method means that it could be transferable to radiolabelling of other cell types, for example for tracking stem cells or to monitor the bio-distribution of transferred immune cells *in-vivo* in cell based immunotherapy.

References

[1] M. Fairclough, C. Prenant, B. Ellis, H. Boutin, A. McMahon, G. Brown, P. Locatelli, A. Jones, *Submitted to Journal of Labelled Compounds and Radiopharmaceuticals* **2015**.

[2] A. J. Varma, S. V. Deshpande, J. F. Kennedy, *Carbohydrate Polymers* **2004**, *55*, 77.

[3] H. Y. Nam, S. M. Kwon, H. Chung, S.-Y. Lee, S.-H. Kwon, H. Jeon, Y. Kim, J. H. Park, J. Kim, S. Her, Y.-K. Oh, I. C. Kwon, K. Kim, S. Y. Jeong, *Journal of Controlled Release* **2009**, *135*, 259.

[4] M. Prabaharan, *International Journal of Biological Macromolecules* **2015**, *72*, 1313.

[5] J. Sarvaiya, Y. K. Agrawal, *International Journal of Biological Macromolecules* **2015**, *72*, 454.

[6] R. Jayakumar, D. Menon, K. Manzoor, S. V. Nair, H. Tamura, *Carbohydrate Polymers* **2010**, *82*, 227.

[7] T. Kean, M. Thanou, *Advanced Drug Delivery Reviews* **2010**, *62*, 3.

[8] P. Calvo, C. Remuñán-López, J. L. Vila-Jato, M. J. Alonso, *Journal of Applied Polymer Science* **1997**, *63*, 125.

[9] Q. Gan, T. Wang, C. Cochrane, P. McCarron, *Colloids and Surfaces B: Biointerfaces* **2005**, *44*, 65.

[10] K. Nagpal, S. K. Singh, D. N. Mishra, *Chemical and Pharmaceutical Bulletin* **2010**, *58*, 1423.

[11] M. L. Thakur, J. P. Lavender, R. N. Arnot, D. J. Silvester, A. W. Segal, *Journal of Nuclear Medicine* **1977**, *18*, 1014.

[12] B. Ellis, in *Sampson's Book of Radiopharmacy* (Ed.: T. Theobold), **2011**, pp. 421.

[13] S. Papadimitriou, D. Bikiaris, K. Avgoustakis, E. Karavas, M. Georgarakis, *Carbohydrate Polymers* **2008**, *73*, 44.

[14] A. Rampino, M. Borgogna, P. Blasi, B. Bellich, A. Cesàro, *International Journal of Pharmaceutics* **2013**, *455*, 219.

[15] I. Canton, G. Battaglia, *Chemical Society Reviews* **2012**, *41*, 2718.

[16] L. Qi, Z. Xu, X. Jiang, C. Hu, X. Zou, *Carbohydrate Research* **2004**, *339*, 2693.

[17] A. Lesniak, A. Salvati, M. J. Santos-Martinez, M. W. Radomski, K. A. Dawson, C. Åberg, *Journal of the American Chemical Society* **2013**, *135*, 1438.

CHAPTER 8: Summary and Future Perspectives

The work presented in this thesis has demonstrated the importance as well as the influence of PET radiochemisty in the field of pain and inflammation. The use of several PET isotopes which have a range of radioactive half-lives and with differing physical properties have been used as tools to radiolabel small molecules, peptides and nanoparticles to help elucidate the biological processes occurring during pain perception and in inflammatory response. The work spans diverse chemistries associated with the variety of radioisotopes used, each of which have their own challenges associated. These range from the constraints of the short radioactive half-life of ^{11}C, to working with ^{18}F where it is necessary to react the $[^{18}F]F^-$ with a small organic prosthetic group before being covalently linked to a macromolecule. The PET radiometals ^{64}Cu and ^{89}Zr have longer radioactive half-lives in comparison to ^{11}C and ^{18}F; however the challenge of working with these isotopes is the coordination chemistry which is required to form a thermodynamically and kinetically stable complex with the radiometal. Having this stability is of high importance to prevent transmetallation in physiological conditions.

What I have also hoped to achieve in this work is to demonstrate to the reader some of the different stages involved in the translation of a PET probe, whether it be a small molecule, a peptide/protein or any other biologically relevant substance, from development of the radiochemistry to preclinical evaluation and finally to clinical PET studies. Radiochemistry development has been demonstrated with [^{11}C]diprenorphine, [^{18}F]IL-1RA and with ^{89}Zr-/^{64}Cu-loaded chitosan nanoparticles and indeed physiochemical development of chitosan nanoparticles themselves. [^{18}F]IL-1RA bio-distribution and pharmacokinetics were evaluated in a preclinical setting[1] and ^{89}Zr- loaded chitosan nanoparticles will be assessed in preclinical experiments to evaluate if this tool can be effectively used for cell trafficking of leukocytes for PET imaging of inflammation. Finally, [^{11}C]diprenorphine was produced in compliance with good manufacturing practice (GMP[4]) standards to produce the radiotracer for a clinical study evaluating acute and chronic pain

[4] Guidelines and principles which are required in the manufacture of pharmaceutical; in Europe, this is set out by EudraLex and is enforced by the Medicines and Healthcare Products Regulatory Agency (MHRA).

perception in arthritis[2]. Therefore, some of the most important stages of PET probe translation have been demonstrated.

[6-*O*-methyl-^{11}C]diprenorphine for assessment of the endogenous opioid system in arthritis.

Work has encompassed ^{11}C radiolabelling of a small opioid receptor molecule, diprenorphine[3], and using PET to convey changes of opioid receptor occupancy in brains of patients under various pain states. The challenge of producing [^{11}C]diprenorphine in compliance with GMP standards was addressed as well as fully automating a reliable and robust [^{11}C]diprenorphine production process to give a clinical dose within the tight time limitations that ^{11}C demands. In addition, a comparison of two different ^{11}C radiolabelling strategies was assessed. [^{11}C]CH_3I and [^{11}C]CH_3OTf were compared as ^{11}C methylating agents, with the aim of increasing the radiochemical yield with the more reactive [^{11}C]CH_3OTf. However, although [^{11}C]CH_3OTf has increased reactivity and as such can be used under mild reaction conditions, there is less selectivity towards the two free hydroxyl groups of the diprenorphine precursor in comparison with [^{11}C]CH_3I. In conclusion it is suggested that [^{11}C]CH_3OTf is not an appropriate route for the radiosynthesis of [^{11}C]diprenorphine. However the automated method for synthesising [^{11}C]diprenorphine with [^{11}C]CH_3I on a GE TRACERlab$_{FXFE}$ radiochemistry system should be the method of choice for [^{11}C]diprenorphine PET studies.

A new method for the reliable quantitative measurement of the metabolites of [^{11}C]diprenorphine using in-line SPE combined with radio-HPLC has also been developed[4]. It is important to be able to measure the ratio of parent radiotracer ([^{11}C]diprenorphine) to metabolites at various time-points of a PET scan in order to accurately model the quantitative binding of [^{11}C]diprenorphine to available opioid receptors. Also being able to calculate an accurate plasma input function for [^{11}C]diprenorphine. The metabolites of [^{11}C]diprenorphine from clinical scanning were compared to *in silico* predictions and metabolites generated from human liver microsomes. It was found that metabolite profile for the same subject over multiple [^{11}C]diprenorphine scans was consistent and as such it may be possible to apply a single set of metabolite data for a participant over multiple scans. The work went on to identify the major metabolite of [^{11}C]diprenorphine as [^{11}C]diprenorphine-3-glucuronide as confirmed by microsomal digest and MALDI-MS. Being able to

identify the major metabolite allows the determination of a number of important issues. First of all, we can determine whether the metabolite may be able to penetrate the BBB. This is an important question to be answered, especially when addressing the question of [^{11}C]diprenorphine neuro-receptor occupancy. The lipophilic nature of [^{11}C]diprenorphine-3-glucuronide suggests that it would be difficult for the molecule to penetrate the BBB by passive diffusion, however there are other systems that molecules can use to pass the BBB such as by active transport and by receptor mediated mechanisms. This leads to the second question: is there competition from the radiometabolite for the same opioid receptors that [^{11}C]diprenorphine is targeting? The answer for [^{11}C]diprenorphine-3-glucuronide is unclear from data in the current literature. We instead can compare how other glucuronides of opiates act on opioid receptors. For example morphine-3-glucuronide has been shown to have a low affinity at μ-receptors[5] whereas buprenorphine-3-glucuronide was reported to have some biological activity which could contribute to the total pharmacology of buprenorphine[6]. It seems apparent that more work need to be completed to analyse the affinity diprenorphine-3-glucuronide may have on opioid receptors.

[^{11}C]diprenorphine produced by the method described in Chapter 2 and with metabolite analysis described in Chapter 3, was used for a clinical PET study investigating opioid receptor occupancy by endogenous opioids as well as up-regulation of opioid receptors in the brain for various pain states of healthy participants and in arthritic patients[2]. The conclusion was that in chronic pain states (such as that experienced by arthritic patients) opioid receptors are up-regulated in the striatum, evidence of an adaptive endogenous opioid system. The availability of opioid receptors of arthritic patients was reduced in the striatum which is consistent with opioid receptor sites being occupied to a greater extent by endogenous opiates. Evidence of an adaptive up-regulation of opioid receptors in chronic pain is important in explaining variability to the resilience of chronic pain and differing response to therapeutic treatments for chronic pain in disease states such as rheumatoid arthritis. This lends further evidence to the importance of PET radiotracers for assessing the biology of pain at the molecular level by being able to measure the occupancy and the up- or down-regulation of opioid receptors.

[^{18}F]IL-1RA to assess IL-1RA as a potential therapy for neuro- and peripheral inflammation

A strategy for the ^{18}F radiolabelling of IL1-ra has also been reported[7]. IL-1RA is an antagonist of interleukin-1, a pro-inflammatory cytokine. By radiolabelling IL-1RA it was possible to measure its bio-distribution, pharmacokinetics and metabolism in rats[1]. A rapid and efficient method for radiolabelling IL-1RA with the prosthetic group, [^{18}F]fluoroacetaldehyde, was reported[7]. This prosthetic group was attractive to use, owing to its simplified purification by distillation from the crude reaction mixture avoiding the use of HPLC or SPE purification methods. [^{18}F]fluoroacetaldehyde could be trapped in a small volume of water and mild radiolabelling conditions were used to randomly radiolabel free lysine residues of IL-1RA under reductive alkylation.

IL-1RA has the potential to be used to prevent damage caused by inflammation in a number of autoimmune diseases, and gaining a better understanding of its bio-distribution pharmacokinetics and metabolism using [^{18}F]IL-1RA PET helps to optimise routes and time-points for administration. [^{18}F]IL-1RA distribution in rats occurred as follows: kidneys >> liver > lungs >> brain[1]. A low uptake of [^{18}F]IL-1RA was seen in the brain of normal rats, additionally [^{18}F]IL-1RA was rapidly metabolised and the metabolites were quickly excreted in the kidney. This study shows how useful pre-clinical PET is as a strategy in the assessment of new molecules which have a therapeutic interest. A low brain uptake in rats was seen with [^{18}F]IL-1RA which means that for neurodegenerative disorders, repeated injections or even infusion is likely to be needed to maintain therapeutic levels of IL-1RA in the brain as treatment for neuro-inflammation. Since the brain uptake of IL-1RA is low, applications of the tracer must focus on peripheral inflammation.

^{89}Zr and ^{64}Cu labelled chitosan nanoparticles for cell trafficking with PET

^{89}Zr radiolabelled chitosan nanoparticles were assessed for white blood cell trafficking with PET as an improved method to the current clinical procedure of white blood cells radiolabelled with SPECT isotopes, ^{99m}Tc and ^{111}In for inflammation imaging. The superior quantification and sensitivity that is possible with PET makes this imaging modality attractive to monitor the infiltration of radiolabelled white blood cells into areas of infection and inflammation. Chitosan

nanoparticles were investigated as a carrier of PET isotopes into mixed human leukocytes cells[8]. The work investigates the loading of chitosan nanoparticles with ^{89}Zr and ^{64}Cu and then goes on to assess the uptake and retention of ^{89}Zr- and ^{64}Cu-loaded chitosan nanoparticles in mixed human leukocytes[8]. The comparison of the radiometals showed that ^{89}Zr-loaded chitosan nanoparticles were taken up in leukocyte cells to a much greater extent than the ^{64}Cu counterpart. In addition ^{89}Zr was retained much better by leukocyte cells than ^{64}Cu which was almost entirely lost after 3 hours. The comparatively poor uptake and retention of ^{64}Cu-loaded chitosan nanoparticles (which was carried out in cell free plasma) may be a result of the competition for ^{64}Cu by copper transporter proteins which are present in human plasma, whereas there are no corresponding zirconium transporter proteins to act as a substrate for ^{89}Zr. Cell uptake measurements indicate that the uptake of ^{89}Zr-loaded chitosan nanoparticles appears to occur in 2 phases, an initial electrostatic interaction between the nanoparticles and the leukocyte cell surface, followed by a second slower step of internalisation[8]. This simplified method for radiolabelling mixed leukocytes with ^{89}Zr has great potential to be used as a probe for inflammation imaging with PET. The technique could provide clinicians with an early diagnostic tool for autoimmune disorders such as rheumatoid arthritis. Also, this technique may provide a way to assess treatment effectiveness and to monitor inflammation at various disease stages. In addition, this technique may be translated to the radiolabelling of similar cell types which rely on cell uptake via phagocytosis or endocytosis. The versatility of this method means that it could be used, for example, for tracking stem cells or to monitor the bio-distribution of transferred immune cells *in-vivo* in cell based immunotherapy such as adoptive T-cell therapy.

It is important to first of all demonstrate ^{89}Zr-loaded chitosan nanoparticles for leukocyte trafficking with PET in a preclinical model of inflammation. There are a number of models which could be potentially used. One such model is the rat air pouch in which sterile air is injected subcutaneously into the back of the animal, this is followed by the injection of carrageenan to induce an inflammatory response[9]. This method can be used to collect leukocyte cells from rats but may also be used to validate the migration of radiolabelled leukocytes to inflammation sites. Other models which could be useful include collagen induced arthritis, antibody induced arthritis and contact hypersensitivity models[10].

Following the initial assessment of this strategy of radiolabelling leukocytes an optimised method of chitosan nanoparticle construction was developed. This optimised method which uses a low concentration of chitosan and of the cross-linking agent as well as a milder purification method of dialysis (compared to centrifugation), allowed for a reliable and reproducible production of chitosan nanoparticles. One observation of this work was the low ^{89}Zr loading capacity compared to the chitosan nanoparticles used previously. An improvement of loading capacity may be seen if the ^{89}Zr-oxalate starting material has the oxalate counter ion exchanged for a chloride ion on an ion-exchange resin is before being loaded into the nanoparticles. In doing so the ^{89}Zr metal should have a greater affinity for the binding sites of the chitosan nanoparticles in preference to chloride.

The future of PET radiochemistry for the assessment of pain

[^{11}C]diprenorphine is not the only PET radiotracer which can be used to study the endogenous opioid system. Diprenorphine is an antagonist with high affinities at all of the classical opioid receptor sub-types (μ, δ and κ). However there are PET ligands available which are selective for single opioid receptor sub-types such as [^{11}C]carfentanil which is selective for the μ-receptor and N1'-([^{11}C]methyl)naltrindole for the δ-receptor, or combinations of receptor sub-types such as [^{18}F]cyclofoxy for the μ and κ-receptors[11, 12]. Opiate receptors can mediate a number of effects such as pain modulation, sedation, addiction and reward, through a single sub-type of receptors or by a combination of receptor types. Therefore PET ligands, such as [^{11}C]carfentanil, become useful when studying biological processes which rely on a single receptor sub-type. [^{11}C]carfentanil is a potent agonist with high affinity for μ-receptors (K_d 0.08 nM) in human brain tissue[12]. The main drawback of using such a high-affinity agonist for PET studies is that [^{11}C]carfentanil must be produced with high specific radioactivity in order to avoid injecting a dose which contains enough carrier ([^{12}C]carfentanil) to elicit a pharmacological effect to the study participant. Producing [^{11}C]carfentanil with a high specific radioactivity is of course possible and the tracer has been used in numerous studies[12, 13] and remains the PET tracer of choice when studying the μ-opiate receptor[11]. Frost *et al.,* compared the kinetic behaviour and opiate binding properties in different brain regions of [^{11}C]carfentanil and [^{11}C]diprenorphine[13]. It was found that the kinetic behaviour of [^{11}C]carfentanil was of a fast association and

dissociation (30 minutes after injection) to μ-receptors in different brain regions, in contrast [^{11}C]diprenorphine showed a slower rate of association to opiate receptors in the brain with little dissociation during a 90 minute PET scan[13].

It is my opinion that for the study of all opiate receptor sub-types and of the endogenous opiate system, the non-selective antagonist [^{11}C]diprenorphine remains the PET ligand of choice. The automation of a reliable and robust [^{11}C]diprenorphine production has been reported in this work[3] along with a metabolite analysis method[4]. This should go some way in making [^{11}C]diprenorphine attractive to use for clinicians wanting to study disease states which are entirely or partly controlled or modulated by the endogenous opioid system. One further step may be to develop an automated process for the production, purification and formulation of [^{18}F]diprenorphine. This would allow for longer PET scans, and indeed [^{18}F]diprenorphine has been compared with [^{11}C]diprenorphine in human PET studies[14]. This work concluded that there were similarities in the pharmacokinetics and opioid receptor binding of the two tracers. However the automation of the production process on a TRACERlab$_{FXFE}$ system would require careful planning as the production process would require the purification of the [^{18}F]fluoroethyl tosylate prosthetic group before it is used to radiolabel the precursor molecule TDPN. Another approach may be to produce a tosylated precursor which could be directly fluorinated with [^{18}F]F^{-}. This would make the automation of [^{18}F]diprenorphine production a more straightforward prospect.

To look to the future of PET radiochemistry for the assessment of pain, perhaps a good place to start would be with the most recent strategies of analgesia which are being reported for the treatment of chronic pain. One which was briefly discussed in the introduction was the use enkephalinase inhibitors which target and inhibit the zinc metallopeptidases that breakdown endogenous opiates Met- and Leu-enkephalin[15]. The hypothesis is that this inhibition of the peptidases causes an increase in the levels of endogenous opiates, therefore producing a greater analgesic effect. Dual enkephalinase inhibitors, which target the two peptidases, neprilysin (NEP) and aminopeptidase N (APN), are in fact in the early stages of clinical trials. Structure activity studies (a widely used technique for designing new drugs) have been essential to the design of dual enkephalinase inhibitors, which have zinc chelating groups to inhibit the peptidases and side groups which allow them to bind

to sub-sites of the peptidases. Some of these inhibitors have been designed to fit binding sites of both NEP and APN, while others (such as RB-101 and PL37) are pro-drugs designed to penetrate the BBB and release selective APN and NEP inhibitors after a disulphide bond cleavage in the brain. Site-directed mutagenesis and docking studies were used in their design and this same approach may well prove useful in the design of new opiates and indeed new radioligands to study the endogenous opioid system. The review from Roques *et al*., mentions the possibility that these dual enkephalinase inhibitors may be of use for the *in vivo* investigation of opioid receptor occupancy using PET.

A similar strategy involves, fatty acid amide hydrolase (FAAH) inhibitors that can be used to prevent the breakdown of endocannabinoids to provide pain relief[15]. This approach may also warrant a PET study to investigate the effect that cannabinoids have upon the endogenous pain system.

The future of PET radiochemistry in inflammation imaging

Although SPECT imaging with radiolabelled white blood cells remains the most widely used technique for imaging inflammation in the clinic, PET has a very important role in the field of inflammation imaging too. [^{99m}Tc]HMPAO and [^{111}In]oxine labelled leukocytes that can be tracked with SPECT imaging to foci of infection and inflammation are used for the diagnosis and assessment of a number of inflammatory disorders[16]. Other imaging modalities may also be applied for imaging of inflammation such as MRI and ultrasound to assess joint synovitis in rheumatoid arthritis by imaging inflamed synovium or bone erosion[17], however they do not provide a quantitative measurement of inflammation. PET can offer improved quantification and sensitivity compared to these other imaging modalities and it is for this reason we endeavoured to develop a PET imaging technique for cell trafficking of leukocytes for inflammation imaging using ^{89}Zr-loaded chitosan nanoparticles[8]. This technique holds great potential and a preclinical model needs to be established to test and validate the technique.

However, both our method using ^{89}Zr-loaded chitosan nanoparticles and the current clinical practice of SPECT imaging involve the radiolabelling of autologous blood products and this may be seen as a rather invasive procedure. There are *in vivo* strategies to radiolabelling white blood cells to localise infectious and inflammatory

foci, and a good example of this is ^{99m}Tc radiolabelled interleukin-8[18]. Interleukin-8 is a cytokine which plays a role in cell recruitment during inflammation and what is useful for this imaging technique is that neutrophils express receptors for interleukin-8. Bleeker-Rovers *et al.*, demonstrated the first clinical trials with ^{99m}Tc-interleukin-8 SPECT and showed that the tracer could successfully detect various infections in patients at 4 hours post injection[18]. With these promising results reported, a promising way forward may be to radiolabel interleukin-8 with a PET isotope such as ^{18}F, ^{64}Cu or ^{89}Zr.

^{18}F radiolabelling of IL-1RA has been reported in this work and the same strategy employed with [^{18}F]fluoroacetaldehyde[7] could be used for the ^{18}F radiolabelling of interleukin-8. This does however depend on the number of lysine residues available to be radiolabelled and lysine residues which are not involved in the affinity of interleukin-8 for receptors on neutrophils. Interleukin-8 is smaller (8.5 kDa) compared to IL-1RA (17 kDa) and so the number of lysine sites may be restricted. Another plan might be to use site-specific ^{18}F radiolabelling strategies. Aminooxy-functionalised interleukin-8 could be reacted with an ^{18}F carbonyl prosthetic group to form an oxime, or alternatively, a maleimide functionality used to target cysteine residues could be utilised[19-21]. Both of these radiolabelling strategies have been used previously to ^{18}F radiolabel proteins and peptides. Another approach may be to utilise ^{18}F click chemistry. This approach exploits the highly selective interaction between an alkyne and an azide to yield a triazole[22]. Alkynes and azides are generally inert to biological processes making this an attractive approach and many ^{18}F prosthetic groups containing azides and alkynes have been reported[23] with many peptides being decorated with a corresponding alkyne or azide functional group. The click reaction between azides and alkynes is catalysed by a source of Cu^{+}, although the reaction may also be driven by the use of a strained alkyne such as cyclooctyne which avoids the use of copper[22]. To apply this approach to ^{18}F radiolabelling of interleukin-8, consideration would need to be made to reaction rates as well as the concentration and mass of interleukin-8 which would be required. What is apparent however is the number of possible ^{18}F radiolabelling strategies that are available to produce [^{18}F]-interleukin-8.

However, consideration needs to be made to the radioactive half-life of ^{18}F ($t_{1/2}$ = 109.7 minutes) compared to ^{99m}Tc ($t_{1/2}$ = 6 hours) which was used by Bleeker-

Rovers *et al*. The time for interleukin-8 to accumulate at neutrophil receptor sites and then for the labelled neutrophil to accumulate at sites of inflammation may pose a challenge for the shorter half-life ^{18}F. However Bleeker-Rovers *et al*., reported the detection of infection 4 hours post injection which is encouraging for ^{18}F (4 hours would account for approximately 2.2 half-lives). Other longer lived PET isotopes are available in ^{64}Cu ($t_{1/2}$ = 12.7 hours) and ^{89}Zr ($t_{1/2}$ = 78.4 hours). The use of these radiometals would require an appropriate chelate such as NOTA for ^{64}Cu or DFO for ^{89}Zr to be linked to interleukin-8 and their effect on the affinity of interleukin-8 would have to be established.

Another strategy for inflammation imaging is to target (with radiopharmaceuticals) mediators of the inflammatory process which migrate to or may already be at the site of inflammation. An example of this would be ^{111}In radiolabelled anti-E-selectin monoclonal antibodies which have been used to image induced arthritis in pigs[24]. E-selectin is an adhesion molecule for leukocytes which is expressed on activated endothelial cells and represents the early stages of migration of leukocytes into tissue. Again, translation of this method or of a similar method for PET could prove fruitful.

Final Remarks

The title of this thesis is 'PET radiochemistry for the investigation of the biology of pain and inflammation'. I believe that this work has demonstrated a number of tools which can be used to study the biological processes involved in pain and inflammation with PET imaging. It has been demonstrated that the opioid system and the occupation of opioid receptors in the brain can be imaged and measured with PET. This means that the activity of endogenous opioids can be indirectly measured in various pain states. Using this we can understand how the endogenous opioid system is able to adapt to different pain states and if the system is failing during disease pathologies. This may give the clinic a new target for analgesics in which the endogenous opioid system is enhanced for example with enkephalinase inhibitors.

Preclinical PET has also been used to demonstrate if centrally acting mediators of the inflammatory process are able to cross the blood brain barrier. IL-1RA holds some therapeutic promise for protection against neuronal injury and its

bio-distribution, pharmacokinetics and metabolism in mice was evaluated. This was only made possible by radiolabelling IL-1RA with ^{18}F so that the preclinical PET investigation could be completed.

Finally, a tool to track the migration of leukocytes to inflammatory foci with PET for the early diagnosis of inflammatory conditions (such as the autoimmune disorder, rheumatoid arthritis) has been explored. With ^{89}Zr-loaded chitosan nanoparticles we have the possibility of a strategy that can exploit the sensitivity, resolution and quantification that PET has to offer[8]. This technique may even allow for an early diagnosis to be made before any physical symptoms of inflammation are apparent.

PET imaging remains one of the most important and powerful molecular imaging modalities available and has applications in many clinical areas including neurological disorders, oncology and infection imaging. In order for PET imaging to provide quality data, the radiotracer used must be suitable. This means designing and implementing the optimum radiochemistry routes which reliably deliver the radiotracer that will answer the biological questions being asked. I hope that with this work the importance of PET radiochemistry in pain and inflammation has become apparent. The journey from designing a PET radiotracer that will bind to the appropriate target and allows us to image that therapeutically significant target or show biological changes at the molecular level in inflammation to then designing a radiochemistry route and finally having that PET radiotracer available for clinical scanning can be a long one. But this translation is an important one, once you can appreciate the significance PET has in imaging pain and inflammation. I believe that PET radiochemistry will continue to be an important topic in the area of pain and inflammation. As well as improving the probes we currently have available, there are clearly emerging targets that will play important roles in pain and inflammation too.

References

[1] C. Cawthorne, C. Prenant, A. Smigova, P. Julyan, R. Maroy, K. Herholz, N. Rothwell, H. Boutin, *British Journal of Pharmacology* **2010**, 659.

[2] C. Brown, J. Matthews, M. Fairclough, A. McMahon, E. Barnett, A. Al-Kaysi, W. El-Deredy, A. Jones, *Pain (in press)* **2015**.

[3] M. Fairclough, C. Prenant, G. Brown, A. McMahon, J. Lowe, A. Jones, *Journal of Labelled Compounds and Radiopharmaceuticals* **2014**, *57*, 388.

[4] M. Fairclough, A. McMahon, E. Barnett, J. Matthews, C. Brown, A. Jones, *Submitted to Journal of Labelled Compounds and Radiopharmaceuticals* **2015**.
[5] S. E. Bartlett, M. T. Smith, *Life Sciences* **1995**, *57*, 609.
[6] S. M. Brown, M. Holtzman, T. Kim, E. D. Kharasch, *Anesthesiology* **2011**, *115*, 1251.
[7] C. Prenant, C. Cawthorne, M. Fairclough, N. Rothwell, H. Boutin, *Applied Radiation and Isotopes* **2010**, *68*, 1721.
[8] M. Fairclough, C. Prenant, B. Ellis, H. Boutin, A. McMahon, G. Brown, P. Locatelli, A. Jones, *Submitted to Journal of Labelled Compounds and Radiopharmaceuticals* **2015**.
[9] T. Oskouei, N. Maleki-dizaji, M. Najafi, *Iranian Journal of Basic Medical Science* **2009**, *12*, 80.
[10] D. R. Webb, *Biochemical Pharmacology* **2014**, *87*, 121.
[11] R. F. Dannals, *Journal of Labelled Compounds and Radiopharmaceuticals* **2013**, *56*, 187.
[12] J. R. Lever, *Current Pharmaceutical Design* **2007**, *13*, 33.
[13] J. J. Frost, H. S. Mayberg, B. Sadzot, R. F. Dannals, J. R. Lever, H. T. Ravert, A. A. Wilson, H. N. Wagner, Jr., J. M. Links, *Journal of Cerebral Blood Flow and Metabolism* **1990**, *10*, 484.
[14] H.-J. Wester, F. Willoch, T. R. Tolle, F. Munz, M. Herz, I. Oye, J. Schadrack, M. Schwaiger, P. Bartenstein, *Journal of Nuclear Medicine* **2000**, *41*, 1279.
[15] B. P. Roques, M. C. Fournie-Zaluski, M. Wurm, *Nature Reviews Drug Discovery* **2012**, *11*, 292.
[16] C. J. Palestro, C. Love, K. Bhargava, K., *Quarterly Journal of Nuclear Medicine and Molecular Imaging* **2009**, *53*, 105
[17] M. Karsdal, T. Woodworth, K. Henriksen, W. Maksymowych, H. Genant, P. Vergnaud, C. Christiansen, T. Schubert, P. Qvist, G. Schett, A. Platt, A.-C. Bay-Jensen, *Arthritis Research & Therapy* **2011**, *13*, 215.
[18] C. P. Bleeker-Rovers, H. J. J. M. Rennen, O. C. Boerman, A. B. Wymenga, E. P. Visser, J. H. Bakker, J. W. M. van der Meer, F. H. M. Corstens, W. J. G. Oyen, *Journal of Nuclear Medicine* **2007**, *48*, 337.
[19] M. Namavari, O. Padilla De Jesus, Z. Cheng, A. De, E. Kovacs, J. Levi, R. Zhang, J. Hoerner, H. Grade, F. Syud, S. Gambhir, *Molecular Imaging and Biology* **2008**, *10*, 177.
[20] T. Poethko, M. Schottelius, G. Thumshirn, U. Hersel, M. Herz, G. Henriksen, H. Kessler, M. Schwaiger, H.-J. Wester, *Journal of Nuclear Medicine* **2004**, *45*, 892.
[21] G. A. Lemieux, C. R. Bertozzi, *Trends in Biotechnology* **1998**, *16*, 506.
[22] O. Jacobson, D. O. Kiesewetter, X. Chen, *Bioconjugate Chemistry* **2015**, *26*, 1.
[23] M. Glaser, E. G. Robins, *Journal of Labelled Compounds and Radiopharmaceuticals* **2009**, *52*, 407.
[24] P. T. Chapman, F. Jamar, E. T. Keelan, A. M. Peters, D. O. Haskard, *Arthritis & Rheumatism* **1996**, *39*, 1371.